Structural Characterization of Crystalline Microporous Materials Using Transmission Electron Microscopy

Dissertation
zur Erlangung des Grades
"Doktor der Naturwissenschaften"
im Promotionsfach Chemie
am Fachbereich Chemie, Pharmazie, Geographie und
Geowissenschaften der Johannes Gutenberg-Universität
in Mainz

Haishuang Zhao
geb. in Henan, China

Mainz, 2019

Dekan:
Erster Berichterstatter:
Zweiter Berichterstatter:
Tag der mündlichen Prüfung: 12. November 2019

For my family

Abstract

In this thesis, the structural characterization of functional, especially crystalline microporous materials, was performed by electron diffraction tomography (EDT) technique using transmission electron microscope (TEM) and supported in combination with complementary methods. The structural elucidation of materials at the atomic level is a key step to understand their chemical and physical properties and is therefore of great importance for the development of specific applications and for the targeted design of novel materials with desired properties.

Microporous materials show unique structural features - a periodic arrangement of cavities and channels with high internal surface areas. This type of material is suitable for numerous applications in industry as well as in daily life. Since microporous materials often emerge with the factors of nano crystal size, disorder, multiple phase and low crystallinity, the structural characterization of these materials is challenging with traditional and conventional diffraction methods like single-crystal X-ray diffraction (XRD) or X-ray powder diffraction (XRPD). The used method in this dissertation, namely automated diffraction tomography (ADT), enables structure analysis directly from single nanosized crystals and can overcome the mentioned challenges. In this work, the structural characterization started with an electron beam stable ceramic ($Al_4B_2O_9$) with a disordered structure and then focused on several beam sensitive microporous materials. The first phase of structural analysis of microporous materials comprises of crystal structure determinations of two metal-organic frameworks (Zr-MOFs) with large lattice parameters and a novel zeolite (THK-2) in a multiphase mixture. Subsequently, zeolites with industrial interests were structurally investigated after targeted modifications. On basis of the known crystal structure, the crystal disorder could be described for the metal interlayer expanded zeolites (M-IEZ-RUB-36) by structural modelling and simulation of electron diffraction patterns in the program package DISCUS. In addition, the positions of organic structure directing agents (OSDAs) in the pore of the porous materials: SSZ-51 and SOD; the Cu atom position in a dehydrogenated selective catalytic reduction (SCR) catalyst (Cu-chabazite) were determined from three-dimensional ADT data. This work provides an important contribution to the overall structure characterization of microporous nanomaterials including *ab initio* structure determination, disorder analysis, determining the position of OSDAs in zeolites and detecting the metal atom position in dehydrated zeolite, which would not be accessible to elucidate the structural features with a reliable accuracy as shown in this work using the conventional methods.

Zusammenfassung

In dieser Dissertation wurde die strukturelle Charakterisierung funktioneller insbesondere kristalliner mikroporöser Materialen über Elektronenbeugungstomographie (EDT) mittels Transmissionselektronenmikroskope (TEM) durchgeführt und in Kombination mit komplementären Methoden untermauert. Die Strukturaufklärung von Materialien auf atomarer Ebene trägt zum Verständnis chemischer und physikalischer Eigenschaften bei und ist damit zur Entwicklung spezieller Anwendungen und für das gezielte Design neuer Materialien mit den jeweils gewünschten Eigenschaften von großer Bedeutung.

Mikroporöse Materialien verfügen über eine einzigartige strukturelle Besonderheit - die regelmäßige Anordnung von Hohlräumen und Kanälen mit großen inneren Oberflächen. Solche Festkörper werden in der Industrie sowie im täglichen Leben für vielfältige Anwendungen eingesetzt. Durch Faktoren wie Nanokristalle, Fehlordnung, Phasengemische und geringe Kristallinität ist die Strukturaufklärung von mikroporösen Materialien mit traditionellen und konventionellen Beugungsmethoden wie der Einkristallstrukturanalyse (XRD) oder Röntgenpulverdiffraktometrie (XRPD) eingeschränkt. Die in dieser Dissertation verwendete Methode der automatisierten Elektronenbeugungstomographie (ADT) erlaubt die die Strukturanalyse direkt an einzelnen Nanokristallen und hebt damit diese Beschränkungen auf. Nach der Charakterisierung einer elektronenstrahlstabilen Keramik ($Al_4B_2O_9$) mit fehlgeordneter Struktur lag der Schwerpunkt auf der Strukturanalyse von mehreren strahlempfindlichen mikroporösen Materialien. Zuerst standen zwei metallorganische Gerüstverbindungen mit großen Gitterkonstanten sowie ein neuartiger Zeolith (THK-2), der in einem mehrphasigen Gemisch vorlag. In einem zweiten Schritt wurden industriell interessante Zeolithe nach gezielter Modifikation strukturell untersucht. Aufbauend auf der in diesen Fällen bekannten Kristallstruktur, konnte für die "metal interlayer expanded zeolites" (M-IEZ-RUB-36) durch Strukturmodellierung und Simulation von Elektronenbeugungsmustern im Programmpaket DISCUS die Fehlordnung beschrieben werden. Außerdem gelang es, in den Poren der porösen Materialen SSZ-51 und SOD die Position der organischen struktursteuernden Agenzien (OSDAs) sowie die Cu-Positionen im dehydrierten SCR-Abgaskatalysator (Cu-Chabasit) aus dreidimensionalen ADT-Daten zu lokalisieren. Diese Arbeit, die *ab initio* Kristallstrukturbestimmung, Fehlordnungsanalyse, Lokalisierungen der OSDAs und Ermittlung der Position von Metallatom abdeckt, leistet einen wichtigen Beitrag zur erweiterten Strukturcharakterisierung mikroporöser nanokristalliner Materialien, was mit den üblichen Methoden zur Aufklärung von Festkörperstrukturen, in dem hier gezeigten Umfang und der erreichten Genauigkeit, nicht möglich gewesen wäre.

Contents

Abstract i

Zusammenfassung iii

1 Introduction 1

2 Principle and methods 5

2.1 Crystallographic basics . . . 5
2.1.1 Basic concepts . . . 5
2.1.2 Crystal systems . . . 6
2.1.3 Reciprocal lattice . . . 7
2.1.4 Structure factor . . . 8
2.1.5 Stacking disorder . . . 9
2.2 Transmission electron microscope . . . 10
2.2.1 Introduction . . . 10
2.2.2 TEM components . . . 11
2.2.3 Imaging system . . . 13
2.2.4 Electron diffraction . . . 14
2.2.5 Scanning electron transmission microscopy . . . 16
2.3 Electron diffraction tomography . . . 16
2.3.1 Principle of ADT method . . . 16
2.3.2 Precession electron diffraction . . . 18
2.3.3 ADT data acquisition and processing . . . 19
2.3.4 Structure determination from ADT data . . . 20
2.4 Energy-dispersive X-ray spectroscopy . . . 23
2.5 X-ray powder diffraction . . . 24
2.5.1 Bragg's law . . . 24
2.5.2 X-ray powder diffraction . . . 25
2.5.3 Structure determination from XRPD data . . . 27

3 TEM and ADT 29

3.1 Introduction . . . 29
3.2 Transmission electron microscope . . . 30
3.3 TEM grid preparation . . . 31
3.4 TEM specimen holder . . . 31

3.5 ADT data acquisition . . . 34
3.6 ADT data analysis . . . 36
  3.6.1 Data pre-processing . . . 37
  3.6.2 Visual analysis of 3D reconstruction . . . 39
  3.6.3 Unit-cell determination . . . 39
  3.6.4 Intensity extraction . . . 40

4 Introduction to investigated materials 41
4.1 Aluminium borate . . . 41
  4.1.1 Mullite . . . 41
  4.1.2 Mullite-type crystal structure . . . 42
  4.1.3 Aluminum borates . . . 43
  4.1.4 Synthesis of $Al_4B_2O_9$ . . . 44
  4.1.5 Research questions . . . 44
4.2 Metal-organic frameworks . . . 45
  4.2.1 Metal-organic frameworks . . . 45
  4.2.2 Synthesis and structure properties . . . 46
  4.2.3 Applications of MOFs . . . 48
  4.2.4 Syntheses of MOFs . . . 49
  4.2.5 Research questions . . . 50
4.3 Zeolites . . . 51
  4.3.1 Introduction . . . 51
  4.3.2 Metal-containing zeolites . . . 51
  4.3.3 Organic structure directing agent in zeolite . . . 52
  4.3.4 Information of investigated samples . . . 53
  4.3.5 Research questions . . . 54

5 Experimental section 55
5.1 $Al_4B_2O_9$ . . . 55
  5.1.1 X-ray powder diffraction . . . 55
  5.1.2 TEM experiments . . . 56
  5.1.3 Lattice parameter determination . . . 57
  5.1.4 Structure solution and refinements . . . 58
  5.1.5 Structure modeling . . . 58
5.2 Zr-MOFs . . . 60
  5.2.1 TEM experiments . . . 60
  5.2.2 Data evaluation . . . 61
  5.2.3 Thermal stability . . . 61
5.3 THK-2 zeolite . . . 62
  5.3.1 TEM experiments . . . 62
  5.3.2 Data evaluation . . . 62

5.4 M-IEZ-RUB-36 zeolites 63
  5.4.1 TEM experiments 63
  5.4.2 Data evaluation 63
5.5 SSZ-51 and SOD zeolites 64
  5.5.1 Synthesis of samples 64
  5.5.2 Solid-state NMR spectroscopy 65
  5.5.3 Thermal Stability 65
  5.5.4 X-ray powder diffraction 65
  5.5.5 TEM experiments 66
  5.5.6 ADT data evaluation 67
5.6 CHA zeolites 68
  5.6.1 TEM experiments 68
  5.6.2 Dehydration of CHA zeolites 68
  5.6.3 X-ray powder diffraction 68
  5.6.4 ADT data evaluation 69

6 Results and discussion 71
6.1 Order and disorder in $Al_4B_2O_9$ 71
  6.1.1 Sample overview and EDX analysis 72
  6.1.2 ADT data processing 73
  6.1.3 Structure determination 74
  6.1.4 Description of the crystal structure 76
  6.1.5 HRTEM and HAADF-HRSTEM 79
  6.1.6 Disorder analysis and simulation 80
  6.1.7 Summary 84
6.2 Crystal structures of Zr-MOFs 85
  6.2.1 Sample overview of CAU-27 86
  6.2.2 ADT data analysis of CAU-27 87
  6.2.3 Structure determination of CAU-27 87
  6.2.4 HRTEM imaging of CAU-27 90
  6.2.5 Crystal structure of CAU-27 91
  6.2.6 Sample overview of CAU-30 92
  6.2.7 ADT data analysis of CAU-30 93
  6.2.8 Structure determination of CAU-30 94
  6.2.9 HRTEM imaging of CAU-30 97
  6.2.10 Crystal structure of CAU-30 98
  6.2.11 Summary 99
6.3 Crystal structure of THK2 zeolite 100
  6.3.1 Sample overview 101
  6.3.2 ADT data analysis 102
  6.3.3 Structure determination 104
  6.3.4 HRTEM imaging 107

6.3.5 Crystal structure description 109
6.3.6 Summary 111
6.4 Disorder in M-IEZ-RUB-36 zeolites 112
6.4.1 General information 113
6.4.2 Interlayer expansion 114
6.4.3 ADT data evaluation 114
6.4.4 Structure solution for the average structures 116
6.4.5 Disorder analysis and simulation 117
6.4.6 Summary 122
6.5 Organic template in SSZ-51 and SOD zeolite 123
6.5.1 Sample overview of TMP-SSZ-51 124
6.5.2 Solid-state NMR 124
6.5.3 Thermal stability of TMP-SSZ-51 126
6.5.4 Temperature-dependent XRPD of TMP-SSZ-51 126
6.5.5 Structure determination of TMP-SSZ-51 128
6.5.6 Structure description of TMP-SSZ-51 132
6.5.7 Organic template in PYS-SOD 134
6.5.8 Summary 137
6.6 Metal atom in the pore of CHA zeolite 138
6.6.1 General information 139
6.6.2 Structure solution 140
6.6.3 Kinematical refinement 140
6.6.4 Dynamical refinement 141
6.6.5 Discussion 142
6.6.6 Summary 144

7 Conclusion **145**

References **149**

Appendix **169**
Appendix A: Supplementary data for $Al_4B_2O_9$ 169
Appendix B: Supplementary data for Zr-MOFs 174
Appendix C: Supplementary data for THK-2 177
Appendix D: Supplementary data for TMP-SSZ-51 178
Appendix E: Supplementary data for dehydrated CHA zeolites 179
Appendix F: Submitted manuscript about TMP-SSZ-51 183

List of Publications **199**

Erklärung **201**

List of Figures

1.1 Project overview of research on porous materials 4

2.1 Unit cell with lattice parameters and a lattice plane 6
2.2 Scheme of the electron interaction with a thin specimen 10
2.3 Diagram of the main components of a conventional TEM 11
2.4 Schematic diagram showing the two basic operations in a TEM 13
2.5 Schematic presentation for the formation of a diffraction pattern 15
2.6 Sketch of reciprocal spaces of a traditional tilt collection 17
2.7 Sketch of PED technique 18
2.8 Schematic representation of ADT acquisition and data processing 19
2.9 Schematic illustration of X-ray emission during electron atom interaction . . 23
2.10 Schematic representation of Bragg's law 24
2.11 Powder diffractometer with two geometry modes 25
2.12 An exemplary powder diffraction pattern 26

3.1 Overview of TEM work process and possible applications 29
3.2 Transmission electron microscopes 30
3.3 Sheme of the procedures for preparation of a TEM grid 31
3.4 TEM specimen holders 32
3.5 Plasa cleaner and pump system 33
3.6 NED and PED patterns of $Al_4B_2O_9$ viewed along $\boldsymbol{c}^*$ direction 34
3.7 A brief diagram of TEM calibration sequence for ADT 36
3.8 Workflow of the program eADT 37
3.9 Electron diffraction pattern processing 37
3.10 Three-dimensional reconstructed diffraction spaces 39
3.11 Electron diffraction pattern processing 40

4.1 Technical applications of mullites 41
4.2 The chain structure of 2:1 mullite 42
4.3 Plot of potential phases in the SiO_2-Al_2O_3-B_2O_3 system 43
4.4 The general classification of porous materials 45
4.5 Examples of organic linkers in MOFs 46
4.6 Schematic illustration for the design of MOFs 47
4.7 Organic carboxylate linkers for the synthesis of CAU-27-BDC 49
4.8 Linker for the synthes of Zr-CAU-30 50

4.9 Building scheme of the crystal structure of CHA 52

5.1 Pawley-fit plot of $Al_4B_2O_9$. 55
5.2 Basic structure components used for constructing superstructure. 59
5.3 Thermogravimetric curve of Zr-CAU-30 61
5.4 The organic SDAs used in this project 64
5.5 XRPD diagrams of SSZ-51 66

6.1 STEM images of $Al_4B_2O_9$ nonaparticles 72
6.2 EDX spectrum of $Al_4B_2O_9$ 73
6.3 3D reconstruction of reciprocal space and 2D slices of $Al_4B_2O_9$ 74
6.4 Electron potential map of structure solution of $Al_4B_2O_9$ 75
6.5 Plot of Rietveld refinement for $Al_4B_2O_9$ 76
6.6 Coordinations of Al and B atoms in $Al_4B_2O_9$ 78
6.7 Building units of $Al_4B_2O_9$ 78
6.8 Crystal structure of $Al_4B_2O_9$ 78
6.9 HRTEM image of $Al_4B_2O_9$ 79
6.10 HAADF-HRSTEM image of $Al_4B_2O_9$ 80
6.11 Single electron nano diffraction patterns of $Al_4B_2O_9$ 81
6.12 Single electron nano diffraction pattern and intensity profiles of $Al_4B_2O_9$ . . 82
6.13 Experimental and simulated electron diffraction patterns of $Al_4B_2O_9$ 83
6.14 TEM images and crystal diameter distribution of CAU-27-BDC 86
6.15 Reconstruction of 3D reciprocal space and 2D slices of CAU-27-BDC 87
6.16 Electron potential map of structure solution of CAU-27-BDC 88
6.17 Plot of Rietveld refinement of CAU-27-BDC 89
6.18 HRTEM image of Zr-CAU-27 90
6.19 Crystal structure of Zr-CAU-27 91
6.20 STEM images and EDX spectrum of Zr-CAU-30 92
6.21 3D reconstruction of reciprocal space and 2D slices of Zr-CAU-30 93
6.22 Electron potential map of structure solution of Zr-CAU-30 95
6.23 X-ray Powder diagrams of Zr-CAU-30 96
6.24 Plot of Rietveld refinement of Zr-CAU-30 96
6.25 HRTEM image of Zr-CAU-30 97
6.26 Crystal structure of Zr-CAU-30 98
6.27 Schematic illustration for the assembly of Zr-CAU-30 99
6.28 TEM and STEM images of zeolite THK-2 101
6.29 EDX spectrum of THK-2 101
6.30 3D reconstruction of reciprocal space of THK-2 (Cry1) 103
6.31 3D reconstruction of reciprocal space of THK2 (Cry2) 103
6.32 3D reconstruction of reciprocal space of MTW 104
6.33 Electron potential map of structure solution of THK-2 105
6.34 Plot of combined Rietveld refinement of THK-2 and MTW 106

6.35 HRTEM image of THK-2 with corresponding structural model 107
6.36 HRTEM image of THK-2 with corresponding structural model 108
6.37 Structure segment of THK-2 109
6.38 Crystal structure of THK-2 110
6.39 General information about M-IEZ-RUB-36 113
6.40 Schematic representation of the interlayer expansion 114
6.41 Overview of reconstructed reciprocal space of Ti-RUB-36 115
6.42 Reconstructed reciprocal space of Ti-RUB-36 115
6.43 Electron potential map of structure solution 116
6.44 Scheme for the process of disorder analysis 117
6.45 Superstructure modelling with ordered stack sequences 118
6.46 Simulated electron diffraction patterns 119
6.47 Possible stacking on layer *A* and an example of constructed supercell 120
6.48 Simulated and recorded electron diffraction patterns of Zn-IEZ-RUB-36 . . . 121
6.49 Simulated and recorded electron diffraction patterns of Ti-IEZ-RUB-36 122
6.50 STEM image and EDX spectrum of TMP-SSZ-51 124
6.51 ^{13}C-CP/MAS NMR spectra of TMP-SSZ-51 and PYS-SOD 125
6.52 DSC/TG curves of TMP-SSZ-51 126
6.53 Temperature dependent XRPD of TMP-SSZ-51 127
6.54 Reconstructed three-dimensional diffraction volumes of TMP-SSZ-51 128
6.55 Fourier potential map of TMP-SSZ-51 129
6.56 Plot of Pawley fit for TMP-SSZ-51 131
6.57 Plot of Rietveld refinement of SSZ-51 131
6.58 Crystal structure of TMP-SSZ-51 132
6.59 Reconstructed three-dimensional diffraction volumes of PYS-SOD 134
6.60 Reconstructed three-dimensional diffraction volumes of PYS-SOD 135
6.61 Plot of Rietveld refinements of PYS-SOD 136
6.62 Possible translationsgleiche subgroups of SOD 137
6.63 XRPD diagram, STEM/TEM images and DTA-TG curve of CHA zeolites . . 139
6.64 Potential maps from structure solutions of CHA zeolites 140
6.65 Difference potential maps from kinematical refinements of CHA zeolites . . 141
6.66 Difference potential maps from dynamical refinements of CHA zeolites . . . 142
6.67 Crystal structure of dehydrated Cu-CHA zeolite 143

List of Tables

2.1 The seven crystal systems . . . 7
2.2 Wavelength of characteristic X-rays generated by different anode materials. . . 25

3.1 Selected instrumental details of applied TEMs . . . 30

5.1 ADT measurements details of $Al_4B_2O_9$ . . . 56
5.2 Lattice parameters of $Al_4B_2O_9$ determined from ADT data . . . 57
5.3 Experimental details of structure solution of $Al_4B_2O_9$ . . . 58
5.4 Experimental details of ADT data collection for Zr-MOFs . . . 60
5.5 Experimental details of ADT data collection for THK-2 . . . 62
5.6 Experimental details of ADT data collection for M-IEZ-RUB-36 zeolites . . . 63
5.7 Parameters of structure solutions of M-IEZ-RUB-36 zeolites . . . 64
5.8 Experimental details of ADT data collection for TMP-SSZ-51 and PYS-SOD . . . 66
5.9 Experimental details of structure solutions of as-synthesized zeolites . . . 67
5.10 Experimental details of ADT data collection for CHA zeolites . . . 68
5.11 Input parameters of reflection extraction in PETS . . . 69

6.1 Quantitative EDX results of $Al_4B_2O_9$ . . . 72
6.2 Parameters of structure solution of CAU-27-BDC . . . 88
6.3 Selected bond distances of CAU-27-BDC . . . 91
6.4 Lattice parameters of Zr-CAU-30 . . . 93
6.5 Parameters of structure solution of Zr-CAU-30 . . . 94
6.6 Crystallographic data obtained from ADT . . . 102
6.7 Parameters of structure solution of THK2 . . . 105
6.8 Selected results of Rietveld refinement of THK2 . . . 106
6.9 Selected bond lengthes of THK-2 . . . 109
6.10 Average lattice parameters of M-IEZ-RUB-36 . . . 116
6.11 Element operation and corresponding shift vector between the layers . . . 121
6.12 Quantitative EDX results of $Al_4B_2O_9$ . . . 124
6.13 Selected crystallographic data parameter of Rietveld refinement of SSZ-51 . . . 130
6.14 Selected bond lengths and bond angles of SSZ-51 . . . 133
6.15 Atomic coordination and occupation parameter of PYS-SOD . . . 135
6.16 Selected parameters of Rietveld refinements of PYS-SOD . . . 136
6.17 Parameters of structure refinements for CHA zeolites . . . 141
6.18 Temperature factors in the refined structures of CHA zeolites . . . 143

6.19 Selected bond lengths and bond angles of dehydrated CHA zeolites 143

List of Abbreviations

XRD X-ray diffraction
TEM transmission electron microscopy
SEM scanning electron microscopy
STEM scanning transmission electron microscopy
SE secondary electron
BSE back scattered electrons
SAED selected area electron diffraction
HRTEM high-resolution transmission electron microscopy
ADT automated diffraction tomography
ED electron diffraction
EDX energy-dispersive X-ray spectroscopy
EELS electron energy loss spectroscopy
NED nano electron diffraction
PED precession electron diffraction
HAADF high angle annular dark field
BF bright field
ADF annular dark field
MRC Medical Research Council
PCPs porous coordination polymers
NMR nuclear magnetic resonance
TGA thermogravimetric analysis
DTA differential thermal analysis
MOFs metal-organic frameworks
1D one-dimensional
2D two-dimensional
3D three-dimensional
SUBs secondary building units
COFs covalent organic frameworks
CCD charge-coupled device
2K 2048 x 2048 pixel
4K 4096 x 4096 pixel
XRPD X-ray powder diffraction
R_{wp} weighted profile R factor
R_{exp} expected R factor

gof goodness of fit
Biso isotropic temperature factor
FWHM full width at half maximum
OSDAs organic structure directing agents
DFT density functional theory
IZA International Zeolite Association
OSDAs organic structure directing agents
FEG field emission gun
SCR selective catalytic reduction
SOD sodalite
PYS-SOD pyrrolidine silica sodalite

1 Introduction

Within last decades, the emergence and widespread application of new advanced solid-state materials ranging from inorganic nano particles to biological macromolecules, have changed the world and thus accelerated the development of human society. The changes cover almost evry aspect of our daily lives as well as the industrial innovation. Scientists from academic research institutes and industrial areas are making great efforts to look for novel materials with the expectation of improved properties.[1,2] The accomplishment of these challenges require the contributions from various fields including chemistry, biology, physics, earth science, computer science, mathematics, engineering, etc. The interdisciplinary cooperation leads to the emergences of plenty of novel materials with outstanding properties.

One of the crucially important tasks in material science lies on finding out the relationship in among structure-property-performance of materials.[3–5] The properties of solids depend not only on the chemical composition but also on the three-dimensional (3D) atomic arrangement inside the matters. The relationship can be exemplified by the polymorphs of diamond and graphite[6,7] which are made of the exact same chemical composition - carbon exhibiting significantly different properties. So far, diamond is known as the hardest substance found on earth and can be applied for cutting, grinding, etc. Graphite is extremely soft and of pliable nature; thus it is widely used in lead pencils. The different structures, namely the atomic arrangement of carbon atoms, result in the diverse physical properties.[7] In diamond, the carbon atoms are sp^3-hybridized to form a three-dimensional network of strong covalent bonds. Whereas in graphite, each carbon atom shares electrons with three neighbouring carbon atoms through a sp^2-hybridization to build a two-dimensional (2D) layered structure. The industrial catalysts aluminosilicate zeolites, consisting of the same chemical composition, show also different properties due to their crystalline structures with various pore sizes or pore styles.[8–10] Hence, the structural characterization of solids is a key step to understand the physical properties in order to optimize the applications or to design novel materials with desired features.

Most substances exist in the form of solids in the natural or in the synthetic state. Major solids occur in crystalline phases, in which the atoms, ions or molecules are arranged periodically in highly ordered structures with a spatially infinite extension.[11,12] Various techniques on basis of modern instruments have been utilized to characterize materials in order to obtain the insights into the atomic arrangement of the solid state. For instance, a lab X-ray diffractometer can be used to identify different phases and deliver the crystallographic information of a crystalline material. Alternatively, dedicated instrumentation can be used to collect neutron diffraction or Synchrotron XRPD data.[13–18]. Utilizing electron radiation like microscopic techniques[19–21], scanning electron microscopy (SEM) and transmission electron microscopy (TEM), can be performed for chemical or structural characterizations by means of modern detectors. So far, an atomic resolution can be reached down to of 0.5 Å in imaging mode with a corrected electron microscope.[22] Depending on the working modes it can provide various information e.g. the chemical composition with energy-dispersive X-ray spectroscopy (EDX), detecting and quantifying the elements present with electron energy loss spectroscopy (EELS), the crystal structure by electron diffraction (ED), or even direct imaging of the atomic arrangement using high-resolution transmission electron microscopy (HRTEM). Depending on the research questions and the properties of materials, electron microscopy is combined with other methods, e.g., solid-state nuclear magnetic resonance (NMR), density functional theory (DFT), differential thermal analysis (DTA) with thermogravimetric analysis (TGA), etc. to characterize materials.[14,23–30]

X-ray crystallography is a well-known and most conventional technique for crystal structure determination often based on a lab X-ray diffractometer with radiations e. g., MoK_α, CuK_α.[31,32] X-ray diffraction including single-crystal XRD and XRPD, are applied as the traditional approaches to gain the structural information at a atomic level.[18,31,33,34] The major requirement for single-crystal XRD is the crystal size which must be at least with a few micrometres. Plenty of crystal structures were determined from single-crystal XRD data.[35,36] In fact, not all the crystals can be grown large enough for single-crystal XRD measurements. XRPD is an alternative option for crystalline materials which are not accessible for single-crystal XRD.[18] As a most-used technique, XRPD can identify the phase of well-known structures as well as provide the crystal structure of an unknown phase. Until now, numerous crystal structures were determined from XRPD data.[37–40] However, there are some limits, e.g., peak overlapping and one-dimensional (1D) information, resulting in the difficulties as impossible indexing for complex structure using XRPD approach.

As compared to the established approach for crystal structure determination by X-ray powder diffraction, electron crystallography has been emerged as an important method and showed its power in structural characterization of nanocrystalline materials.[41,42] The method is based on two techniques, ED and HRTEM, using an conventional transmission electron microscope. In comparison to the X-ray beam, electrons have a stronger interaction with matters[21], enabling to elucidate the crystal structure of nanocrystalline material. An unknown crystal structure can be solved from ED data and the atomic arrangement can even be directly visualized in a HRTEM image. Since the last decade, several advanced techniques have been developed to acquire and analyse three-dimensional electron diffraction data focusing on single nano-scaled crystals. In general, the method for automatically collecting 3D data is named electron diffraction tomography (EDT). The first EDT method, named ADT[43–47], enables a fully automated acquisition of 3D tomographic electron diffraction data. The ADT technique was developed by U. Kolb and the co-workers in 2007 and combines nano electron diffraction, tilt series acquisition and precession electron diffraction (PED) to derive the crystal structure from a single nano crystal.[45] The next emerged technology is rotation electron diffraction (RED)[48–52] using a combination of beam tilt and crystal tilt. Recently, new techniques, e.g. fast electron diffraction tomography[53] and ultra-fast electron diffraction tomography[54], were developed on a continuous tilt of a selected crystal. The fast EDT methods allow a fast collection of ED data using modern high-speed detection cameras and are ideal for the structure determination of beam sensitive materials.[54–56] EDT methods have been applied to plenty of complex crystal structures and become an efficient methods in crystal structure characterization.[34,52,57–63] Dynamical effects are already significantly reduced for ED data acquisition and can be further reduced by applying electron beam precession.[64–66] The structural characterization of electron beam sensitive materials like organic compounds and metal-organic frameworks (MOFs) are accessible by EDT methods under mild electron beam radiation or sample cooling with liquid nitrogen.[67] In recent years, ADT approach was applied to characterize various crystal structures with complicate crystallographic features as low-crystallinity sample, multiphase, twinning, disorder, large unit-cell, etc.[47,57,58,68–73]

In this dissertation, structural investigations using ADT and further complementary characterization methods started with the ceramic material aluminium borate $Al_4B_2O_9$ and focused on subsequently beam sensitive microporous materials - zeolites and MOFs. Aluminum borates, members in the mullite-type family, are a series of silicon-free boron compounds with various Al_2O_3:B_2O_3 ratios according to the binary Al_2O_3-B_2O_3 system.[29,74–79] Aluminum borates can be synthesized from a mixture of Al_2O_3 and B_2O_3 by a solid-state reaction at high temperatures[76,78], sol-gel synthesis, thermal evaporation and one-step combustion.[29,74,77,80]. Due to the Al:B ratio and possible vacancy of oxygen atom, defects or disorder often occur in the structure of aluminium borate. Aluminum borates are important mullite-type ceramic raw materials with high thermal and chemical stability, outstanding mechanical properties and low temperature expansion.[76,80–82]. Microporous crystalline materials are a class of solids with unique structural features and are constructed by secondary building units (SUBs). The assembly of SBUs results in a periodic and porous network containing pores or channels with high surface area and large pore volume.[8,83,84] Microporous materials have pore sizes of less than 2 nm[85,86] and can be metal-organic compounds MOFs, inorganic zeolites and even pure organic novel porous materials like covalent organic frameworks (COFs)[87]. MOFs are a new class of organic-inorganic hybrid porous solids constructed by metal ions/clusters with bridging organic linkers.[84,88] Zeolites are a series of aluminosilicate minerals with a 3D framework constructed by interlinked TO_4 tetrahedra (T = Si, Al).[9,10,89] T site can also be B, P, Ga, etc. Zeolites occur originally from the nature but are nowadays widely synthesized in the industry. Due to the architecture with pores and changeable building units, microporous materials show the important applications in various areas as catalysis, gas storage, drug delivery, etc.[88,90–102] Zeolites and zeolite-type porous compounds are widely used as catalysts in petroleum cracking and selective catalytic reductions (SCRs) as well as reforming processes.[91,92,103–111] The structural characterizations of these materials are always challenging with traditional X-ray crystallography due to the following reasons: disordered structure in mullite-type compounds; low crystallinity and large or extra-large unit-cell of nanocrystalline MOFs; stacking disorder, inter-growth, low crystallinity, nano-scaled crystals and multiple phases in zeolites. ADT technique, as an efficient structure characterization method, shows its power and advantage to solve these complicate problems.

The research tasks of this thesis are the structural characterizations of crystalline materials at atomic level by means of transmission electron microscope. The major objective is to solve the crystallographic problems only accessible with ADT method and to deliver a proof for the applicability of ADT to advanced structural investigation. The study of these structural features may be supported by a combination of other methods as XRPD, HRTEM, EDX, TG, structural modelling, simulation for an unbiased structural characterization.

- **Aluminum borate**: $Al_4B_2O_9$. The structural order and disorder phenomena in $Al_4B_2O_9$ should be described and elucidated by combined approaches including structure determination, high-resolution imaging, structural modelling and disorder simulation.
- **Microporous materials**: Zr-MOFs, metal-containing zeolites and as-synthesized zeolites. For a series of selected materials, important features like the framework topology, including size and shape of the cavities as well as crystallographic faults, the position of template molecules, or active centres in zeolite should be investigated. As summarized in Fig. 1.1, the research questions consist of two topics: (1) **arrangement of atom in the framework** on basis of *ab initio* structure determinations of beam sensitive MOFs with large crystal lattice and a novel zeolite from polyphasic sample and disorder elucidation of metal-containing zeolites; (2) **arrangement of guest molecule or ion in the pore** on basis of determining the position of organic molecules in as-synthesized zeolites and detecting the location of metal atom in dehydrated zeolite.

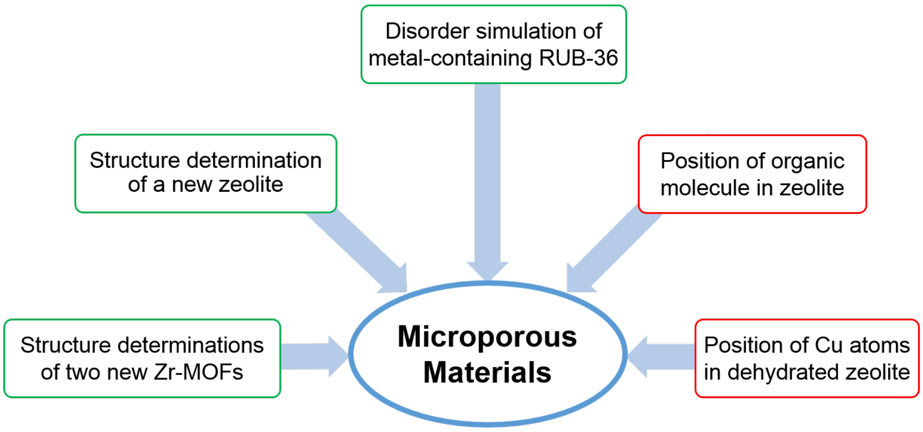

Figure 1.1: Project overview of research on porous materials in the dissertation. Projects about topic (1) marked with green boxes and topic (2) with red bosxes.

2 Principle and methods

This chapter comprises of crystallographic basics, the brief introduction to TEM including its components and work modes, the description of ADT technique, EDX, X-ray powder diffraction and the introduction to crystal structure determination from ADT and XRPD data.

2.1 Crystallographic basics

2.1.1 Basic concepts

A *crystal* is a solid matter formed of a highly ordered three-dimensional periodic arrangement of components which can be atoms, molecules or ions.[31,112] The description of the arrangement is the *crystal structure* and a compound consisting of crystal particles is considered as *crystalline phase*. Matters have the tendency to grow as crystals through a *nucleation* and *crystallization* process, since the crystalline phase usually is the state of lowest energy.[112] A solid without a long-range 3D structural periodicity is partly or fully *amorphous* like glass.[113] The phenomenon that crystalline compounds are made of some chemical compositions but exist in more than one crystal structure is called *polymorphisms*.

A crystal lattice, as a mathematical concept, describes the crystal structure as the geometrical basic. A *lattice* is a 3D periodic arrangement of points, which own the same local surroundings. Each lattice point can be generated from one to another by translation vector $\boldsymbol{r}$ which can be described by equation 2.1:

$$\boldsymbol{r} = n_1\boldsymbol{a} + n_2\boldsymbol{b} + n_3\boldsymbol{c} \tag{2.1}$$

with n_1, n_2, n_3 integers.[31] The independent vectors are called *basis vectors*: $\boldsymbol{a}$, $\boldsymbol{b}$, $\boldsymbol{c}$ describing the translation of the basic unit along three main orientations of the lattice space. The smallest 3D repeat unit in a lattice is the *unit cell*, as shown in Fig. 2.1. It must be noted that each corner of the unit cell must own the identical surroundings. Since there is more than one way to present the periodicity, the selection of the origin, the shape and size of unit cell is highly arbitrary. The shape of a unit cell is decided by *lattice parameters* including a, b, c (lattice constants = lengths of the basis vector) and α, β, γ (unit cell angles) as shown in Fig. 2.1. A crystal structure is generated through an ideal three-dimensional stacking of unit cell.

If the perfect periodic arrangement of unit cell is interrupted by factors like missing atoms, the behaviour of deviation from an ideal crystal is called *crystal defect*.[112]

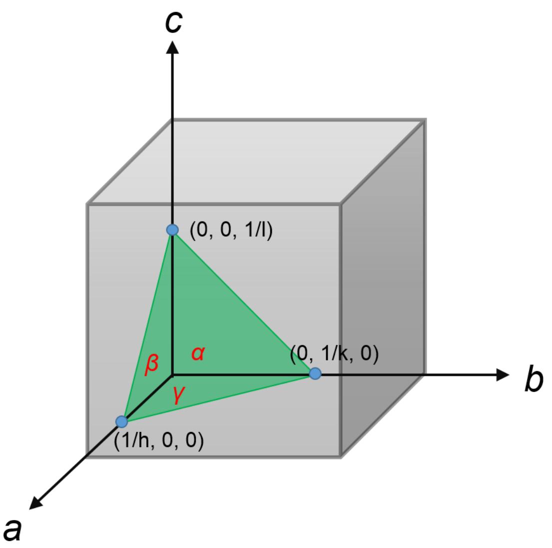

Figure 2.1: Unit cell with lattice parameters and a lattice plane (marked in green).

A *lattice plane* can be any plane passing through at least three nonlinear lattice points.[114] A series of equivalent lattice planes creates a family of parallel planes. As illustrated in Fig. 2.1, the green lattice plane intersects the three main axes at the lattice points: ($1/h$, 0, 0), (0, $1/k$, 0), (0, 0, $1/l$). The inverse values of the intercepts on the axes are called *Miller indices*[31,112,115] (hkl) where h, k, l are three integers. Miller indices determine the lattice plane orientation. If the lattice plane runs parallel to one axis, then the index on this axis is zero. The distance between two neighbouring lattice planes is called *interplanar distance* $d_{(hkl)}$, e. g. for the cubic crystal system with $a = b = c$ and $\alpha = \beta = \gamma = 90°$, $d_{(hkl)}$ can be calculated with equation 2.2:

$$d_{(hkl)} = \frac{a}{\sqrt{h^2 + k^2 + l^2}} \tag{2.2}$$

2.1.2 Crystal systems

Beside the periodic characteristic, the crystal may bear symmetry as another important feature, which has direct influence on the physical properties of crystals.[116] The nature of lattice constants and lattice angles defines the symmetry possibilities of a lattice. According to the symmetric features, the lattice can be divided in seven *crystal systems*: triclinic, monoclinic, orthorhombic, tetragonal, rhombohedral, hexagonal, and cubic (Table 2.1). Based on the number of lattice points and their positions in a unit cell the lattice can be distinguished with five *lattice types*: primitive (P), body centred (I), face centred (F), base centred (A, B, C), rhombohedral (R). 14 *Bravais lattices* are resulted from the possible combinations of seven crystal systems and five lattice types as concluded in Table 2.1.[11,114]

Table 2.1: The seven crystal systems.[11,114]

Crystal system	Lattice parameters	Possible lattice type
triclinic	$a \neq b \neq c, \alpha \neq \beta \neq \gamma$	P
monoclinic	$a \neq b \neq c, \alpha = \gamma = 90°, \beta \neq 90°$	P, C
orthorhombic	$a \neq b \neq c, \alpha = \gamma = \beta = 90°$	P, F, I, A (B, C)
trigonal	$a = b = c, \alpha = \gamma = \beta \neq 90°$	R
hexagonal	$a = b \neq c, \alpha = \beta = 90°, \gamma = 120°$	P
tetragonal	$a = b \neq c, \alpha = \gamma = \beta = 90°$	P, I
cubic	$a = b = c, \alpha = \gamma = \beta = 90°$	P, F, I

The operation (*rotation*, *reflection* and *inversion*) leaving an object identically after a movement is a *symmetry* operation. The symmetry operation constitutes of *symmetry elements*: a point (*centre of inversion*), a line (*axis of rotation*) or a plane (*mirror plane*). If these mentioned symmetry elements combine with translation, two more symmetry elements: screw axis (rotation + translation) and glide plane (reflection + translation) can be generated. The combination of all symmetry elements results into 17 two-dimensional *plane groups* (also referred to as *Wallpaper groups*) and 32 *crystal classes* (also called 32 *point groups*).[117] Further combinations of the 32 crystal classes and the above mentioned 14 Bravais lattices produce 230 three-dimensional *space groups*. Various information about the crystallographic details are summarized in the book *International Tables for Crystallography: Space-Group Symmetry (Vol. A)*[116].

2.1.3 Reciprocal lattice

A supporting mathematical tool *reciprocal lattice* is introduced to describe the diffraction phenomena of a crystal and represent the diffraction experiment in a simple way.[31] The experimental diffraction pattern is an image of reciprocal lattice and is generated by a Fourier transformation of crystal lattice. Each family of lattice planes in a crystal produces a single point in reciprocal lattice, where the vector is perpendicular to the lattice planes. Similar as in the direct space, a reciprocal unit cell can be defined using reciprocal axes (a^*, b^*, c^*,) and reciprocal angles among them (α^*, β^*, γ^*). The construction relationships between the direct and reciprocal lattices can be described as equation 2.3:

$$\boldsymbol{a}^* = \frac{\boldsymbol{b} \times \boldsymbol{c}}{V}; \quad \boldsymbol{b}^* = \frac{\boldsymbol{a} \times \boldsymbol{c}}{V}; \quad \boldsymbol{c}^* = \frac{\boldsymbol{a} \times \boldsymbol{b}}{V} \tag{2.3}$$

where V is the volume of unit cell, ***a***, ***b***, ***c*** are the direct space lattice vectors, ***a****, *b**, ***c**** are reciprocal basic lattice vectors. It is also fulfilled that ***a*** x ***a**** = ***b*** x ***b**** = ***c*** x ***c****= 1 and ***a*** x ***b**** = ***b*** x ***a**** = 0.

Each *reciprocal lattice vector* ***h*** is perpendicular to plane (*hkl*) and can be described as a linear combination of the three reciprocal vectors as equation 2.4:

$$\boldsymbol{h} = h\boldsymbol{a}^* + h\boldsymbol{b}^* + l\boldsymbol{c}^* \tag{2.4}$$

and the *interplanar distance* d_{hkl} (see chapter 2.1.1) is the reciprocal value of magnitude $|\boldsymbol{h}|$ (equation 2.5).

$$|\boldsymbol{h}| = \frac{1}{d_{hkl}} \tag{2.5}$$

2.1.4 Structure factor

During the scattering process, the interaction of radiation with matter varies with the type of incident waves. While X-rays, as electro-magnetic radiation, interact with the spatial distribution of electrons, electron radiation, which are charged particles and interact by coulomb forces, are scattered mainly by the atomic nuclei and by electrons. The scattering power of a single isolated atom is the *atomic form factor* also known as atomic scattering factor. It is proportional to the square root of the cross section, which depends on the atom type, scattering angle and radiation type. The cross section increases with atomic weight, thus, the atomic form factor is proportional to the atomic number. In addition, the atomic form factor reduces with an increasing scattering angle. The *structure factor* F_{hkl} describes the amplitude and phase of an incident wave scattered from lattice planes.[31] The structure factor, as a parameter in reciprocal space, is dependent on the atom positions in *real space* (or *direct space*) and the individual atomic form factors. It can be calculated for all atoms in a unit cell by equation 2.6:

$$F_{hkl} = \sum_j f_j \; e^{2\pi i(hx_j + ky_j + lz_j)} \tag{2.6}$$

where f_j is the atomic form factor and x_j, y_j, z_j are the positional coordinates.

In a diffraction experiment intensities of a scattered wave are measured and they are proportional to the square of structure factor (equation 2.7):

$$I_{hkl} \sim |\boldsymbol{F_{hkl}}|^2 \tag{2.7}$$

In the kinematic diffraction theory, *electron density* ρ(*x,y,z*) (or more specific for electrons *function of scattering power*) comprises the Fourier transformation of the scattering factors and the phase information. It can be described by equation 2.8. The maxima in the electron density map indicate the location of atoms in the unit cell. The phase problem, namely loss of phase information in the experiments, should be solved in the process of structure solution.

$$\rho(x,y,z) = \frac{1}{V_{EZ}} \sum_{hkl} F_{hkl}\, e^{-2\pi i(hx_j+ky_j+lz_j)} \tag{2.8}$$

Equation 2.7 is an ideal case valid in kinematical diffraction theory which can be applied e.g. for X-ray diffraction. However, due to a stronger interaction with matter multiple scattering occurs violating equation 2.7 in the case of electron diffraction. Up to a certain level of dynamical effect a crystal structure analysis is still possible and dynamical diffraction theory can be applied for a better description of the structure.

2.1.5 Stacking disorder

During crystallization, many crystals do not always grow ideally to form an infinite periodic dimension, irregular atomic arrangements in a crystalline matter.[118,119] Crystal defects are classified by the defect dimension including following types: point defects, line defects, planar defects and bulk defects. One kind of planar defects (two-dimensional defects) are *stacking faults*[120] which exist in various materials, such as layered materials like graphite und layered silicate, porous materials such as zeolite beta[73,121–123] and ITQ-39[124] or organic pigments[70]. The basic construct units are structurally well-defined layers, which can be stacked on top of each other by a *stacking sequence*. The layers may follow a structurally meaningful relationship, which is achievable by a certain translation vector or exhibit a free shift. If the stacking sequence of the layers is not regular but in a disordered fashion or a periodic sequence inserts differently without translation relationship to basic layers, the disorder faults will occur.

During the structural analysis of disorder defaults in nano sized crystals, electron diffraction is more powerful than 1D XRPD data. A regular periodic atomic arrangement will generate a regular electron diffraction pattern with discrete reflections. In the three-dimensional electron diffraction data diffuse scattering of stacking faults appears along the stacking direction. The style of the diffuse scattering is dependent on the type of the layer shifts and the probability of the irregular stacking. The `DISCUS` program package[120,125] serves as a reliable tool to analyse crystal disorder. The main functions comprise of the design of expected layer types with various shifts, the construction of a superstructure with desired stacking sequences using a defined crystal size, the expected introduction of layers at certain position, the simulation of corresponding patterns such as powder diffraction and electron diffraction patterns. In this dissertation, the analyses of stacking defaults from ED data were carried out with `DISCUS` for disordered ceramic material - aluminium borate $Al_4B_2O_9$ (section 6.1) and porous material - metal interlayer expanded M-RUB-36 zeolites (section 6.4).

2.2 Transmission electron microscope

2.2.1 Introduction

Electron microscopy is an important and powerful technique for materials characterization at nano scale. The electron beam can be described as a wave as well as a charged particle beam. The electron particles interact strongly with the electrostatic potential of matter and generate different signals as shown in Fig. 2.2[21]. The resulting signals consist of primary, secondary or Auger electrons, partly accompanied by energy loss from the interaction with matter and electro-magnetic waves (X-ray, visible light) used for various analytical approaches delivering chemical composition, particle morphologies, atomic arrangement and plenty of other matter information. For instance, SEM images[20] are formed with secondary electron (SE) producing high-resolution images of surface topography, with back scattered electrons (BSE) producing images a deeper surface. Energy-dispersive X-ray spectroscopy techniques in TEM and SEM utilize the characteristic X-rays for elemental analysis which can even achieve a quantitative chemical characterization from a nano particle. The electrons which pass through the thin specimen are applied for imaging or diffraction.

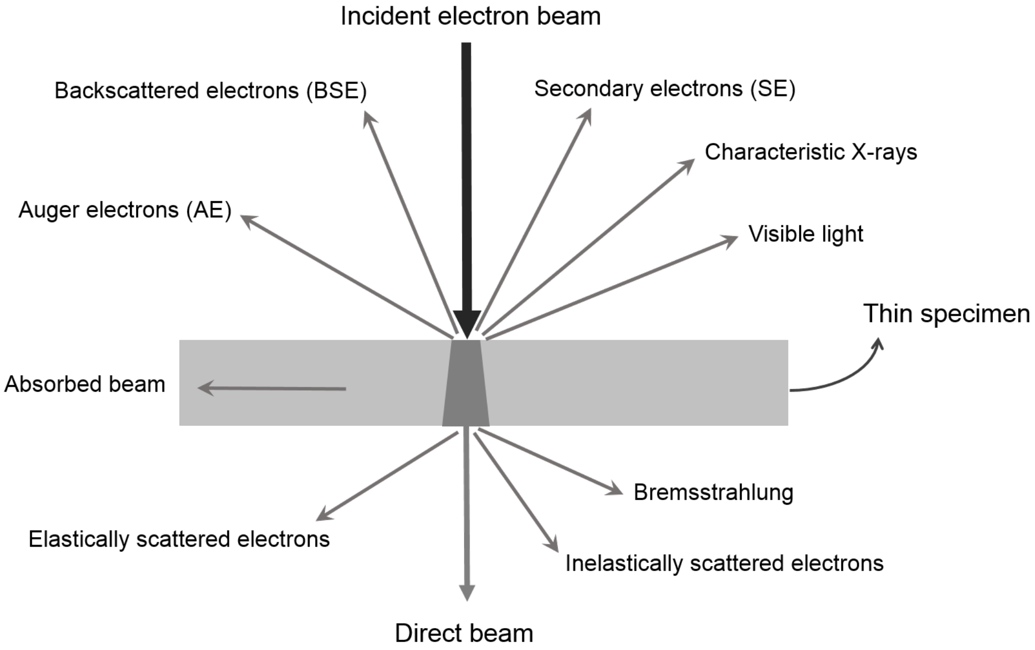

Figure 2.2: Scheme of the electron interaction with a thin specimen including the generated signals. Adapted from the ref.[21].

2.2.2 TEM components

A conventional TEM consists of several basic components along the electron column: the electron beam source (electron gun), illumination system (lenses and apertures), specimen stage, objective lens, objective and selected area aperture, intermediate lens, magnification system and detector, as shown in Fig. 2.3. A higher vacuum system and cooling system are also required.

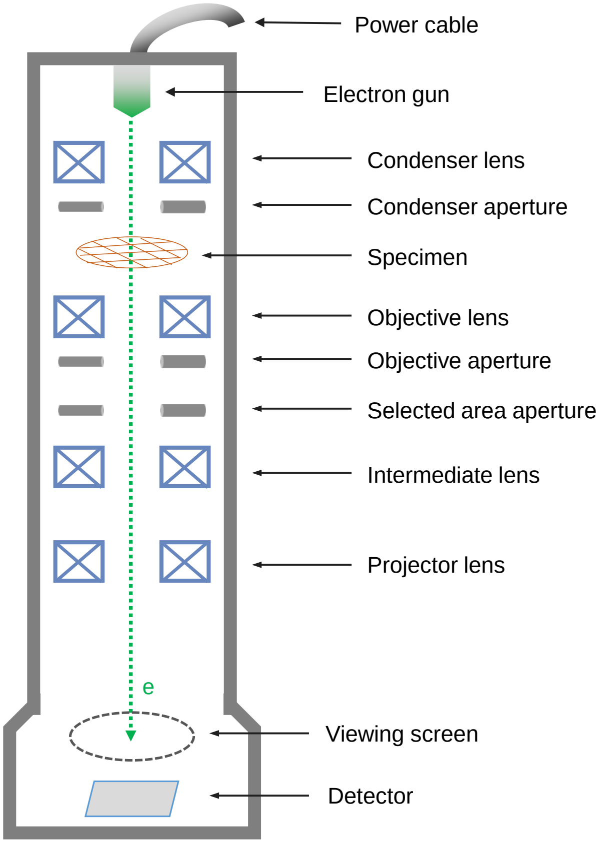

Figure 2.3: Diagram of the main components of a conventional transmission electron microscope.

- **Electron gun**
  As a part of illumination system, the electron gun produces a beam of high energy electrons accelerated in the electrostatic potential applied between anode and cathode. There are two types of electron sources: thermionic emission and field emission.[21]. Thermionic gun provides electrons from heated lanthanum hexaboride (LaB_6) single crystal (commonly) or tungsten (W) filament (nowadays rarely). Field emission gun works based on the tunnelling effect due to a high extraction potential onto a fine and sharp tungsten (W needle) tip. The wavelength λ (in nm) is dependent on the electron voltage U (in eV). Ignoring the relativistic effect, their relationship can be described

with equation 2.9:

$$\lambda = \frac{h}{\sqrt{2em_0U}} = \frac{1.226}{\sqrt{U}} \tag{2.9}$$

But the relativistic effect can not be ignored for energy higher than 100 keV[21] and must be taken into account, the wavelength λ can be calculated as equation 2.10:

$$\lambda = \frac{h}{\sqrt{2em_0U(1+\frac{eU}{2m_0c^2})}} = \frac{1.226}{\sqrt{U}}(1+9.79) \tag{2.10}$$

where h: the Planck's constant, c: the speed of light, m_0: the electron mass, e: the electron voltage, U: the accelerating voltage . For instance, a TEM at a operation power of 300 keV produces an electron beam with relativistic wavelength of 0.0197 Å[21].

- **Electromagnetic lenses**
  The lenses installed in electron microscopes are electromagnetic and are applied to shape the electron beam. A lens is constructed of a coil of metal wire in which the current is running and a hole in the middle for the electron beam. There are four types of lenses in the TEM: condenser lens, objective lens, intermediate lens and projector lens. Dependent on the type two or three lenses are typically applied. The lens aberrations, comparable to those known from optical lenses, limit the resolution. Important aberrations are for example chromatic aberration, spherical aberration, defocus and astigmatism. Correction for the latter two are available in a standard TEM, for chromatic aberrations dependent on the desired correction a monochromator, Cc corrector or energy filter is necessary, for spherical aberrations Cs-correctors need to be applied.

- **Aperture**
  Apertures are annular thin metallic plates with aperture strip containing holes of different sizes. They are placed in the path of electron beam in order to reject the off-axis and off-energy electrons going down the column. Apertures are available in connection with the condenser lenses to adjust the beam to the desired size, intensity and convergence; in the back focal plane of the objective aperture to enhance image contrast and in the first image plane to select the area of diffraction.

- **Vacuum system**
  In order to avoid scattering of electrons by gas molecules, a high vacuum is required during the electron microscopy experiments. An ultra-high vacuum is necessary for a high-voltage TEM (higher than 10^{-7} Pa) with field emission gun. The ultra-high vacuum condition is especially crucial for the experiment of a high resolution imaging.

Instrumental parameters of applied TEMs, the details of sample preparation and sample holders are described chapter 3 (see sections 3.2, 3.3, 3.4).

2.2.3 Imaging system

Imaging and diffraction experiments are performed under two different modes; imaging mode and diffraction mode as illustrated in Fig. 2.4. The electron diffraction pattern can be even collected from a selected area of specimen. A modern TEM enables the switching between two modes very easily.

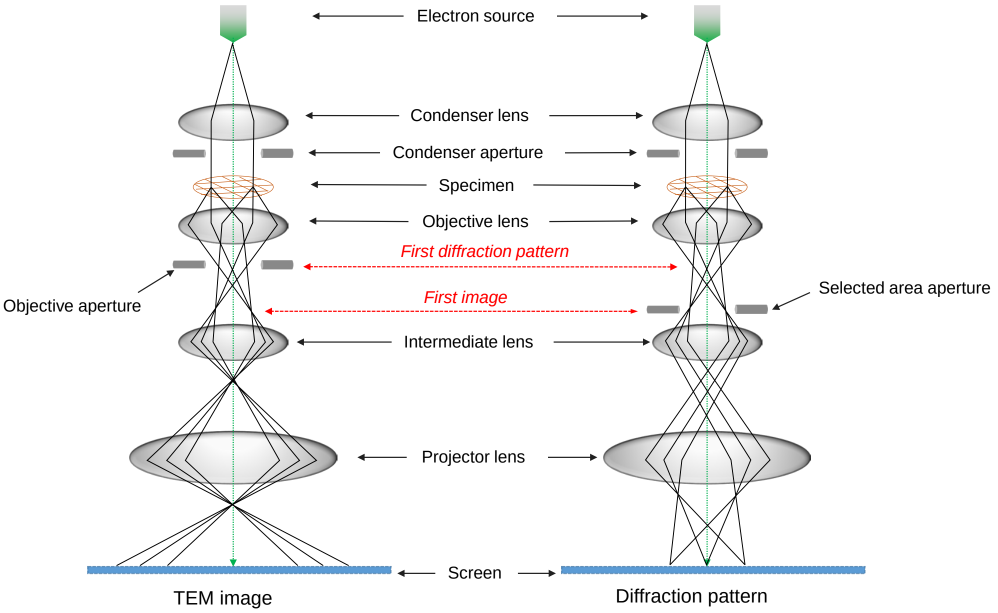

Figure 2.4: Schematic diagram showing the two basic operations in a TEM: imaging mode and diffraction mode.

The key components in the imaging system are the lens systems which allow to shape the electron beam for different work modes. The system includes three sections: illumination system normally at least with two condenser lenses, objective lens and projection systems containing intermediate and projective lenses. In both operation modes, the electrons supplied by the electron gun are shaped using condenser lenses (e.g., C1 and C2) and condenser apertures to form a parallel beam or to focus the electrons onto the specimen (Fig. 2.6). The objective lens focuses the beam from the specimen to generate the first intermediate image and contributes the magnification of images. Intermediate lens magnifies the initial image (or diffraction pattern) formed by the objective lens. The projector lens serves as magnification system for expanding the beam onto a detector device with high magnifications. The range of image magnification and diffraction camera lengths can be set based on different adjustments of projector systems. It must be noted that the work process of the illumination system is different underscanning transmission electron microscopy (STEM) imaging. At this situation, the condenser lenses do not generate a parallel beam, where the illumination system creates a focus probe by converging the beam with an additional condenser into a sub-nanosized spot. The produced spot scans over the specimen resulting a scanning mode if necessary.

In the imaging mode, the objective aperture locates in the back focal plane where the first diffraction pattern are generated. The objective aperture selects the central beam and filters out the residual electrons, thus resulting in a bright field image. However, using the signal of a diffracted beam leads to a dark field image. The projection system magnifies the first intermediate image and projects the final image on a screen. In the diffraction mode, the selected area aperture is inserted in the first image plane of the objective lens. The projection system magnifies the information of the back focal plane of the objective lens and produces a diffraction pattern of the specimen.

2.2.4 Electron diffraction

As one of the powerful methods, electron diffraction can supply plenty of information which are impossible to collect by any other methods. One important application is to determine whether the material owns a crystalline phase. For a monocrystalline material, discrete diffracted spots are projected onto the viewing screen, while the electron diffraction pattern is composed of a series of concentric rings for amorphous materials or polycrystalline phases. Analysis of the diffraction pattern of crystalline materials can deliver various reliable crystallographic parameters as crystal lattice parameter, crystal symmetry etc. or even detecting crystal defects inside. With a sufficient 3D electron diffraction data set, a complete crystal structure solution is nowadays frequent applied. The technique of tomographic electron diffraction, used for quick and simply ED data collection, is described in the section 2.3.1.

The incident electron beam is diffracted by the crystallographic planes *hkl* of a thin crystalline sample if the Bragg condition is satisfied. The electron waves interact with atomic planes and are focused at the back focal plane of the objective lens, generating electron diffraction pattern which is actually a Fourier transformation of electron wave. The traditional approach is called *selected area electron diffraction (SAED)*[21,126] which is accomplished by inserting the selected area aperture into the first image plane to select a specific part of the specimen. Only the beams passing through the selected area contribute to the diffraction pattern. The alternative diffraction mode is named *nano diffraction*, which uses a small beam with size of nanometre. In this mode, the free selection of electron beam size is possible. The effective distance from the specimen to the detector with projected image is called *camera length* (L), as shown in Fig. 2.5. The space between pattern reflections increase with a larger camera length. Fig. 2.5 illustrates the formation of a diffraction pattern (reciprocal space) including the Ewald sphere and reciprocal lattice.

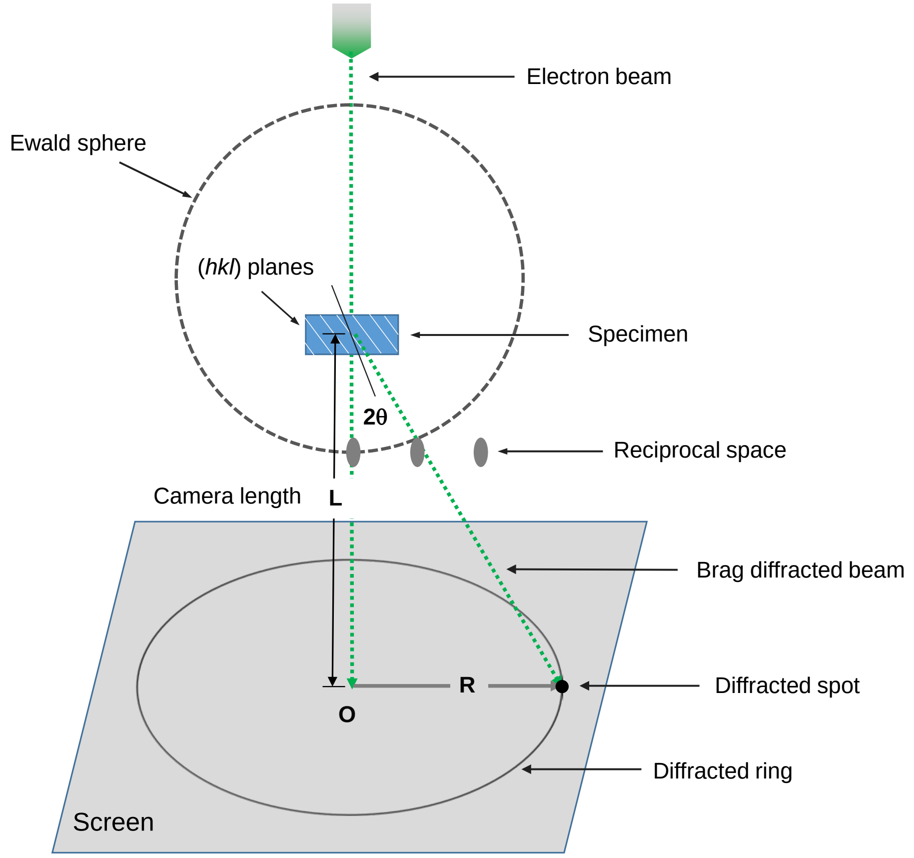

Figure 2.5: Schematic presentation for the formation of a diffraction pattern including Ewald sphere and reciprocal lattice.

Camera length can be calculated where the *Bragg angle* (θ) and electron *beam wavelength* (λ) play an important role.[21] Note that due to the small wave length most materials have a Bragg angle much less than 1° (for small θ, sinθ = tanθ = θ). As shown in Fig. 2.5, the electrons which are scattered at an angle of 2θ changes its trajectory and generates a spot with a distance R to the primary beam centre O or a diffracted ring with a radius of R. The relationship among them is written as equation 2.11:

$$\frac{R}{L} = tan2\theta = 2\theta \tag{2.11}$$

Bragg's Equation describes the interaction as following:

$$\lambda = 2dsin\theta = 2d\theta \Rightarrow 2\theta = \frac{\lambda}{d} \tag{2.12}$$

Then it can be concluded the camera constant:

$$\frac{R}{L} = \frac{\lambda}{d} \Rightarrow camera\ constant\ K = Rd = L\lambda \tag{2.13}$$

2.2.5 Scanning electron transmission microscopy

Scanning electron transmission microscope (STEM) combines the principles of the electron microscopes TEM and SEM.[21] Like TEM, the specimen must be thin enough to allow the electron to transmit through the specimen bulk. In STEM mode, the electron beam is focused strongly by condenser lenses and forms a fine spot. Comparable to the beam in SEM, the focused beam is scanned across the sample surface in a rectangular box. In comparison to the signals of backscattered electrons or secondary electrons collected above the sample, detecting the signal of transmitted beam depends on thin samples and thus shows a higher spatial resolution. Different types of detectors can be equipped for the formation of STEM image. A bright field (BF) detector, located in the travel path of transmitted beam, intercepts the electrons and acquires the electron signal sequentially to generate an image. In contrast to TEM bright-field imaging where the image is formed directly. The annular dark field (ADF) collects the signal of the scattered electron around the transmitted beam. An image with atomic resolution can be achieved by the application of a high-angle annular dark-field (HAADF) detector. In STEM mode, additional detectors can be installed for possible analysis techniques like EDX and EELS.

2.3 Electron diffraction tomography

2.3.1 Principle of ADT method

The ADT technique enables to automatically acquire reliable diffraction data of a random orientated single crystal, which can be achieved through a crystal tilt with a small controllable angular step. ADT exhibits obvious advantages such as low dynamical effects and large coverage of reciprocal space in structure analysis using electron diffraction data.

In the traditional collection of diffraction tilt series, a crystal tilt around an appropriate crystallographic axis must be selected and used as the tilt axis. It means that the measured crystal should be specially orientated to arrange the crystallographic axis parallel to the tilt axis of the goniometer. Because of the low crystallographic index axis prominent two dimensional in-zone diffraction patterns (Fig. 2.6 left) show a large number of low-indexed reflections. Three-dimensional data is obtained after combining a set of electron diffraction patterns including oriented zones. It is possible to index the single zones with a known cell matrix or to derive from two orthogonal tilt series unknown cell parameters and further to extract reflection intensities.[127] For instance, the crystal structure of Pigment Red 53:2 was solved using electron diffraction data which was recorded by tilting the crystal sequentially around a main crystallographic axis.[128] There are some disadvantages[45] in this in-zone diffraction method, in spite of the fact that orientated zone diffraction data has been used for successful structure solution. At first, it takes a lot of time to align the crystal with one crystallographic axis along the goniometer axis of the TEM. Secondly, only using the orientated zones with low-indexed reflections ignores plenty of high-indexed reflections, resulting in an insufficient number of reflections for the crystal structure solution (low completeness). Thirdly, the multiple scattering in the in-zone patterns is much stronger, leading to strong dynamical effects, which reduces the quality of data because of the unreliable extracted intensity. At last, finding a good oriented crystal increase the illumination time, which enhances the risk of radiation damage.

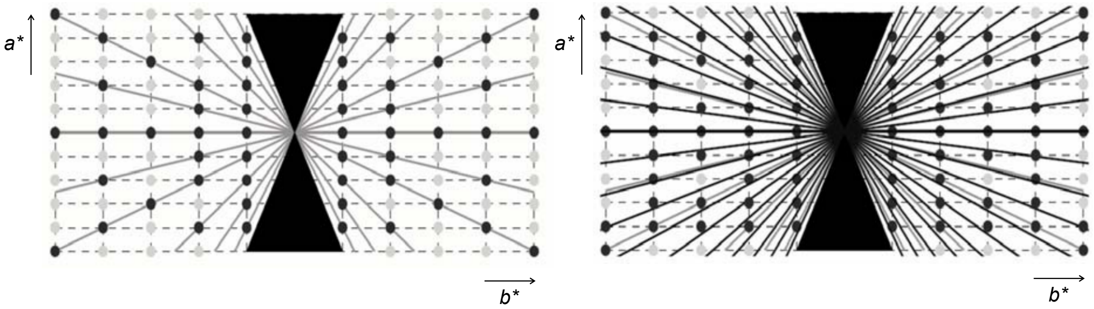

Figure 2.6: Sketch of reciprocal spaces of a traditional tilt collection including prominent zones (left) and a scan of diffraction space using ADT approach (right) viewed along the tilt axis c*.[45] Due to the short wave length of electrons, the Ewald sphere cuts are approximated as two-dimensional planar slices. Dark spots: recorded reflections; bright spots: missed reflections. The black areas show the missing cones (not accessible region limited by TEM geometry).

ADT enables to speed up the 3D diffraction data collection in an easy way. The biggest difference to conventional in-zone tilt series collection is that ADT data is acquired through a tilt around an arbitrary axis from a random oriented crystal. In addition, the off-zone diffraction tilt series (Fig. 2.6 right), recorded by a fixed controllable tilt step, allow a scan of the diffraction volume in the range of the reachable goniometer tilt and thus increase the number of recorded reflections (including a vast number of high-indexed reflections). The increased coverage of reciprocal space is crucial for the structure solution for low symmetry crystal systems as triclinic and monoclinic lattices. In comparison to traditional electron diffraction acquisition, the ADT method shows several significant advantages concluded as following.

- **Weak beam damage.** The utilization of an arbitrary tilt axis and no requirement of manual orientation of crystal reduces the illumination time on the sample, decreasing the radiation damage.
- **Low dynamical effect.** The multiple scattering effects are much lower in the collection of off-zone diffraction patterns, as few spots are simultaneously excited.[129] Additionally, PED approach can also decrease the dynamical scattering.
- **High *hkl* completeness.** The data collection in a high tilt range increases the coverage of reciprocal space. The off-zone diffraction patterns deliver a large number of high-indexed reflection.

- **Easy and fast measurement.** After a good alignment, the process for data acquisition runs in fully automatic way. Therefore, using ADT saves a lot of measurement time in comparison to manual setting.

2.3.2 Precession electron diffraction

In order to improve the quality of extracted reflection intensity data, Precession electron diffraction (PED) technique can be combined with ADT approach.[45] PED was first developed by Vincent et al.[130] to reduce dynamical scattering for collecting electron diffraction patterns. As shown in Fig. 2.7, the electron beam is precessed around the vertical axis forming a conical path. The incident beam penetrates the sample from different orientations, leading to a movement of the Ewald sphere. The resulted "wedge" integrates the reciprocal volume between the tilted slices, enabling the reflection cut close to the reflection centre and reducing the uncertainty of intensity extraction caused by excitation error[21]. Hence, the intensity of a diffracted spot is a merged integration collected from each azimuthal position of the beam, resulting in quasi-kinematic diffraction intensities. The available hardware, e.g. DigiStar unit designed by the company NanoMEGAS[64], is now on the market and fulfils the requirement of coupling PED approach with ADT. Until now, a large number of structural investigations have been performed successfully on the base of reliable datasets recorded using the combination of ADT and PED.[40,47,57,65]

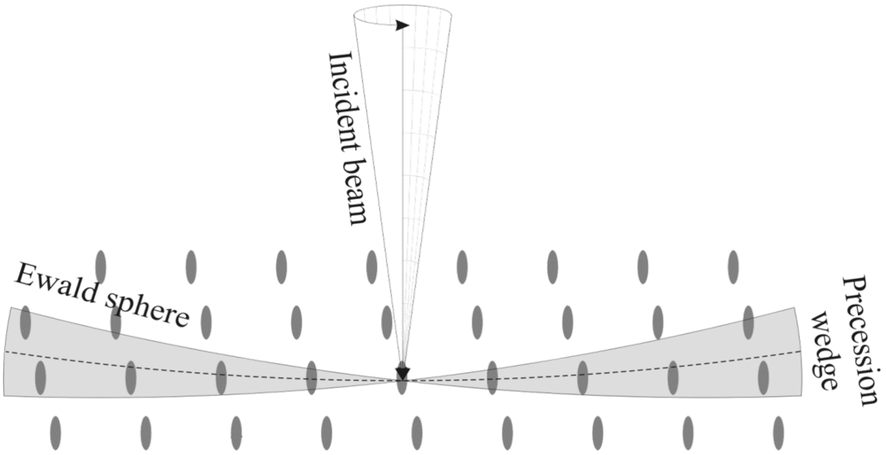

Figure 2.7: Sketch of PED technique showing the electron beam precession and the movement of Ewald sphere. Image taken from Kolb et al.[42]

2.3.3 ADT data acquisition and processing

A special developed model implemented to a computer-controlled FEI TEM realizes the full automation of data acquisition including crystal tilting, crystal tracking, collection of diffraction pattern and data saving.[43,131] The diffraction patterns are taken sequentially after each tilting using nano electron diffraction mode. The crystal position is tracked by microprobe scanning electron microcopy (μSTEM) imaging. The automatic crystal tracking procedure relies on the cross-correlation of two neighboring tilt STEM images. Several related alignments and parameter settings should be done before starting ADT data collection. The diffraction patterns are saved at the end of each tilt (Fig. 2.8) and stored finally as a file in the Medical Research Council (MRC) file format[132]. The process repeats automatically if all the calibrations are set in a perfect condition. Samples can be measured under room temperature, high or low temperature. The details about the data acquisition are described in the section 3.5 of chapter 3. As the raw ADT data is a stack of off-zone diffraction patterns it cannot be directly indexed. It should be reconstructed to a three-dimensional space by the programs `ADT3` or `eADT`[44]. Lattice parameters, orientation matrix information, possible space groups, and reflection indexing can be obtained after the reconstruction. ADT softwares are also used to extract the intensities of reflections applied for structure solution. For details about ADT data processing see section 3.6.

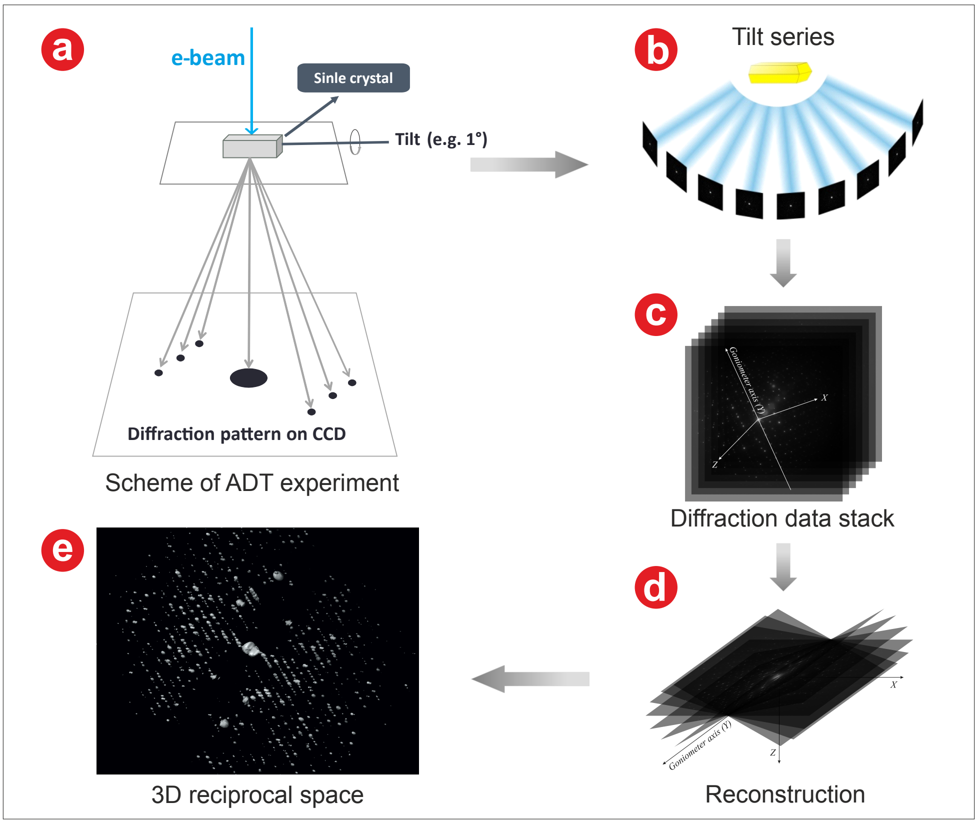

Figure 2.8: Schematic representation of ADT acquisition and data processing. Adapted from Kolb et al.[42] and Mugnaioli et al.[133]

2.3.4 Structure determination from ADT data

Ab initio crystal structure solution can be performed using the (*hkl*) file extracted from ADT data with direct methods and real space method (simulated annealing) in the program `SIR2014`[134], the least-squares refinement performed with the program `SHELX97`[135] or Charge Flipping in `JANA2006` software packet[136]. It is assumed that the kinematic approximation $I_{hkl} \sim |F_{hkl}|^2$ is valid assuming a low level of multiple scattering. The structural model, solved from structure solution, can be directly refined based on the kinematical diffraction theory. If multiple scattering effects in electron diffraction need to be taken into account, structure refinement from electron diffraction data (dynamical refinement) can be carried out in the software packet `JANA2006` and `Dyngo`[136]. In this work, the structure determinations were performed in three programs: structure solution in `SIR2014`, kinematical structure refinement in `SHELX97` and dynamical structure refinement in `JANA2006`.

Structure solution in SIR2014

An example of input data for structure solution in `SIR2014` is shown in the following list 2.3.1 containing in the data section (*%data*): unit cell (*Cell*), space group (*space group*), chemical content of the full unit cell (*Content*), used radiation type (*electrons*), name of reflection file (*reflections*), format of the reflection file (*format*), resolution cut off in Angstrom (*resm*), data type as intensity = F_{obs}^2 (*Fosq*), used wavelength (*wavelength*). The structure solution section (*%phase*) contains method for structure solution (*BEA*), number of refinement cycles (*250*), resolution limit for phasing (*resid*) and the size of the structure (*S: small*) which means that the asymmetric unit contains less than 80 atoms. Note that BEA (*Best Equivalent Amplitude*) algorithm is applied for diffraction intensities extracted electron diffraction data.[137]

Listing 2.3.1: An exemplary *input file* for the structure solution in `SIR2014`.

```
%Job Structure solution of Al4B2O9
%Structure aluminum borate
%Data
    Cell 14.81 5.54 15.06 90.00 90.9 90.00
    Spacegroup c 2/m
    Content Al 32 B 16 O 72
    Electrons
    Reflections reflection_file_Al4B2O9.hkl
    Format(3i4, 2f8.2)
    ResM  0.6
    Fosq
    Wavelength 0.019700
%Phase
    BEA     250
    Resid   1.00
    size    S
%End
```

Dynamical structure refinement in `JANA2006`

As mentioned above, dynamical effects in electron diffraction data can be reduced using precession electron diffraction (PED) data. PED data is considered as pseudo-kinematical file delivering reflection information with an increased number of structure factors. In comparison with pure electron diffraction tomographic data the combination with PED increases the refinement stability and results in more accurate structural parameters.[66,138,139] Hence, the dynamical refinements in this work were performed against PED data in order to obtain a reliable structure. The dynamical refinement is more complicate than kinematical refinement since the reflection intensities are dependent on the thickness and orientation of measured crystal as well as on the structure factors influenced by other reflections.[139] Thus, for the acquisition of suitable tomographic data sets with polycrystallinity and disorder effects should be avoided. For a known structural model, the implementation of dynamical refinement comprises of three main steps[139,140]: extraction of reflection intensities; the refinements of crystal thickness and orientation; dynamical least-squares refinement. The details of the refinements steps and examples are concluded in the "*Jana2006 Cookbook*".[140]

The first step is to extract the reflection intensities from electron diffraction data. The raw electron diffraction data must be *.tif*-format which is accepted the program. For a *mrc*-type file, each frame can be exported into single *.tiff*-file using a script implemented in the `DigitalMicrograph` software or in `Matlab`. Similar to data processing in `ADT3D` (see details in section 3.6), there are mainly three steps[139]; determination of reflection position on each diffraction pattern using `PETS`[141]; determination of lattice parameters and orientation matrix in `JANA2006`: integration of diffraction intensities in `PETS`.

Listing 2.3.2: An exemplary *input file* for data processing in `PETS`.

```
noiseparameters 3.25 38
background 0
lambda 0.033492
Aperpixel 0.00261
dstarmax 1.2
phi 1.0
omega -90
center auto
pixelsize   0.005
reflectionsize 18
I/sigma 6
bin 1
beamstop no
imagelist
img\FastADT_Data_cry2_1.tif    -33.00    0.00
.....
etc.
img\FastADT_Data_cry2_78.tif    42.00    0.00
endimagelist
```

An exemplary input file with *,pts*-format for the program `PETS` is shown in the list 2.3.2. Selected explanations to the key words are concluded as following[141]: the value of relativistic wavelength of the incident electron beam in Angstroms (*lambda*); the size of one pixel in reciprocal angstroms (*Aperpixel*); the resolution limits as d* (*dstarmax*); precession angle in degrees (*phi*); orientation of the tilt axis of the sample holder with respect to the positive horizontal axis of the image (*omega*); intensity over sigma ratio for peak search.; yes/no for the application of beamstop (*beamstop*); multi-line (file name; tilt angle and zero) keyword and each line contains one image (*imagelist – endimagelist*). The output file from `PETS` is CIF-like file with the *_dyn.cif_pets*-format which consists of a list of reflections with their indices, intensities on an arbitrary scale and estimated standard deviations of the intensities.[139]

Subsequently, the dynamical structure refinement starts with a known structural model or from the structure solution with charge-flipping approach in `JANA2006`. With a known structural model, the general steps are shown as following[140]:

- import the *_dyn.cif_pets* file in Jana2006 (*"File → Structure → New"*), where the commands "Single crystal: known diffractometer format" and "Pets – electron diffractometer" should be selected;
- import the structural model from the known *CIF* file (*"File → Import model from → CIF"*);
- parameter setting (*"Parameters → Electron diffraction"*, where "Use dynamic approach" is selected and "For Fourier rescale to Fcalc" is checked.
- starting the thickness optimization (*checking "Thickness" → "Run optimization"*, where the thickness plots should be checked;
- starting the orientation optimization (*checking " orientation " → " Run optimization"*, where the thickness plots should be checked;
- first dynamical least-squares refinement (*"Right-click Refine → Various → Fixed commands"*, where all the atoms are chosen and the 'All parameters' is checked. Then starting with *"Refine"*;
- repeating the process of orientation optimization;
- final dynamical least-squares refinement with the refinements of coordinates, isotropic (if needed, anisotropical at last step), thermal factors and occupancies. In this step, the *R*-value should be strongly reduced.

- checking the temperature factor, occupancies, final *R*-value etc. in the final refinement list;
- visualizing the electron potential maps and the structure in the program `VESTA`.[142]

2.4 Energy-dispersive X-ray spectroscopy

EDX is a conventional approach for the analysis of elemental composition of solid samples. The applications comprise the identification and quantification of elements for a selected single point or the elemental distribution of an area in form of EDX-mapping.[143] The EDX unit is used either together with a SEM[26,144] or with a TEM[21] (preferably under STEM work mode) and utilizes detection and measurement of the energies of characteristic X-ray emissions caused by the interaction between incident electron beam and studied material. While the atom is hit by an incident electron beam, it receives some energy from the electron at the same time. Due to the energy transfer from external condition the electrons at low-energy shells in the atom start to jump a higher shell or even leave from the atom. This movement causes a vacancy in the orbital with a transition state, as shown in Fig 2.9. When the electrons from outer-shells fill up the vacant sites, the energy difference will be released in form of X-rays. For example, the transition of electron from L-shell to a vacant state in the K shell, characteristic X-ray emission occurs and corresponding line is called Kα (Fig. 2.9).

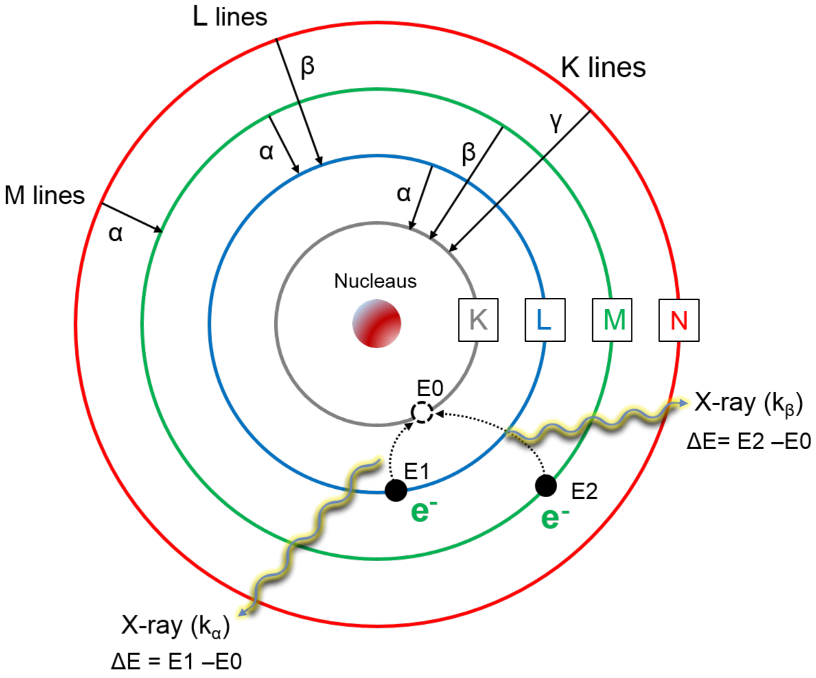

Figure 2.9: Schematic illustration of X-ray emission during electron atom interaction. Electron transitions presents the production of some typical spectral lines.

In fact, the electrons in K-shell own the highest ionization energies compared electrons of outer shells for a given atom. It means that more energy is needed to ionize the K-shell, resulting to a higher energy of the characteristic X-ray line than L or M line series ($E_K > E_L > E_M$). For the characteristic X-ray of different atoms, the relationship of the energy and atomic number can be described by Moseley's law[145] (equation 2.14):

$$E = c_1(Z - c_2)^2 \tag{2.14}$$

E: energy of characteristic X-ray, Z: atomic number, c1 and c2: constants for a given X-ray. It indicates that the energy is proportional to the square of the atomic number and increases with a higher atomic number for a given line type. Hence, measuring the number and energy of characteristic X-ray can be used to identify the elemental composition even in a quantitative way.

2.5 X-ray powder diffraction

X-ray powder diffraction (XRPD) is a rapid analytical approach to identify the crystalline or amorphous nature of solid matter.[18] Simple sample preparation, quick data collection under different modes and no damage of the sample make XRPD as a standard but powerful characteristic technique not only in the academic research but also for the area in production in the industry. The XRPD pattern is generated by interaction between incident X-ray and atomic planes of microscaled powder or the surface of investigated crystalline materials.

2.5.1 Bragg's law

The basic description of the formation of a XRPD pattern is the Bragg's law with following equation[18,146] 2.15 written as:

$$\lambda = 2dsin\theta \tag{2.15}$$

where n: a positive integer, λ: the wavelength of incident beam, d: interplanar distance, q: scattering angle. The law explains the relationship between the wavelength, the lattice distance and the scattering angle.

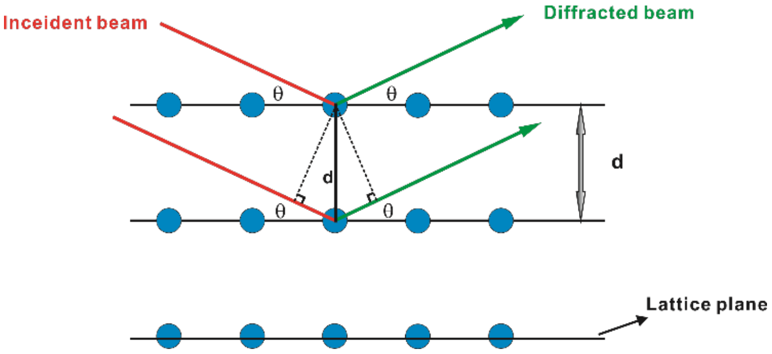

Figure 2.10: Schematic representation of Bragg's law.

As illustrated in Fig. 2.10, the constructive interference occurs only when the difference of the travel path lengths between the two incident beam waves is equal to an integer multiple of the beam wavelength. It means that a diffraction ray is generated if this condition is satisfied. When the beam waves are out of phase, destructive interference occurs, thus no diffraction pattern will be created.

2.5.2 X-ray powder diffraction

- **X-ray powder diffractometer**

The three key components of a powder diffractometer are X-ray tube, sample stage and detector. X-ray tube provides characteristic X-ray spectra, whose emission is illustrated in Fig. 2.10. The wavelengths of X-ray source are dependent on the material type of target anodes. The wavelengths of normal used metals are summarized in Table 2.2. The most common target materials are Cu and Mo. The sample stage holds the sample holder and can rotate the sample holder in some work modes. For in-situ experiments, other equipment as heating oven or cooling system can also be combined with the sample stage. The detector, e.g. `position sensitive detector` (PSD), records the numbers of scattered X-ray beam for the intensity determination.

Table 2.2: Wavelength of characteristic X-rays generated by different anode materials.[33]

Anode	Cu	Mo	Cr	Fe	Ag	Co
λ (K_{α_1})(Å)	1.54059	0.70932	2.28975	1.93609	0.55942	1.78901
λ (K_{α_1})(Å)	1.54441	0.71361	2.29365	1.94003	0.56381	1.79290

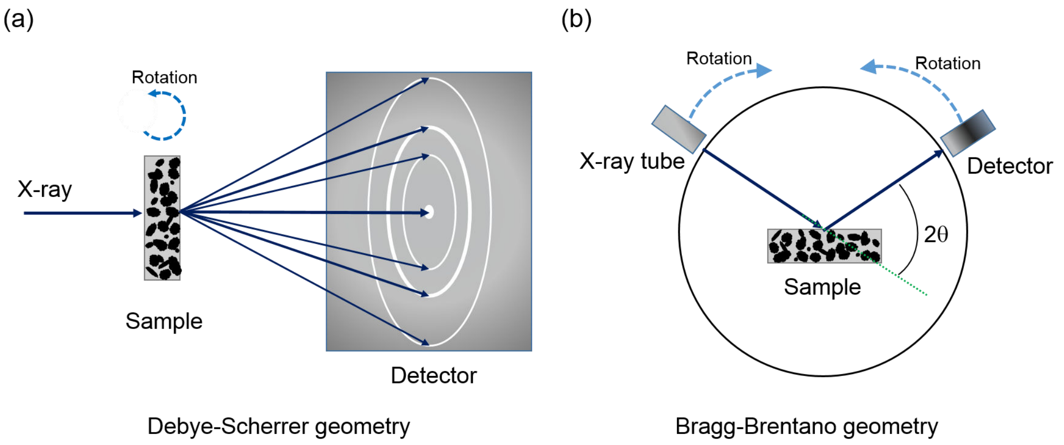

Figure 2.11: Powder diffractometer with two geometry modes: (a) Debye-Scherrer geometry and (b) Bragg-Brentano geometry.

A powder diffractometer differs from its geometry, e. g., Debye-Scherrer mode or Bragg-Brentano geometry mode as shown in Fig. 2.11. In Debye-Scherrer mode, the sample, stored in a capillary, rotates and the position of X-ray tube is fixed during the measurement. The X-ray transmit and forms Debye rings in the detector (Fig. 2.11). Whereas, in the Bragg-Brentano the sample is prepared on a flat support, the X-ray tube and detector can be rotated by -θ and θ in the diffractometer. The incident X-ray beam is reflected on the sample surface and detected by the movable detector.

- **XRPD pattern**

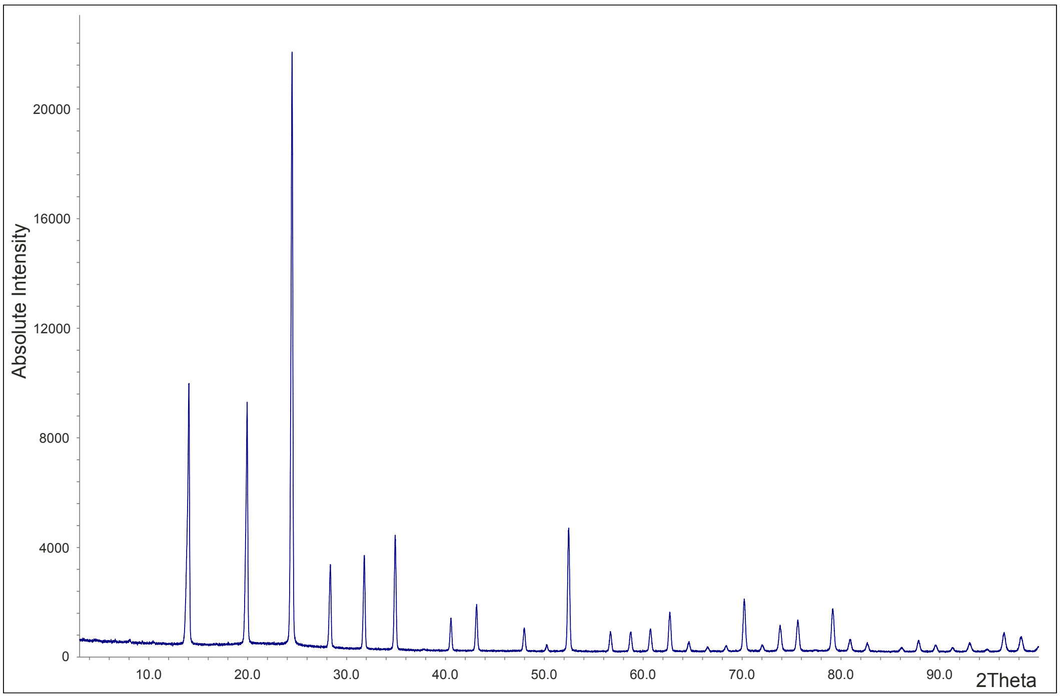

Figure 2.12: An exemplary powder diffraction pattern collected from sodalite silicate using a Stadi-P powder diffractometer equipped with a linear position-sensitive detector (PSD) using Cu Kα1 radiation (λ = 1.5406 Å). Lattice parameters of sodalite silicate: $a = b = c = 8.88$ Å and $\alpha = \beta = \gamma = 90°$.

A XRPD diagram is a plot of the intensity of X-ray beam scattered at different Bragg angles by the atomic planes. Only crystalline materials can produce a peaked diffraction diagram since they consist of atoms of a periodic array with long-range order. Fig. 2.12 shows the XRPD diagram of sodalite silicate collected by a powder diffractometer using Cu anode as X-ray source. The sharp peaks with strong intensity and low background indicate an excellent crystallinity of the material. Due to the high symmetry of sodalite silicate (cubic crystal system), there is a small number of peaks in the XRPD pattern. The style of a XRPD diagram is influenced by several factors, as concluded following:

- Lattice parameters (a, b, c, α, β, γ) decide the peak positions.
- Atom type and its arrangement determine the peak intensity. The diffraction intensity is proportional to the sum of square of structure factors of corresponding atoms.
- Factor like crystallite size, crystal shape, crystal defects and diffractometer optics determine show effect on the peak width and peak form.
- Sample holder and amorphous parts in sample determine the background.
- A higher symmetry increases the possibility of systematic extinction, resulting a systematic absences of *hkl* reflections.

• Applications of XRPD

X-ray powder diffraction is widely applied for the identification and characterization of different materials ranging from inorganic matters, organic and pharmaceutical compounds, metal, ceramics, etc. The main common applications are summarized as following:

- Quick phase identification;
- Examination of the crystallinity;
- Quantitative analysis of sample with multiphase;
- Texture and orientation analysis;
- Determination of unknown crystal structure using Rietveld methods.

In addition, in-situ experiments can be performed by changing the factors, e.g., temperature (sample heating or cooling), physical pressure, to observe the phenomena as phase transformation or order-disorder transformation.

2.5.3 Structure determination from XRPD data

• Indexing

The assignment of the (*hkl*) reflexes to lattice planes is referred to as indexing[18,146] which is the first step in the structure determination. Since one-dimensional information is obtained from the XRPD data, reflection overlapping occur very often, which depends on the Bragg angle θ. After the indexing process, the lattice parameters of three-dimensional unit cell can be determined from the observed reflections. The programs as `McMaille`[147], `DICVOL04`[148], `N-TREOR`[149] are used to index XRPD data and indexing can be performed in the software like `WinXPOW`[150], `DASH`[151] and `EXPO2013`[152]. The absence of certain reflections is called systematic extinction. This kind of peak absence is caused by the symmetry operations and applied to determine the extinction symbol which provides the corresponding possible space groups of the crystal structure.

• Structure solution

As mentioned before, the intensity of each reflection is proportional to the square of the structure factor F_{hkl}. Thus, the magnitude value of F_{hkl} can be obtained from the experimental diffracted intensity. The absence of the phase information during a diffraction measurement is called phase problem. A Fourier transformation on the structure factor and the phase information is used to calculate the electron density map, in which the maxima is corresponding the atom position. A structure solution is aimed to find a meaningful structural model (the atomic coordinates) which are dependent on the distribution of the electron density. Until now, different methods[45] are available to solve the phase problem: direct method, Patterson method, maximum entropy, charge flipping etc. The available programs for structure solution are for example `EXPO2013` and `DASH`.

• Rietveld refinement

Rietveld refinement is the last step in the process of structure determination against XRPD data. The refinement is performed to check the structural model obtained from structure solution. The least-squares method[18,146,153,154] is applied at the refinement process. The difference between the simulated powder diagram from the structural model and the experimental powder diagram is observed and expected to reduce to a minimum state if all the parameters are refined to reach a best fit of the total experimental diffraction profile. Usually the following parameters need to be refined in the Rietveld refinement:

- Zero point
- Background
- Lattice parameters
- Atomic fractional coordinates
- Atomic displacement or thermal parameters as isotropic temperature factor (Biso)
- Preferred orientation (if present)
- Profil function
- Absorption
- Crystallite size and strain
- Over all scale factor

The quality of the fit between the observed and calculated XRPD diagrams is described by the following functions:

- The weighted profile R factor (R_{wp}) (equation 2.16):

$$R_{wp} = \sqrt{\frac{\sum w(Y_o - Y_c)^2}{\sum wY_o^2}} \tag{2.16}$$

  where Y$_o$: observed intensity, Y$_c$: calculated intensity; w weighting factor.

- The statistically expected R factor (R_{exp}) (equation 2.17):

$$R_{exp} = \sqrt{\frac{N - P}{\sum wY_o^2}} \tag{2.17}$$

  where N: number of overall points; P: number of refined parameters.

- The goodness of fit (gof) (equation 2.18):

$$\chi^2_{red} = \frac{R_{wp}}{R_{exp}} = \sqrt{\frac{\sum w(Y_o - Y_c)^2}{N - P}} \tag{2.18}$$

3 TEM and ADT

3.1 Introduction

This section includes a basic description of the TEMs and relative instruments in this dissertation as well as corresponding methods e.g. preparation of a TEM grid. ADT data acquisition and the work-flow for data analysis will be also illustrated in details. In addition, it includes the experimental details of related TEM techniques. A standard TEM can deliver a large range of characterization approaches (Fig. 3.1) for nano-scaled materials at atomic level. After mounting the grid with sample particles onto the specimen holder, the assembly is inserted into the TEM. The strong coulombic interaction between materials and electrons enables that TEM shows unique capacities or applications under different operation modes.

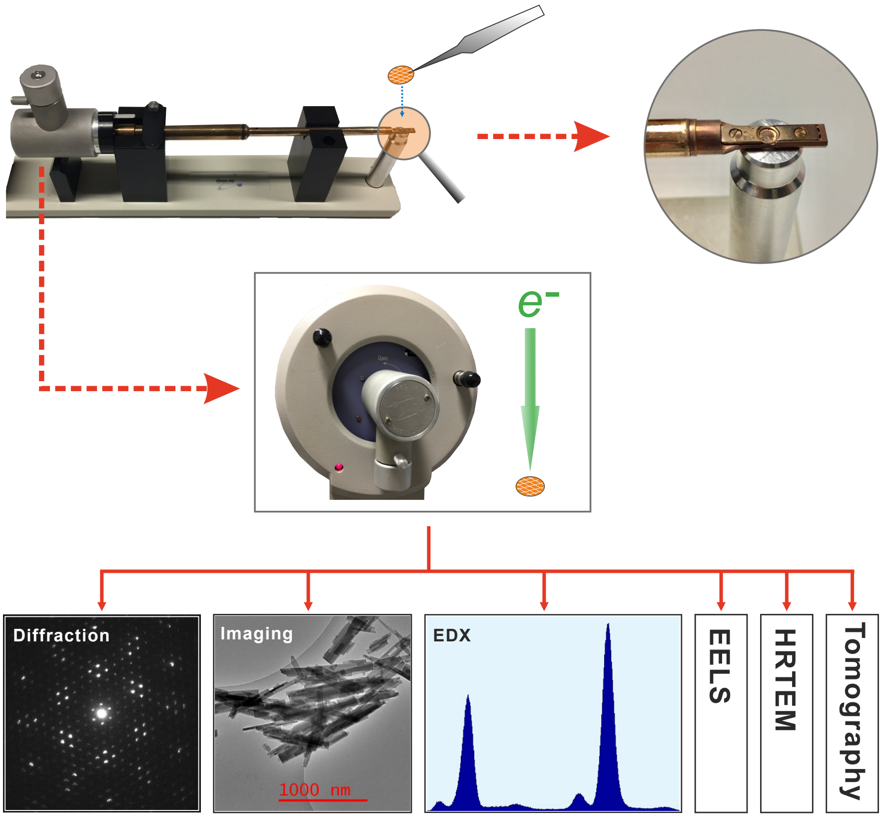

Figure 3.1: Overview of TEM work process and possible applications of TEM.

3.2 Transmission electron microscope

Fig. 3.2 exhibits two TEM devices in *Electron Mircoscope Center Mainz* (EMCM). All the TEM experiments were carried out using these two TEMs except the high angle annular dark field (HAADF)-STEM studied with a Jeol TEM at the Technical University of Darmstadt. Selected instrumental information are listed in Table 3.1. TEM measurements including phase contrast TEM, STEM, EDX are available for both TEMs. *TEM Imaging and Analysis* (`TIA`) was used to collect STEM image and EDX spectrum. TEM image, electron diffraction pattern as well as ADT data were acquired or viewed by Gatan `Digital Micrograph` software[155]. STEM images were collected using a Fischione HAADF detector.

Table 3.1: Selected instrumental details of applied transmission electron microscopes at the University of Mainz.

TEM type	FEI Tecnai F30 S-TWIN	FEI Tecnai G2 Spirit
Acceleration voltage	300 kV	120 kV
Electron Source	field emission gun (FEG)	Thermionic Gun: LaB_6 emitter
Camera type	Gatan US4000 4kx4k CCD	Gatan US1000 2kx2k CCD
STEM resolution	0.2 nm	1.0 nm
(S)TEM imaging	Yes (Fischione detector)	Yes (Fischione detector)
EDX measuremnet	Yes (EDAX spectrometer)	Yes (Oxford spectrometer)
ADT measurement	ADT and Fast ADT	Only Fast ADT

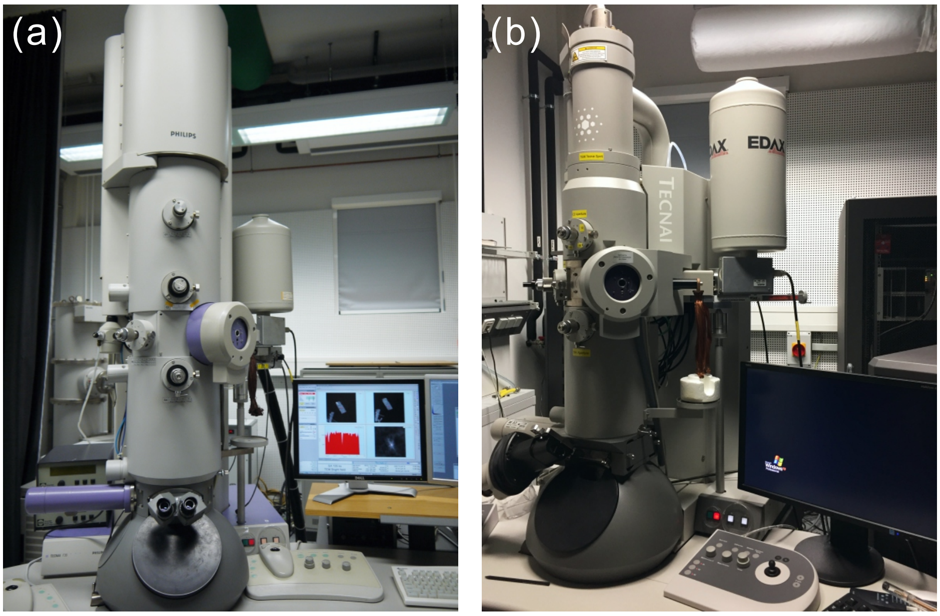

Figure 3.2: Transmission electron microscopes at the University of Mainz applied in this thesis. Left: FEI Tecnai F30 S-TWIN TEM, right: FEI Tecnai G2 Spirit.

3.3 TEM grid preparation

In order to avoid crystal agglomeration and form a homogeneous distribution of particles on the grid, we prepare the TEM grid very carefully using a method show in Fig. 3.3. There are different kinds of grids, such as continuous, holey, lacey carbon filmed grids or Cu, Ni, Au grids. The selection of the grid for application is determined by the purpose of TEM experiments. Before dispersing sample particles onto the grid, it is sometimes necessary or beneficial to clean grids in a plasma cleaner. For the grid preparation, a small amount of the sample is ground in an agate mortar. The sample is mixed and then dispersed in corresponding solution (e. g., ethanol, water) which is not a solvent of the material, using an ultrasonic bath. The suspension is transferred into a caved tip with a pipette and then sprayed onto a thin amorphous carbon film, suspended on standard Cu TEM grids, using an ultrasonic vaporizer[65]. The grid is dried under vacuum. Utilization of this approach enables a better distribution of nanoparticles on the grid film, which is very helpful for the investigation especially for ADT measurement.

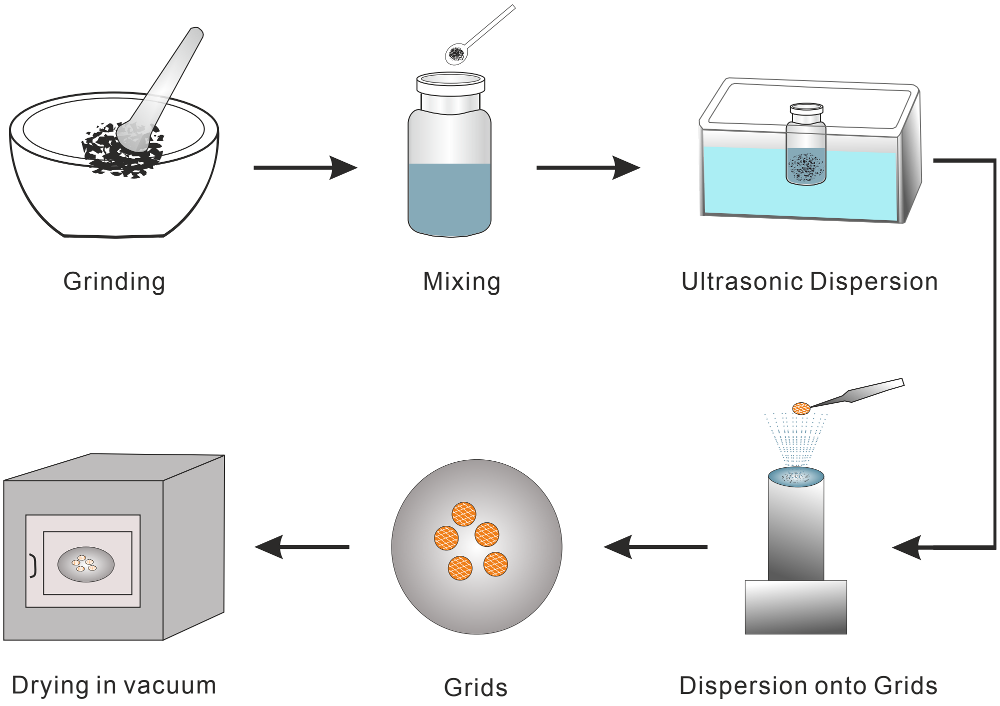

Figure 3.3: Sheme of the procedures for preparation of a TEM grid using dispersion method.

3.4 TEM specimen holder

Five types of TEM holders as shown in Fig. 3.4 are introduced. According to the research motivation and the holder speciality, we can select different holders for the measurements. The specifications of each holder are given as following.

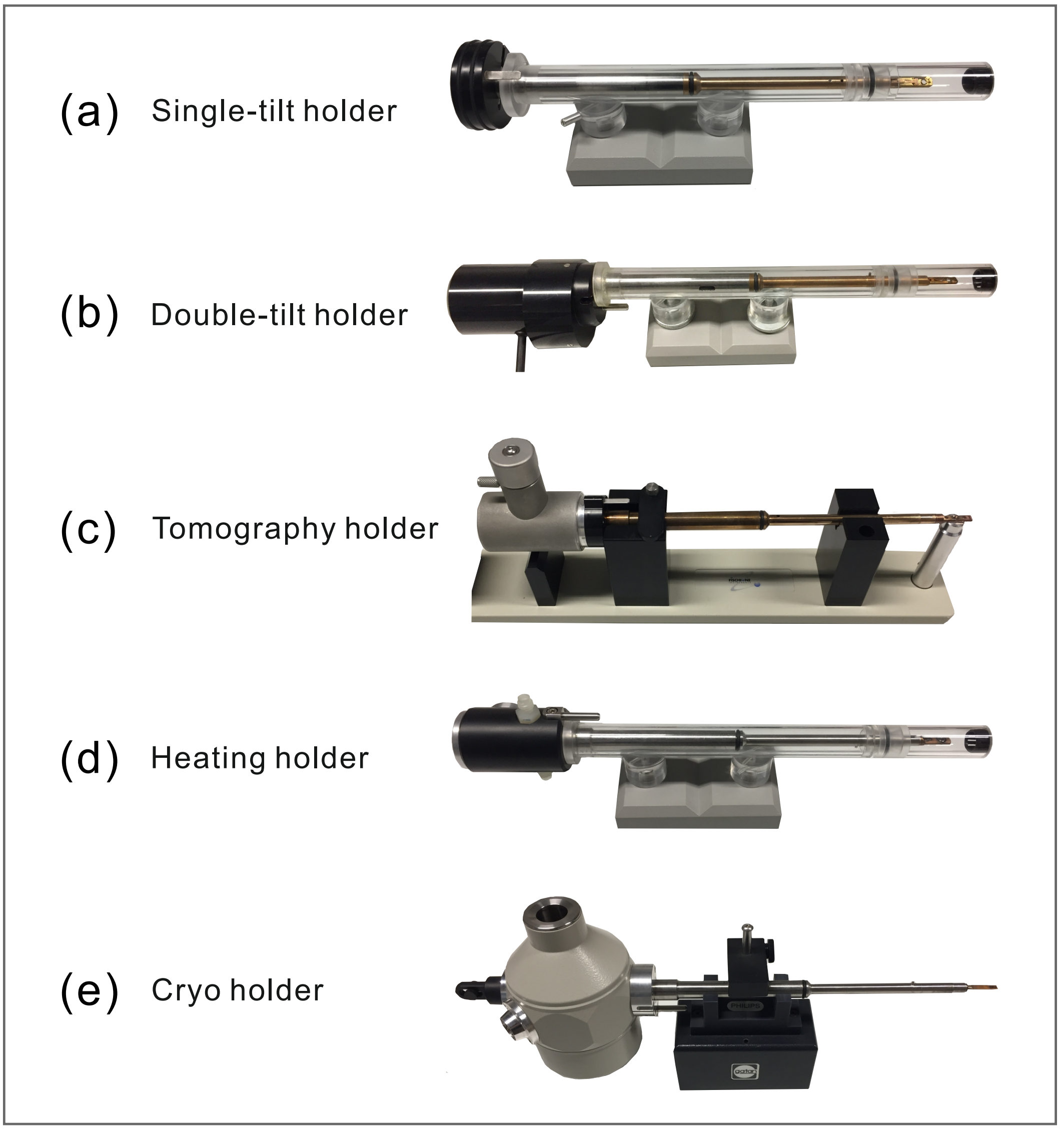

Figure 3.4: TEM specimen holders applied in the dissertation.

Single-tilt Holder (FEI)
The single tilt is easy to load and designed for general application such as a quick sample review. A tilt angle up to ± 60° is enough for the usual investigations. The holder movement is controlled by the TEM CompuStage.

Double-tilt Low Background Holder (FEI, model PW6595/15)
The double-tilt holder is connected with the Compustage. Beside the standard goniometer movements, there is a second stage tilt, allowing a maximum beta tilt of ± 30° for Tecnai TEMs. This holder is suitable for HRTEM measurements.

Dual-Axis Tomography Holder (Fischione, model 2040)
The tomo-holder is designed by the company Fischione Instruments, Inc. It has a tilt angular range almost through 360° plus a 90 degree planar specimen rotation. The extended speci-

men movability can maximize the tomographic data. The high accuracy and stability make it an optimal holder for electron diffraction and imaging tomography at room temperature. We used it in this work for the ADT data acquisition at room temperature.

Single Tilt Heating Holder (Gatan, model 628)
This holder is designed to heat the sample for TEM investigation at a high temperature. The temperature can be controlled by a Smartset Hot Stage Controller (model 901). It is possible to operate directly without any cooling system if the temperature is lower than 500 °C. If the desired temperature above 500 °C (max. 1300°C) a water recirculator must be connected. The maximumtilt range is ± 45°.

High Tilt Liquid Nitrogen Cryo Transfer Tomography Holder (Gatan, model914)
The cryo holder (tilt range: ± 80) is used to investigate the materials at a liquid nitrogen temperature achieved by a liquid nitrogen dewar at the end of the holder. The sample can be cooled before or after inserting the specimen holder into TEM. It is connected with a Smartset Cold Stage Controller (model 900) to check and control the specimen temperature.

Preparation for inserting TEM specimen holder
If the specimen allows it, the TEM holder and the grid with specimen are plasma cleaned by gas or a gas mixture as Argon or Oxygen to remove the organic contamination of materials. In this thesis, Plasma Cleaner model PC2000 CE (South Bay Technology, Inc. USA) is applied for the plasma cleaning (Fig. 3.5a). Before cooling experiments, the cryo holder must be evacuated using a pumping station and heated with a zeolite bake out cycle by Smartset Stage Controller for at least two hours. In this work, pumping on the dewar was carried out by Turbomolecular Drag Pumping Station (model TSH 071E, Pfeiffer Vacuum GmbH, Asslar, Germany) as shown in Fig.3.5b.

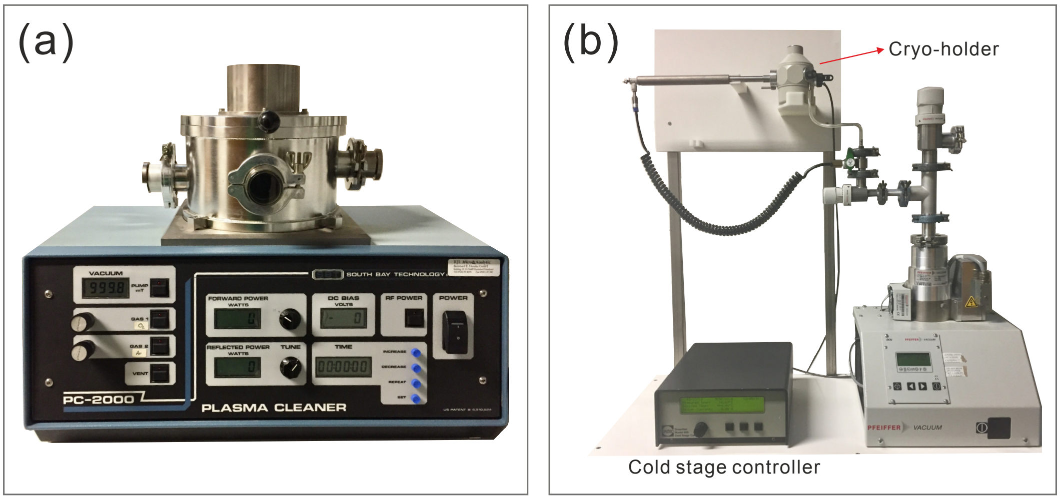

Figure 3.5: (a) Plasa cleaner for sample and holder cleaning and (b) pump system for cryo holder pumping.

3.5 ADT data acquisition

Using automated diffraction tomography, electron diffraction tilt series are collected accompanied by tilting around the TEM goniometer stage. In order to realize this specialty, an automated acquisition module was developed for FEI microscopes[43], which owns routines enabling crystal tracking under STEM imaging mode after each tilt step and to acquire diffraction patterns with nona-diffraction mode sequentially. The module consists of totally three types of calibrations: basic TEM calibration, specimen-holder calibration and diffraction-setting calibration. The specimen-holder calibration can be done and saved as a file in advance. If there is no changes about the physical settings of TEM, the calibration files are available and reliable to be used throughout several months. The ADT measurement is carried out using a TECNAI F30 TEM operating at 300 kV. Microprobe STEM imaging is used for tracking the measured crystal during the tilting process.

In order to reduce dynamic effects for a better quality of reflection intensity extraction, ADT was coupled with precession electron diffraction (PED)[65], which is realized by a DigiStar unit designed by the company NanoMEGAS[64]. Usually, the precession angle is set as 1° for data acquisition. nano electron diffraction (NED) data is collected without electron beam precession and hence there is no reflection splitting in the data. NED data is suitable for determination of accurate cell parameters. AS shown in Fig. 3.6, the diffracted spots cover a larger area in PED pattern than NED pattern. PED enables a quasi-kinematic diffraction intensities. Hence, the crystal structure solution is usually performed on PED data.

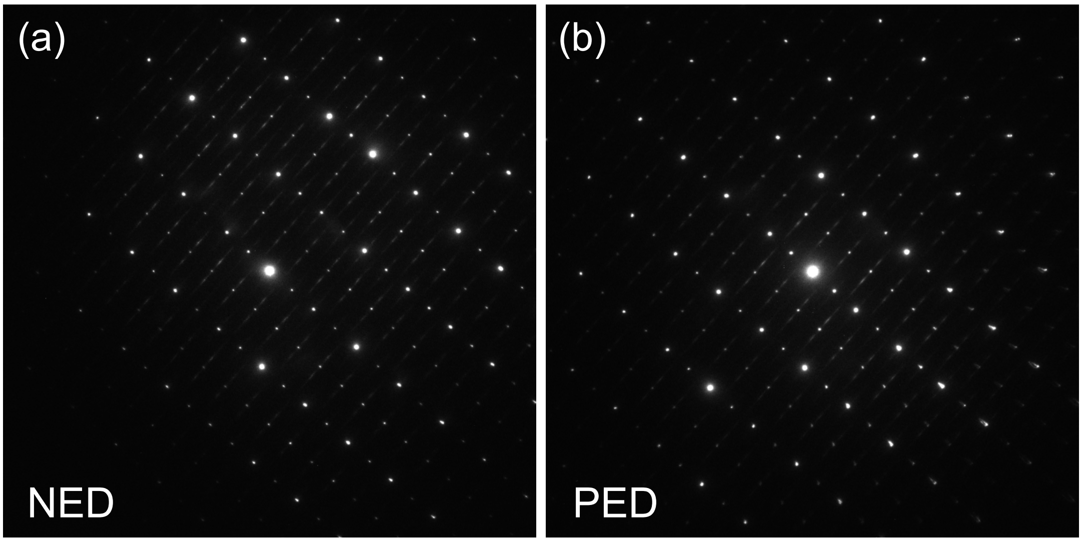

Figure 3.6: Single ED patterns of $Al_4B_2O_9$ viewed along $\boldsymbol{c^*}$ direction. (a) NED data collected without precession and (b) PED data with precession.

ADT measurements depend on a number of TEM alignments as shown in Fig. 3.7.

- The first step is to check C1 and C2 aperture. Normally, diffraction tomography is working with a large C1 (250 μm) and a small C2 (10 μm), which enables a semi-parallel electron beam and is referred to as NED mode. Based on the beam stability of samples, the illumination conditions are selected and controlled by means of operating voltage, selection of gun lens and spot size. For example, gun lens of 8 and of spot size of 8 or even 10 is normally good for beam sensitive materials.
- The second procedure is to align the TEM and STEM basic settings, which include gun shift, beam shift, beam tilt pivot point and beam focus in *TEM Tune* and *STEM Tune*, respectively. Noted that STEM calibrations and later imaging for crystal tracking are performed under microprobe mode. A rough HAADF centring with different camera lengths should also be done. The calibrations should be repeated if the beam changes a lot after the ADT calibration.
- The following process, also as the most important calibration, is to calibrate the diffraction settings. A number of substeps will be done as accurate as possible. The corresponding setting parameters are given according to the sample properties such as beam sensitivity, crystal size, crystal lattice. To view the real image of the crystal under investigation, the HAADF will be shifted in the middle. Beam size and diffraction camera length are set based on the crystal habit and the expected length of cell axes. In addition, the beam should be focused and then centred on the charge-coupled device (CCD) camera with a data size of 2048 x 2048 pixel (2K) or 4096 x 4096 pixel (4K). Once the calibration runs successfully, all the setting parameters will be used for the data acquisition.
- The final step is tilt-series acquisition. Selection of a single crystal or big enough corner of a embedded or agglomerated crystal. A good adjustment of specimen position (Z height) is crucial to make the crystal stable and visible during the tilt process. CCD exposure time, tilt angular range (initial and final tilt angle), tilt step as well as switch on/off of precession unit should be carried out before starting the collection process. The procedure starts with the beam centring on the fluorescent screen and the stage rotates to the initial tilt angle (max. or minimum tilt angle) where the first diffraction pattern is collected. Then the selected crystal must be shifted to the beam position in the STEM image. After centring the electron diffraction pattern on CCD camera the tilt-series collection will start. Electron diffraction patterns of each tilt step will be recorded sequentially and saved as a MRC format data at the end of the procedure.

Beside using low beam illumination (such as low operating voltage, big gun lens or big spot size), there are some tricks to avoid or reduce beam damage. If the selected crystal is larger than beam size, we can manually shift the beam from the illuminated area to the fresh part of the crystal. The other available way is sample cooling, especially for beam sensitive materials as organic compounds and MOFs.

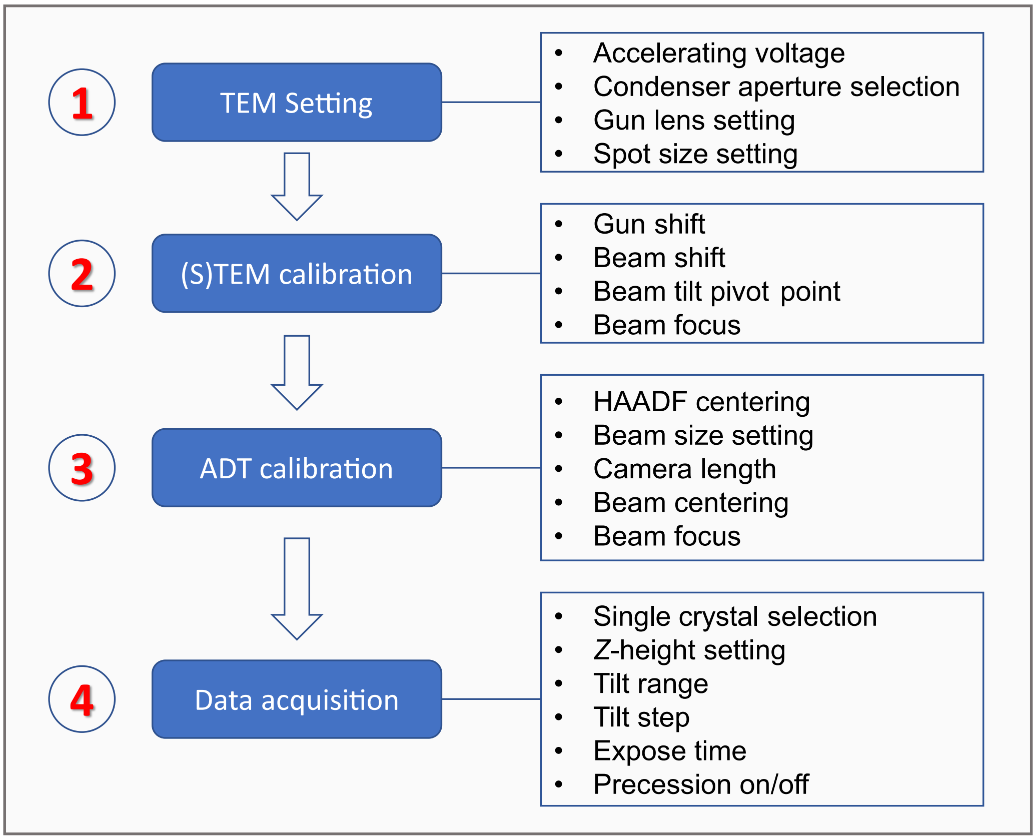

Figure 3.7: A brief diagram of TEM calibration sequence for ADT data acquisition using a FEI electron microscope.

3.6 ADT data analysis

`ADT3D` and `eADT` softwares are utilized to view and process the recorded electron diffraction raw data. The purpose of ADT data analysis is to deliver the reliable crystallographic information of investigated materials as much as possible. Some of the detected features may be problematic or even impossible to analyse using other methods. As described in section 2.3 of chapter 2, the recorded raw MRC data is actually a stack of 2D non-oriented diffraction patterns which cannot be directly indexed. Therefore, the first key step is to transform the set of 2D diffraction patterns into 3D reciprocal space. Based on visual inspection and careful handling of reconstructed reciprocal space, the analysis should deliver unit-cell parameters, symmetry information, indexing of reflections and intensities of acquired reflections. In addition, other related potential information such as diffuse scattering, twinning, or intensities of polycrystalline phase can also be delivered through visualization of diffraction volume. A successful data processing always relies on a datasets of required quality. The practical operations in the program `eADT` consist of several steps as shown in Fig. 3.8. A detailed description of the key procedures, including e.g. preprocessing, tilt axis determination, lattice determination, intensity extraction, etc., is presented below.

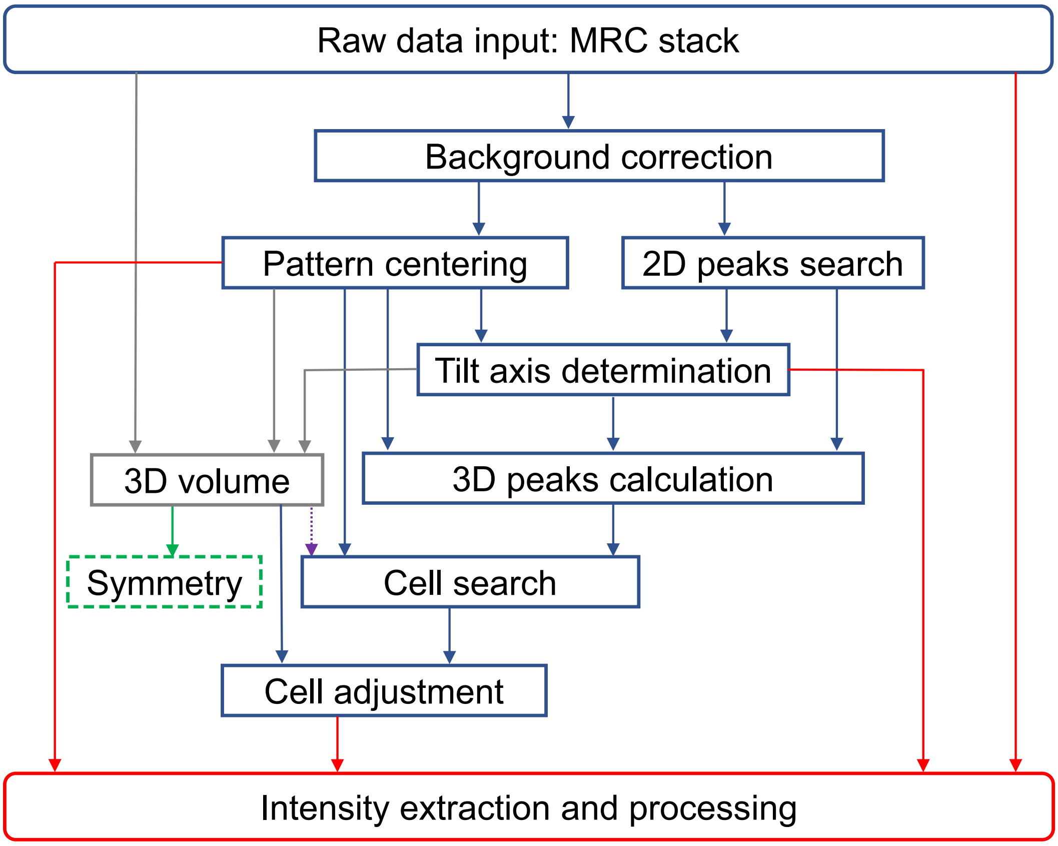

Figure 3.8: Workflow of the program eADT to process three-dimensional electron diffraction data. Notice: several functions as data binning, filtering of diffraction slice and pattern blur are not shown here. It is possible to reload the *shift file* for centering, *2D peaks*, *3D peaks*, *unit-cell* and *extracted intensity file*.

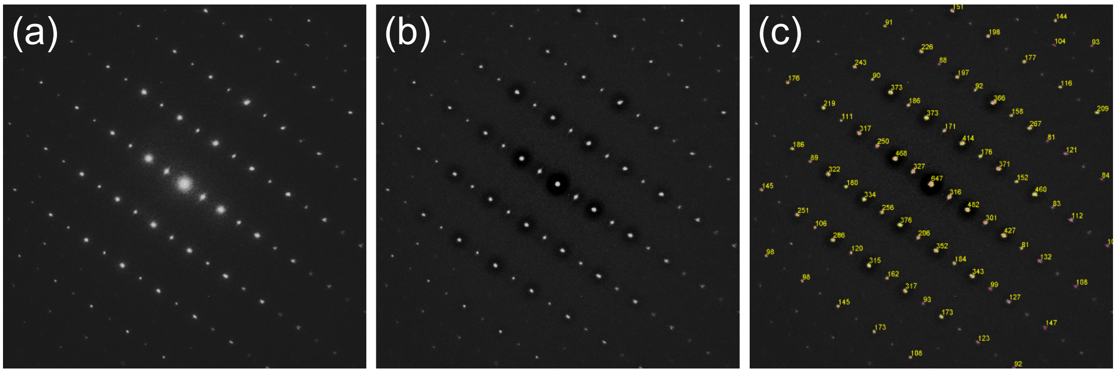

Figure 3.9: Electron diffraction pattern processing (example sample: aluminium borate). (a) Raw recorded diffraction pattern, (b) the same pattern after background correction and (c) 2D peaks found on the pattern.

3.6.1 Data pre-processing

- **Background correction.** The background subtraction is carried out for the 2D diffraction patterns. It simplifies to find the reliable centres of the diffracted spots at the procedures of "*2D peaks search*" and "*patterns centring*". It is crucial in particular for the diffraction peaks with weak intensity. As presented in Fig. 3.9b the diffraction pattern show the bright spots with smaller radius. Furthermore, background subtraction speed up the calculation rate of 3D reciprocal volume.

- **Centring of diffraction patterns.** During ADT data collection the centre of electron diffraction patterns cannot always ideally locate at the same position, namely the centre shifts slightly in a stack, even under a perfect measurement alignment. Normally, the reason results from the beam shift on the sample and the related electron beam shift for crystal tracking. Other factors such as physical stability of holder and goniometer stage, holder calibration or ADT calibration can also contribute to the centre shift. Patterns centring is of importance for a successful reconstruction of 3D reciprocal space. The normal two approaches, searching the centre of strongest beam and analysing the primary beam shape, can deliver a good result only if the primary beam appears as the strongest spot in the patterns. The centre of the Friedel pair can be considered as pattern centre in the case that the data is collected with a beam stopper. Other optional method is that the user can manually set the centre in the program `eADT`.
- **Tilt axis determination.** The search and refinement of tilt axis position depend on the pattern centring and 2D peaks extracted from each diffraction patterns. The process can be performed using an automatic model in an angle range from -180° to 180° or by an appointed angular rang and step. The found tilt axis position shows a pronounced maximum in the variance plot. A accurate value of tilt axis delivers sharp and bright stereographic projections of the 3D reciprocal space. A correct tilt axis ensures the 3D reconstruction without distortion, the possibility of unit-cell determination as well as reliable intensity extraction.

3.6.2 Visual analysis of 3D reconstruction

This step is the key step to analyse the tilt series data for much more information of the sample. With known pattern centres and refined tilt axis, the 3D reconstruction of reciprocal space can be achieved by recalculation of 2D pixel-data stack into 3D voxel-data.[42] It should be observed at first sight whether the quality of the tilt series is good and to which resolution the reciprocal space is covered. A wrong tilt axis leads to a distorted reciprocal volume. After careful inspection of the reconstructed data, structural features as diffuse scattering (Fig. 3.10b), polycrystallinity, twinning, superstructure can be directly visualized. Using derived cell vectors, the unit-cell parameters can be refined in combination with the 3D reconstructed volume. The projections of main crystallographic direction and well-known pixel size provide the crystal system and Bravais lattice. Once the correct unit-cell is determined, the single zones required from extinction analysis can be cut from the 3D volume. The extinction conditions, namely the appearance of reflections in the single zones, indicate possible space groups.

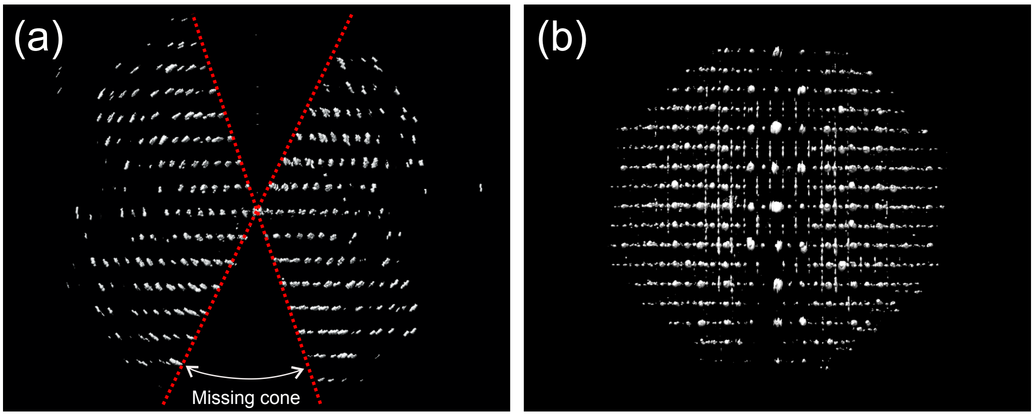

Figure 3.10: Three-dimensional reconstructed diffraction spaces of (a) zeolite chabazie showing the missing cone and (b) disordered $Al_4B_2O_9$ including diffuse scattering.

3.6.3 Unit-cell determination

The extraction of 2D peaks from single stack slices (as shown in Fig. 3.9c) combines with tilt axis and the file of pattern centring to construct the 3D reflection positions in the reciprocal space. Because of the missing cone it happens not often all the three main axis to be present together in one dataset. The procedure to determine cell vectors, comprising lattice parameters and orientation matrix, is performed based on clustering of difference vectors.[44,156] The difference vectors of all selected recorded reflections are calculated and they show the autocorrelation of the peaks based on clustering routine. When the three shortest linearly independent vectors can be found, it will deliver the initial primitive unit-cell. Normally, the primitive lattice cannot demonstrate the real crystallographic feature when the sample has a high symmetry. For instance, there are two methods to solve the problem if the crystal lattice is actually centred. The extracted intensities can be converted into an intensity file based on `MatLab` scripts. Alternatively, the initial primitive unit-cell can be directly transformed into a centred lattice in the reciprocal space using a transformation matrix. For example, the initial primitive triclinic unit-cell (a = 14.55 Å, b = 14.44 Å, c = 4.99 Å, α = 99.0 °, β = 89.7 °, γ = 119.6 °) of zeolite THK-2 can be transformed into a orthorhombic lattice (a' = 24.72 Å, b' = 14.55 Å, c' = 4.99 Å, $\alpha' = \beta' = \gamma' \approx 90°$) in the reciprocal space with matrix [0 -0.5 0; 1 -0.5 0; 0 -0.5 0]. The unit-cell parameters determined from ADT data are not accurate and shows a error of about 2-5%.[44]

3.6.4 Intensity extraction

With the known unit-cell vectors the recorded reflections in all the 2D diffraction patterns can be indexed and the corresponding intensities can be integrated. A box overlaid on the reflection is used for the intensity integration (Fig. 3.11a). The box size depends on the diameter of the reflection with strongest intensity and the unit-cell parameters. Since the reflections penetrate normally through several neighbouring slices, the same index may appear extracted with different intensities on different frames. As shown in Fig. 3.11, the $(\bar{1}\bar{1}0)$ reflection can be detected from frame 84 to frame 90 and has an intensity maximum in the frame 87. Only the extracted maximal intensity value is taken in account and used as the intensity of the reflection. The square of responding reflection intensity is calculated to serve as the intensity error. The resulting *hkl* file consists of the indices, corresponding intensities and intensity errors. Some intensities cannot reach maximal values because the reflection locates at the edge of missing cone. Therefore, such unreliable reflections should be deleted with `Matlab` script.

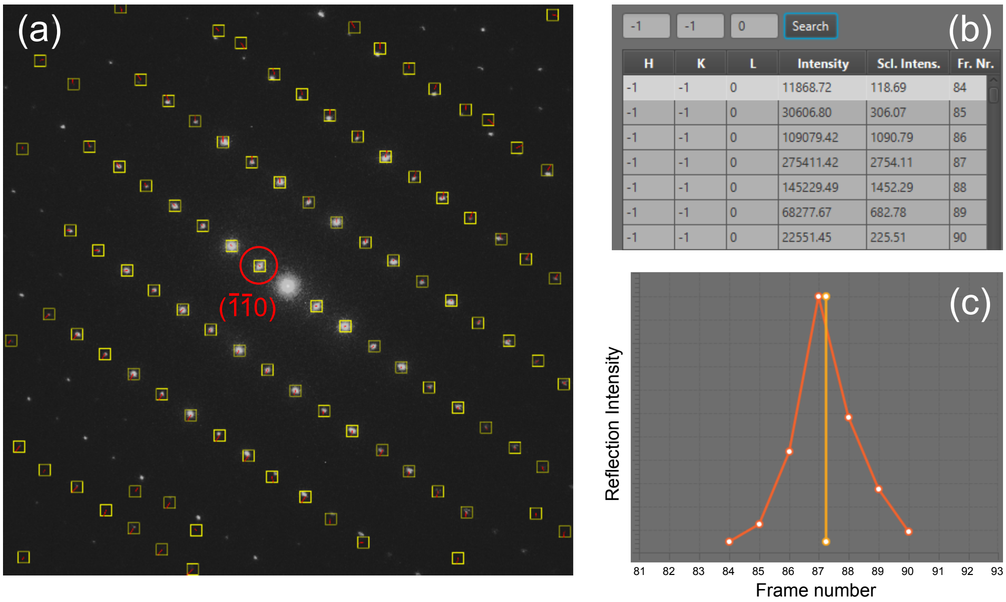

H	K	L	Intensity	Scl. Intens.	Fr. Nr.
-1	-1	0	11868.72	118.69	84
-1	-1	0	30606.80	306.07	85
-1	-1	0	109079.42	1090.79	86
-1	-1	0	275411.42	2754.11	87
-1	-1	0	145229.49	1452.29	88
-1	-1	0	68277.67	682.78	89
-1	-1	0	22551.45	225.51	90

Figure 3.11: Reflection intensity extraction in the program eADT. (a) Electron diffraction pattern overlaid with integration boxes; remarked circle shows the position of reflection $(\bar{1}\bar{1}0)$. (b) List of the extracted intensities of remarked reflection $(\bar{1}\bar{1}0)$ in different frames. (c) Curve of the intensities distribution; the yellow line shows the theoretic frame number of maximum intensity.

4 Introduction to investigated materials

4.1 Aluminium borate

4.1.1 Mullite

Mullite can be found as a mineral in sandstones and in volcanic rocks in the nature.[157] Nowadays, a vast number of mullites and related mullite-type compounds are produced artificially for industrial applications as ceramic materials. The synthetic procedures starting with different ratios of SiO_2:Al_2O_3 can be performed through varying reaction conditions to form various of mullites with general composition of $Al_{4+2x}Si_{2-2x}O_{10-x}$ with x ranging from 0.18 to 0.88[158] in the SiO_2-Al_2O_3 system. The most common types are 3:2 mullite ($3Al_2O_3{\bullet}2SiO_2$) and 2:1 mullite ($2Al_2O_3{\bullet}1SiO_2$), respectively. As described by Schneider et al.[159], it is possible to incorporate transition metals as Ga, Ti, V, Mn, Cr atoms into the mullite structure. The amounts of transition metal ions rely on the reaction conditions. Beside the aluminosilicate composition of mullite, plenty of silicon-free compounds including e.g. aluminium borates[74,76,78] as $Al_{18}B_4O_{33}$ and Al_5BO_9 as well as gallium borates like $Ga_4B_2O_9$[160] have been captured attention and and many reports were published in recent. All those compounds show similar remarkable structural characteristics to mullite and form a series of important ceramic materials described as mullite-type compounds.

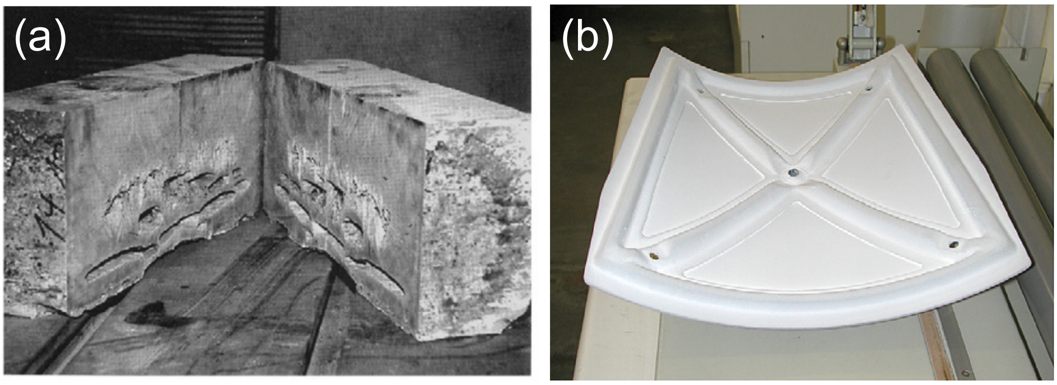

Figure 4.1: Technical applications of mullites. (a) Mullite-based refractory bricks. (b) Mullite-coated composite in panel for reentry space vehicle. Adapted from Schneider et al.[157].

There are several methods to synthesize mullites[159,161]: (1) solid-state processes, (2) solution process and (3) gas-state process. For instance, the 3:2-mullite crystallizes from a solid-state reaction by means of heating the educts below their melt points. Mullite belongs to one of the important constituents of ceramic materials and shows its importance in industry due to its physical properties[82,157,161] including thermal stability, low density, low-electric conductivity, excellent creep resistance, high-chemical stability, high-temperature strength, etc. The main technical applications of mullite comprise of the following three areas[157,159]: monolithic mullite ceramics , mullite coatings (Fig. 4.1b) and mullite matrix composites. For instance, mullite can be applied as refractory bricks (Fig. 4.1a) in glass melting tanks due to its high corrosion resistant.

4.1.2 Mullite-type crystal structure

The most prominent characteristics of the mullite-type structure are linear edge-sharing MO_6 (M = octahedral coordinated cations such as Al, Ga, Fe) octahedral forming parallel octahedral. These octahedral chains build up the backbone of the whole framework. Another important feature is that all mullite-type compounds must crystallize in a subgroup of the tetragonal space group $P4/mbm$ (No. 127).[162]

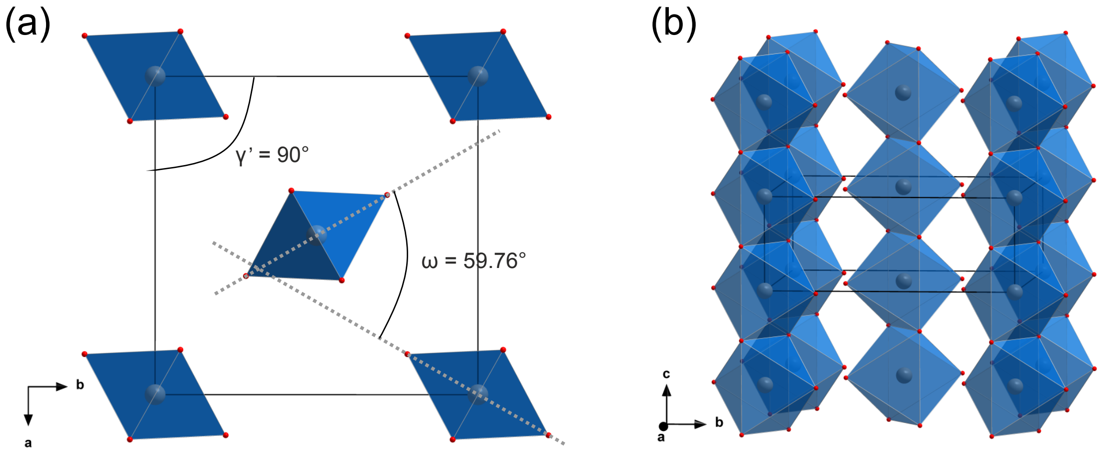

Figure 4.2: The chain structure of 2:1 mullite (modified after R. X. Fischer et al.[162], crystallographic data from Angel et al.[163]), viewed parallel to axis c in (a) and a in (b). γ' shows the angle between the a and b basis vectors; ω represents the tilt angle between neighbouring octahedral chains.

Fig. 4.2 illustrates the chain structure of 2:1 mullite in the orthorhombic space group $Pbam$ (No. 55). The AlO_6 chains perpendicular to (ab)-plane have two types of arrangement, leading a rotation angle (ω) between the adjacent chains (ω = 59.76° for 2:1 mullite see Fig. 4.2a). In a mullite-type crystal structure, the value of the rotation angle ranges from 30° to 90° and γ' should be in the range of 85° - 95°.[159]. The octahedral chains are cross-linked by various inter-chain units to form different connections, enriching the member in the mullite-type family. In inter-chain units can be five-, four- or three-fold coordination units involving e. g. AlO_5, TO_4 (T = B, Al or Si), or BO_3. For instance, O atom bridges the TO_4 (T = Al, Si) units between the octahedral chains in 2:1 mullite. Due to the substitution of Si^{4+}

by Al^{3+}, oxygen vacancy is introduced on the basis of $2Si^{4+} + O^{2-} \rightarrow 2Al^{3+}$ + vacancy □, which makes an extended linkage. The possible logical oxygen vacancy may also occur in the structure. Furthermore, the coordination and connection of linkage units can result a complex structure in mullite-type compounds. All the different units in various possible connections increase the variety of mullite-type family and lead to disordered structures due to the complex linkages between the chains. Therefore, the diversity of inter-chain units including the types and corresponding arrangements, the distribution of Si and Al in tetrahedral centre, the vacancy of oxygen atoms or even the synthesis conditions can lead to defects in crystals or order-disorder phenomena, which causes difficulties in crystal structure characterization of mullite-type compounds.

4.1.3 Aluminum borates

The phenomena of B atoms substituting Si atoms to form BO_4 tetrahedral connecting AlO_6 octahedral chains in mullite was first suggested by Dietzel and Scholze[164]. This discovery extended the binary SiO_2-Al_2O_3 system to a ternary SiO_2-Al_2O_3-B_2O_3 system and added a large number of new members in mullite-type family. As shown in Fig. 4.3, the SiO_2-Al_2O_3-B_2O_3 system covers all the possible boron-mullite introduced by Werding and Schreyer.[165] The grey field represents the potential intermediate phases between aluminosilicate mullite compounds and aluminum borates.

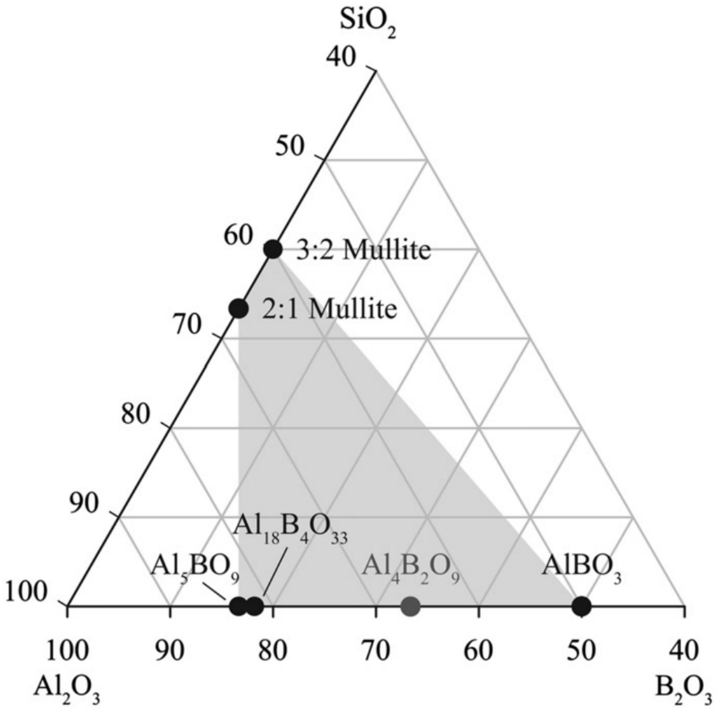

Figure 4.3: Plot of potential phases in the SiO_2-Al_2O_3-B_2O_3 system (Plot taken from Fischer et al.[78]). The grey area shows the boron-mullite stability field according to Werding et al.[165].

One of the most-researched aluminum borates is $Al_4B_2O_9$. Scholze et al.[166] investigated $Al_4B_2O_9$ for the first time and reported an orthorhombic lattice (a = 14.8(2) Å, b = 15.1(2) Å, c = 5.6(1) Å, and Z = 8) with possible space groups of *Cmm2*, *Cm2m*, *C222*, or *Cmmm*. The crystal structure was further studied by Mazza et al.[167] who described an orthorhombic structure (space group: *Pbam*) with a pseudo tetragonal symmetry. In the last decades, the group of Fischer (Bremen, Germany) has made advance in the research of $Al_4B_2O_9$ including the synthesis and crystal chemical characterization. Fischer et al.[77] tried to described the crystal structure of $Al_4B_2O_9$ in a monoclinic crystal system using a Rietveld refinement fromXRPD data and investigated additionally with solid-state NMR spectroscopy.

4.1.4 Synthesis of $Al_4B_2O_9$

Aluminium borate $Al_4B_2O_9$ was synthesized with sol-gel synthesis approach.① The initial ratio of Al_2O_3/B_2O_3 was set to 35/65 in the precursor phase using the nitrate decomposition method described in the literature[29,168,169]. The mixture of aluminum nitrate nonahydrate $Al(NO_3)_3 \cdot 9H_2O$ and boric acid $B(OH)_3$ was dissolved in 10 wt.% glycerol. The produced foam was dried and then crushed into powder. The sample was continuously heated using covered platinum crucibles at 1223 K for 44 hours. The sample was cooled to room temperature. In order to remove the possible excess boric acid, the final sample was washed with hot deionized water and dried to obtain white powder.

4.1.5 Research questions of $Al_4B_2O_9$

In the previous study of Fischer et al.[77], $Al_4B_2O_9$ was characterized by a combination of XRPD and solid-state NMR and the crystallographic information. The crystal structure was reported in a monoclinic crystal system for the first time. However, due to disorder phenomenon in the mullite-type family, two oxygen atoms could not be revealed clearly. Furthermore, one-dimensional XRPD approach has limits on the study of disordered materials and further is hampered to clarify crystal chemical properties of $Al_4B_2O_9$ in details. On the other side, the achievable small crystal size limited the investigation using single crystal X-ray diffraction. For these reasons, the material was reinvestigated using TEM approach to explain the crystal structure feature including following points.

- Finding the disordered crystals or domains
- *Ab initio* structure solution of ordered crystal from ADT data
- High-resolution TEM imaging of ordered crystal
- Determination of disorder type
- Structural modelling ans electron diffraction pattern simulation

---

①Note: the synthesis of $Al_4B_2O_9$ was carried out by Dr. Kristin Hoffmann (University of Bremen, Germany)

4.2 Metal-organic frameworks

4.2.1 Metal-organic frameworks

Metal-Organic Frameworks (MOFs), also known as porous coordination polymers (PCPs), are a new class of organic-inorganic hybrid solids which first appeared about two decades ago. In recent years, MOFs, as a new type of advanced porous solid materials as shown in Fig. 4.4, are being drawn particularly strong attention by researchers due to the various outstanding industrial applications.[88,98–100] The potential applications of this type of crystalline materials are based on the unique structural attributes with ultrahigh porosity[170], enormous internal surface areas (up to 14600 m^2/g)[171], uniform channels and thermal stability. In consideration of the high degree of design-ability for the structure, various novel MOFs have been designed and successfully synthesized for the attainment of specific properties and the optimizations of applications. The design options of MOFs rely on the controllable synthesis conditions, the extraordinary variable and modifiable structure building units (metal ions/clusters and linkers) as well as the huge number of potential combinations of organic ligands, types of transition metals, co-ligands and structure directing agents.[88,172,173] Currently, the number of members in MOF-family is still increasing rapidly. The investigations on the synthesis, characterization and application of new MOFs are emerging in an immense number of research articles.

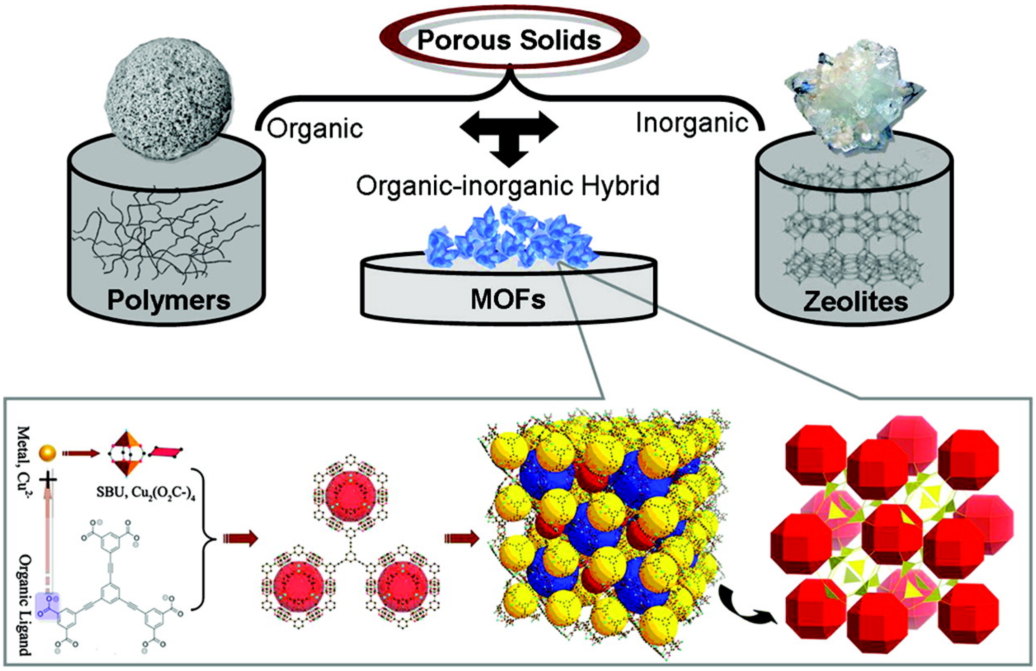

Figure 4.4: The general classification of porous materials. Top: porous organic polymers; organic-inorganic porous hybrid solids (MOFs) and porous inorganic zeolites. Bottom: an example for the classic construction procedure of a MOF from organic linkers and inorganic metal. Reproduced from ref. of Li et al.[172].

4.2.2 Synthesis and structure properties

One of the most significant motivations for synthesis of new MOFs is to find sufficiently robust and porous solids which can fulfil the technical requirements. The synthesis procedure of MOFs is typically straightforward and at moderate temperature (< 250°C)[174]. The synthesis conditions (temperature, pH, solvent, and stoichiometry) play a significant role in modifying the network topologies.[88] The infinite extended metal-organic porous structures are established by self-assembly of organic and inorganic building blocks under the conditions as temperature setting and synthesis time. The well-soluble salts serve as the source for metal elements, e.g. metal nitrates or sulfates. The metal ions are mainly transition-metal ions. The organic linkers are typical bidentate ligands or multidentate molecules with two or more N or O donor atoms. They can be carboxylate linkers such as di-, tri- and tetracarboxylic acids, imidazolate type linkers[175] as well as phosphonate linker as show in Fig. 4.5. As compared to azolate- and phosphonate-based frameworks, a major part of the known MOFs are in fact based on bridging ligands of carboxylate linkers[176]. Using rigid linear dicarboxylates (denoted as L), Yaghi and co-workers[177] synthesized a big series of compounds which share the same formula of $Zn_4O(L)_3$. One of the well-known azolate-based MOFs is for instance zeolitic imidazolate framework-8 (ZIF-8), which was first reported by Yaghi et al.[175] and consists of zinc atoms linked by 2-methy-imidazole molecules.

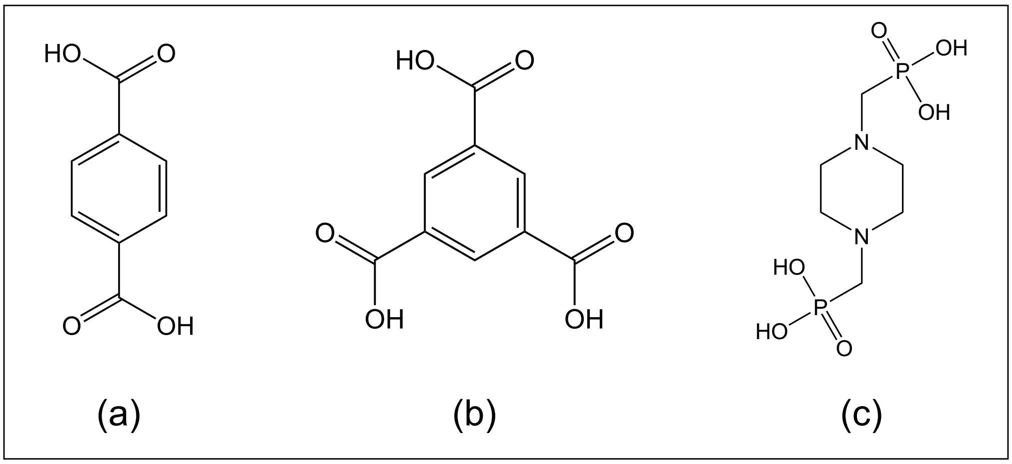

Figure 4.5: Examples of organic linkers in MOFs. The emerged organic linkers own normally rigid backbone. Carboxylate linkers: (a) bipodal linker BDC for MOF-5 and (b) tripodal linker BTC for HKUST-1. Phosphonate linker: (c) bipodal methylenephosphonic acid for phosphonate frameworks.[178]

Most studies about MOFs were focused more on the design of novel types, synthesis and characterization in the form of traditional bulk crystalline compounds. However, the applications of MOFs are reliant not only on the controllability of chemical structure but also on factors as micro/nano-structure, crystal size and morphology. For instance in biology and medicine, due to the required application of penetration into cells, only nano-sized materials are achievable, where bulk MOFs show the limits. Therefore, rational design of

MOFs is crucial for the consideration of the practical needs as crystal size, shape, rigidity in the aimed investigation.

MOFs can be synthesized by various possible approaches. In the conventional synthesis method, MOFs are generated by mixing the starting materials under hydrothermal or solvothermal conditions at room temperature or through electric heating. For instance, the well-known MOF-5 and HKUST-1 were synthesized with the direct mixing of reagents at room temperature. Many other advanced methods are summarized by Stock and co-workers in the review paper[88]. Recently, the conventional solvothermal synthesis, the microwave-assisted method, mechanochemical synthesis, the surfactant-assisted method, the coordination modulation method, and the solvent induced precipitation have been reported in the MOFs synthesis.[88,99,179–181] In comparison to the solvothermal synthesis, the new strategies have exhibited several advantages like less time-consumption, controllable crystal morphology and size, solvent-free, etc. In particular, some of these methods are very helpful to gain nano-scaled or hierarchical MOFs. Kitagawa and co-workers[182] designed a simple approach - coordination modulation method, using the capping reagents to control the crystal growth of nano-scaled porous coordination polymers. The other example is the synthesis of thin patterned MOFs films (SURMOFs) due to the application as sensor[183]. The highly oriented growth of homogeneous MOFs crystals are obtained by so-called layer-by-layer (LBL) growth at liquid-solid interface under control conditions.[184–186]

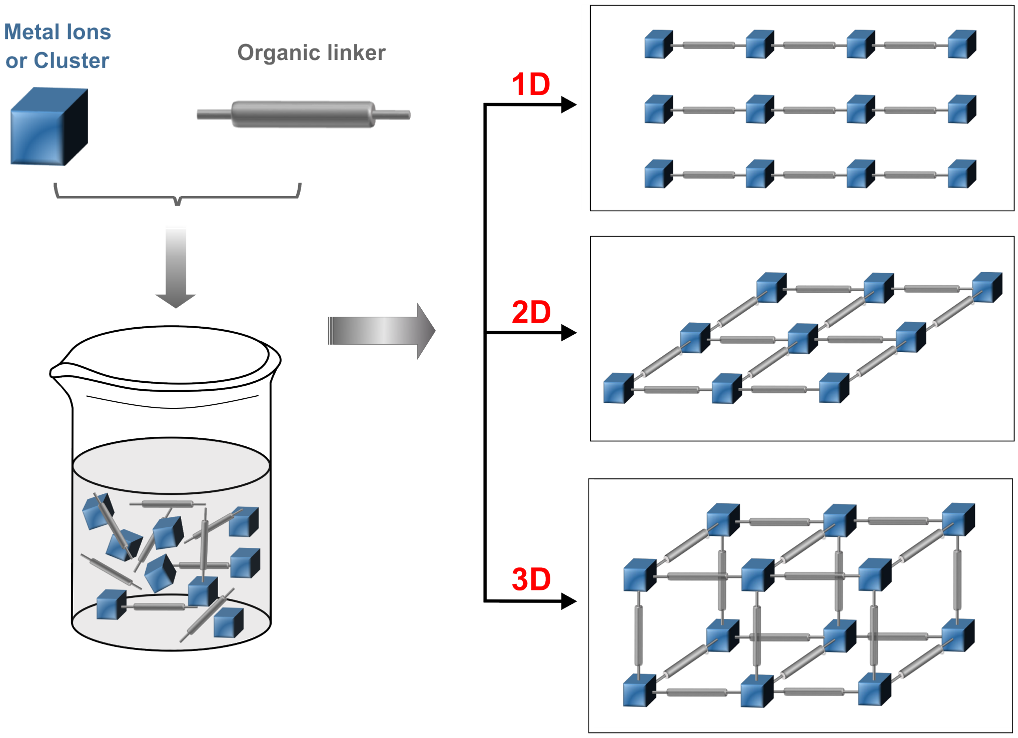

Figure 4.6: Schematic illustration for the design of MOFs involving general networks structure with 1D, 2D and 3D topologies. The topology of the products is depend on the coordination of metal ions, the geometry of bridging ligands as well as the synthesis conditions.

In order to describe the subunits of a MOF, the term of secondary building units (SBUs), also called as inorganic building units, has been introduced to organize the classification of MOF structures. SBUs are metal-containing clusters and molecule complexes.[176] Depending on the types of bridging linker and coordination number of transition metal atoms, the porous supramolecular network can be designed or achieved 1D (chains), 2D (layers) or 3D (framework) architectures, as shown in Fig. 4.6. MOFs can be characterized by numerous approaches including single crystal X-ray diffraction (if the crystal big enough), X-ray powder diffraction (XRPD), transmission electron microscopy (TEM)[68], nuclear magnetic resonance (NMR)[187,188], thermogravimetric analyses (TGA), etc.

4.2.3 Applications of MOFs

Based on the specific structure feature, chemical design-ability and thermal stability, MOFs have a vast number of potential industrial applications, which comprise the use as storage media for gases like hydrogen and methane[95,189,190], heterogeneous catalysis[68,93,94,100], drug delivery[101,102,191,192], gas separation. Additional applications in membranes, thin film devices[184–186,193,194], and biomedical imaging[191] are increasingly gaining importance. Some of the applications are detailed as examples below.

- **Gas separation/storage**

High efficient gas separation/storage are of high importance in the industrial process. MOFs demonstrate the performance in gas separation. For instance, Cu-BTC (HKUST-1) serves as a excellent CO_2 adsorbent for a gas mixture of CO_2/N_2 or CO_2/CH_4.[98,190]

- **Drug delivery**

The other important application of MOF nanoparticles is for drug delivery in biomedical area. Horcajada and coworkers[101] investigated the drug delivery of MOF materials based on MIL-100 and MIL-101 and reported for the first time the outstanding capacity for hosting and controllable delivery. Afterwards they published another article[191] about specific non-toxic porous iron(III)-based MIL series MOFs for efficient controlled drug delivery.

- **SURMOF**

The formation of MOF thin films or membranes with well-defined porosity make them suitable as candidates for the applications like smart membranes, chemical sensors, catalytic coatings and related nanodevices.[195] The thin films are grown on selected substrates as gold or silica surface through the controllable stepwise layer-by-layer method. The materials comprise for instance HKUST-1 thin film[193,194,196] and ZIF-8 membranes[197].

4.2.4 Syntheses of MOFs

$$Zr^{4+} + AcOH \ \& \ BDC \Rightarrow [Zr_5O_4(OH)_4(OAc)_4(BDC)_2]$$

$$Zr^{4+} + Ni\text{-}H_8TPPP \Rightarrow [Zr_2(Ni\text{-}H_2TPPP)(OH/F)_2]\cdot 23\ H_2O$$

Two new zirconium metal-organic frameworks (Zr-MOFs), $[Zr_5O_4(OH)_4(OAc)_4(BDC)_2]$ and $[Zr_2(Ni\text{-}H_2TPPP)(OH/F)_2]\cdot 23H_2O$ (denoted as CAU-27-BDC and Zr-CAU-30, respectively), were designed based on the Zr^{4+} and the bridging ligands of AcOH and BDC for CAU-27-BDC (Fig. 4.7) as well as NiH_8TPPP for Zr-CAU30 (Fig. 4.8), respectively. The syntheses of both Zr-MOFs ② are briefly described as in the original literature[72,198].

Synthesis of CAU-27-BDC

The CAU-27-BDC was prepared by a hydrothermal method: 232.6 mg terephthalic acid and 20 mL acetic acid were first placed in a PTFE lined steel autoclave. Then 0.892 mL zirconium acetate solution mixed in dilute acetic acid were added and the autoclave was sealed. The mixture was heated to 220 °C in one hour and then kept at the temperature for 238 hours. Finally, the mixture was cooled down to room temperature, 526.8 mg of a white/greyish solid were yield via filtration and subsequent drying for 1 hour at 60 °C.

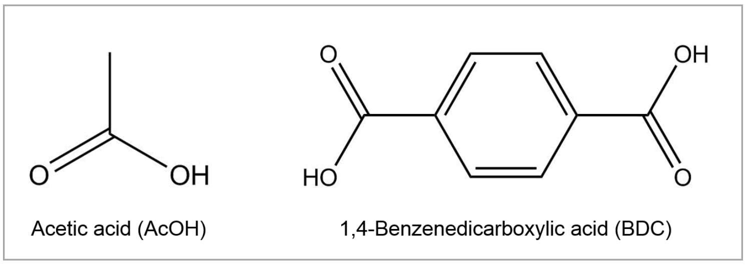

Figure 4.7: Organic carboxylate linkers for the synthesis of CAU-27-BDC.

Synthesis of Zr-CAU-30

The Zr-CAU-30 was synthesized using hydrothermal syntheses method. Previous synthesized Ni-tetra(4-phosphonophenyl)porphyrin (referred to as NiH_8TPPP) serves as bridging linker. The reagents were mixed from $NiH_8TPPP/ZrOCl_2\cdot 8H_2O/NaF/NaOH$ with a molar ration of 1 : 2 : 60 : 8. The reaction mixture was stirred in a glass reactor. Using a enlarged scale of 12 compared to initial amount settings, highly crystalline and stable powder was obtained at 160 °C for 3 h. In order to obtain the dehydrate phase of Zr-CAU-30, the

---

② Note: CAU-27-BDC and Zr-CAU-30 were prepared by S. Leubner and Dr. T. Rhauderwiek (Both from University of Kiel, Germany), respectively.

as-made sample was calcined at 250 °C under reduced pressure of 100 kPa in a 0.5 mm glass capillary.[72]

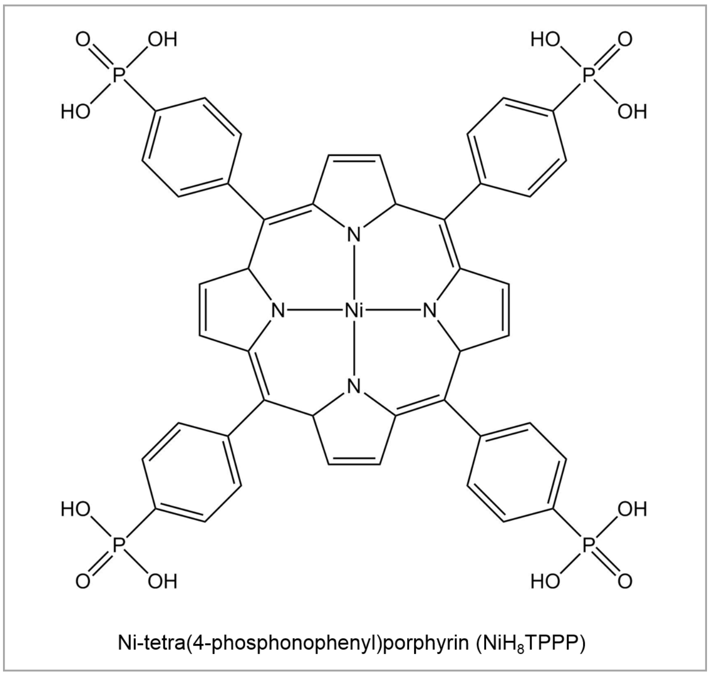

Figure 4.8: Linker for the synthes of Zr-CAU-30. Phosphonate linker as tetrapodal ligand coordianted with Zr atoms.

4.2.5 Research questions of Zr-MOFs

The Stock's group from Kiel (Germany) has designed and synthesized various novel MOFs including the CAU-series[61,68,199,200] in the last two decades. Most of the crystal structures in the CAU-family were solved straightforward by X-ray diffraction methods. However, due to limited crystal size, low crystallinity, twinned crystals and the extra large unit-cell it impeded to elucidate the crystal structure using single crystal or powder X-ray diffraction. Electron diffraction tomography was proved as efficient method to solved this kind of difficulties even for the beam sensitive materials[61,68,201]. The new Zr-MOFs, BDC-CAU-27 and Zr-CAU-30, prepared in form of nanocrystals, are impossible to investigate using single crystal X-ray diffraction. In addition, the determination of lattice parameters and symmetry information are also challenging by means of XRPD. Therefore, the Zr-MOFs were investigated using electron diffraction tomography focusing on single nanocrystals but delivering three-dimensional diffracted reciprocal space. The main works are summarized as following:

- Determination of lattice parameter
- Determination of possible space group
- *Ab initio* structure solution from ADT data
- High-resolution TEM imaging

4.3 Zeolites

4.3.1 Introduction

Since the first zeolite synthesis by Barrer and Milton, numerous zeolites were synthesized increasing the number of zeolite and zeolite-type materials.[202,203] More than 200 zeolites are registered in the zeolite data base of International Zeolite Association (IZA).[8] In general, zeolites are synthesized with an organic structure directing agents (OSDAs)[204] under hydrothermal conditions between 100 and 200 °C. Due to the pore size less than 2 nm, zeolite and zeolite-type compounds are crystalline microporous materials with 1D, 2D or 3D frameworks.[86,205] The networks are construed corner-sharing building units - TO_4 tetrahedra with T = Si, Al, P, Ga, Ti, Sn, Ge, etc. to form periodic channels, pores or cavities with well-defined sizes and shapes. Various zeolites were designed and synthesised based on the flexibility of combination with different TO_4 types under different conditions. The numerous possibilities in combination and and connection make the structural diversity of zeolites and zeolite-type compounds. It is common that the disorder phenomena occurs in the structure not only in the natural but also synthesized zeolites. There are several reasons like connection and type possibilities of the basic units as well as the formation conditions. Due to the highly chemical and physical stabilities, zeolite and zeolite-type materials are applied in different areas, e. g., catalysis, gas separation, gas adsorption, electronics, ion exchange, and biomedicine. For instance, zeolites are widely applied as catalysts in the petroleum and petrochemical industry.[105,206]

4.3.2 Metal-containing zeolites

Metal-containing zeolites are prepared by ion-exchange process using metal atoms like Al, Cu, Co, Ti,Fe, Pt, Pd, Sn.[207–212] This type zeolites have attacked strong attention due to the catalytic performance in selective oxidation.[212–215]

Two type of metal-containing zeolites were studied in this work. The interlayer expanded zeolites M-IEZ-RUB-36 materials are colourless samples. They were synthesized using a zeolite precursor as-made RUB-36[216]. M-IEZ-RUB-36 materials show highly disordered structures, but nevertheless show a highly shape-selective catalytic activity and an efficient catalytic activities in oxidation reactions.[214,215] The industrial applied Cu-CHA, a copper-based ion exchanged zeolite catalyst, shows excellent activity for the selective catalytic reduction (SCR) of NOx with NH3.[108–111] Chabazite is also called SSZ-13 and occur in the nature or can be prepared. CHA crystallizes in a trigonal system with space group of $R\bar{3}m$ (No. 66). The basic building unit of CHA is the double 6 ring consisting of two single 6 ring. The double 6 rings stack with a sequence of *AABBCC* to construct a 3D framework structure.[8] The scheme to build the framework is shown in Fig. 4.9 where 8 rings are formed after the stacking. The Cu position serves as the catalytically active sites during SCR reactions. It was described that the Cu atoms distribute in the six and eight ring through a ratio which is decided by the water atmosphere in the cage. In order to understand the catalytic mechanisms, the active Cu site in the framework was investigated at high temperature by electron diffraction in this work.

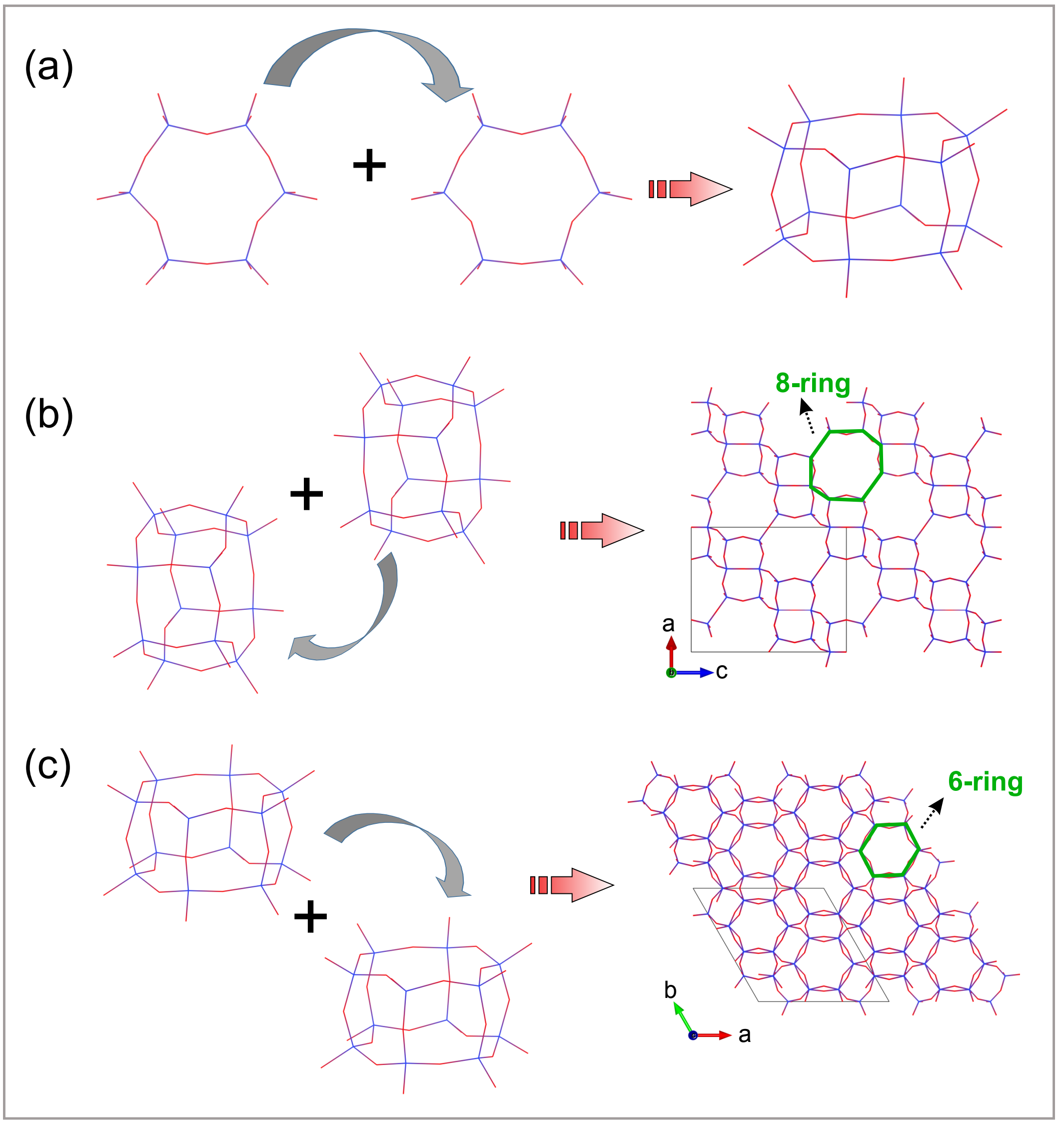

Figure 4.9: Building scheme of the crystal structure of CHA. (a): Two single 6-rings stack to build a double 6-ring; (b, c): The stacking of double 6-rings construct the 3D-structure.

4.3.3 Organic structure directing agent in zeolite

Numerous zeolites were prepared using OSDAs with hydrothermal synthesis approach.[204] Often specially designed OSDAs were used to synthesize zeolites with new framework structures, for example, the zeolites ITQ series synthesised using novel OSDAs by the Corma group.[57,97,124,217]. The application of OSDAs play a very important role in the construction of the unique structure during the synthesis of novel porous materials. Charge distribution, molecule size and geometry of OSDAs are the important factors for the effect of structure-directing.[218]

The elucidation of crystal structures of as-synthesized phases, especially finding the position of SDAs in the framework, is important for the understanding of synthesis mechanisms and crystallization processes. For instance, single crystal X-ray diffraction was applied to determine 4-dimethylaminopyridine in the crystal structure of as synthesized aluminophosphate SSZ-51.[219] In fact, plenty of porous materials cannot grow as single crystal of hundreds of micrometers and are thus not suitable for single crystal structure analysis. X-ray powder diffraction reveals the position of pyrrolidine molecule in RUB-10 using the difference electron density map.[220] Yan et al.[221] investigated the locations of guest molecules in SAPO-34/44 by means of Rietveld refinement combined with simulated annealing. Burton et al.[222] utilized the approach of molecule modelling to study the location of SDA in the channel of as synthesizes SSZ-55. However, there are certain limits of XRPD to characterize the OSDAs location. Firstly, some of the new porous materials can only be prepared in a nano-sized form, not accessible for XRPD; secondly, it is difficult to directly detect the position of OSDAs from the structure solution from one-dimensional XRPD data. Because of weak interactions between organic compounds and framework, the organic molecules/cations often show some disorder thus smearing out the low electron density of carbon and nitrogen atoms. Moreover, compared with the corresponding calcined phase, porous materials in the as-synthesized state possess more independent atoms and also may possess a different symmetry, which complicate the structural elucidation.

4.3.4 Information of investigated samples

- **THK-2 zeolite**: The THK-2 sample was delivered by Dr. Yasuhiro Sakamoto from Japan and synthesized by group of Prof. Dr. Yamamoto.
- **M-IEZ-RUB-36 zeolites**: M-IEZ-RUB-36 (M = Zn, Ti) zeolites were supplied by Isabel Großkreuz (Group of Prof. Dr. Hermann Gies, Ruhr-University Bochum, Germany). Both samples were synthesized in an acidic hydrothermal reaction from as-made RUB-36 and the corresponding metal-acetylacetonate as the metal sources. The XRPD data were collected at Ruhr-University Bochum and dilevered by by Isabel Großkreuz.
- **SSZ-51 and SOD**: SSZ-51 was supplied and synthesized by Hao Xu (Zhejiang University, China). The synthesis information is summarized in section 5.5.1. As-synthesized and calcined SOD samples were delivered by Dr. Bernd Marler (Ruhr-University Bochum, Germany).
- **CHA zeolites**: Cu-CHA zeolite was delivered by Prof. Dr. Xiangju Meng (Zhejiang University, China). The synthesis approach is described in the Ren et al.[108] H-CHA zeolite was supplied by BASF SE, Ludwigshafen Germany.

4.3.5 Research questions

Structure determination of THK-2 zeolite

The THK-2 zeolite occurs in mixture sample (with MTW zeolite) with micrometers crystal size. The *ab initio* structure solution was changeable using XRPD method. The aim is to solve the crystal structure from ADT data collected under sample cooling condition. The structural investigation in this work consist of:

- Determination of lattice parameter and space group
- *Ab initio* structure solution from ADT data
- High-resolution TEM imaging

Disorder simulation of M-IEZ-RUB-36 materials

The disordered structure should be explained by the comparison of calculated and recorded ED patterns. The calculated ED pattern was generated through structure modelling and disorder simulation in the program `DISCUS`.

- Confirmation of disorder in the materials
- Determination of disorder type
- Structure solutions of average structures from ADT data
- Structural modelling and disorder simulation

Determination of OSDAs positions in zeolites

ADT technique should deliver the positions of organic templates in SSZ-51 and sodalite (SOD), respectively. Further structure refinement was performed against XRPD data. Solid-state NMR confirm the existence of OSDAs in the pores of the framework.

- *Ab initio* structure solutions from ADT data
- Structure refinements with Rietveld method
- Additional approaches as solid-state NMR and in-situ XRPD

Determination of Cu position in dehydrated Cu-CHA zeolite

Two materials, Cu-CHA and H-CHA (as reference), should be heated at high temperature for dehydration and further investigated by ADT method. Dynamical structure refinements were performed to indicate the position of partial occupied Cu in the CHA framework.

- Structure solutions from ADT data
- Kinematical structure refinements
- Dynamical structure refinements

5 Experimental section

5.1 $Al_4B_2O_9$

5.1.1 X-ray powder diffraction

X-ray powder diffraction data was collected on a Philips X'Pert diffractometer (Cu$K_{\alpha 1,2}$ radiation) using Bragg-Brentano geometry at room temperature. In the primary beam the instrument was equipped with a 0.25° divergence slit, a 0.5° anti scatter slit, a soller slit of 0.04 rad and a mask of 10 mm. In the secondary beam, a soller slit (0.04 rad), a Ni-filter and a X'Celerator detector system was applied. XRPD data was recorded from 3° to 120° with a step size of 0.0167° and the measurement time of 50 s per step. The tube settings are 45 kV and 40 mA. Pawley fit and Rietveld refinement based on XRPD data were carried out in the program `TOPAS-Academic`[223]. The unit-cell parameters derived from ADT data (see 5.1.3) were further corrected with XRPD data. As shown in Fig. 5.1, the Pawley-fit converged with an excellent goodness of fit (*gof* = 1.422)and delivered the refined the Pawley-fit converged with an excellent goodness of fit (*gof* = 1.422) and delivered the refined lattice parameters used for the *ab initio* structure solution from ADT data.

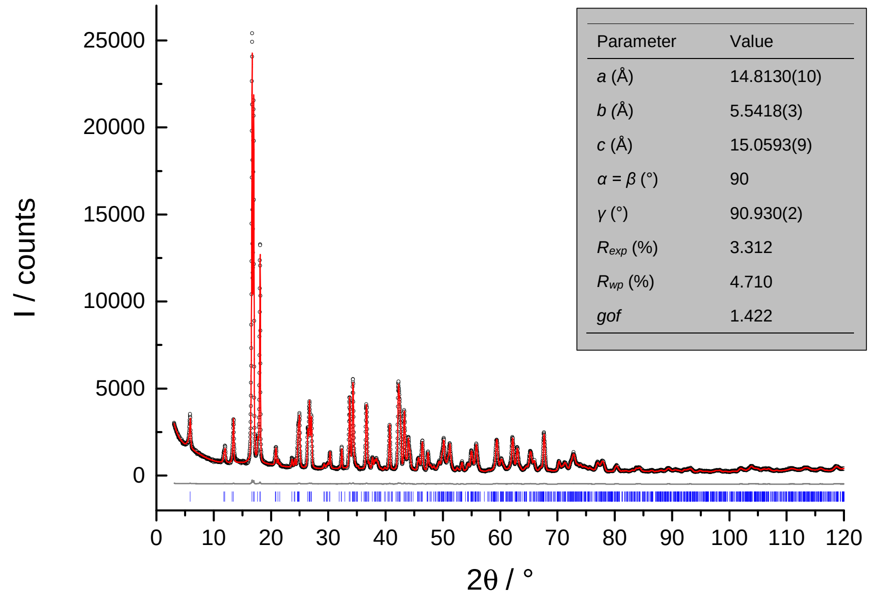

Parameter	Value
a (Å)	14.8130(10)
b (Å)	5.5418(3)
c (Å)	15.0593(9)
α = *β* (°)	90
γ (°)	90.930(2)
R_{exp} (%)	3.312
R_{wp} (%)	4.710
gof	1.422

Figure 5.1: Pawley-fit plot of $Al_4B_2O_9$. Black circles: observed powder diagram; red solid line: simulated powder diagram; gray solid line: difference profiles; and blue ticks: reflection positions. Inserted table: parameters of Pawley-fit.

5.1.2 TEM experiments

TEM experiments including TEM and STEM imaging, EDX, HRSTEM and ADT data collection were performed for the investigation of $Al_4B_2O_9$.

Table 5.1: ADT measurements details of $Al_4B_2O_9$.

Parameter	Value
Temperature (°C)	RT
Holder	Tomo-Holder
Number of spot size	8
Number of gun lens	8
Beam diameter (nm)	75
Tilt angular range (°)	$\pm$ 70
Tilt angular step (°)	1
Exposure time for each frame (s)	4
Precession angle (°)	1
Electron dose rate ($e \cdot Å^{-2} \cdot s^{-1}$)	10

- **ADT experiment**

ADT experiments were processed with TECNAI F30 TEM as the description in section 3.5. Details of ADT data acquisitions are summarized in Table 5.1. Cu-TEM grids were prepared as described in section 3.3.

- **HRTEM-Holography**

HRTEM image series were acquired using TECNAI F30 TEM under suitable TEM settings. TEM in-line holography was achieved using focal image series reconstruction.[224] Twenty HRTEM images were collected at a primary magnification of 790,000 with a focal increment of 6 nm. Hence, the images comprise a focal range of 114 nm including Gaussian focus. The accumulated dose per focal series was calculated as about 21,000 $e \cdot Å^{-2}$. The initial images were binned by hardware and an additional software sequentially, which resulted 1k x 1k images with a pixel size of 0.0576 nm. After image alignment, a small region of 350^2 pixel was selected for exit wave reconstruction, employing a Gerchberg-Saxton algorithm written in Python[225]. Residual axial aberrations were corrected by an automated minimization routine also implemented in Python.[224] Simulation of TEM exit waves were carried out using a multi-slice algorithm included in the `Dr.Probe` software[226].

- **HAADF-HRSTEM**

All the aberration-corrected HAADF-HRSTEM images were collected on a probe-corrected JEM-ARM200F TEM equipped with a Schottky emitter. For data acquisition, the TEM was operated at 200 kV, with a 0.08 nm probe, 22 mrad convergence and HAADF angles of 90 - 370 mrad. Cu-grid with holey amorphous carbon film was used for the HAADF-STEM experiments. HAADF-STEM images were recorded by the Gatan's `DigitalMicrograph` software[155]. In order to reduce noise, the HAADF-STEM images were processed using Fourier filtering. Simulation of HAADF-STEM image was performed in the `QSTEM` software[227].

5.1.3 Lattice parameter determination

In order to check the purity of the sample and to record reliable data, several ADT tilt series were recorded from randomly selected single crystals. The crystal lattice was determined after a reconstruction of 3D reciprocal space of ADT raw data in the program `eADT`[44,65]. After reconstruction of eight datasets, all the ADT data delivered *C*-centred unit-cells (Table. 5.2), similar as the *C*-centred lattice in Fischer et al.[77]. No diffuse scattering were observed in the diffraction volume. The mean values of parameters determined from four NED data (a = 14.73 Å, b = 5.54 Å, c = 15.14 Å, α = 89.9°, β = 90.9° and γ = 90.3°) were further refined by Pawley-fit from XRPD data (see 5.1.1). The refined values from XRPD data were put into use for the structure solution.

Table 5.2: Lattice parameters of $Al_4B_2O_9$ determined from ADT data.

	a(Å)	b(Å)	c(Å)	α(°)	β(°)	γ(°)	Precession
Cry I	14.66	5.54	15.21	89.2	90.7	89.4	off
Cry II	14.61	5.49	15.41	89.8	92.1	91.4	off
Cry III	14.89	5.55	14.96	89.9	89.9	89.9	off
Cry IV	14.77	5.58	14.99	90.5	91.1	90.3	off
Mean (I - IV)	**14.73**	**5.54**	**15.14**	**89.9**	**90.9**	**90.3**	✗
XRPD	14.81	5.54	15.17	90.0	90.9	90.0	✗
Cry V	14.61	5.57	15.18	87.9	90.8	88.8	on
Cry VI (Dataset ❶)*	14.91	5.48	15.12	90.3	91.3	90.1	on
Cry VI (Dataset ❷)*	14.68	5.52	15.24	90.6	91.4	90.5	on
Cry VII	14.90	5.45	15.23	89.7	92.1	88.7	on

* Both datasets were collected from the same crystal with different initial orientations.

5.1.4 Structure solution and refinements

Table 5.3: Experimental details of structure solution of $Al_4B_2O_9$.

ADT data	Dataset ❶
Tilt range (°)	-66/+69
No. of total reflections	7009
No. of independent reflections	2251
Resolution (Å)	0.6
Independent reflection coverage (%)	70
R_{int}	0.142
Overall U (Å^2)	0.094
Residual R (SIR2014)	0.259
Space group	$C2/m$
No. of independent atoms	25

The reflection intensities were integrated in `eADT` from the dataset ❶ (Cry VI) which covered a large tilt range and showed a high data quality. The *ab initio* structure solution based on electron diffraction data was performed using direct methods in the program `SIR2014`[134]. The parameters for the structure solution are giving in Table 5.3.

Based on the solved model from ADT data, the ordered crystal structure was refined with a kinematic refinement using the electron diffraction data in program `SHELX97`[135]. The refinement was performed on the assumption that the intensity is proportional to the square of the structure factor. In the refinement, the resolution of the reflection was set as 1.0 Å and the bond distances of B-O and Al-O were slightly restrained using the commands "*DFIX*" and "*SADI*". The refined structure was input originally into the program `TOPAS-Academic` for a Refinement using Rietveld method from XRPD data. For the Rietveld refinement, the atom positions and corresponding temperature factors and occupancies remain during the refinement. Only the parameters as background corrections, zero error, the lattice parameters, the profile function, crystal size were refined.

5.1.5 Structure modeling

Since diffuse scattering could be observed in some the electron diffraction patterns. Structure models with various kinds of disorders were taken into account for the simulation. The type and form of modulated diffuse streaks indicated a mean superstructure with a threefold ***b*** axis, associated with stacking faults. In order to build up the structure models, the *ac* plane of the initial structure of $Al_4B_2O_9$ was considered as a layer *A* and after a shift of the *A* layer with ½***a*** and ½***c*** was named as layer *B* (Fig. 5.2). The two type of layers were the basic initial components to construct the superstructure models.

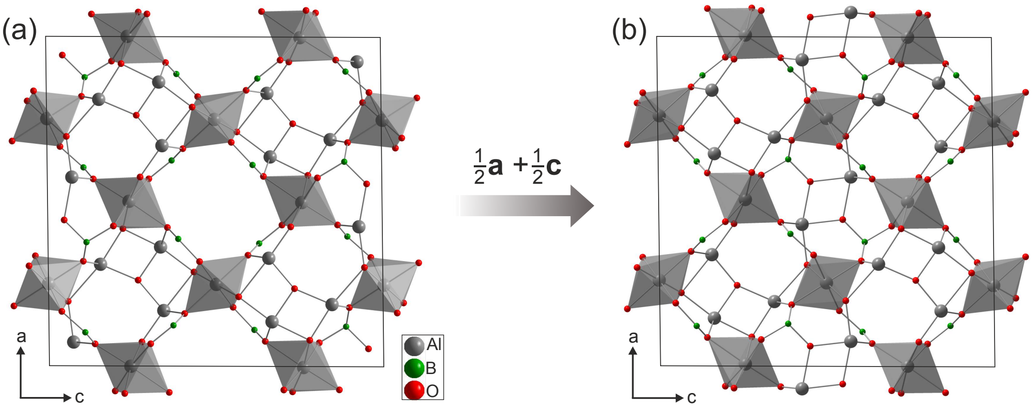

Figure 5.2: Basic structure components used for constructing superstructure. Layer *A*: *ac* plane of $Al_4B_2O_9$ and layer *B*: after a shift of ½***a*** and ½***c*** of layer *B*.

The construction of superstructures and corresponding simulation of the electron diffraction patterns were performed using the software package `DISCUS`[125]. The superstructure consists of a main sequence of *AAB•AAB•AAB*. Random layers must occur meanwhile among *AAB* three-fold units, resulting stacking disorder in the crystal structure. In oder to build up an approximately three-fold superstructure, a Monte Carlo approach was used to produce a imperfect sequence of the layers. In order to build up a mean three-fold superstructure, the stacking sequences comprise two main types of units: double layers *AA* and single layers *B*. The superstructural models were assembled by a dominant alternating sequence of the two units *AA* and *B*, producing a sequence as •••*AABAABAABBAAAABAABBBAA*•••. The maxima of diffuse streaks close to ⅓***b**** was caused by the lack of a strict periodicity of the three-fold layer stacks.

There are two ways to calculate the diffraction pattern of a defected layer structure. The crystal is considered as a whole unit for the calculation in the first way. The atom coordinates of all the atoms were generated explicitly based on the given sequences of the stacked layers. A list of atom coordinates is obtained for the whole crystal. The diffraction pattern is then yielded by an accurate calculation using the term $I(hkl) = [\sum_j^N f_\mathrm{j}\, e^{2\pi i(hx_j + ky_j + lz_j)}]^2$. Since the layers stack with each other with different sequences of non-uniform units, the sum includes not only the atoms in one unit-cell but all the atoms within the whole crystal, which differs from structure factor calculation for Bragg scattering. However, due to a large number of atoms this method results in a slow calculation process. In comparison, the second scheme allows a faster calculation. A layered structure can be generated by a convolution product of the atom positions in a single layer type with the list of the layer positions. Based on the convolution theorem, the diffraction pattern is the Fourier transform of the convolution product, namely the regular product of the individual Fourier transforms. Therefore, it is enough to simulate the atom positions in just a single layer and the list of layer positions. It takes much less time to calculate the individual Fourier transforms than that of the whole crystal. If several types of layers occur, an outer sum of calculations of all the layer types is sufficient to fully describe the modelled structure. In this project, the second way to simulate the diffuse streaks in `DISCUS` was used. The individual layers were simulated from a 10 x 1 x 10 (***a*** x ***b*** x ***c***) super-cell. For the the construction of superstructure, 200 of these layers were stacked along the crystallographic ***b*** axis. It means that the final model is a 10 x 200 x 10 superstructure, which was used for the simulation of electron diffraction pattern.

5.2 Zr-MOFs

5.2.1 TEM experiments

TEM experiments of both Zr-MOFs include the data acquisition and data evaluation of ADT, S(TEM), HRTEM and EDX. Cu-TEM grid, covered with a thin amorphous carbon film, were prepared using ethanol for the dispersion. The statistic of particle size (diameter of nanorods) was analysed in the program `ImageJ`[228]. All experiments were carried out using a TECNAI F30 S-TWIN. TEM in-line holography of Zr-CAU-30 was performed same as previous mentioned data precessing in section 5.1.2. ADT data were recorded following the description in section 3.5. The experimental parameters of ADT data collection are listed in Table 5.4.

Table 5.4: Experimental details of ADT data collection for Zr-MOFs.

Sample	BDC-CAU-27	Zr-CAU-30
Temperature*	ca. -176 °C	ca. -176 °C
Holder	Cyro-holder	Cyro-holder
Number of spot size	8	8
Number of gun lens	8	8
Beam diameter (nm)	100	75
Exposure time for each frame (s)	3	4
Precession angle (°)	1	1
Tilt angular step (°)	1	1
Tilt angular range (°)	-65/+58	± 70

*Sample cooling at liquid nitrogen temperature.

5.2.2 Data evaluation

The ADT data were processed with the computer program `eADT`[44,65]. The crystallographic data including lattice parameters, symmetry information and extraction of reflection intensities were yield based on the analysis of ADT data. "*hkl*" reflection data were imported to the program `SIR2014`[134] for structure solution. The Fourier potential map with corresponding models was illustrated with the program `VESTA`[142]. Pawley fits were implemented to refine the unit-cell from XRPD data. The final crystal structures were refined using Rietveld-method in `TOPAS-Academic`[223].

5.2.3 Thermal stability

The thermal stability of Zr-CAU-30 was investigated by a Netzsch-STA 409 CD thermal gravimetric analyzer to study the water release and the stability of framework. Two mass loss steps can be observed from TG curve (Fig. 5.3). The first step indicates the liberation of waters in the pore of Zr-MOF. The framework starts to decompose at about 400 °C.

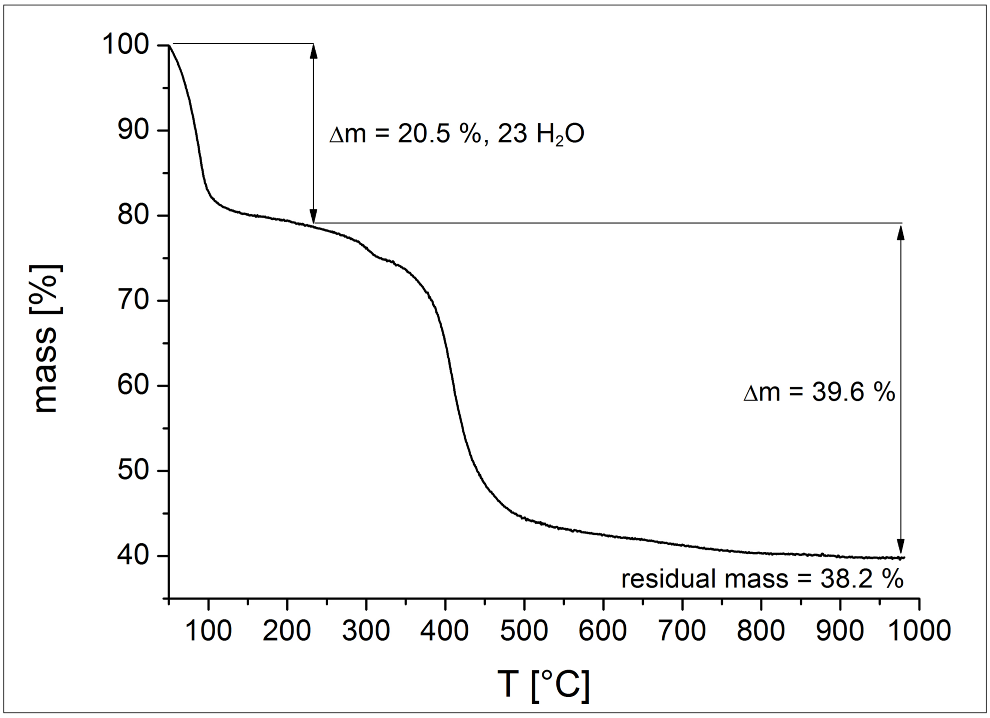

Figure 5.3: Thermogravimetric curve of Zr-CAU-30. Reprinted from ref. of Rhauderwiek et al.[72]

5.3 THK-2 zeolite

5.3.1 TEM experiments

TEM experiments comprise of ADT data acquisition, TEM, STEM, and HRTEM imaging with a TECNAI F30 S-TWIN TEM. The Cu TEM grids were prepared using ethanol for the dispersion. ADT data were recorded following the description in section 3.5. The experimental parameters of ADT data collection are listed in Table 5.5.

Table 5.5: Experimental details of ADT data collection for THK2.

Sample	Zeolite THK-2
Temperature	Room temperature
Holder	Tomo-holder
Number of spot size	8
Number of gun lens	8
Beam diameter (nm)	75
Exposure time for each frame (s)	3
Precession angle (°)	1
Tilt angular step (°)	1
Tilt angular range (°)	-60/+65

5.3.2 Data evaluation

The ADT data were processed with the program `eADT`[44,65] and delivered the crystallographic data including lattice parameters, symmetry information and reflection intensities. The *ab initio* structure solution with direct methods approach implemented in `SIR2014`[134] was based on the reflection intensities derived from electron tomography diffraction by assuming the kinematic approximation $I_{hkl} \sim |F_{hkl}|^2$. Pawley fits were implemented to refine the unit-cell from XRPD data.

5.4 M-IEZ-RUB-36 zeolites

5.4.1 TEM experiments

TEM experiments comprise of ADT data acquisition, EDX, TEM and STEM imaging with a TECNAI F30 S-TWIN TEM. The Cu TEM grids were prepared using ethanol for the dispersion. ADT data were recorded following the description in section 3.5. The experimental parameters of ADT data collection are listed in Table 5.6.

Table 5.6: Experimental details of ADT data collection for M-IEZ-RUB-36 zeolites.

Sample	Zn-IEZ-RUB-36	Ti-IEZ-RUB-36
Temperature	Room temperature	Room temperature
Holder	Tomo-holder	Tomo-holder
Number of spot size	8	8
Number of gun lens	8	8
Beam diameter (nm)	100	100
Exposure time for each frame (s)	4	4
Precession angle (°)	1	1
Tilt angular step (°)	1	1
Tilt angular range (°)	-51/+48	-52/+50

5.4.2 Data evaluation

ADT data were processed with the program `eADT`[44,65] and delivered the crystallographic data including lattice parameters, symmetry information and reflection intensities. The average structures were solved with direct methods approach implemented in `SIR2014` (Table. 5.7). The solutions were based on the reflection intensities derived from electron tomography diffraction by assuming the kinematic approximation $I_{hkl} \sim |F_{hkl}|^2$. The structural modelling and simulation of electron diffraction pattern were performed in the `DISCUS` software packet[125].

Table 5.7: Parameters of structure solutions of M-IEZ-RUB-36 zeolites.

Sample	Zn-IEZ-RUB-36	Ti-IEZ-RUB-36
Space group	*Immm*	*Bbmm*
No. of total reflections	3339	2134
No. of independent reflections	712	406
Resolution (Å)	0.9	1.1
Independent reflection coverage (%)	68	70
R_{int}	0.189	0.138
Overall U (Å^2)	0.065	0.045
Residual R (SIR2014)	0.218	0.154
No. of independent atoms	14	15

5.5 SSZ-51 and SOD zeolites

5.5.1 Synthesis of samples

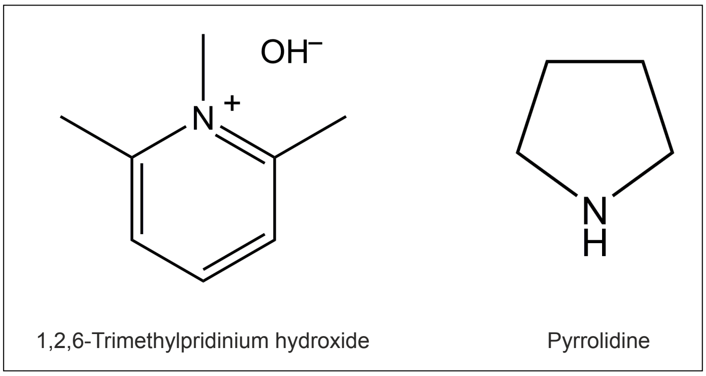

Figure 5.4: The organic SDAs used in this project. Right: 1,2,6-trimethylpyridinium hydroxide. Left: Pyrrolidine.

As-synthesized SSZ-51

A novel organic structure directing agent - 1,2,6-trimethylpridinium (TMP, as shown in Fig. 5.4), which was recently reported for the preparation of RTH aluminosilicate zeolite[107], was used to synthesize as-synthesized TMP-SSZ-51. A synthetic reaction mixture with a molar ratio of 1Al_2O_3: 2 TMPOH: 1P_2O_5: 2HF: 40H_2O (TMPOH represents 1,2,6-trimethyl-pyridinium hydroxide) was transferred into an autoclave and sealed for further crystallization at 180 °C for 24 h.. The final product was collected by filtration, washed with by distilled water and dried at 100 °C for 4 h. The as-synthesized phase was calcined at 550

°C in air for 4h to obtain the guest-free SSZ-51.

As-synthesized SOD

The pyrrolidine silica sodalite (PYS-SOD) sample was supplied by Dr. Bernd Marler from Ruhr University of Bochum Germany. The synthesis approach was described by Werthmann et al.[229]

5.5.2 Solid-state NMR spectroscopy

Solid-state NMR spectra of TMP-SSZ-51 was recorded on a Bruker Avance 400 DSX NMR spectrometer at a ^{13}C frequency of 100.55 MHz. A commercial two-channel 2.5 mm Bruker probe head at 20 kHz MAS was used for all experiments. For the solid state ^{13}C cross-polarisation (CP) MAS NMR experiments, an initial 90° pulse with 4.0 μs length and 3 s recycle delay were used. A ramped CP pulse (64-100%) with duration of 2 ms was used. Two pulse phase modulation (TPPM) ^{1}H decoupling scheme was used while acquiring the ^{13}C signal. Transients of 50 k were averaged for the CP experiments. The spectra were baseline-corrected, and a broadening of 50 Hz was applied.

5.5.3 Thermal Stability

Thermal stability experiments including differential scanning calorimetry and thermogravimetric analysis (DSC/TGA) were performed with Perkin-Elmer TGA 7 unit in air with a heating rate of 10 K/min in the temperature range from room temperature to 815 °C.

5.5.4 X-ray powder diffraction

Stadi-P diffractometer equipped with a Ge(111) monochromator and a linear position-sensitive detector (PSD) using Cu$K\alpha 1$ radiation (λ = 1.540598 Å) for templated and calcined SSZ-51. The specimens were measured in borosilicate glass capillaries with a diameter of 1.0 mm at room temperature. The data was acquired with the program `WinXPOW`[150]. The temperature dependent XRPD measurements for TMP-SSZ-51 were performed on a STOE Stadi-P diffractometer equipped with a ceramic oven and an imaging plate position-sensitive detector using Cu$K\alpha 1$ radiation. The measurements were carried out in a 1.0 mm glass capillary under static air. The templated phase TMP-SSZ-51was heated from 50 °C to 840 °C, while the XRPD data were collected.

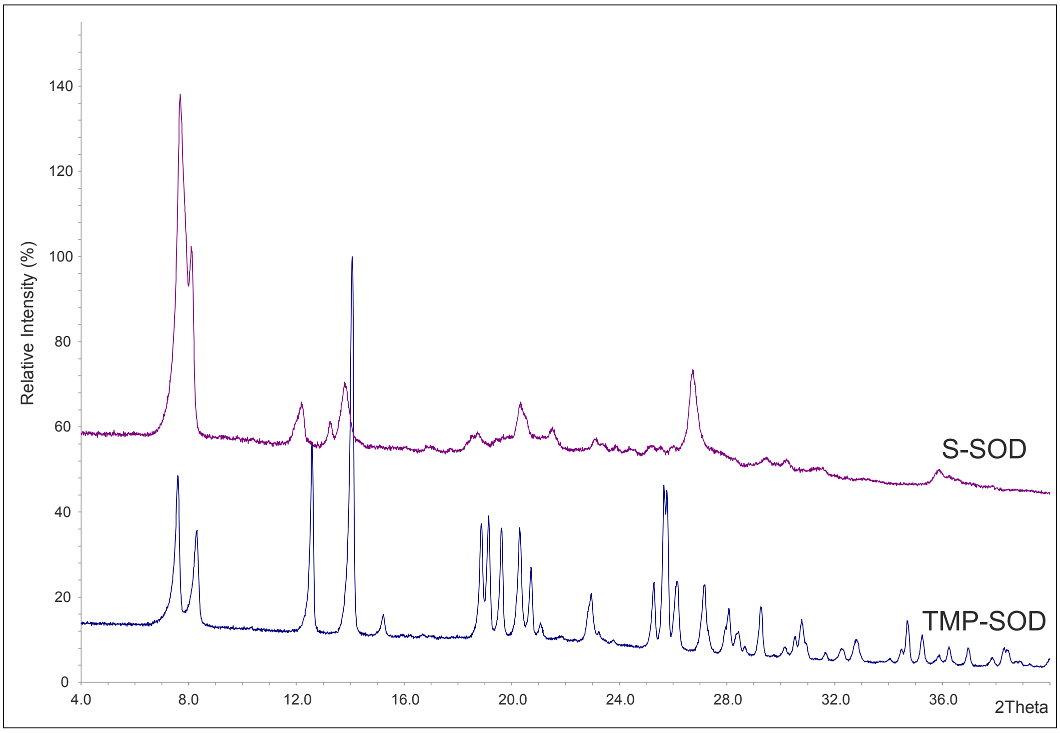

Figure 5.5: XRPD diagrams of SSZ-51 with Cu$K\alpha 1$ radiation (λ = 1.540598 Å).

5.5.5 TEM experiments

Table 5.8: Experimental details of ADT data collection for TMP-SSZ-51 and PYS-SOD.

Sample	TMP-SSZ-51	PYS-SOD
Temperature	ca. -176 °C	ca. -176 °C
Holder	Cyro-holder	Cyro-holder
Number of spot size	8	8
Number of gun lens	8	8
Beam diameter (nm)	200	200
Exposure time for each frame (s)	1.5	1.5
Precession angle (°)	1	1
Tilt angular step (°)	1	1
Tilt range (°)	±60	±60

Phase contrast TEM, scanning TEM (STEM), energy dispersive X-ray (EDX) spectroscopy and fast automated diffraction tomography (Fast-ADT) measurements were carried out using a Tecnai F30 S-TWIN TEM. The experimental details were summarized in Table 5.8. Cu-TEM grids were prepared as described in section 3.3.

5.5.6 ADT data evaluation

Experimental electron diffraction data were reconstructed in software `eADT`[44,65] and further evaluated to deliver crystallographic information as lattice parameters, crystal symmetry and indexed reflection with intensities. The found unit-cell parameters were refined with a Pawley fit against XRPD data for a higher accuracy. The *ab initio* structure solution was carried out with direct methods approach implemented in `SIR2014`[134] based on the extracted reflection intensities from electron diffraction data. The experimental parameter for both structure solutions are concluded in Table 5.9.

Table 5.9: Experimental details of structure solutions of as-synthesized zeolites.

Sample	TMP-SSZ-51	PYS-SOD
Space group	$C2/c$	$I\bar{4}3m$
No. of total reflections	9451	1912
No. of independent reflections	3011	94
Resolution (Å)	0.8	0.8
Independent reflection coverage (%)	72	100
R_{int}	0.256	0.193
Overall U (Å^2)	0.027	0.030
Residual R (SIR2014)	0.195	0.054

In the Rietveld refinement of TMP-SSZ-51, the T-O bond lengths of the tetrahedral AlO_4 and PO_4 units were restrained for Al-O: 1.76 Å and P-O: 1.53 Å, bond angles T-O-T (T = Al or P) as 109.5°. In AlO_4F unit, bond lengths Al-O were restrained as 1.80 Å and Al-F bond lengths as 1.92 Å. For the template cation 1,2,6-trimethylpyridinium, the initial position of C and N atoms from structure solution were used for the refinement with restraints applied to bond lengths and bond angles. The restrained values for bond lengths and bond angles were extracted from a statistical mean value based on 53 crystal structures from Cambridge structural database (CSD)[230,231]. The values of isotropic thermal parameters of H atoms were constrained to be 1.2 times of those of the carbon atom connected the pyridine ring (C-Ar). The temperature factor for water oxygen atom was set as 5 time of the framework oxygen atom.

5.6 CHA zeolites

5.6.1 TEM experiments

ADT data were collected with TECNAI F30 S-TWIN TEM for Cu-CHA and FEI Tecnai G2 Spirit for H-CHA. The Cu TEM grids were prepared using ethanol for the dispersion. The experimental parameters of ADT data collection are listed in Table 5.10.

Table 5.10: Experimental details of ADT data collection for CHA zeolites.

Sample	H-CHA	Cu-CHA
Modul of data acquisition	Fast-ADT	ADT
Measurement temperature	Room temperature	Room temperature
Holder	Heating-holder	Heating-holder
Number of spot size	8	8
Number of gun lens	✗	6
Exposure time for each frame (s)	1	1
Precession angle (°)	1	1
Tilt angular step (°)	0.5	1
Tilt angular range (°)	-33/+42	-41/+36

5.6.2 Dehydration of CHA zeolites

The chabazite nano particles were loaded firstly on the TEM grids and inserted into TEM with a heating-holder. The samples were heated by controlling a *Smartset Hot Stage Controller* (model 901) in vacuum of TEM at 400 °C for 2 h.

5.6.3 X-ray powder diffraction

Stadi-P diffractometer equipped with a Ge(111) monochromator and a linear position-sensitive detector (PSD) using Cu $K_{\alpha 1}$ radiation (λ = 1.540598 Å) for templated and calcined SSZ-51. The specimens were measured in borosilicate glass capillaries with a diameter of 1.0 mm at room temperature. The data was acquired with the program `WinXPOW`[150].

5.6.4 ADT data evaluation

All ADT data were processed with the program `PETS`[139,141], which enables to extract and output the reflections intensities from a series of diffraction patterns. The input parameter are concluded in Table 5.11. *Ab initio* structure solutions were carried out with Charge Flipping algorithm approach[232]. The kinematical and dynamical structural refinements were done in programs `JANA2006` and `Dyngo`[136] without any restraints on bond lengths and bond angles. Coulomb potential maps of the structure solutions and refinements were plotted with the program `VESTA`[142].

Table 5.11: Input parameters of reflection extraction in PETS.

Sample	H-CHA	Cu-CHA
Number of frame	151	78
Wavelength (Å)	0.033492	0.019687
dstarmax ($Å^{-1}$)	1.2	1.2
Reflection size	18	30
I/sigma in peak search	6	10

6 Results and discussion

This chapter provides for all investigated materials a description of the experimental results and the structural analyses carried out. Experimental details are described in chapter 5. In addition, the derived results will be discussed.

6.1 Order and disorder in $Al_4B_2O_9$

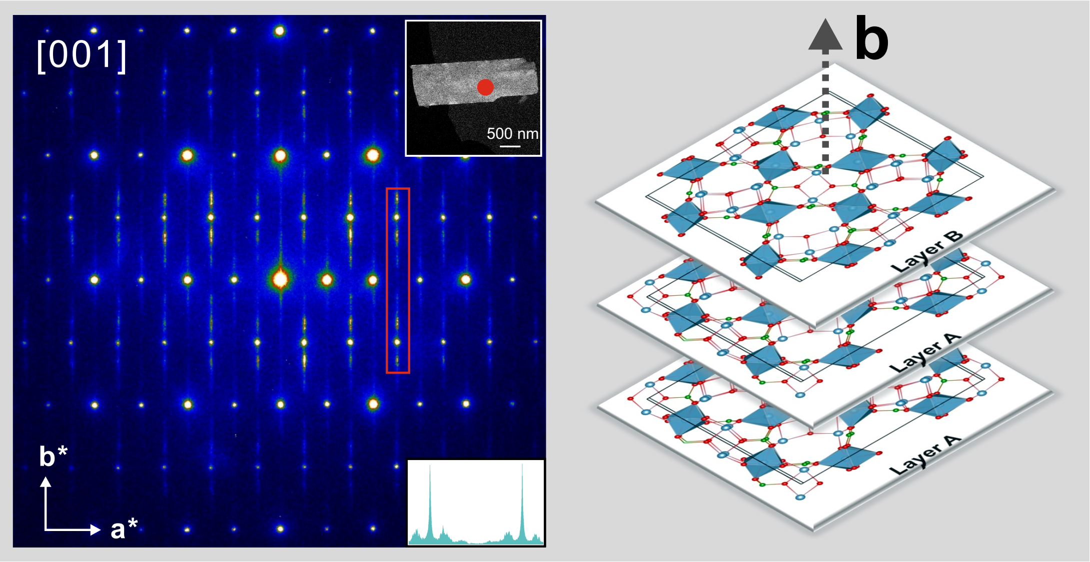

Order and disorder phenomena in $Al_4B_2O_9$ explained by electron diffraction tomography

The project about structural investigation on $Al_4B_2O_9$ was cooperated with the group of Prof. Dr. Reinhard X. Fischer from University of Bremen, Germany. The results were published by Zhao et al.[30] as a front cover paper (front cover see *Appendix A1* in section Appendix) entitled "Elucidating structural order and disorder phenomena in mullite-type $Al_4B_2O_9$ by automated electron diffraction tomography" in "*Journal of Solid State Chemistry*", 249 (2017), page 114-123, Doi: 10.1016/j.jssc.2017.02.023. The contents in sections 5.1 and 6.1 are adapted and partly reprinted from this publication.

6.1.1 Sample overview and EDX analysis

The crystals of $Al_4B_2O_9$ exhibit a needle-type morphology, nanorods as shown in Fig. 6.1, with diameters are in a range of a few tens to some hundred nanometers. which are suitable for TEM experiments. As an inorganic material, $Al_4B_2O_9$ particles are stable under mild electron illumination conditions in TEM. The powder was dispersed in an ethanol solution to distribute the particles on the grid. Preliminary nano electron diffraction which were performed on various regions of different crystals provided mainly clear reflections other areas showed diffuse streaks.

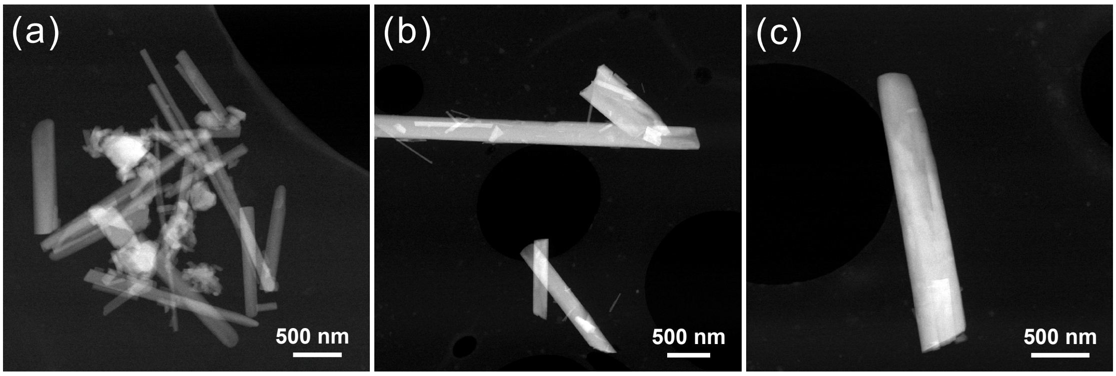

Figure 6.1: STEM images of $Al_4B_2O_9$ nonaparticles: (a) an overview of the sample; (b) nanorods with whiskers and (c) single nano crystal.

EDX analysis was utilized for quantitative determination of the chemical composition of $Al_4B_2O_9$. The EDX spectrum (Fig. 6.2) was recorded in STEM mode from a box region of a single $Al_4B_2O_9$ nanorod. Due to the limit of the EDX instrument, it was difficult to detect the boron signal. The quantitative analyses of five datasets (see Table 6.1) resulted in an average Al/O ratio of 1/2.32, which is close to the expected calculated ratio of 1/2.25 in $Al_4B_2O_9$. The accordance of the detected and theoretical chemical proportions confirmed the formation of aluminum borate with the chemical formula $Al_4B_2O_9$ in the Al_2O_3-B_2O_3 system.

Table 6.1: Quantitative EDX results taken from different single crystals.

Dataset	Nr. 1	Nr. 2	Nr. 3	Nr. 4	Nr. 5	**Mean**
Al (%)	69.93	71.90	68.39	69.06	69.86	**69.83**
O (%)	30.07	28.10	31.61	30.94	30.14	**30.17**
Al/O	2.33	2.56	2.16	2.23	2.32	**2.32**

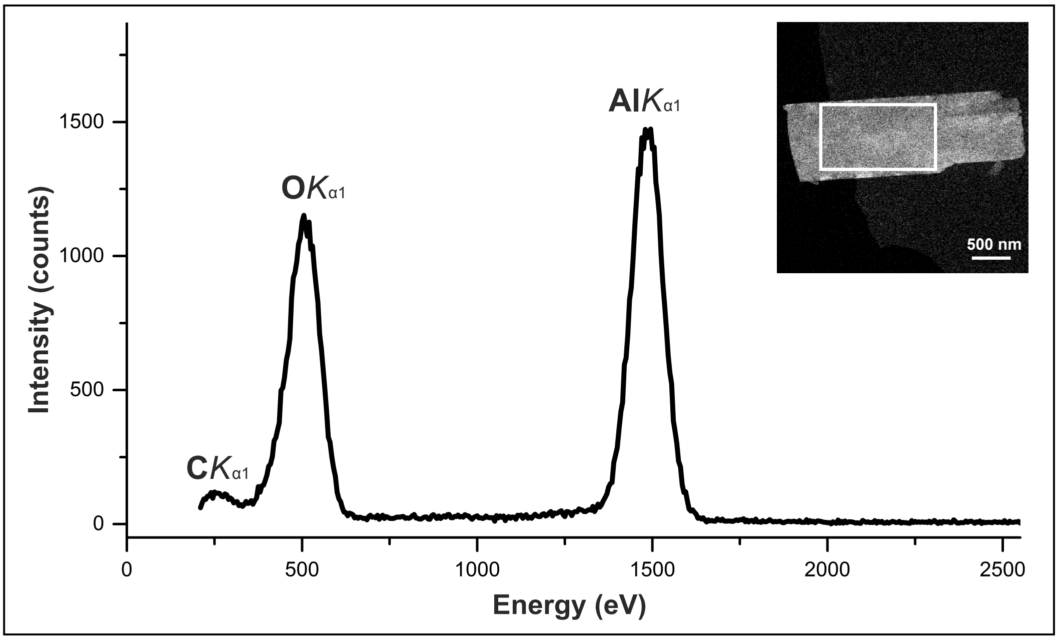

Figure 6.2: EDX spectrum of $Al_4B_2O_9$. The signal of carbon was caused by the amorphous carbon film on the TEM grid. Inset: STEM image of selected crystal for EDX measurement; the detected region is remarked with white box.

6.1.2 ADT data processing

ADT data was collected in a first step from an area with plain reflections allowing for an unbiased structure characterization and a full description of the crystal features. Subsequently, ADT diffraction data with diffuse streaks delivering information about disorder were recorded and compared to electron diffraction patterns simulated from a modelled superstructure.

In Fig. 6.3a-c, the three dimensional reconstruction of ADT/PED data without diffuse streaks from an ordered crystals is shown. A *C*-centred unit-cell with average lattice parameters of a = 14.73 Å, b = 5.54 Å, c = 15.14 Å, α = 89.9°,β = 90.9° and γ = 90.3° could be determined. As all the angles are close to 90° within the error margins, it is difficult to distinguish whether it is an orthorhombic or monoclinic (pseudo orthorhombic) lattice. The systematic extinction with $h + k = 2n$ for all reflections indicated a *C*-centred Bravais lattice. The cut slices from reciprocal volume (Fig. d-f) delivered further sytematic extinction concluded as following: $k = 2n$ for $0kl$ plane; $h= 2n$ for $h0l$ plane and $h + k = 2n$ for $hk0$ plane. As a result, if the lattice has an orthorhombic setting, the extinction symbol was determined as $C - - -$, associated with the five possible space groups *C*222 (No. 21), *Cmm*2 (No. 35), *Cm*2*m* (No. 38), *C*2*mm* (No. 38) and *Cmmm* (No. 65). In the case of a lower symmetry of a monoclinic lattice, the corresponding extinction symbol is $C\ 1 - 1$, consistent with the space groups *C*2 (No. 5), *Cm* (No. 8) and *C*2/*m* (No. 12). As described in section 5.1.4, the reflection file was obtained from PED data collected from an ordered crystal with a tilt range of -66/+69.

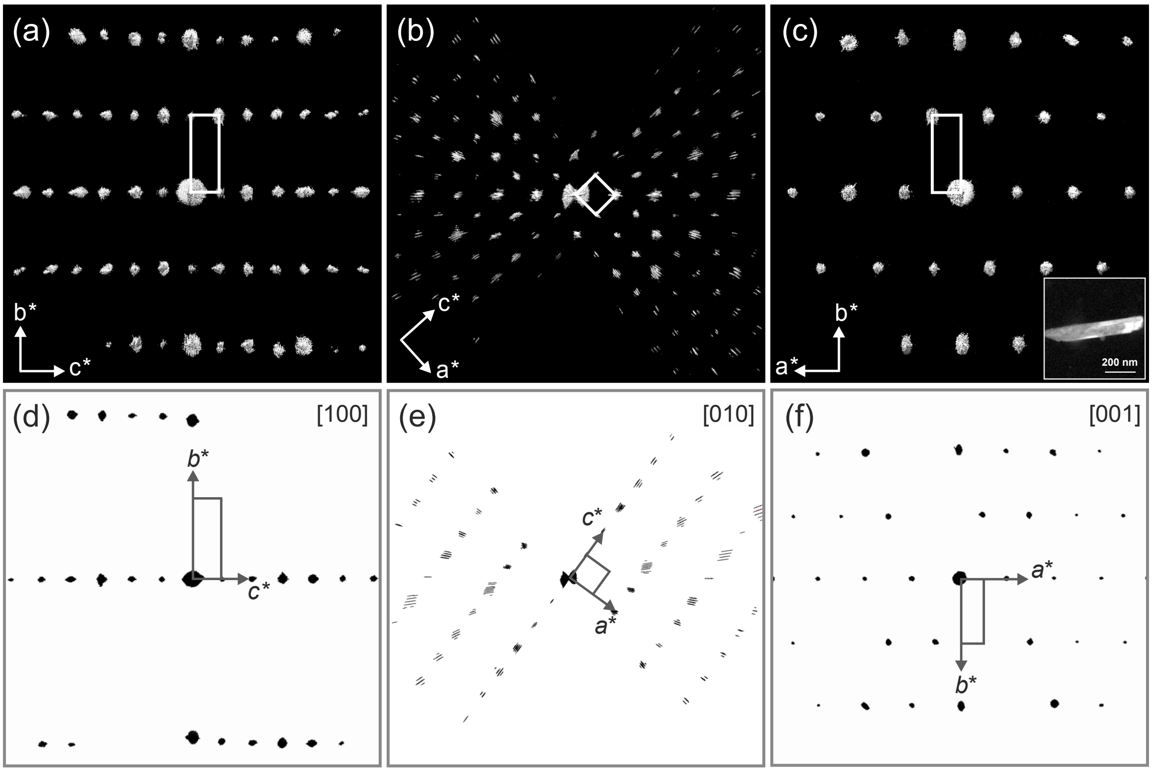

Figure 6.3: (a-c) Reconstructed 3D reciprocal space of $Al_4B_2O_9$, viewed along the main directions ***a****, ***b****, ***c****. Corresponding derived lattice parameters: a = 14.73 Å, b = 5.54 Å, c = 15.14 Å, α = 89.9°, β = 90.9° and γ = 90.3°. Two-dimensional slices cut from reconstructed 3D reciprocal space: (d) 0*kl*, (e) *h*0*l* and (f) *hk*0 planes.

6.1.3 Structure determination

Structure solution from ADT data

Since no chemical meaningful structure could be delivered from the structure solutions in any of the orthorhombic space groups. The lattice parameters were refined in a monoclinic crystal system [a = 14.8130(10) Å, b = 5.5418(3) Å, c = 15.0593(9) Å, β = 90.930(2)°] by Pawley fit from XRPD data for a higher accuracy for structure solution. The excellent final fit supported the monoclinic cell metric once again. The *ab initio* structure solution based on electron diffraction data was carried out with direct methods in the monoclinic space group $C2/m$. The final residual R converged to 0.259. The process resulted in a reasonable model of the mullite-type structure with all atoms except of one missing B atom in the final output file and delivered a well-resolved potential map (Fig. 6.4). Seven strong maxima were observed (from 3.9 to 2.5 $e^-/Å^3$), corresponding to the seven independent Al atoms. The next peaks belong to fourteen O atoms found in a scattering potential range of 2.6 down to 1.7 $e^-/Å^3$. The maxima consistent with four independent B atoms detected with a height of 2.0 to 1.6 $e^-/Å^3$. The missing B atom was clearly visible in Fourier potential difference maps. No extra potential describing an additional O position was detected. The final chemical composition was determined as $Al_4B_2O_9$, which is in line with the expected synthetic stoichiometry of the Al/O ratio and EDX results.

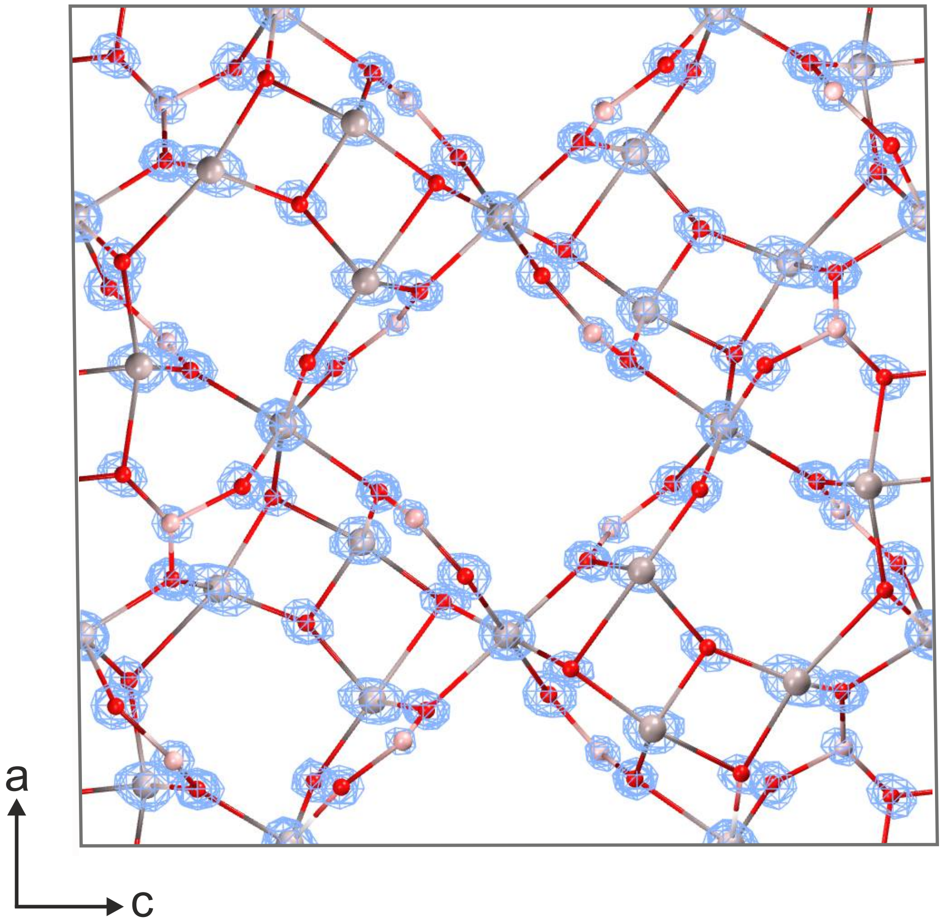

Figure 6.4: Electron potential map of structure solution of $Al_4B_2O_9$ in SIR2014 overlaid with the atomic model, viewed in [010] direction. Red: O; gray: Al; light gray: B. The well-solved potential map indicates a ordered and chemical meaningful crystal structure of $Al_4B_2O_9$.

Structure refinement from ADT data

The least-squares refinement was performed by `SHELX97` from electron diffraction data with a resolution of 1.0 Å. The refinement converged to a final residual $R1$ of 0.296 with soft geometrical constraints and restraints for the BO_3 and BO_4 groups. The structure remained stable with regular coordination polyhedra for the Al atoms and rational geometries of tetrahedral BO_4 and trigonal planar BO_3 groups. The refined structure was considered as the final crystal structure of ordered $Al_4B_2O_9$. The details of the crystallographic data is included in the supplementary data *Appendix A2* in section Appendix.

Structure refinement from XRPD data

In order to check the matching degree of ordered structure to the whole sample, structure refinement was carried out with Rietveld-method against XRPD data. The atomic coordinates obtained from least-squares refinement in `SHELX` were input and fixed in the refinement process. The final R_{wp} converged to 13.02% (R_{exp} = 3.604%; R_p = 9.601% and $gof = R_{wp}/R_{exp}$ = 3.612). Since the disorder was totally ignored in the refinement, a high R_{wp} value was produced, which was illustrated by the strong fluctuation in the difference profile as shown in the Plot of Rietveld refinement in Fig. 6.5. However, the model can in principle describe the whole sample as an average structure.

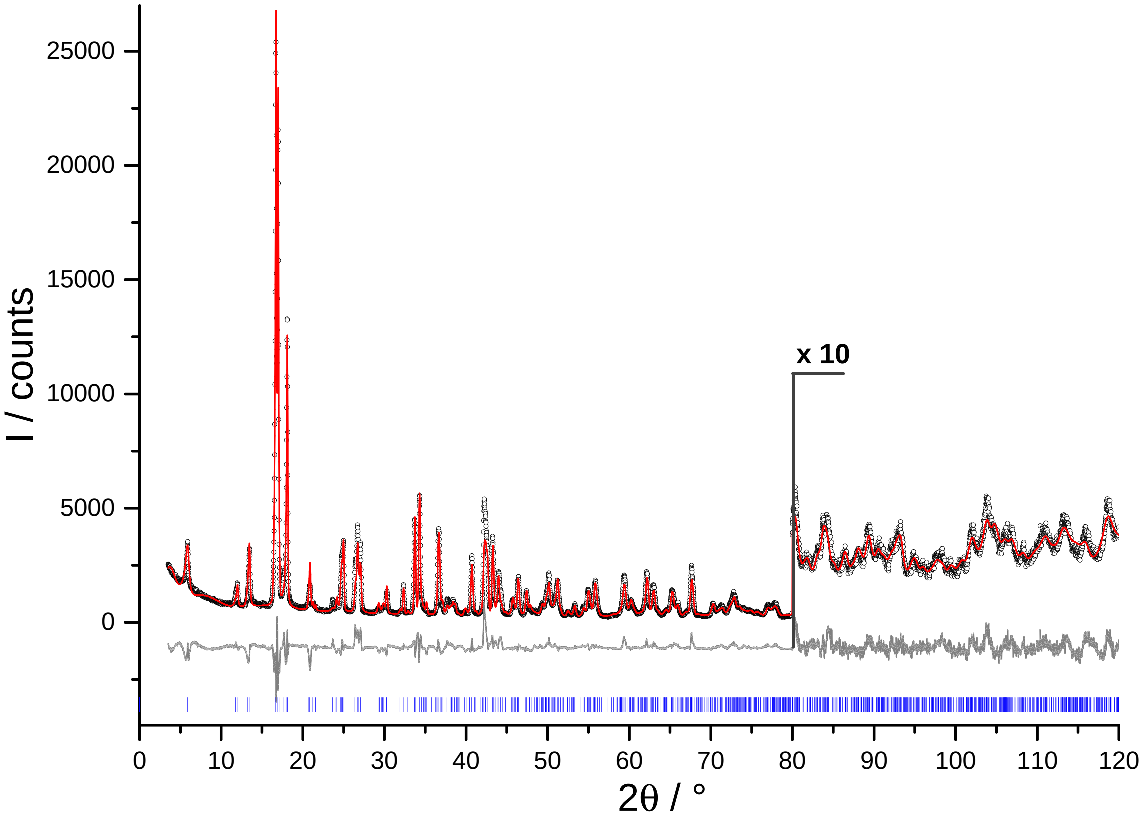

Figure 6.5: Plot of Rietveld refinement $Al_4B_2O_9$ with ordered structural model. Observed XRPD diagram (black circles), simulated XRPD diagram (red solid line), difference profiles (grey solid line), and reflection positions (blue tickmarks. Change of the scale with factor of 10 is shown in the diagram.

6.1.4 Description of the crystal structure

Ordered $Al_4B_2O_9$ crystallizes in a mullite-type structure. The splitting phenomena of oxygen atoms (O5 and O10) derived from XRPD data[77] was not observed in the ADT structure, i. e., no O5 position and O10 position with a full occupancy. Al atomes show five- and six-fold coordinations, while B atoms coordinate with O atom in two forms: BO_3 and BO_4 (Fig. 6.6). The AlO_6 octahedra share edges to form an one-dimensional linear chains (Fig.

6.7a). The octahedra chains extend infinitely along the ***b*** axis to constitute the backbone as a characteristic of the mullite-type structure (Fig. 6.8). The chains distribute with similar distances and are cross-linked by building units of AlO_5 trigonal bipyramids, BO_4 tetrahedra and BO_3 triangles (Fig. 6.7). Atoms Al1, Al2, Al3 and Al4 occupy five-fold coordinations in a slight distorted trigonal bipyramidal geometry. The average values of Al-O bond distances are 1.832 Å for Al1, 1.883 Å for Al2, 1.863 Å for Al3 and 1.923 Å for Al4. Atoms Al5, Al6 and Al7 are well-defined octahedrally coordinated with average Al-O bond distances of 1.928 Å for Al5, 1.870 Å for Al6 and 1.921 Å for Al7 and rational Al-O angles. Two types of B groups BO3 and BO4 show reasonable geometries (Fig. 6.6). The B-O bond lengths in BO3 groups (B1, B3, B4) are in the mean value of 1.385 Å for B1, 1.378 Å for B2, 1.386 Å for B4 and that for BO4 group of B2 is 1.439 Å. The building units are linked at the edged O sites to three-dimensional structure. The selected bond lengths and angles are listed in the in the supplementary data *Appendix A3* in section Appendix.

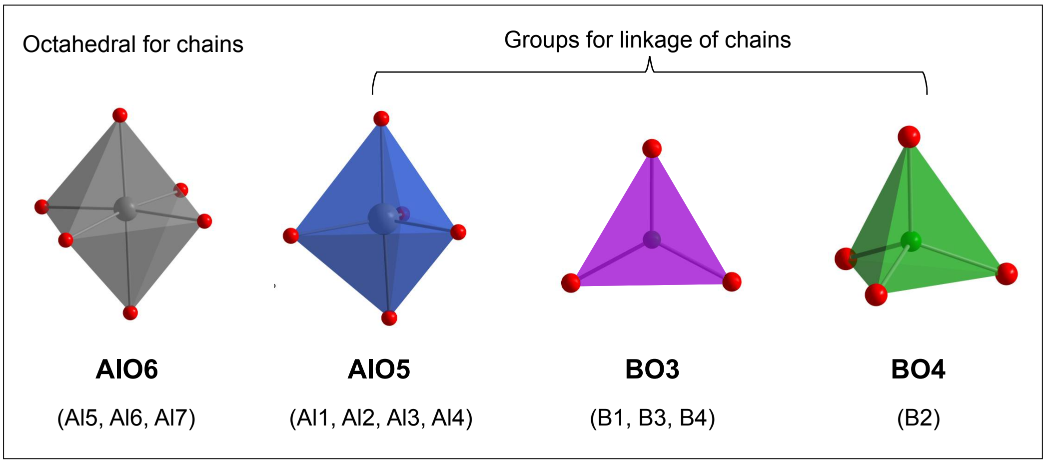

Figure 6.6: Coordinations of Al and B atoms showing the smallest building groups in the structure of $Al_4B_2O_9$.

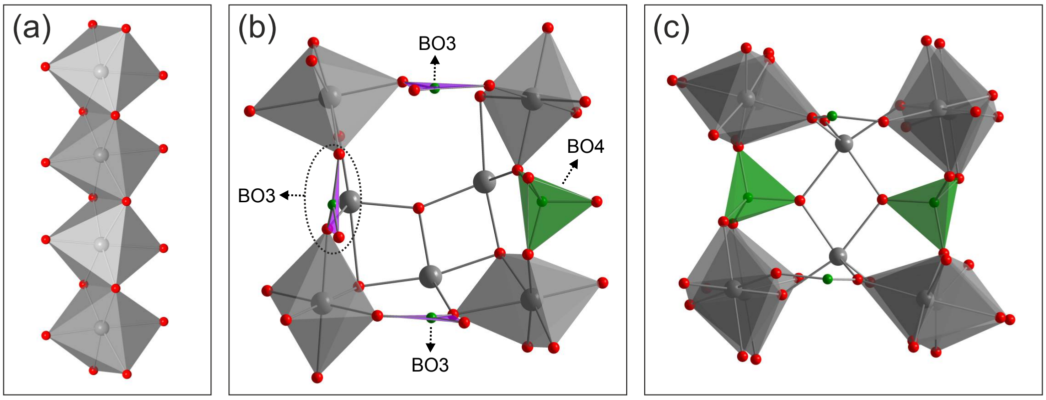

Figure 6.7: Building units cut from the structure of $Al_4B_2O_9$. (a) Edge sharing AlO_6 octahedral chain; (b, c) building units of the structure.

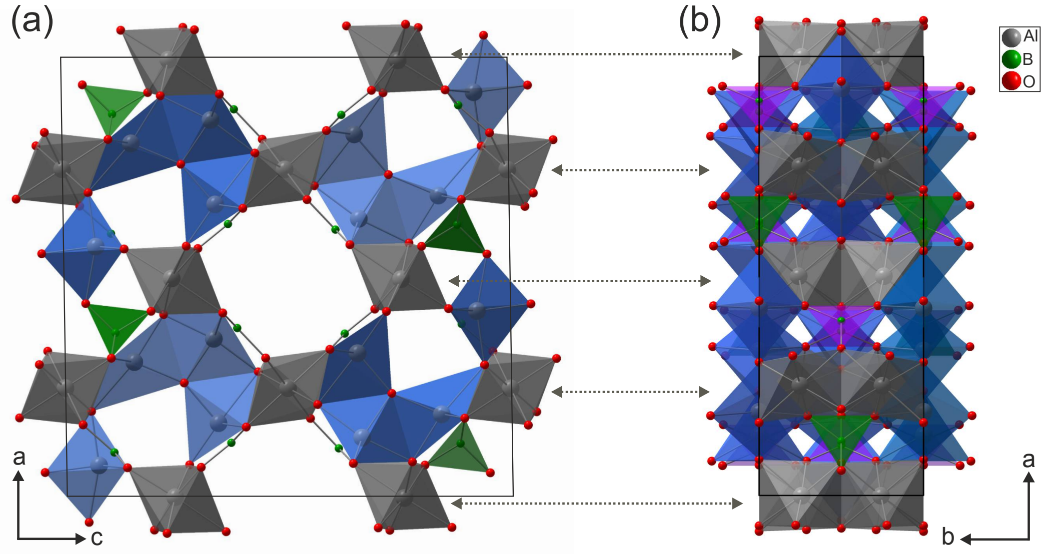

Figure 6.8: Crystal structure of $Al_4B_2O_9$ viewed along ***b*** and ***c*** axis, respectively.

6.1.5 HRTEM and HAADF-HRSTEM

In order to confirm the unbiased structure determination from electron diffraction tomography data, ordered $Al_4B_2O_9$ nanorods were characterized by high-resolution imaging techniques using TEM. The techniques include TEM holography and high resolution HAADF-STEM imaging, in which the features of the the crystal structure can be directly visualized at an atomic scale.

The HRTEM holography image and HAADF-STEM image including the corresponding simulations and structural model are illustrated in Fig. 6.9 and Fig. 6.10. The high resolution images were recorded from two different ordered nanorods but oriented in the same direction, i.e., along [101] zone axis. Squared modulus of the 2D Fourier transforms generated from HRTEM (insert in Fig. 6.10a) and HRSTEM (Fig. 6.10b) are in line with the simulated electron diffraction pattern (Fig. 6.10c). The overview of HAADF-STEM image (Fig. 6.9a) shows an excellent crystallinity of the $Al_4B_2O_9$ and indicates that the nonarod grows along the crystallographic ***b*** axis. The ordered structure is printed overlaid both, experimental HRTEM (Fig. 6.9b) and HRSTEM (Fig. 6.10e) images. The frames of quasi-six rings comprised from O and Al columns can clearly be seen in both experimental images and show good agreements. In particular, the closest packed Al columns signal the strongest intensity in form of white spots in the experimental and simulated HAADF-HRSTEM image. In the TEM hologram phase image, the signal of one B column (B1 and B4) enclosed by six oxygen columns (2xO9, 2xO4, O15 and O6) can be detected in the middle of rings as a single phase peak. The multislice-simulations of both TEM exit waves (Fig. 6.9c) and HAADF-STEM images (Fig. 6.10f) were performed from the ordered $Al_4B_2O_9$ structure and exhibit good agreements to the experimental images, confirming again the correction and reliability of the structure model determined from ADT data.

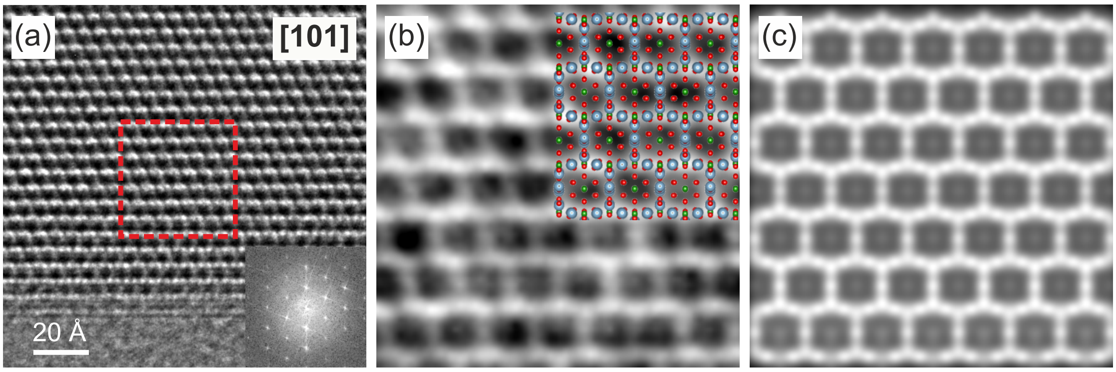

Figure 6.9: HRTEM image of $Al_4B_2O_9$ nanorod recorded along [101] zone axis. (a) Overview (insert: squared modulus of the 2D Fourier transform); (b) Enlarged phase image from the boxed area in (a), overlaid by the $Al_4B_2O_9$ model viewed along [101] (blue: Al, red: O, green: B); (c) Phase of simulated 300 kV exit wave produced by the ADT structure along [101] direction.

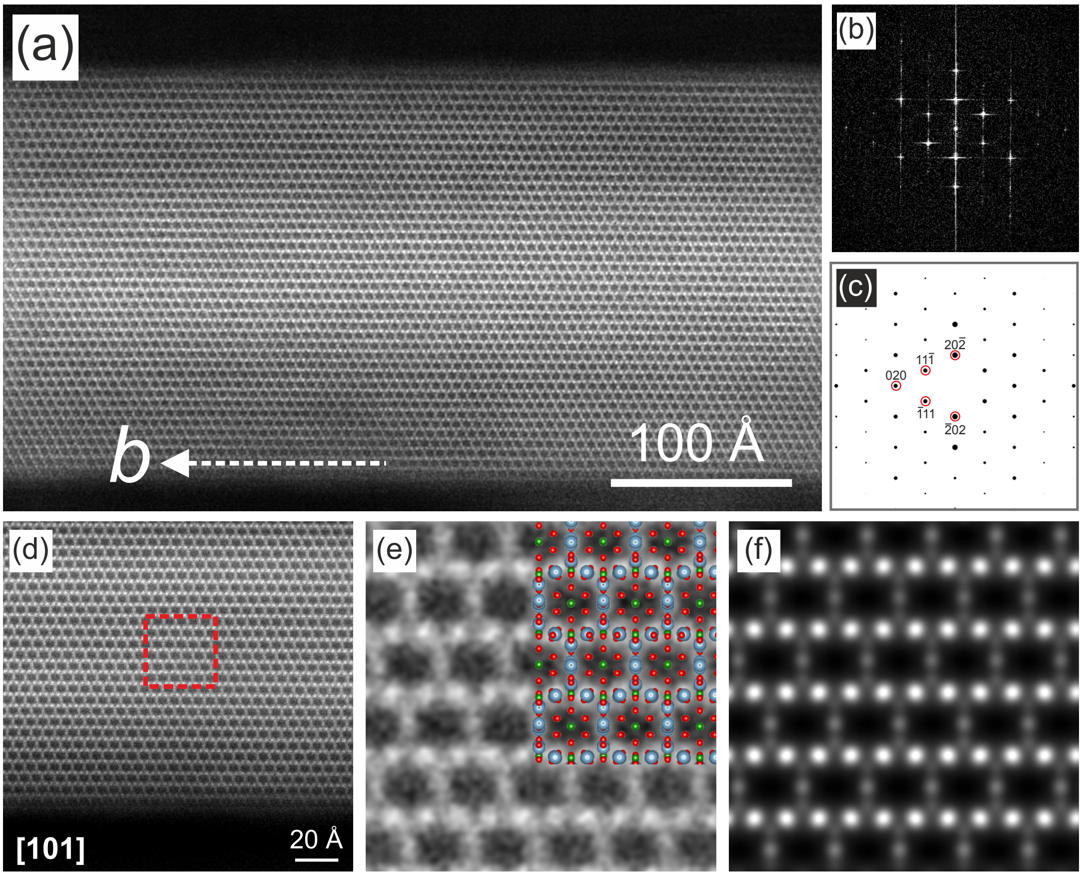

Figure 6.10: HAADF-HRSTEM image of $Al_4B_2O_9$ nanorod recorded along [101] zone axis. (a) Overview; (b) Squared modulus of the 2D Fourier transform and (c) simulated electron diffraction pattern; (d) Selected HAADF-HRSTEM image; (e) Enlarged image from the selected area of (d) with $Al_4B_2O_9$ structure model. (f) Simulated HAADF-HRSTEM of $Al_4B_2O_9$ viewed along [101] zone axis.

6.1.6 Disorder analysis and simulation

Since the order and disorder phenomenon in the structure of $Al_4B_2O_9$ was observed by electron diffraction, the explanation of disorder should be done subsequent to the structural analysis of ordered single nano crystals. Therefore, we changed the focus to the additional diffraction intensities observed in some of the measured areas. For comparison single diffraction patterns recorded from two different nano-scaled regions of an identical nanorod realized using nano diffraction beam, are as shown in Fig. 6.11. The diffraction pattern taken from the ordered region (Fig. 6.11a) consists of discrete peaks without any satellite reflection or diffuses scattering. However, diffraction on a different section of the same crystal (Fig. 6.11b) delivered strong and modulated diffuse streaks parallel to the ***b**** axis. After analysing the three-dimensional reconstructed reciprocal volume it could be confirmed that these are indeed one-dimensional streaks. Fig. 6.11c and 6.11d illustrate the intensity profiles between Bragg reflections 510 and $50\bar{1}$ of the well ordered and disordered regions, respectively. No extra intensity occurs between the two reflections in Fig. 6.11c. In contrast, Fig. 6.11d exhibits clearly broad diffuse peaks at approximately $51^1/_3$ position. The observations indicate a predominantly three-fold superstructure parallel to the crystallographic ***b*** axis in the real space.

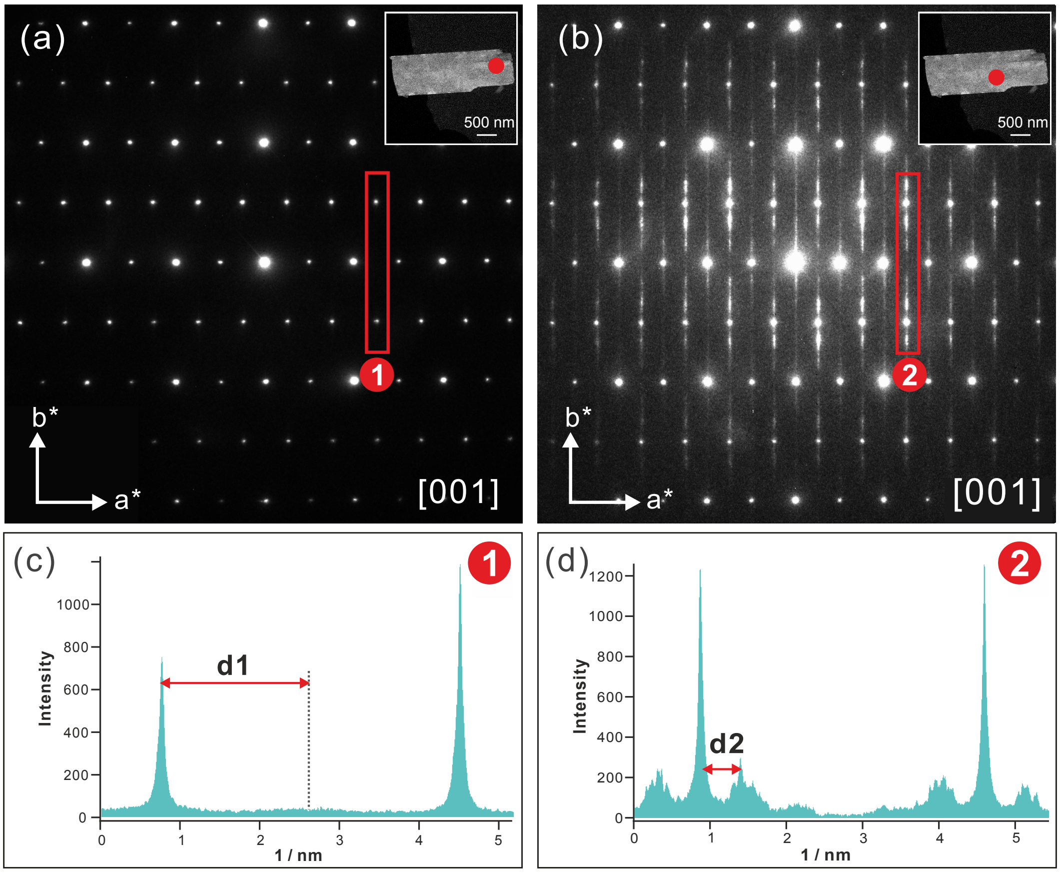

Figure 6.11: Single electron nano diffraction patterns of $Al_4B_2O_9$ recorded from different regions of an $Al_4B_2O_9$ crystallite oriented in [001] direction, as marked in the STEM insets on the upper right. (a) Highly ordered region. (b) Disordered area giving rise to modulated streaking in the pattern. (c) and (d): Intensity profiles taken along corresponding diffraction lines marked in (a) and (b) by red rectangles; $d_1 \approx 3d_2$ in reciprocal space.

Due to the rod-like observed diffuse streaks in reciprocal space the disorder in direct space must be caused by a stacking sequence along the ***b*** axis that deviates from the perfect stacking sequence of an ordered structure. It can be derived that the weak diffuse streaks along the main ***b**** axis at $0k0$ positions and through reflections $h00$ with h even decreases monotonically away from reflection positions at k integer (Fig. 6.12). In hence, the stacking sequence should be composed of several layer types which own an identical structure model in projection onto the ***b*** axis. The simplest model which fulfills the requirement comprise identical layers shifted by some amount within the *ac*-plane. An alternative model is constructed from stacked layers differing only slightly in the x and/or z coordinates. But it is doubtful that it would not cause an additional distortion along the ***b*** axis at the same time. The diffuse intensity along each rod is zero at all $h + k = 0$, showing its preservation of the extinction rule for the average structure.

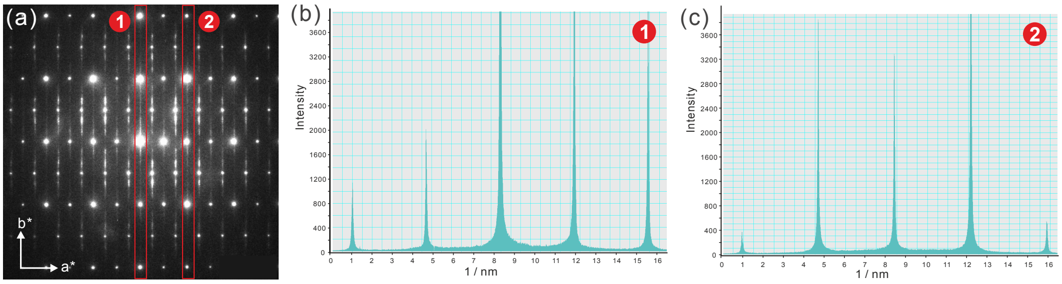

Figure 6.12: (a) Single electron nano diffraction pattern od $Al_4B_2O_9$ viewed in [001] direction. (b, c): Intensity profiles taken along corresponding diffraction lines marked in (a) by red rectangles.

Aforementioned in section 5.1.5, the measured diffraction pattern can be treated as the product of the diffraction pattern of a single layer with the Fourier transform of the list of layer positions in the stacking direction. Therefore, when either of the factors is zero, the diffracted spots will disappear and certainly no diffuse scattering will appear. This is satisfied, if each layer preserves the symmetry condition of $C2/m$, revealing that all layer types are identical only with a difference of a shift in the *ac*-plane. The slices cut from three-dimensional reconstructions show that no diffuse rods exist through Bragg reflections in the [010] zone with $h + l$ even (Fig.6.13). The extinction condition for the diffuse streaks plus the running direction of diffuse streaks indicates that the disorder is caused by layers shifted by $\frac{1}{2}\boldsymbol{a} + \frac{1}{2}\boldsymbol{c}$. The position of any layer within the *ac*-plane is denoted as $\Delta\mathrm{x} + \Delta\mathrm{z}$. The shift values with zero (or identical) for all layers will lead to an ideal crystal structure model. Consequently, the contribution to the diffraction pattern by any such layer can be described as: $I(hkl) = [\sum_j^N f_\mathrm{j}\, e^{2\pi i(h(x_j + \Delta\mathrm{x}) + ky_j + l(z_j + \Delta\mathrm{z}))}]^2$. The terms with $\Delta\mathrm{x}$ and $\Delta\mathrm{z}$ can be factored out to obtain: $I(hkl) = [\sum_j^N f_\mathrm{j}\, e^{2\pi i(hx_j + ky_j + lz_j)}\, e^{2\pi i(h\Delta\mathrm{x} + l\Delta\mathrm{z})}]^2$. Layer without any shift delivers $\Delta\mathrm{x} = 0$ and $\Delta\mathrm{z} = 0$, resulting the second exponential $e^{2\pi i(h\Delta\mathrm{x} + l\Delta\mathrm{z})} = 0$. On this occasion, the diffraction pattern seems identically as that from a ordered crystal, i.e., no diffuse scattering occurs. In combination with the symmetric conditions of emergence and disappearance of the diffuse streaks, it can be deduced as following (*equation* 6.1) to result in $\Delta x = \frac{1}{2}$ (similar for $\Delta z = \frac{1}{2}$).

$$\left.\begin{array}{r}\left.\begin{array}{r} e^{2\pi i(h\Delta x + l\Delta z)} = 1 \Rightarrow h\Delta x + l\Delta z = N \\ \text{no diffuse scattering} \Rightarrow h + l = 2n \end{array}\right\} \Rightarrow h(\Delta x - \Delta z) + 2n\Delta x = N \\ \text{no diffuse scattering } h = 0 \ (l = \text{even}) \\ \text{for the natural number } N = 1 \end{array}\right\} \Rightarrow \Delta x = \frac{1}{2} \qquad (6.1)$$

Layers *A* and *B*, as initial construction complement, was described in section 5.1.5. They differ only by the shift of $\frac{1}{2}\boldsymbol{a} + \frac{1}{2}\boldsymbol{c}$. Under this kind of shifts, the connection of octahedral chains does not change the sequence as *AAB*•*AAB*. In general, two types of three-fold modulated disordered stacking sequences, *AAB*•*AAB*•*AAB* and •*ABC*•*ABC*, are conceivable. As the shift between layer types must be $\frac{1}{2}\boldsymbol{a} + \frac{1}{2}\boldsymbol{c}$, the third layer in a sequence *ABC* would be identical as the initial *A* layer. Therefore, the layer sequence is restricted to *AAB* as main form to describe the three-fold superstructure. A 10 x 1 x 10 (***a*** x ***b*** x ***c***) super-cell derived from the ordered crystal structure was used as basic layer type. 200 of the basic layers were applied for the construction of the superstructure model for the simulations of electron diffraction patterns.

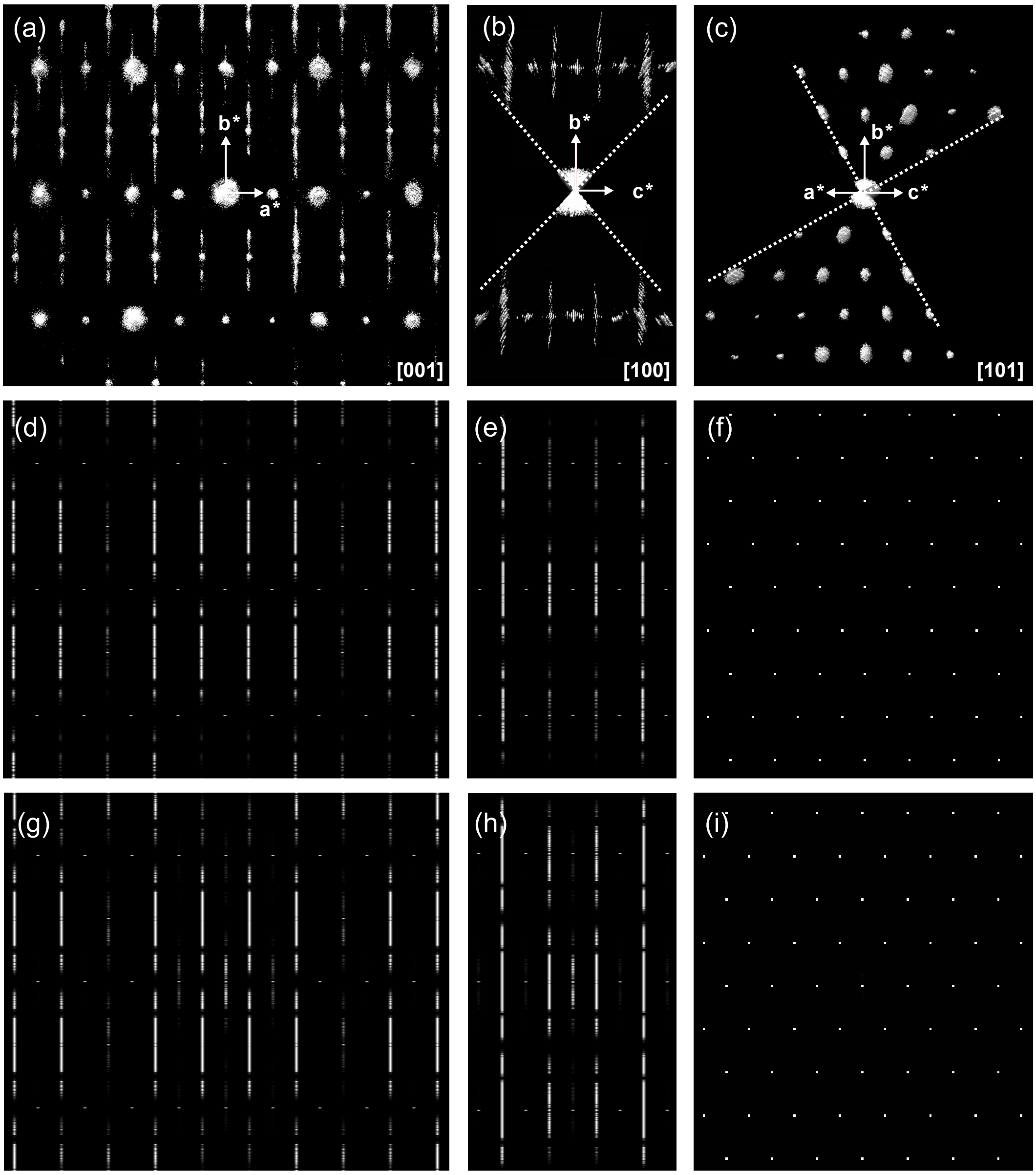

Figure 6.13: Experimental electron diffraction patterns of [001], [100] and [101] zones cut from the reciprocal volume (a-c). Corresponding simulated electron diffraction patterns of the three-fold superstructure (d-f) and with additional chemical changes (g-i). The part of the reciprocal space is marked with white dotted line in (b) and (c).

As shown in Fig. 6.13d-f, the final simulated electron diffraction patterns of zones [001], [100] and [101] of the modelled structures repeat the three-fold modulation of the ***b****** axis and the diffuse streaks quite well. The strong modulated diffuse scattering along ***b**** axis occurs for $h = 2n + 1$ and $l = 2n + 1$ in the *hk*0 and 0*kl* slices, which is caused by the shift of ½***a*** + ½***c*** . In comparison, the [101] zone presents no diffuse scattering. Since the weak diffuse scattering along ***b**** axis at the *hk*0 rods with *h* even were also observed (Fig. 6.12) the effect of a varying stoichiometry must be taken into account. In order to describe the streaks in a complete way, as an alternative solution to the previous described models with pure shifts, stoichiometric variations in the of layer *B* were performed for the simulation as well. In view of excessive initial boron in the reagent during the synthesis, some of the tetrahedral Al2 or Al4 sites in the model might be partly occupied by B atoms. The simulated electron diffraction patterns provided in Fig. 6.13g-i show no big difference with the diffraction pattern without substitution with B atoms (Fig. 6.13d-f) and are still in line with the experimental diffraction patterns (Fig. 6.13a-c).

6.1.7 Summary

The crystal structure of $Al_4B_2O_9$, was successfully characterized by TEM techniques. A full description of the atomic arrangement in ordered and disordered areas was achieved by structure determination from ADT data, HRTEM, HAADF-HRSTEM, structural modelling and disorder simulation.

6.2 Crystal structures of Zr-MOFs

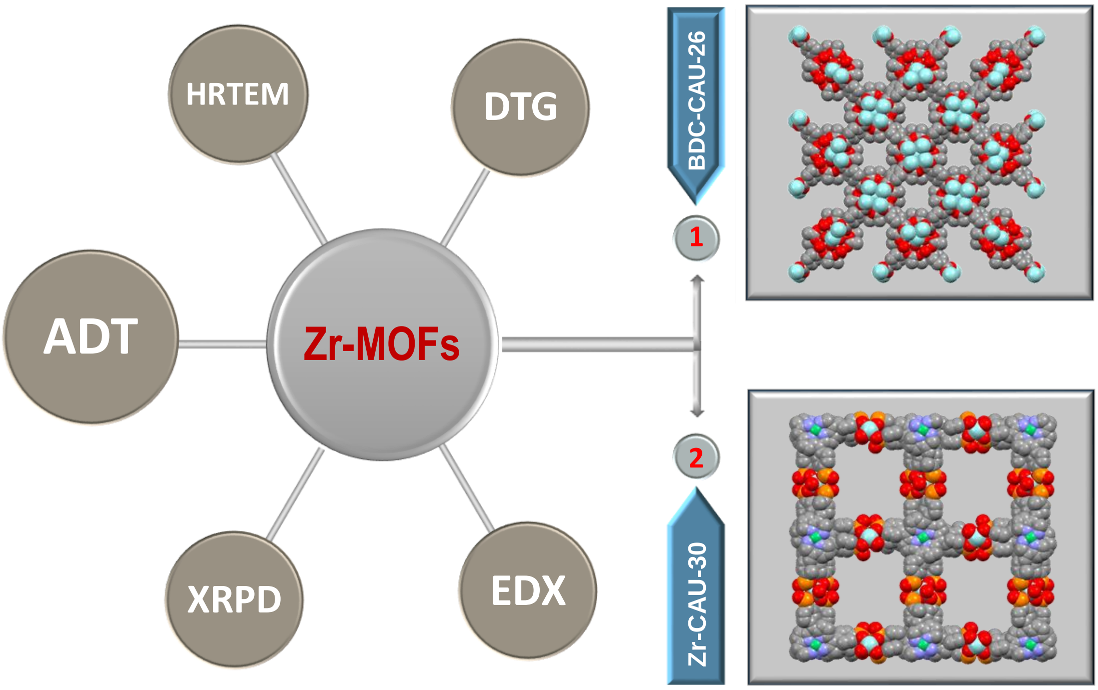

New crystal structures of Zr-MOFs solved by electron diffraction tomography

The crystal structure determinations of two new Zr-MOFs, CAU-27-BDC and Zr-CAU-30, were performed in a collaboration with the group of Prof. Dr. Norbert Stock from University of Kiel, Germany. The results of CAU-27-BDC were concluded in the paper "Expanding the Variety of Zirconium-based Inorganic Building Units for Metal-organic Frameworks" Sebastian Leubner; Haishuang Zhao; Haishuang Zhao, Niels Van Velthoven, Mickael Henrion, Helge Reinsch, Dirk De Vos, Ute Kolb, Norbert Stock. "*Angewandte Chemie*", Helge Reinsch; Ute Kolb and Norbert Stock, 2019.[198] DOI: *https://doi.org/10.1002/anie.201905456*. The results of structural investigation of Zr-CAU-30 were published with following information[72]: "Highly stable and porous porphyrin-based zirconium and hafnium phosphonates – electron crystallography as an important tool for structure elucidation." Timo Rhauderwiek, Haishuang Zhao, Patrick, Hirschle, Markus Döblinger, Bart Bueken, Helge Reinsch, Dirk de Vos, Stefan Wuttke, Ute Kolb and Norbert Stock. "*Chemical Science*", 9 (2018), page: 5467–5478. DOI: *10.1039/C8SC01533C*. My work contributions on the structural characterizations of both MOFs are concluded in this dissertation. The contents about experimental section in 5.2 as well as discussion and result in section 6.2 are adapted and reused from the published results.

6.2.1 Sample overview of CAU-27-BDC

CAU-27-BDC consists of needle-like nano particles as show in Fig. 6.14. No other crystal morphology nor second phase was observed in the sample. Fig. 6.14c shows the nanorod diameter histogram and normal distribution of CAU-27-BDC. The average nanorod diameter and standard deviation with 41.8 ± 20.1 nm were calculated based on measurements from 350 single nano particles. The material is crystalline and suitable for the studies with TEM under low electron dose.

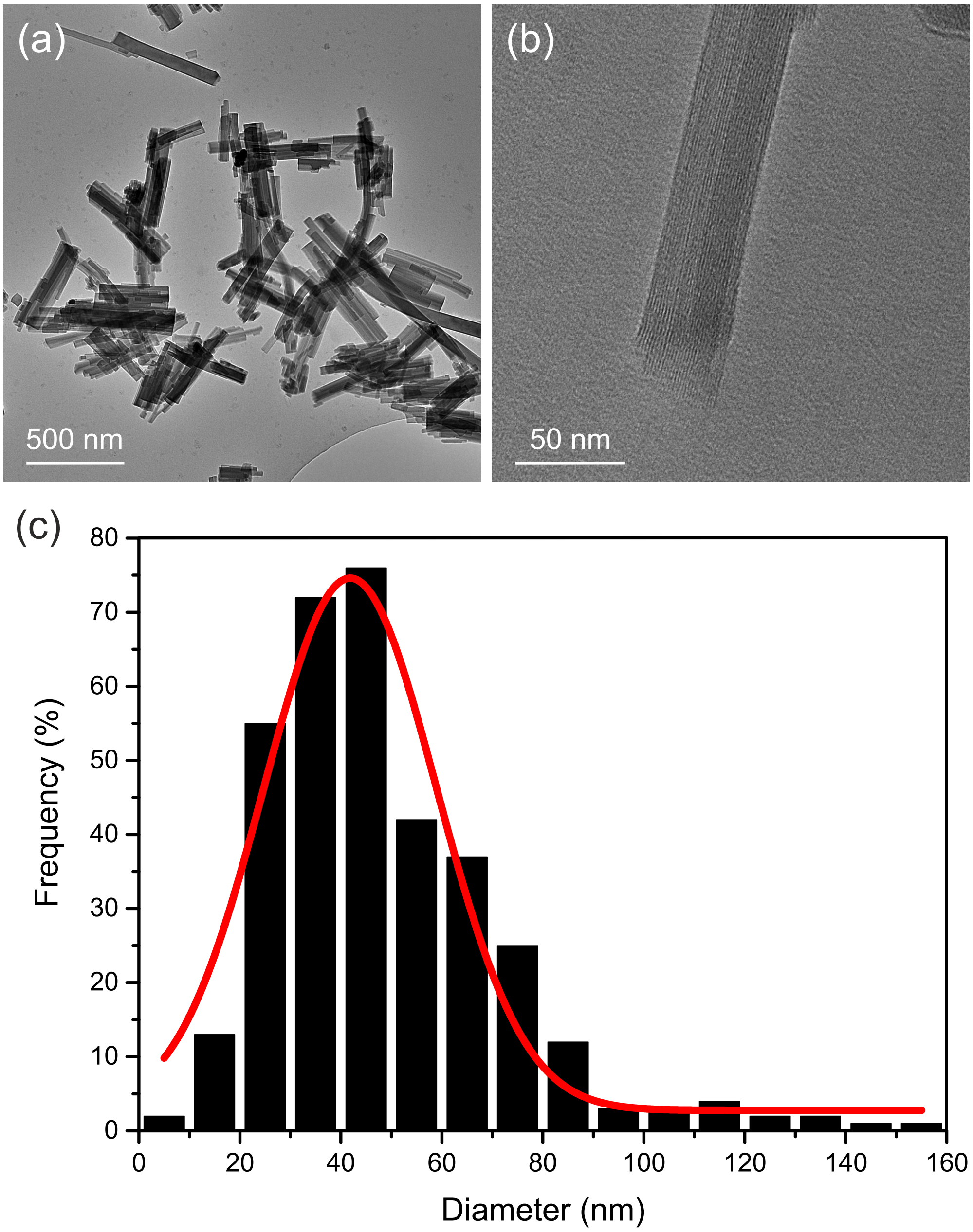

Figure 6.14: TEM images (a) overview and (b) single nanorod, (c) diameter distribution of CAU-27-BDC nanorods.

6.2.2 ADT data analysis of CAU-27-BDC

ADT data taken from an approximately 200 nm thick rod was reconstructed and delivered a body-centered tetragonal lattice with a = 20.53 Å, b = 20.39 Å and a = 21.67 Å (Fig. 6.15a-c). The deviation between a and b is in the tolerance area of electron diffraction data. The rule of systematic extinction with $h + k + l = 2n$ for *hkl* reveals an *I*-centred Bravais lattice for CAU-27-BDC. In order to obtain further symmetric information, three major 2D-slices of *hk*0, 0*kl* and *hhl* (Fig. 6.15d-e) were cut from the reconstructed ADT data. The symmetry conditions of $h + k = 2n$ for *hk*0, $k = 2n$ and $l = 2n$ for 0*hl*, and $h = 2n$ and $l = 2n$ for *hhl* lead to the extinction symbol *I* - *c* -, corresponding to three possible space groups: *I*4*cm* (No. 108) or *I*4*c*2 (No. 120) or *I*4/*mcm* (No. 140).

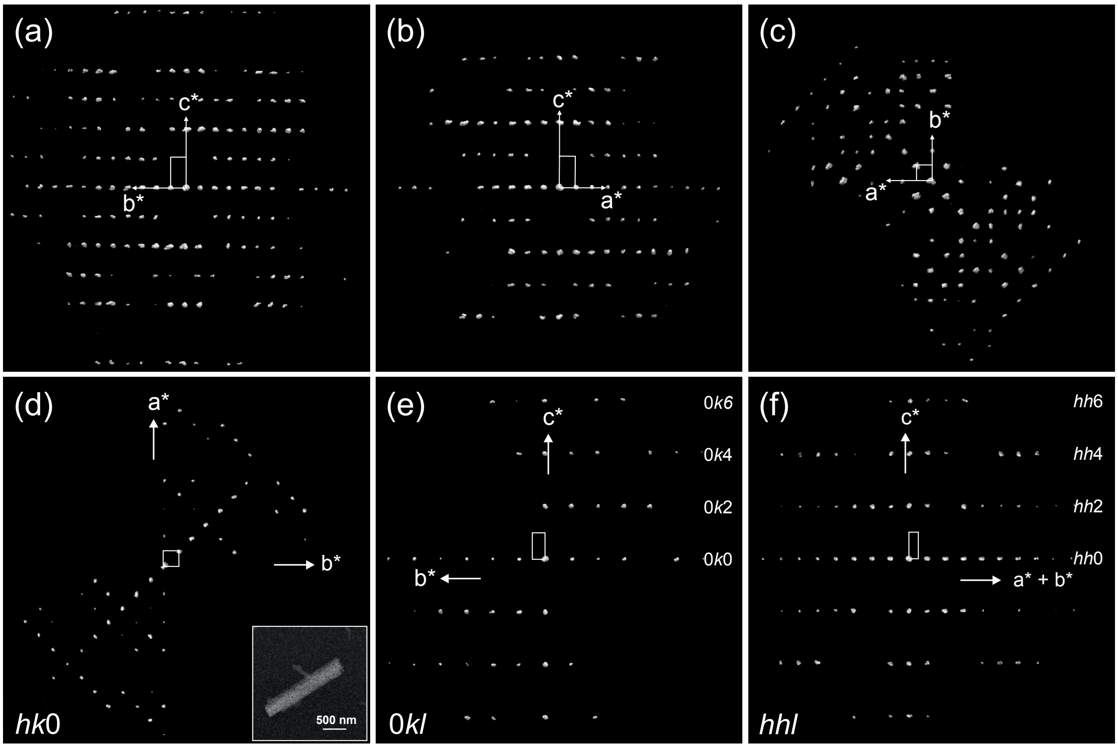

Figure 6.15: (a-c) Reconstructed 3D reciprocal space viewed along the main directions for CAU-27-BDC. (d-e) Three 2D slices with *hk*0, 0*kl* and *hhl* planes cut from reconstructed 3D reciprocal lattice. The crystal for ADT data acquisition is shown as an inset in (d).

6.2.3 Structure determination of CAU-27-BDC

Structure solution from ADT data

The lattice parameters derived from reconstructed ADT data were further refined against XRPD data and used for structure solution. The *ab initio* structure solution of CAU-27-BDC was successfully performed with direct methods in the space group of *I*4/*mcm* from ADT data and converged with a final residual R of 0.127, resulting in a reasonable structure model and a well-resolved Fourier potential map (Fig. 6.16). The two strongest maxima (3.51 and 3.28 $e^-/Å^3$) are corresponding to the two independent Zr atoms, respectively. The following maxima from 0.93 $e^-/Å^3$ to 0.36 $e^-/Å^3$ consistent with the O and C atoms.

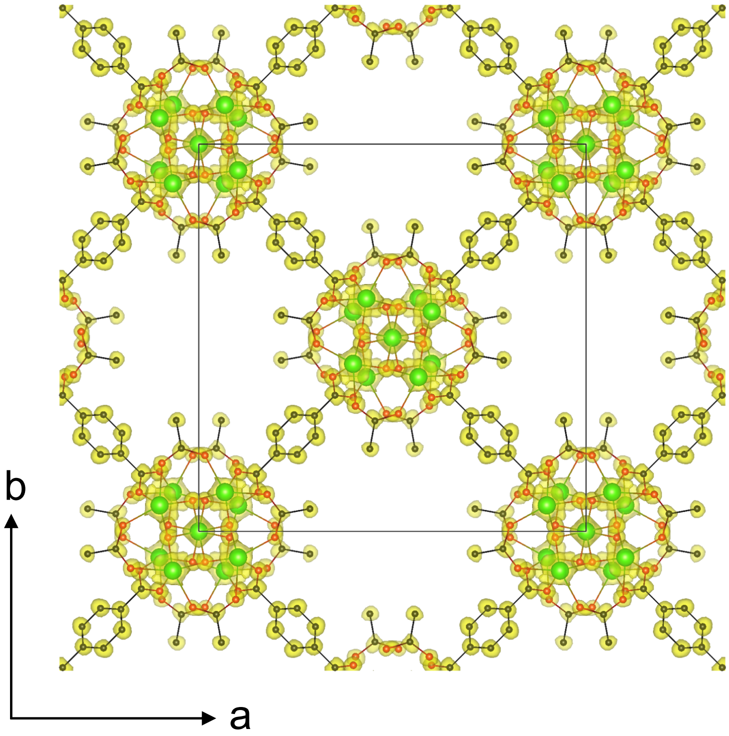

Figure 6.16: Electron potential map of structure solution of CAU-27-BDC overlaid with the atomic model, viewed in [001] direction. Zr in green, O red, C black.

Table 6.2: Parameters of structure solution of CAU-27-BDC from ADT data.

Parameter	Value
Tilt range (°)	-50/+60
No. of total reflections	3560
No. of independent reflections	629
Resolution (Å)	1.0
Independent reflection coverage (%)	100
R_{int}	0.168
Overall U ($Å^2$)	0.031
Residual R (SIR2014)	0.127
Space group	$I4/mcm$
No. of independent non-H atoms	11

Structure refinement from XRPD data

The crystal structure was refined with Rietveld-method from XRPD data. A preferred orientation along (020) was detected during the refinement. The refinement converged to a excellent value of R_{wp} = 8.22 % with a *gof* of 2.17. The plot is shown in Fig. 6.17. Crystallographic data of CAU-27-BDC is listed in the supplementary data *Appendix B1* in section Appendix.

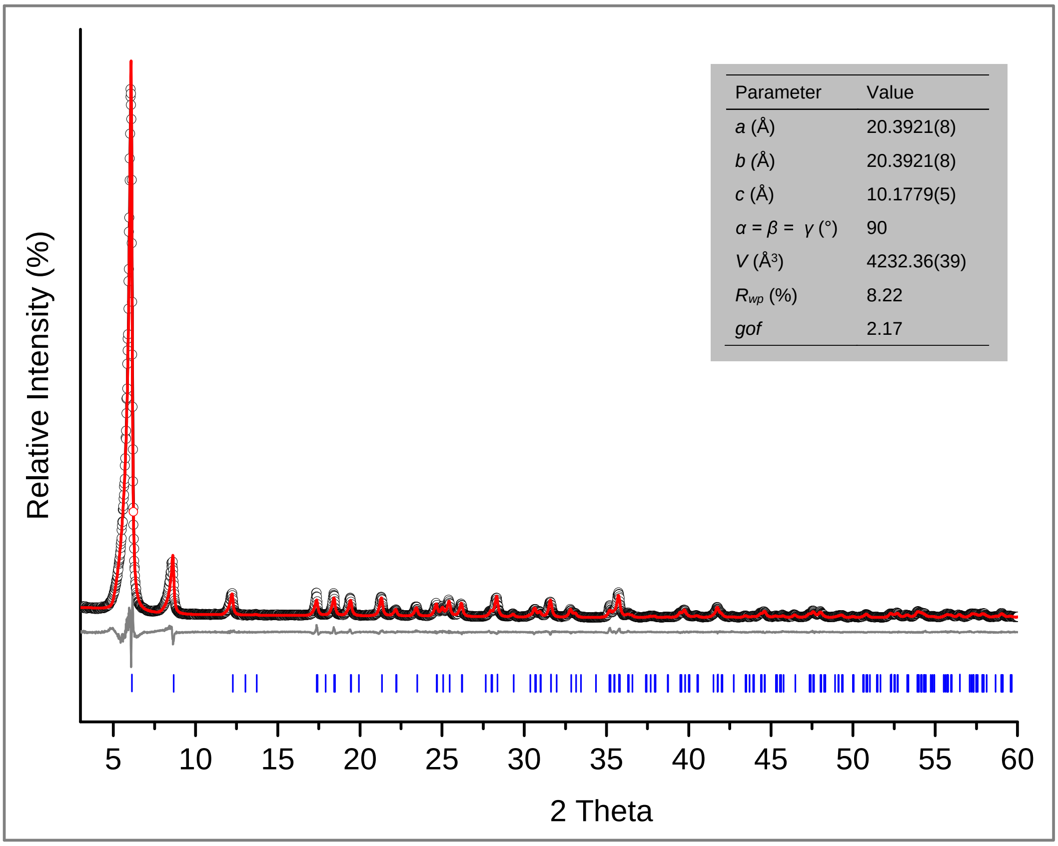

Parameter	Value
a (Å)	20.3921(8)
b (Å)	20.3921(8)
c (Å)	10.1779(5)
$\alpha = \beta = \gamma$ (°)	90
V (Å³)	4232.36(39)
R_{wp} (%)	8.22
gof	2.17

Figure 6.17: Plot of Rietveld refinement of CAU-27-BDC. Observed powder diagram (black circles), simulated powder diagram (red solid line), difference profiles (gray solid line), and reflection positions (blue vertical lines). Inserted table: parameters of Rietveld refinement. Adapted from ref. of Leubner et al. [cite 2019]

6.2.4 HRTEM imaging of CAU-27-BDC

High-resolution transmission electron microscopy (HRTEM) was carried out to observe the real atomic structure information of CAU-27-BDC. The HRTEM images viewed along [110] (Fig. 6.18) are in good agreement with the backbone constituted from ZrO-clusters running along the ***a*** axis, confirming the correction of the determined crystal structure.

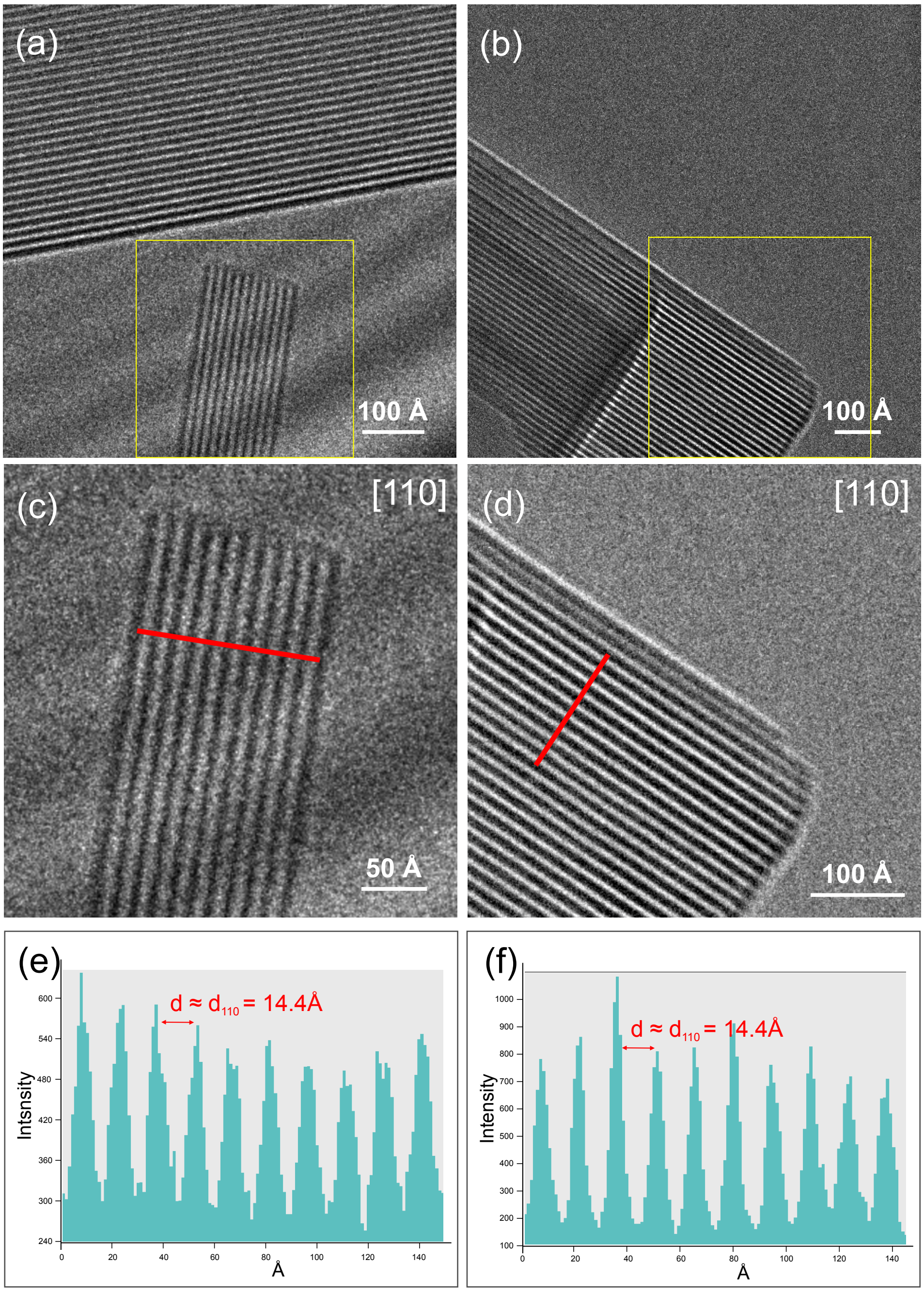

Figure 6.18: High-resolution TEM images of CAU-27-BDC recorded along [110] zone axis. (a, b) overview. (c, d) Enlarged images from the boxed areas in (a) and (b), respectively. (e, f) Intensity profiles taken along the corresponding selected areas remarked in (c) and (d) by red lines.

6.2.5 Crystal structure description of CAU-27-BDC

Fig. 6.19 illustrates the crystal structure of CAU-27-BDC. One Zr atom is coordinated by eight O atoms to form a ZrO_8 polyhedron (Fig. 6.19c) with reasonable Zr-O bond distances (Table 6.3). Six polyhedra are face-sharing connected by μ_3-O atoms to build a Zr_6O_8 cluster (Fig. 6.19d), in which a Zr_6 octahedron can also be observed. The bidentate acetate ligands link the Zr_6 octahedral corner. The clusters stack along the crystallographic ***a*** axis to construct one-dimensional chains (Fig. 6.19e) which serve as the backbone of the whole crystal structure. The organic linker consisting of ions interconnect the chains to form a three-dimensional framework with a 1D-channel of a about 7 Å diameter (Fig. 6.19b).

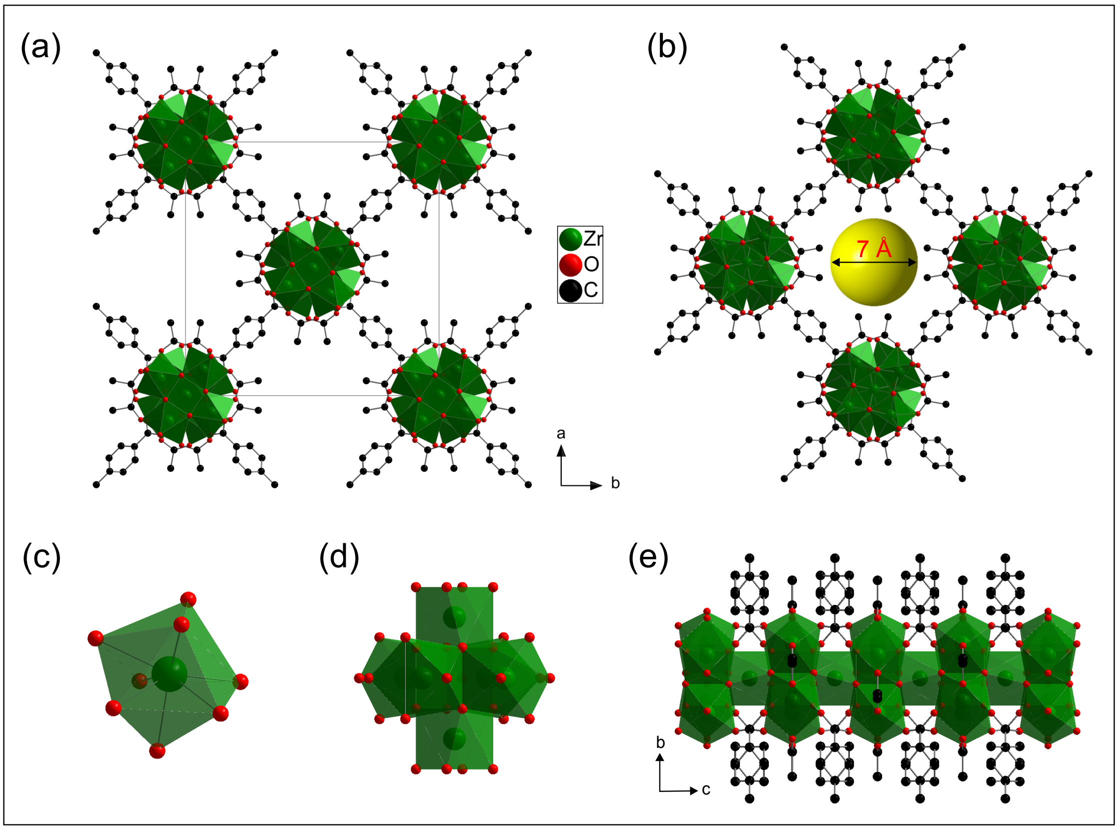

Figure 6.19: Crystal structure of Zr-CAU-27 (a) viewed along the crystallographic ***a*** axis with unit-cell and (b) showing the channel diameter of 7 Å; (c) single ZrO_8 polyhedron; (d) Zr_6O_8 cluster; (e) one-dimensional inorganic chain with connected Zr_6O_8 clusters. H atoms and water molecules in the pores are omitted for clarity.

Table 6.3: Selected bond distances in ZrO_8 polyhedral of CAU-27-BD.

	Zr1-O1	Zr2-O1	Zr2-O2	Zr2-O3	Zr2-O4
d(Å)	8x2.081(11)	2x2.171(12) 2x2.174(10)	2x2.136(10)	1x2.199(10)	1x2.225(9)

6.2.6 Sample overview of Zr-CAU-30

Needle-like crystals with different sizes were observed in the STEM images (Fig. 6.20a-c). The diameters of the nanorods are from a few tens up to about 500 nm. Crystals in such sizes are suitable for TEM investigations. Nano electron diffraction and HRTEM show the nonarods are crystalline. If the electron beam was shifted onto the flocculated particles, no diffraction pattern could be observed, indicating an amorphous phase. The crystals stay stable under sample cooling conditions and low beam illumination.

EDX element analysis revealed the chemical composition in the nano particles. As shown in Fig. 6.20d the signals of metal atoms Ni and Zr can be clearly seen, meaning the formation of Zr-MOF. The quantitative analyses delivered a Zr/Ni ratio are more than 2, e. g. Zr/Ni = 3.62 in Fig. 6.20d. The experimental values of Ni/Zr ratio are larger than that of the solved structure (Zr/Ni = 2), the discordance can be explained due to the appearance of a secondary phase[72] of very small particles (3–5 nm) on the surface of the Zr-CAU-30 nanorods.

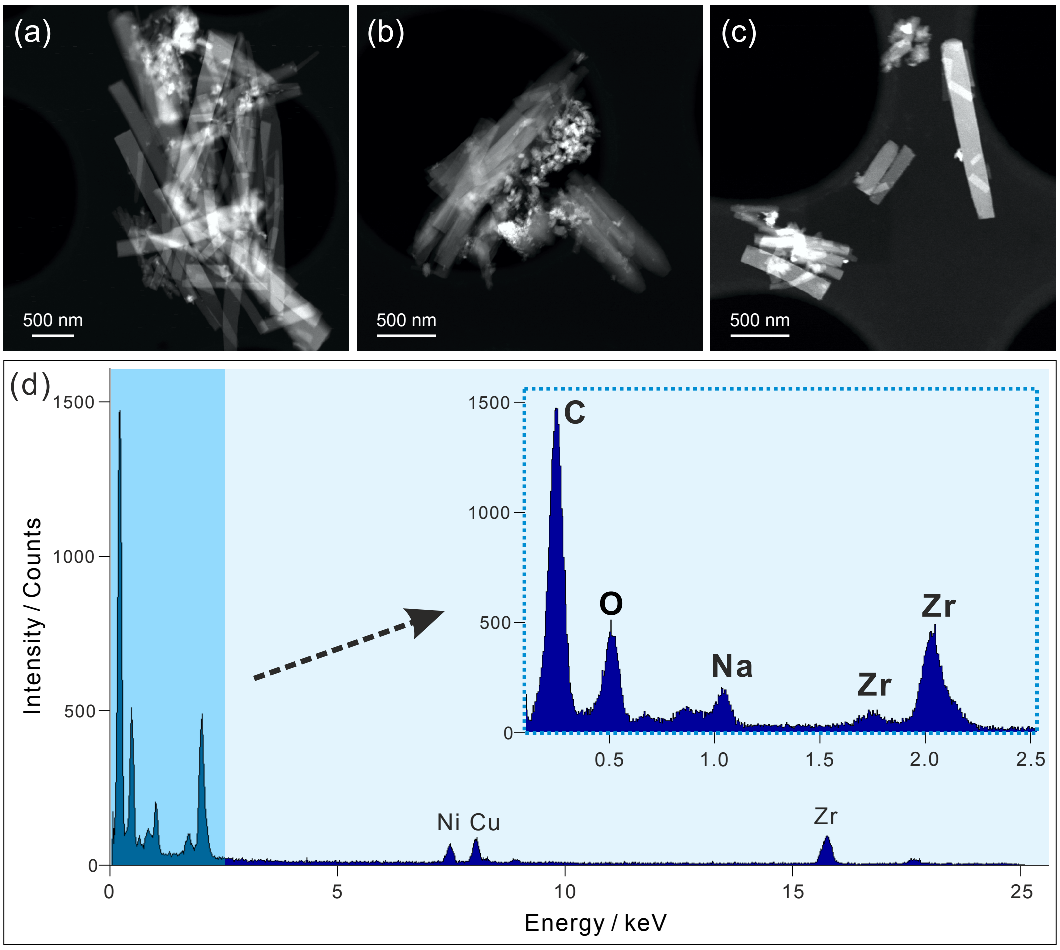

Figure 6.20: STEM images (a-c) and EDX spectrum (d) of Zr-CAU-30. The strong signal of carbon in (d) was partly contributed by the amorphous carbon film of the TEM grid. The spectrum from 0 to 2.5 keV in (d) is enlarged for clarity.

6.2.7 ADT data analysis of Zr-CAU-30

The diffracted spots became weaker and disappeared slowly during the tilt at room temperature, which was caused by the beam sensitivity of Zr-CAU-30. Therefore, the sample was cooled using a cryo-transfer holder and measured at liquid nitrogen temperature for ADT experiments in oder to reduce the radiation damage. The reconstructions of five datasets delivered similar unit-cells in a tetragonal crystal system (Table. 6.4 and Fig. 6.21). Symmetry analysis was based on the reconstructed electron diffraction reciprocal space. Systematic extinction with $h + k + l = 2n$ for hkl reflections indicated an I-centred Bravais lattice. The reflection conditions can be observed from 2D-slices cut from the reconstructed lattice (6.21) as following $h = 2n$ and $k = 2n$ for $hk0$; $k = 2n$ and $l = 2n$ for $0kl$; $2h + l = 4n$ for hhl resulting the extinction rule $Iacd$ associated with the space group $I4_1/acd$ (No.142).

Table 6.4: Lattice parameters of tetragonal Zr-CAU-30 derived from reconstructed ADT data.

Parameter	Cry I	Cry II	Cry III	Cry IV	Cry V	**Mean**
a (Å)	46.09	45.17	45.07	44.95	45.19	**45.28**
b (Å)	45.74	45.07	45.17	45.29	45.06	**45.23**
c (Å)	7.81	7.64	7.62	7.69	7.56	**7.66**

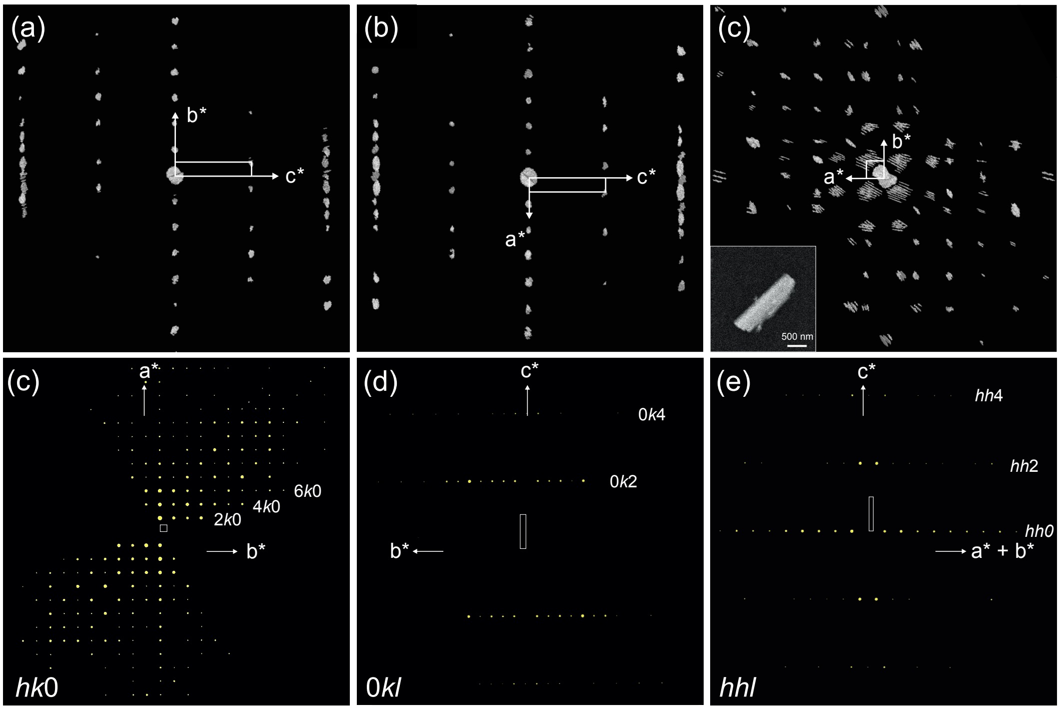

Figure 6.21: (a-c) Reconstructed 3D reciprocal space of Zr-CAU-30, viewed along the main directions. Dataset acquired from Cry I with lattice parameter : a = 46.09 Å, b = 45.74 Å, c = 7.81 Å. (d-e) Three 2D slices with $hk0$, $0kl$ and hhl planes cut from reconstructed 3D reciprocal lattice. STEM image of Cry I is shown in the inset of (c)

6.2.8 Structure determination of Zr-CAU-30

The crystal structure determination was conducted using a combination of structure solution of as made phase with ADT data and structure refinement of activated phase with XRPD data. Thermogravimetric (TG) measurement, as shown in Fig.5.3, shows the amount of water molecules with 20.5 wt% in Zr-CAU-30.[72] The crystallized or free water hampered the structure refinement from XRPD data. In hence, the structure was refined against XRPD data of activated phase.

Structure solution from ADT data

For structure solution, the cell parameters from ADT data were refined by Pawley fit from XRPD data which delivered $a = b = 45.121(5)$ Å and $c = 8.090(2)$ Å. Reflection data were extracted from the ADT dataset collected with electron beam precession. *Ab initio* structure solution was performed with direct methods and converged with a final residual R of 0.173 (Table 6.5). The structure solution delivered a well-resolved Fourier potential map (Figure 6.22) with a chemical meaningful framework. Some extra potentials can be found in the middle of the channels, probably corresponding to partly remaining water positions in the structure. These positions have been not taken into account for the structural description of the framework. In the output file, the two strongest maxima (2.24 and 1.63 $e^-/Å^3$) correspond to the two types of metal atoms Zr and Ni, respectively. The next maximum with 1.24 $e^-/Å^3$ is consistent with the P atom. The following peaks for O, N and C atoms were detected with a range of 0.98 down to 0.49 $e^-/Å^3$. One missing O atom located at P could only be detected from the calculation of difference of Fourier map.

Table 6.5: Parameters of structure solution of Zr-CAU-30 from ADT data.

Parameter	Value
Tilt range (°)	-65/+58
No. of total reflections	18149
No. of independent reflections	2021
Resolution (Å)	1.0
Independent reflection coverage (%)	99
R_{int}	0.344
Overall U (Å^2)	0.023
Residual R (SIR2014)	0.173
Space group	$I4_1/acd$
No. of independent atoms*	19

*Only for framework atoms. H atoms and H_2O were not taken in account.

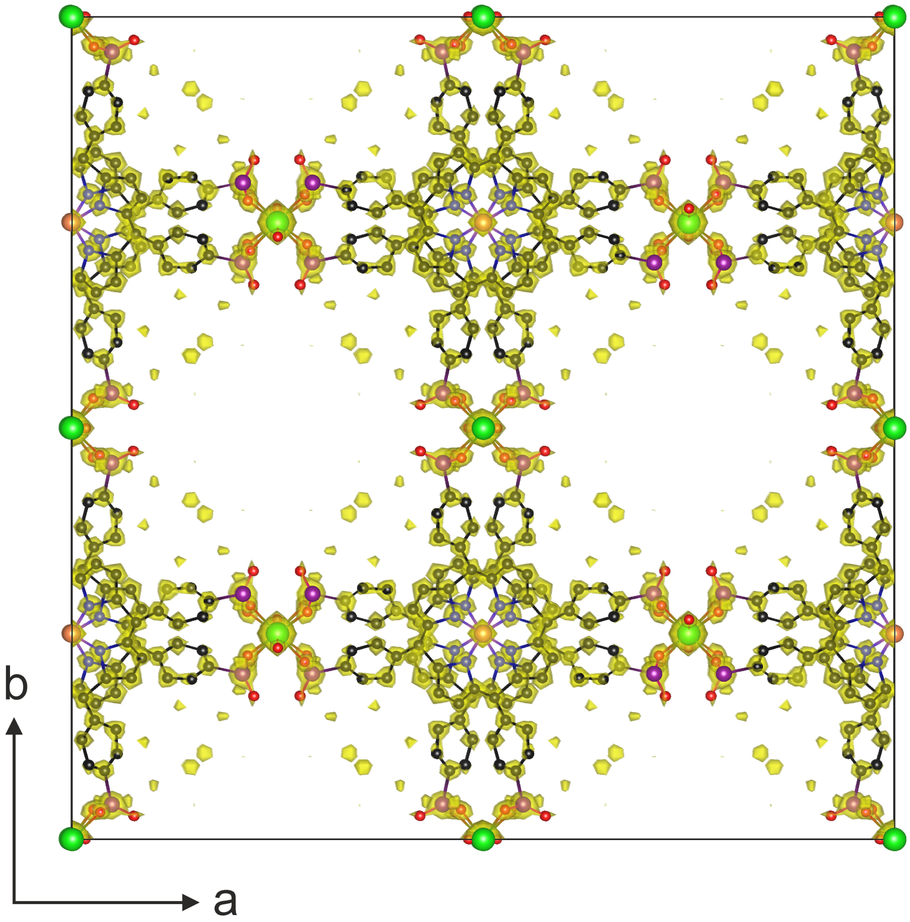

Figure 6.22: Electron potential map of structure solution of Zr-CAU-30 overlaid with the atomic model, viewed in [010] direction. Zr in green, Ni yellow, P violet, O red, C black, N blue. The residual potentials in the channels were caused by water molecules.

Structure refinement from XRPD data

Fig. 6.23 shows the XRPD diagrams of Zr-CAU-30 with as-made and activated phases, respectively. The biggest difference locates at the remarked reflections ❶ at 6.2° in activated phase and ❷ at 8.7° in as made phase. The phenomena was caused by the loss of water in the dehydration process, which further resulted to a symmetry reduction from $I4_1/acd$ of as made phase to $I4_1/cd$ of activated phase. The structural information obtained from ADT data was used as initial model for the structure refinement from XRPD data of activated phase. The program `Powdercell`[233] was used to convert the space group from $I4_1/acd$ to $I4_1/cd$. The model was then optimized using universal force filed as implemented in the program `Materials Studio`[234]. The transformed model was used as starting model for Rietveld refinement, in which the porphyrin moiety was fixed and the phenylphosphonate units were set as rigid bodies. The refinement converged with a R_{wp} of 3.8 % with a preferred orientation along (110). The result of Rietveld refinement was shown the inserted table of Fig. 6.24. Crystallographic data of Zr-CAU-30 is listed in the supplementary data *Appendix B2* in section Appendix.

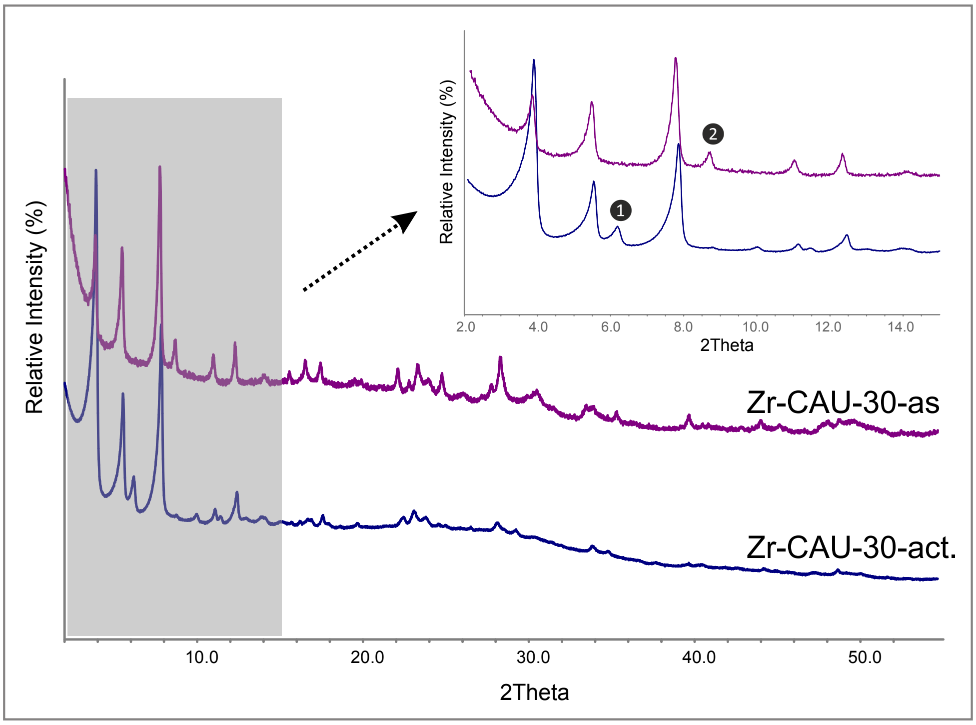

Figure 6.23: X-ray Powder diagrams of Zr-CAU-30. Lilac for as made phase and blue for activated phase. The 2θ in the range of 2-15° was enlarged for clarity.

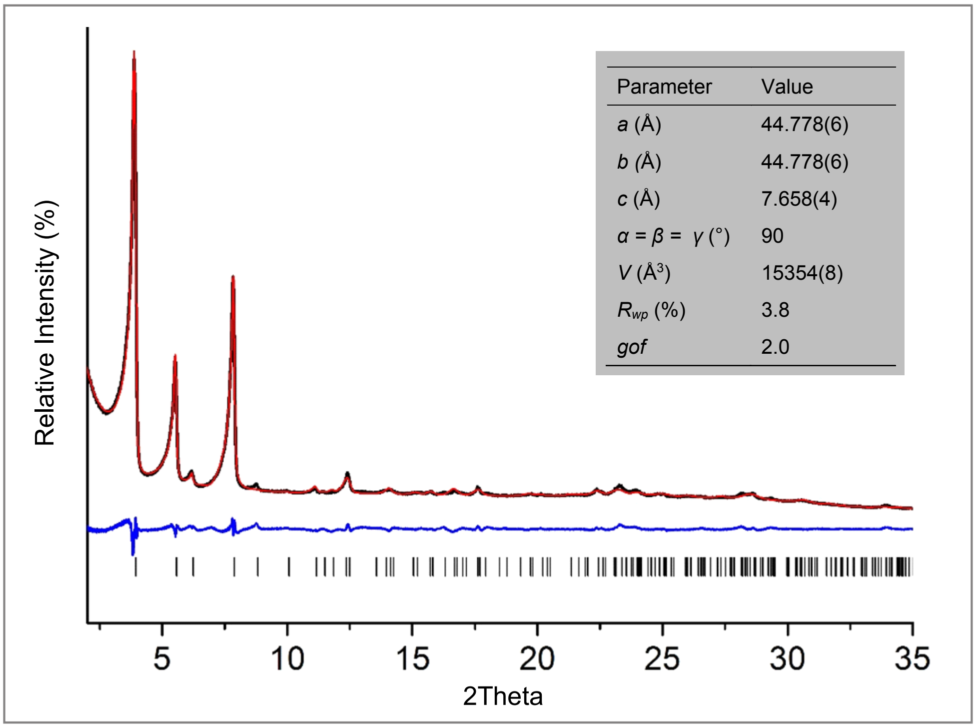

Parameter	Value
a (Å)	44.778(6)
b (Å)	44.778(6)
c (Å)	7.658(4)
$\alpha = \beta = \gamma$ (°)	90
V (Å^3)	15354(8)
R_{wp} (%)	3.8
gof	2.0

Figure 6.24: Plot of Rietveld refinement of activated Zr-CAU-30 of as made phase. Observed powder diagram (black solid line), simulated powder diagram (red solid line), difference profiles (gray solid line), and reflection positions (black vertical lines). Inserted table: results of Rietveld refinement. Adapted from Rhauderwiek et al.[72]

6.2.9 HRTEM imaging of Zr-CAU-30

HRTEM with low electron dose was carried out to visualize structural details of the Zr-CAU-30. Figure 6.25 shows reconstructed phase image, intensity profile, structural model, corresponding fast Fourier transform (FFT) and simulated electron diffraction pattern calculated from cystal structure solved from ADT data. A direct comparison with the crystal structure of Zr-CAU-30 viewed along [010] reveals already a high resemblance. The backbone of the structure shows the appearance in the HRTEM image. In addition, Fig. 6.25c presents the intensity profile of the lilac marked line in Fig. 6.25b, showing two type of intensities. The crystal structure viewed along the crystallographic ***b*** axis depicts two major columns, one containing Zr and Ni clusters (marked as **1**) and another only with Zr clusters (marked as **2**). The enhanced density of column **1** is evident in the extracted intensity profile. Furthermore, the simulated electron diffraction pattern is in line with the FFT image. The information from HRTEM image confirmed the crystal structure solved from electron diffraction data.

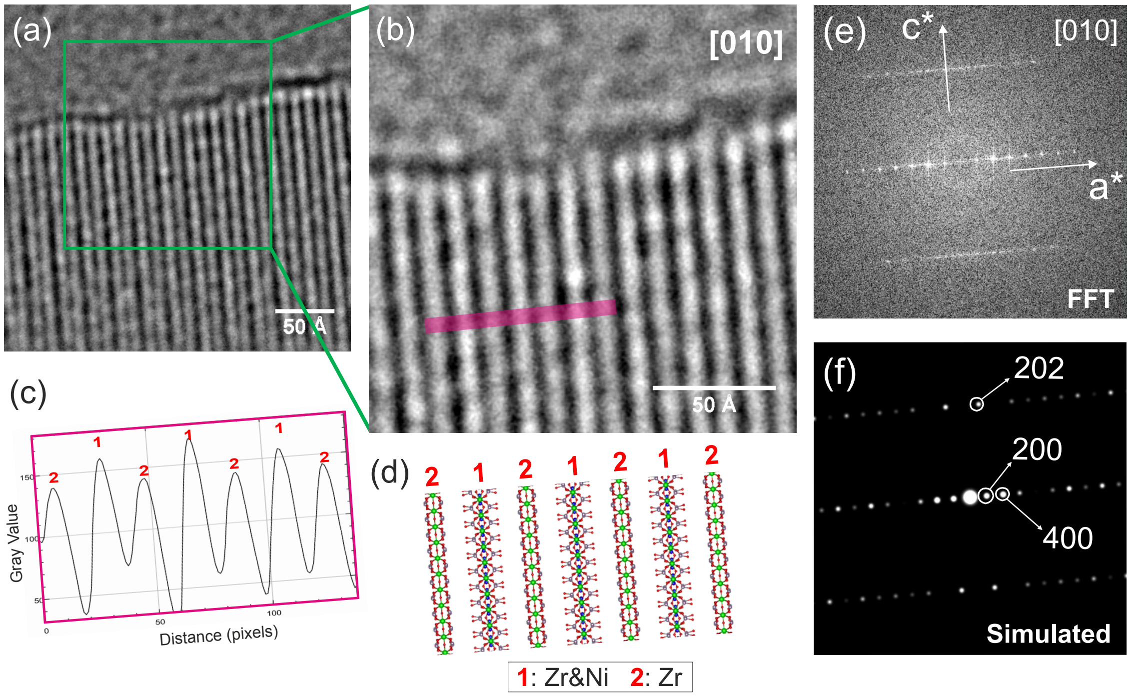

Figure 6.25: Reconstructed phase HRTEM image of Zr-CAU-30 recorded along [101] zone axis. (a) Overview of reconstructed phase image; (b) Enlarged phase image from the boxed area in (a); (c) Intensity profile of lilac remarked region in a (b); (d) Zr-CAU-30 structure model with Zr, Ni, P, and O atoms; (e) Squared modulus of the 2D Fourier transform; (f) Simulated electron diffraction pattern.

6.2.10 Crystal structure description of Zr-CAU-30

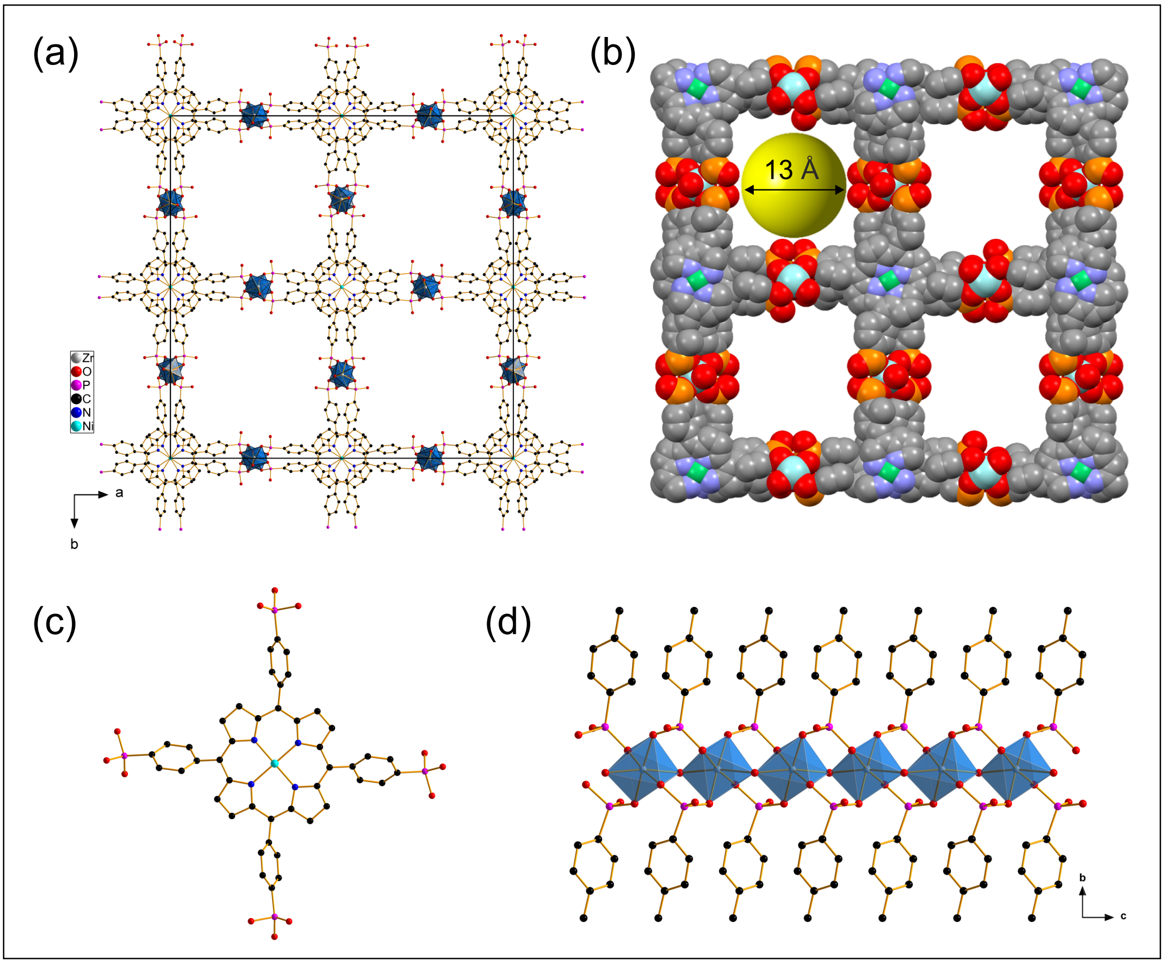

Figure 6.26: Crystal structure of Zr-CAU-30. (a) Overview with the unit-cell viewed along the crystallographic ***a*** axis and (b) space filling showing the pore diameter of 13 Å. Structure fragments of (c) the ligand and (d) inorganic chain with corner-sharing ZrO_6 octahedra chain (in blue). All H atoms and water molecules in the pores are omitted for clarity.

Fig. 6.26 illustrates the crystal structure including fragments of Zr-CAU-30. The 3D framework was build up by tetratopic Ni-H_4TPPP^{4-} linkers and Zr cluster chains. The resulted square 1D channels run along crystallographic ***a*** axis and exhibit a diameter of about 13 Å. The Zr atom coordinates two bridging O atoms and four O atoms from four different phosphonate groups, forming a ZrO_6 octahedra with an meaningful averaged Zr-O distance① of 2.035 Å. The 1D corner-sharing octahedra chains are interlinked by PCO_3 tetrahedra, which increase the stability of the Zr-cluster. The rotation of phenyl-section makes that the atoms of ligand are not in one plane. The distance of neighbored Ni atoms is the half of ***a*** axis of 3.829 Å.

---

①Note: d(Zr1-O1): 2.0943(302) Å, d(Zr1-O1′): 2.1568(335) Å, d(Zr1-O2): 2.0416(472) Å, d(Zr1-O3): 1.9109(227) Å, d(Zr1-O5): 2.0383(473) Å, d(Zr1-O6): 1.9681(285) Å.

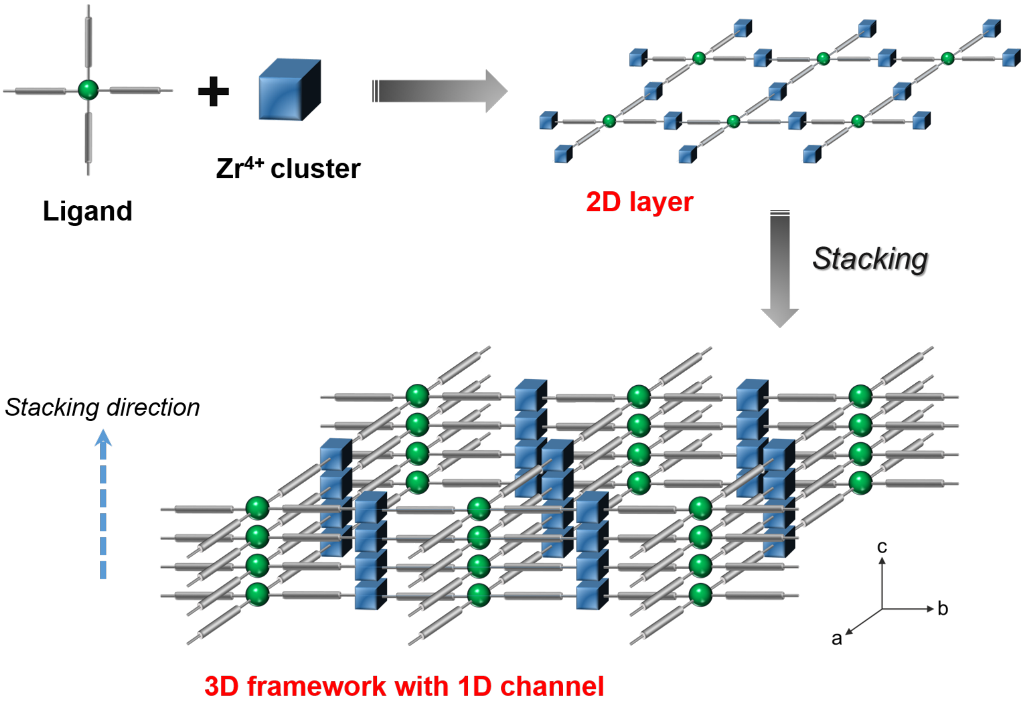

Figure 6.27: Schematic illustration for the modular assembly process of the extended 3D framework.

In order to explain the crystallization and formation steps of the 3D framework with 1D channels, the modular assembly was detailed by schematic illustration in Fig. 6.27. The ligand molecule coordinates with Zr^{4+} atom to form a 2D layer structure. The 2D layers serve as the basic building units and stack through the interconnection by bridging O atoms at the Zr^{4+} clusters. This kind of stacking forms a 3D framework with a square channel along the crystallographic $\boldsymbol{a}$ axis.

6.2.11 Summary

Electron beam sensitive materials, two Zr-MOFs, were measured under sample cooling with liquid nitrogen. *Ab initio* structure solutions were performed for two novel Zr-MOFs from ADT data. Rietveld refinements and HRTEM were performed to confirm the crystal structures.

6.3 Crystal structure of THK2 zeolite

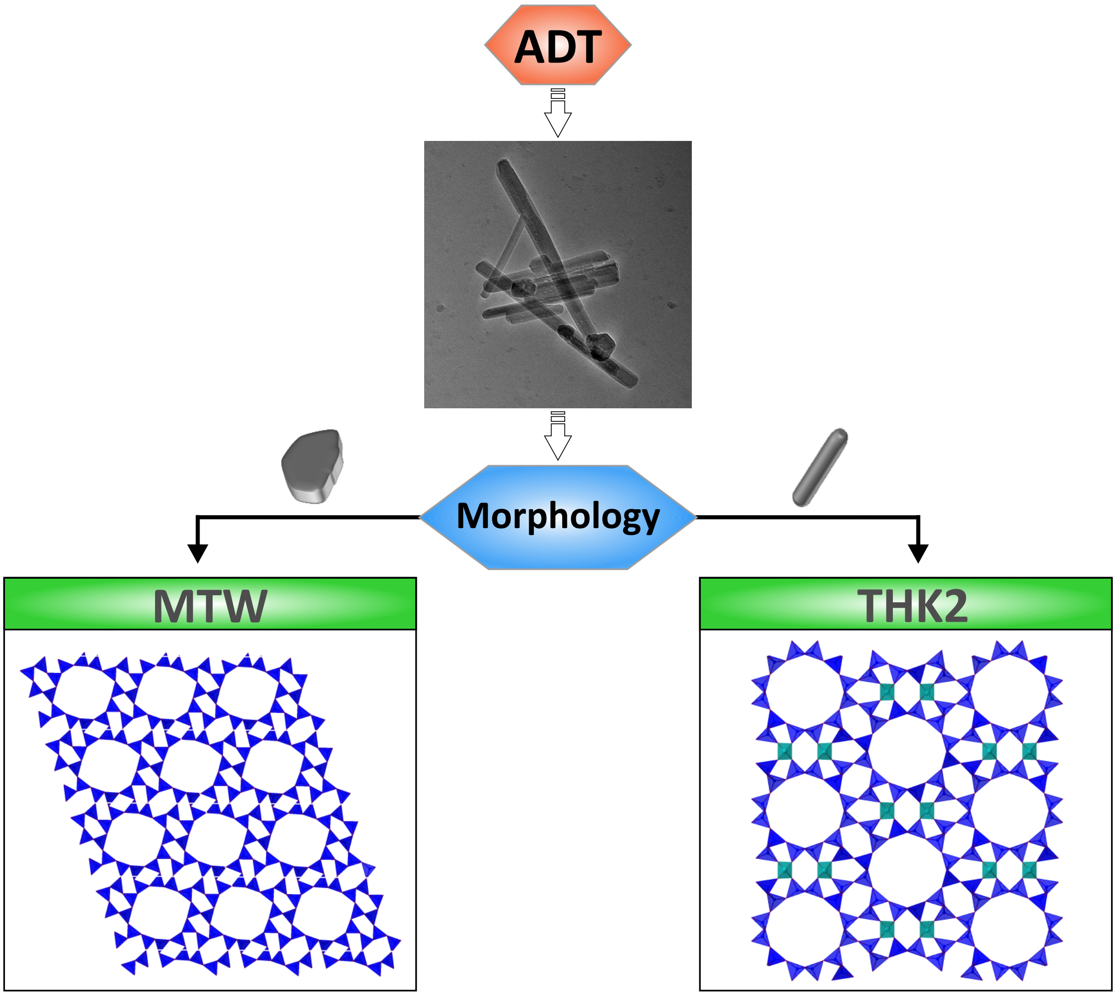

Crystal structure of THK-2 solved by electron diffraction tomography from a phase mixture

The project was a collaboration with Dr. Yasuhiro Sakamoto at University of Osaka Japan. The goal of the work was solving the crystal structure of a new phase in a zeolite mixture. Experimental details are listed in section 5.3. My work on this project was the crystal structure solution of THK2 and confirmation of the phase MTW from ADT data. The results of structure characterization are summarized in section 6.3 and are being prepared for publication.

6.3.1 Sample overview

Two types of crystal morphologies, nearly isotropic particles and nanorods, could be observed in the sample, as shown in TEM and STEM images (Fig. 6.28). The crystal sizes are ideal for TEM experiments. Nano electron diffraction indicate that the material is crystalline and stable under mild electron doses. Reconstruction of 3D ADT data confirmed that the crystals with different morphologies own different crystal lattices.

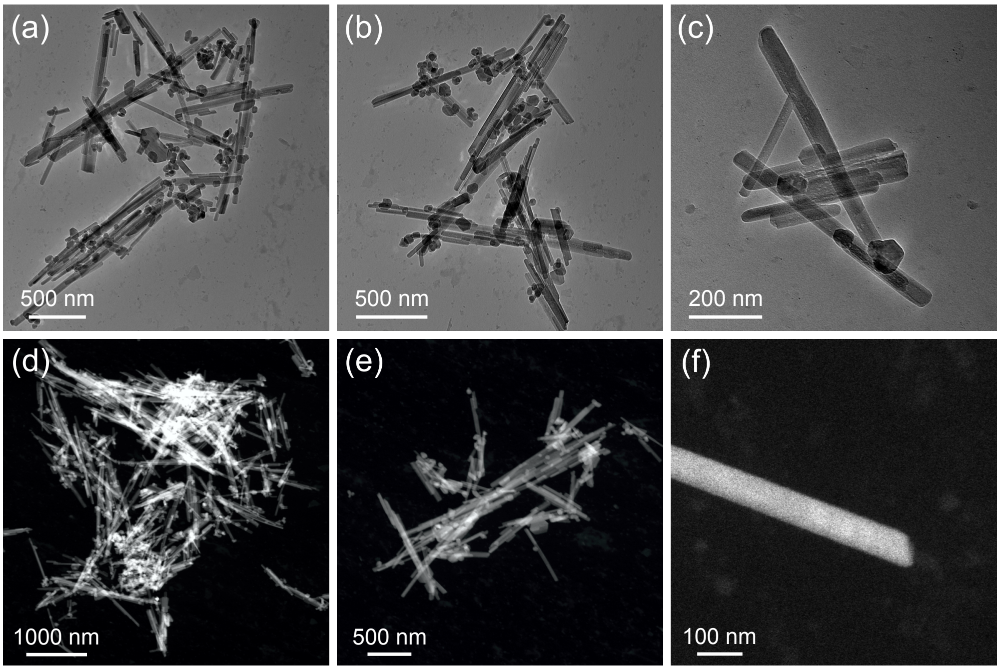

Figure 6.28: TEM and STEM images of zeolite THK-2. (a-c) TEM images and (d-f) STEM images. Single nano rod with about 100 nm diameter shown in (f).

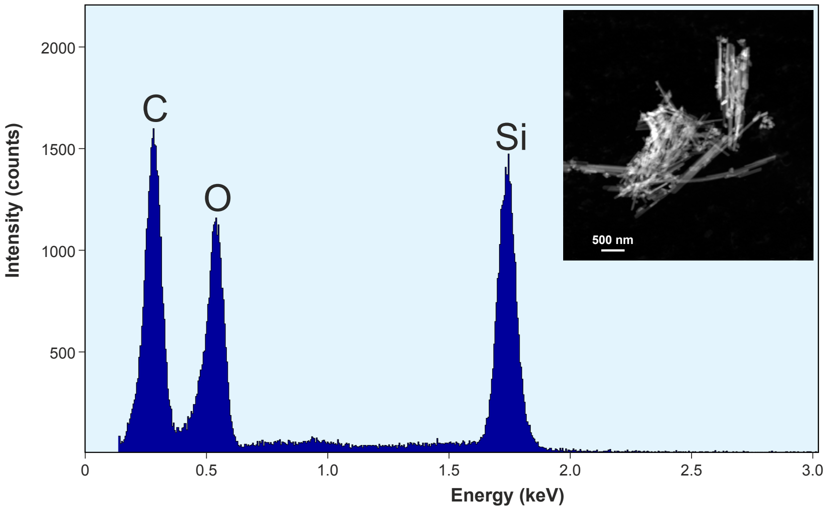

Figure 6.29: EDX spectrum of THK-2. The signal of carbon was caused by the amorphous carbon film on the TEM grid. Insert: STEM image of selected crystals for EDX measurement.

EDX spectrum (Fig. 6.29) was recorded in STEM mode from a region of accumulated crystals to detect the composition. Quantitative analysis resulted in a Si/O ratio of 1/2.13, which is close to the expected calculated ratio of 1/2 in both zeolites. Due to the resolution limit of EDX detector and the low content of Zn, the signal of Zn could not be detected and it resulted in an aberration of Si/O ratio.

6.3.2 ADT data analysis

ADT measurements were performed from single crystals with both morphologies. The reconstruction of the three-dimensional ADT datasets confirmed two phases within the sample. All the datasets collected from needle-shaped crystals could be indexed with primitive orthorhombic lattice parameters. On the other hand, the dataset acquired from the smaller crystals was reconstructed with $h + \mathrm{l} = 2n$ for all hkl as well as $h = 22n$ and $\mathrm{l} = 22n$ for the reflections in $h0l$ slice, corresponding with a *C*-centred monoclinic lattice system with extinction symbol of $C\ 1\ c\ 1$. Taking into account the cell parameters and the known zeolite framework types in the *Database of Zeolite Structures*[8], the orthorhombic lattice was confirmed a new zeolite phase of THK-2 while the monoclinic lattice was identified as the known phase of MTW[235]. The unit cell parameters and symmetry information are concluded in Table 6.6. The projections of reconstructed 3D reciprocal space are shown in Fig. 6.30 and Fig. 6.31 for THK-2 and Fig. 6.32 for MTW. The violation of the extinction rule ($h = 2n + 1$ systematically absent in the $h0l$ plane) was not clearly visible in the reconstructed reciprocal space of Cry1 (Fig. 6.30e) but obvious in the reconstructed data of Cry2 in Fig. 6.31. Combining the observed information from the three main planes of both crystals cut from 3D volumina, the reflection conditions can be concluded as following: $l = 2n$ for $0k$; $l = 2n$ for $h0l$ plane; $h + k = 2n$ for $hk0$ plane, indicating the extinction symbol *Pccn*, associated with the only possible space group *Pccn* (No. 56).

Table 6.6: Crystallographic data obtained from reconstructed electron diffraction volume.

Material	THK-2	MTW
Crystal system	orthorhombic	monoclinic
Space group	*Pccn*	$C\ 2/c$
a (Å)	24.70	25.09
b (Å)	14.55	5.00
c (Å)	4.99	24.15
α (°)	90	90
β (°)	90	108.1
γ (°)	90	90

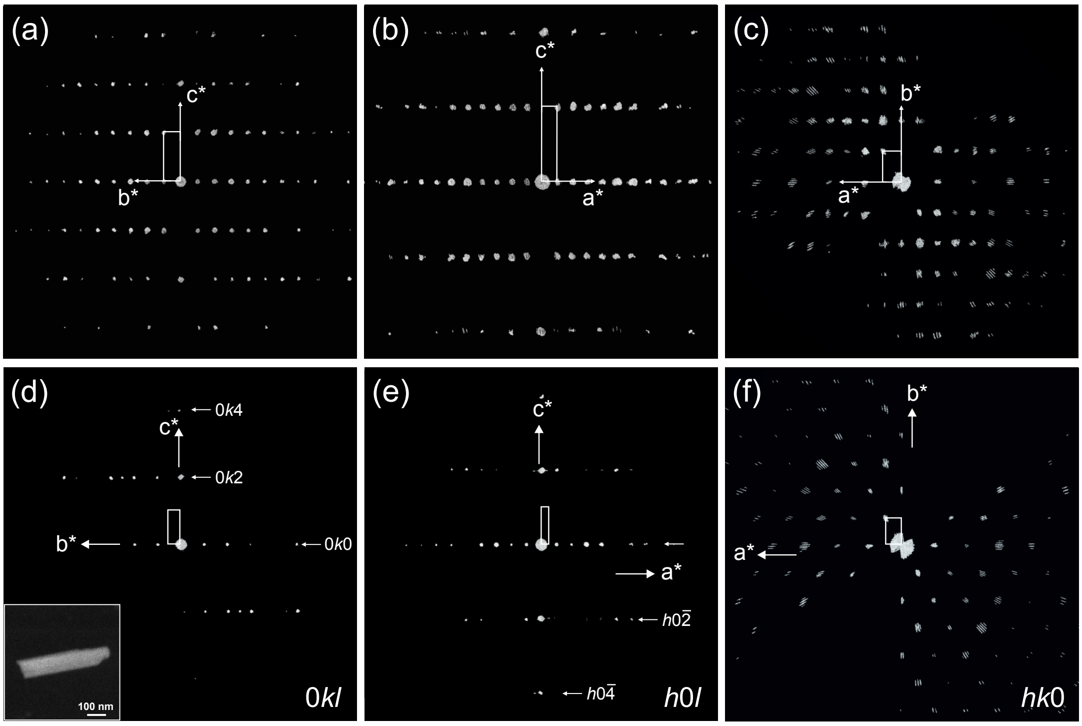

Figure 6.30: (a-c) Reconstructed 3D reciprocal space of THK-2 (Cry1) viewed along the main directions. (d-e) Three 2D slices with *hk*0, 0*kl* and *hhl* planes cut from reconstructed 3D reciprocal lattice. The crystal for ADT data acquisition is shown as an inset in (d).

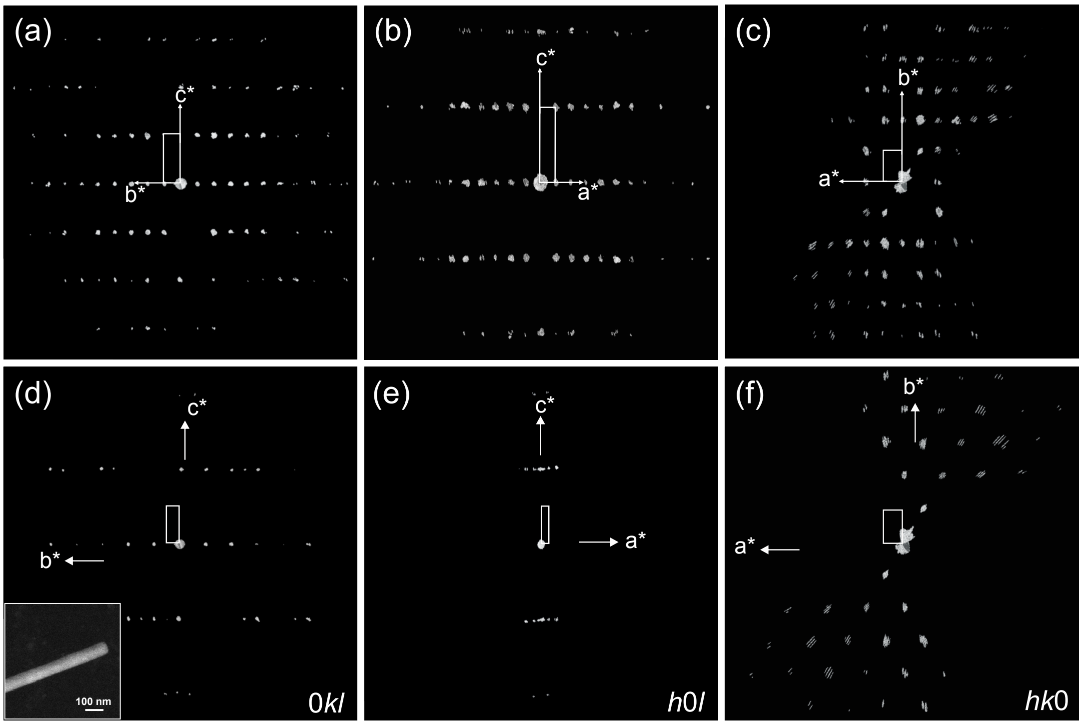

Figure 6.31: (a-c) Reconstructed 3D reciprocal space of THK-2 (Cry2) viewed along the main directions. (d-e) Three 2D slices with *hk*0, 0*kl* and *hhl* planes cut from reconstructed 3D reciprocal lattice. The crystal for ADT data acquisition is shown as an inset in (d).

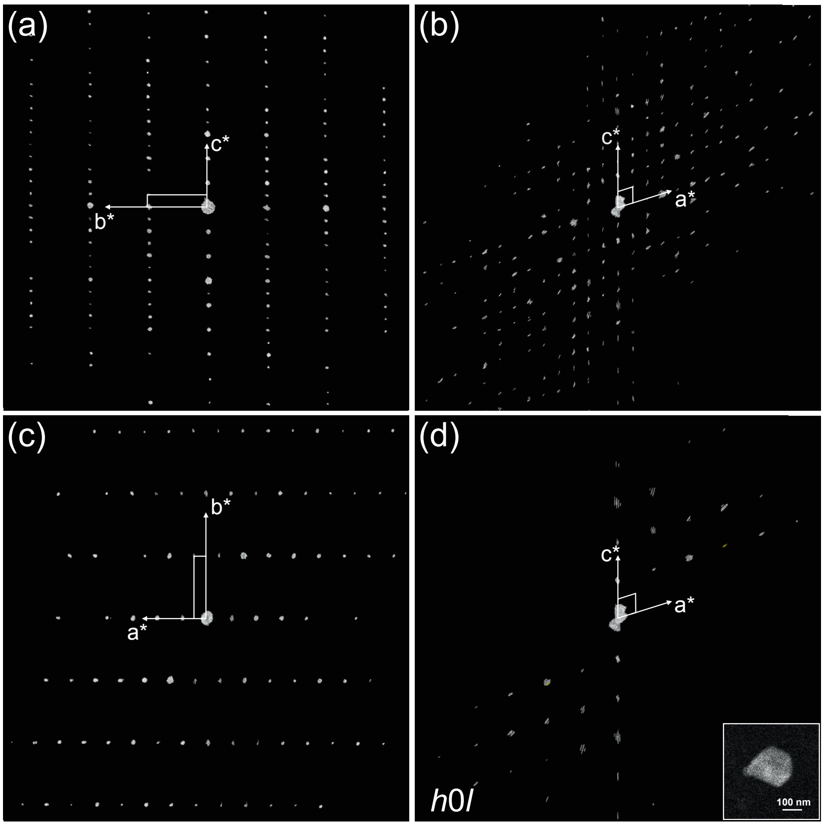

Figure 6.32: (a-c) Reconstructed 3D reciprocal space of MTW viewed along the main directions. (d) 2D slice of h0l plane cut from reconstructed 3D reciprocal space. The crystal for ADT data acquisition is shown as an inset in (d).

6.3.3 Structure determination

Structure solution from ADT data

Ab initio structure solution of THK-2 was performed in the space group *Pccn* with direct methods on basis of ADT reflection intensities extracted from dataset of Cry1. In order to increase the accuracy, the starting unit cell parameters were further refined with a Pawley-fit from XRPD data. The parameter details for the structure solution are listed in Table 6.7. The structure solution converged with a final residual of 0.127 and delivered a well-resolved Fourier potential map (Fig. 6.33) overlaid by a meaningful framework of all atoms. No potential for water molecule in the zeolite pore was detected because of the high vacuum condition in TEM. Four strongest potential maxima ranged from 1.34 to 1.09 $e^{-}/Å^{3}$ are corresponding to Si atoms. The following potential maxima from 0.80 to 0.50 $e^{-}/Å^{3}$ are consistent with O atoms. The partially occupied Zn atom could be found on a maximum of 0.66 $e^{-}/Å^{3}$ comparable to a value of one O atom. All atoms own reasonable positive temperature factors.

Table 6.7: Parameters of structure solution of THK2 from ADT data.

Parameter	Value
Space group	*Pccn*
No. of total reflections	3339
No. of independent reflections	705
Resolution (Å)	1.1
Independent reflection coverage (%)	99
R_{int}	0.227
Overall U (Å^2)	0.047
Residual R (SIR2014)	0.17
No. of independent atoms	14

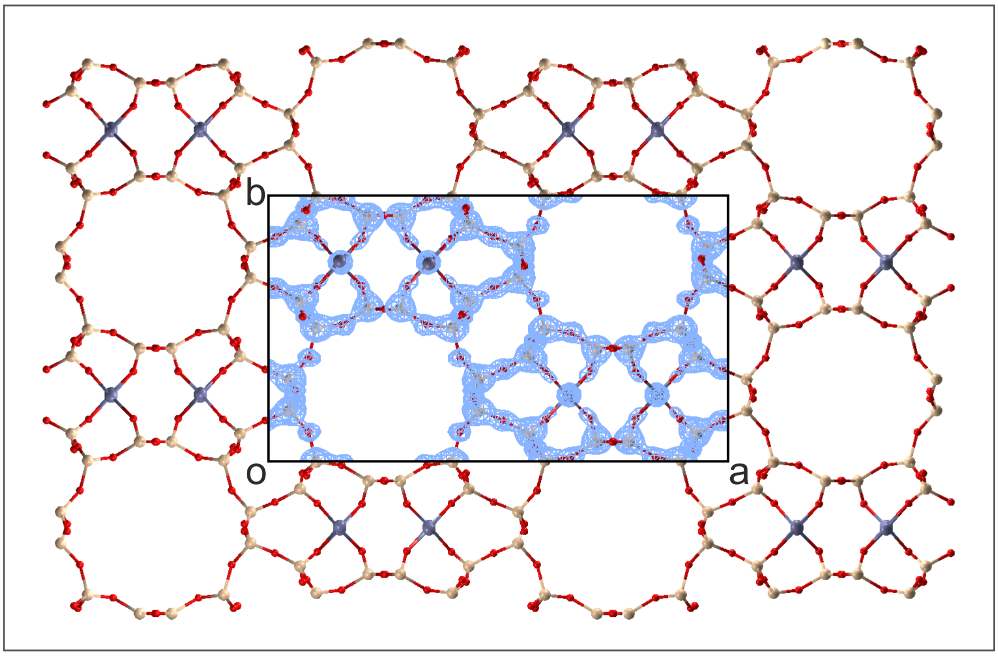

Figure 6.33: Electron potential map of structure solution of THK-2 overlaid with the atomic model, viewed along [001] zone. Si: light yellow, Zn: grey, O: red.

Structure refinement from XRPD data

The structure obtained from structure solution by ADT data was used as the initial model for the structure refinement from XRPD data.② The refinement converged with a R_{wp} of 3.26% (Table 6.8). Fig. 6.34 shows the plot of combined Rietveld refinement of THK-2 and

---

②The combined Rietveld refinement was carried out by Dr. Ikeda, AIST, Japan.

MTW. The chemical composition derived from the quantitative analysis indicate the sample consists of 82.35 wt% THK-2 and 17.65% MTW. The occupancy of Zn position was refined to 0.2806. The details of the crystallographic data of THK-2 is included in the supplementary data *Appendix C* in section Appendix.

Table 6.8: Selected results of Rietveld refinement of THK2.

Crystallographic data		Rietveld parameters	
Space group	*Pccn*	R_{exp} (%)	1.70
a (Å)	24.789(3)	R_p (%)	2.42
b (Å)	14.378(2)	R_{wp} (%)	3.26
c (Å)	5.035(1)	*gof*	1.92
$\alpha = \beta = \gamma$	90	B_{Si} (Å^2)	2.49(4)
Z	8	B_O (Å^2)	2.57(14)
V (Å^3)	1794.5(4)	B_{Zn} (Å^2)	5.069

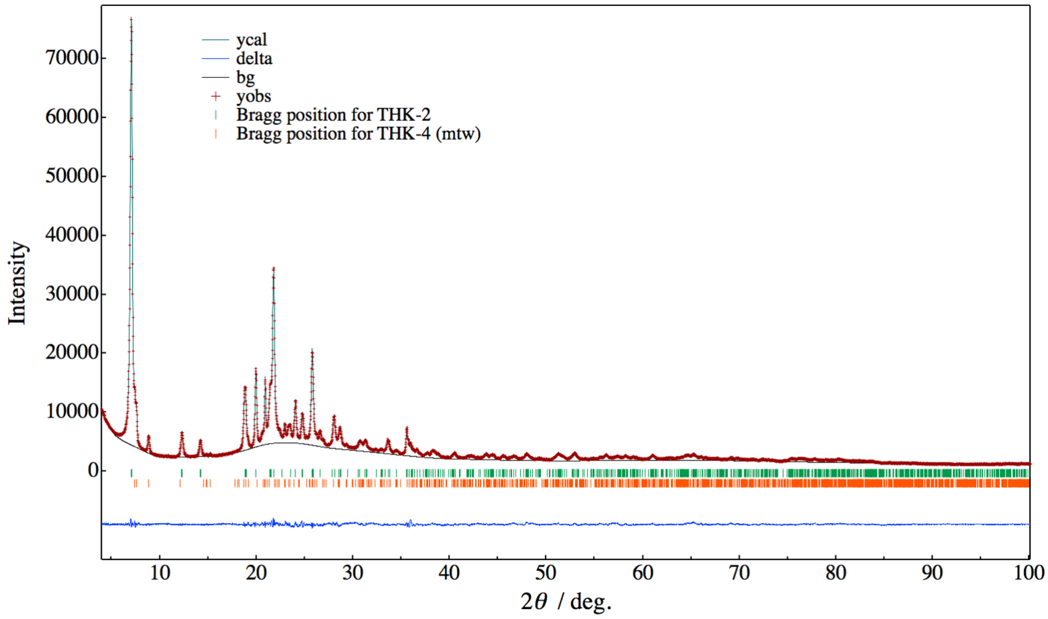

Figure 6.34: Plot of combined Rietveld refinement of THK-2 and MTW. Observed powder diagram (red plus), simulated powder diagram (green solid line), difference profile (blue solid line), and reflection positions (green vertical line for THK-2 and yellow vertical line for MTW). Adapted from ref. of Sakamoto et al.[236]

6.3.4 HRTEM imaging

High-resolution transmission electron microscopy (HRTEM) was conducted to study the real atomic arrangement in crystals and to confirm the correctness of the determined crystal structure. In this work, HRTEM images, viewed along [110] zone (Fig. 6.35) and [100] zone (Fig. 6.36), were acquired from two different crystals and show a perfect ordered structure without any stacking disorder.

Fig. 6.35a was gained from a nanorod with a diameter of about 240 Å. Several vertical parallel lines (or called as columns) can be clearly visualized. The distance between two neighbouring lines is about 12.38 Å , which is comparable with the calculated distance between (110) lattice planes (d_{110} = 12.44 Å). The structure model viewed along [110] zone axis in real space repeats the form of the collected high-resolution image, which confirms the solved structure. On the other hand, the information also indicates that the crystallographic ***a*** axis (smallest axis) runs parallel to the nanorod.

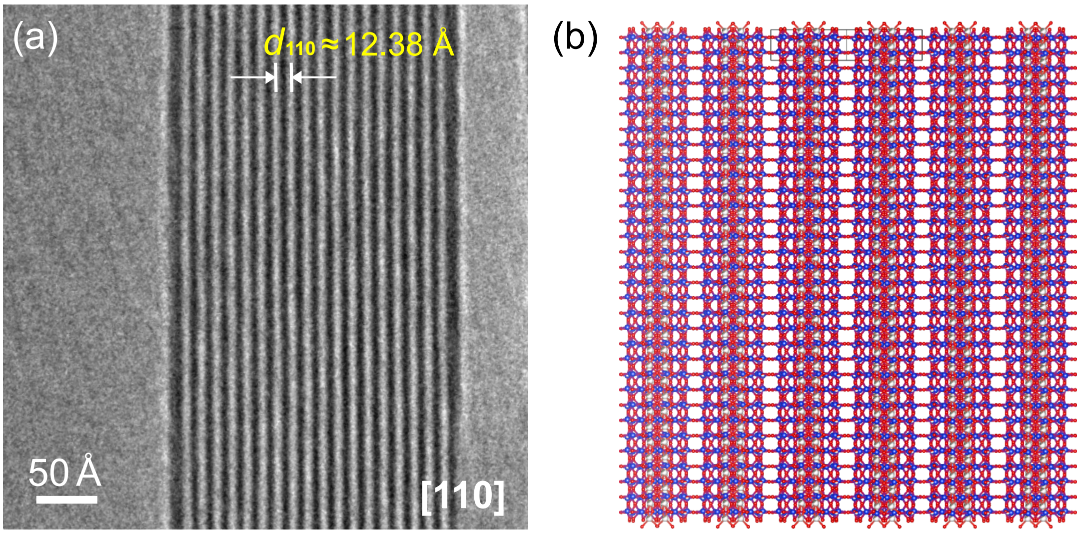

Figure 6.35: (a) HRTEM image of THK-2 recorded along the [110] zone axis. (b) THK2 structural model viewed along the [110] zone axis.

In addition, a HRTEM image shown in Fig. 6.36a, provided by Dr. Yasuhiro Sakamoto, is collected from a cross-section of nanorod, namely, perpendicular to the (*ab*) plane. The cut of nanorod shows a form of irregular hexagon. The fast Fourier transform (FFT) image (6.36b) is in consonance with the electron diffraction pattern simulated in the program `CrystalMaker`[237] (Fig. 6.36c). The enlarged image (Fig. 6.36d) is overlaid by the structure model viewed along the ***a*** axis. The real space structure shows a good agreement with the collected HRTEM data. In particular, the regular white circles indicate the 12-ring channels of THK-2 along the ***a*** axis. The small channels between the large circles can even be observed in Fig. 6.36d.

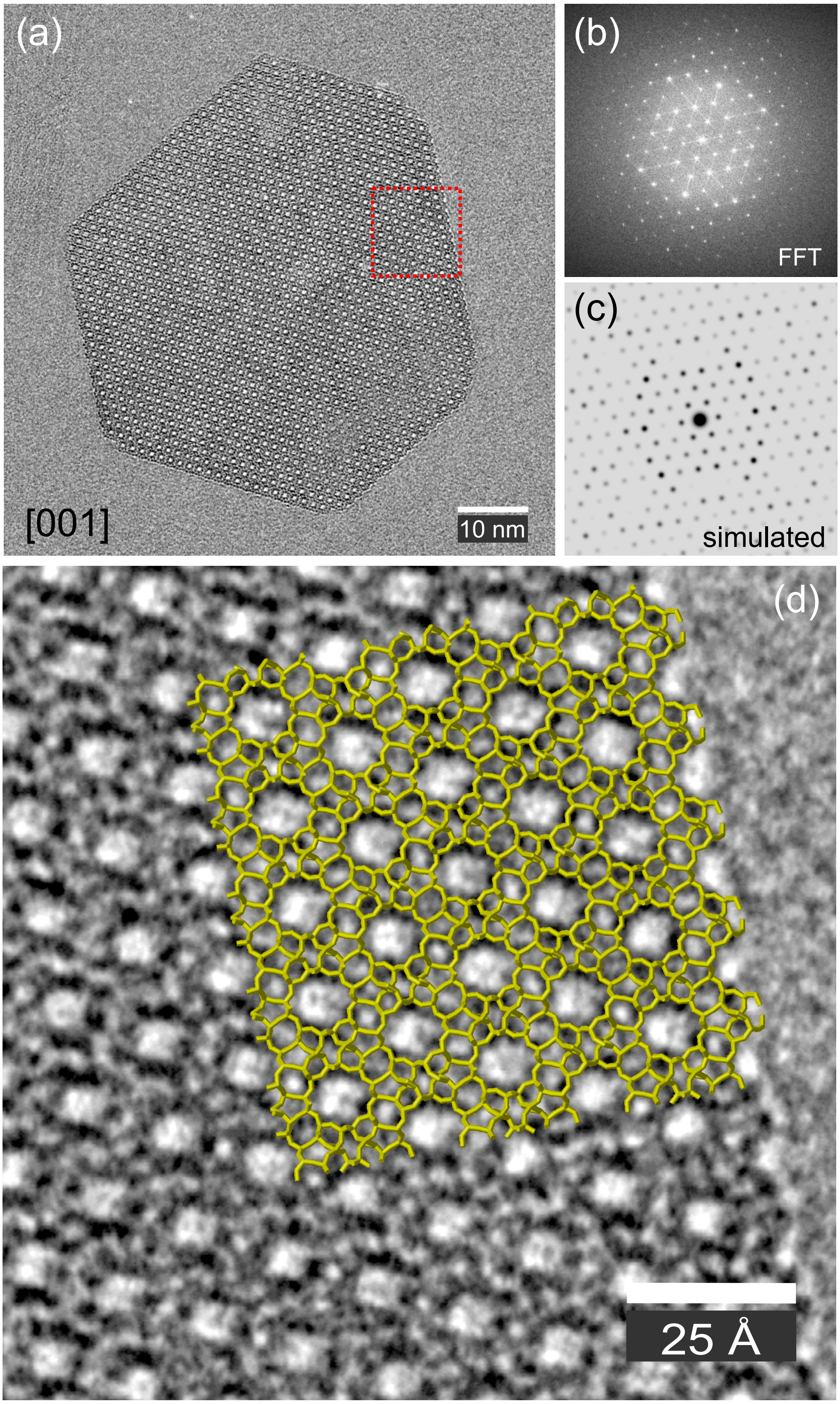

Figure 6.36: HRTEM image of THK2 recorded along the [001] zone axis. (a) Overview of the nanorod cross-section; (b) Squared modulus of the 2D Fourier transform (FFT); (c) Simulated electron diffraction pattern; (d) Enlarged phase image from the boxed area in (a) overaid with structure model of THK-2. The HRTEM was delivered by Dr. Yasuhiro Sakamoto.

6.3.5 Crystal structure description

The new porous zincosilicate THK-2 crystallizes in an orthorhombic crystal lattice. THK-2 has a framework density of 17.83 silicon atoms and 1.25 Zn per 1000 $Å^3$ and chemical formula of $[Si_{32}O_{72}Zn_{2.24}]$ in the calcined phase. It comprises two types of symmetry-independent T atoms in the structure model, namely four Si atoms and one partially occupied Zn atom. Each T atom coordinates with oxygen atoms to form TO_4 tetrahedral. Disordered edge-sharing ZnO_4 tetrahedra in the crystal structure construct a 1D infinite chains running along c axis (Fig. 6.37 and Fig. 6.38). All tetrahedra are collected to build up four-, five-, and six-membered rings (Fig. 6.38c), which are the backbone of the structure. Those rings are linked together leading to a three-dimensional framework with one-dimensional 12-ring channels running along [001]. Each 12-ring channel has six neighbouring 12-ring channels which do not intersect.

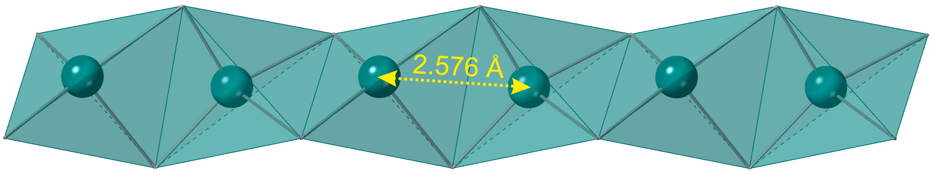

Figure 6.37: Structure segment of THK-2. 1D chain formed by edge-sharing ZnO_4 tetrahedra. The distance between two neighboring Zn atoms is marked.

T-O bond lengthes, concluded in Table 6.9, are in a reasonable range for Si-O and Zn-O distances.

Table 6.9: Selected bond lengthes (Å) in crystal structure of THK-2.

Si-O bond lengthes in SiO_4 tetrahedra							
Si1-O4	1.565(23)	Si2-O7	1.525(20)	Si3-O7	1.514(11)	Si4-O6	1.529(13)
Si1-O1	1.578(23)	Si2-O8	1.534(10)	Si3-O1	1.561(25)	Si4-O6	1.592(20)
Si1-O9	1.641(16)	Si2-O4	1.541(23)	Si3-O8	1.631(17)	Si4-O2	1.663(23)
Si1-O9	1.653(20)	Si2-O5	1.558(24)	Si3-O3	1.674(21)	Si4-O3	1.667(21)
Mean	1.609(20)		1.540(19)		1.595(18)		1.613(19)
Zn-O bond lengthes in ZnO_4 tetrahedron							
Zn1-O2	1.707(26)	Zn1-O5	1.892(21)	Zn1-O5	2.060(25)	Zn1-O2	2.089(16)
Mean	1.937(22)						

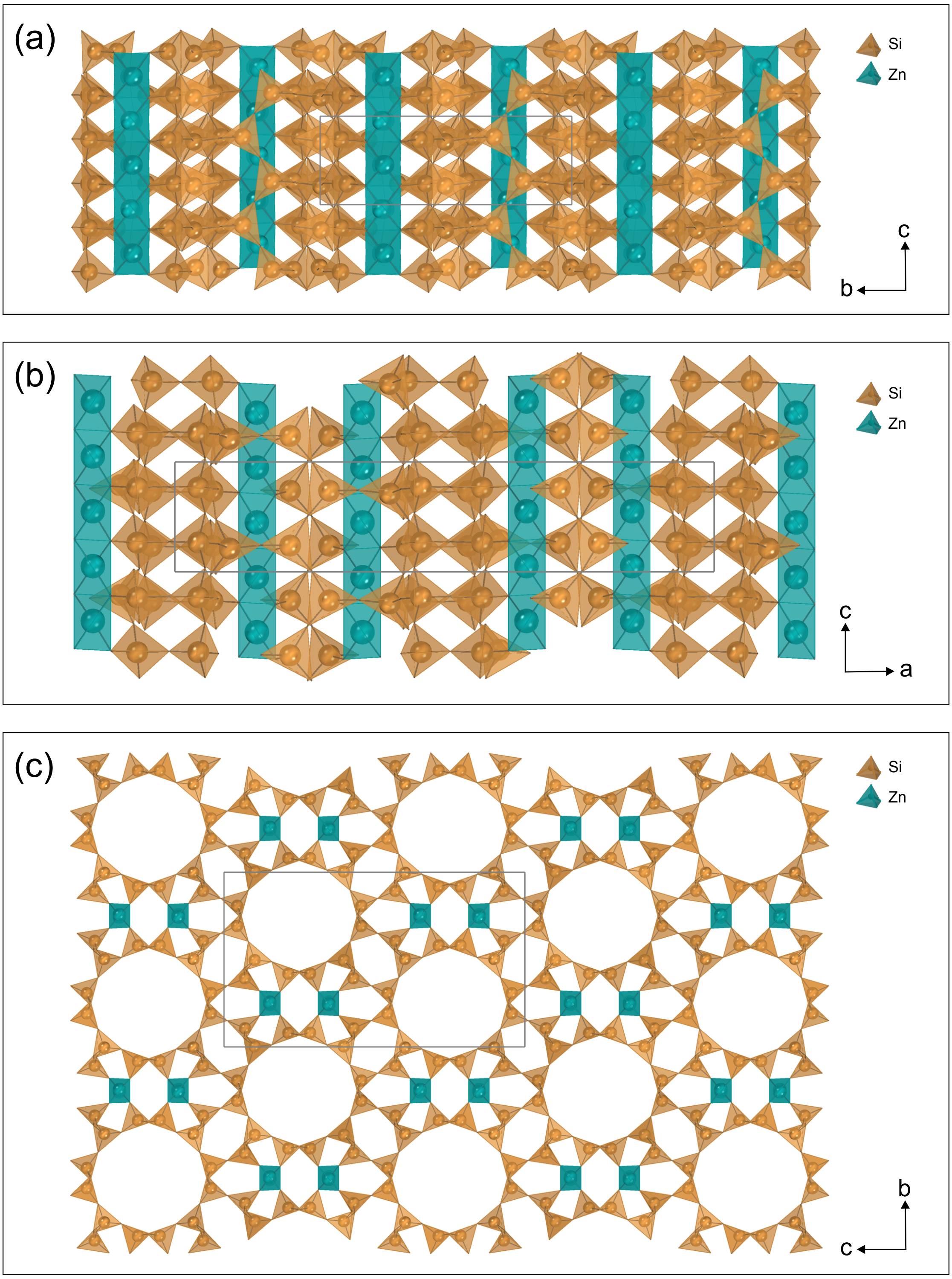

Figure 6.38: Crystal structure of THK-2 viewed along the three main crystallographic axes.

6.3.6 Summary

The crystal structure of a new zeolite was determined from a polyphasic sample using electron diffraction tomography technique. The structural characterization indicates that the zinc atom locates in the framework with an occupancy of 0.2806. Combined structure refinement with input of MTW structure delivered a chemical composition of 82.35 wt% THK-2 and 17.65% MTW in the mixture. HRTEM imaging confirmed the final crystal structure of THK-2.

6.4 Disorder in M-IEZ-RUB-36 zeolites

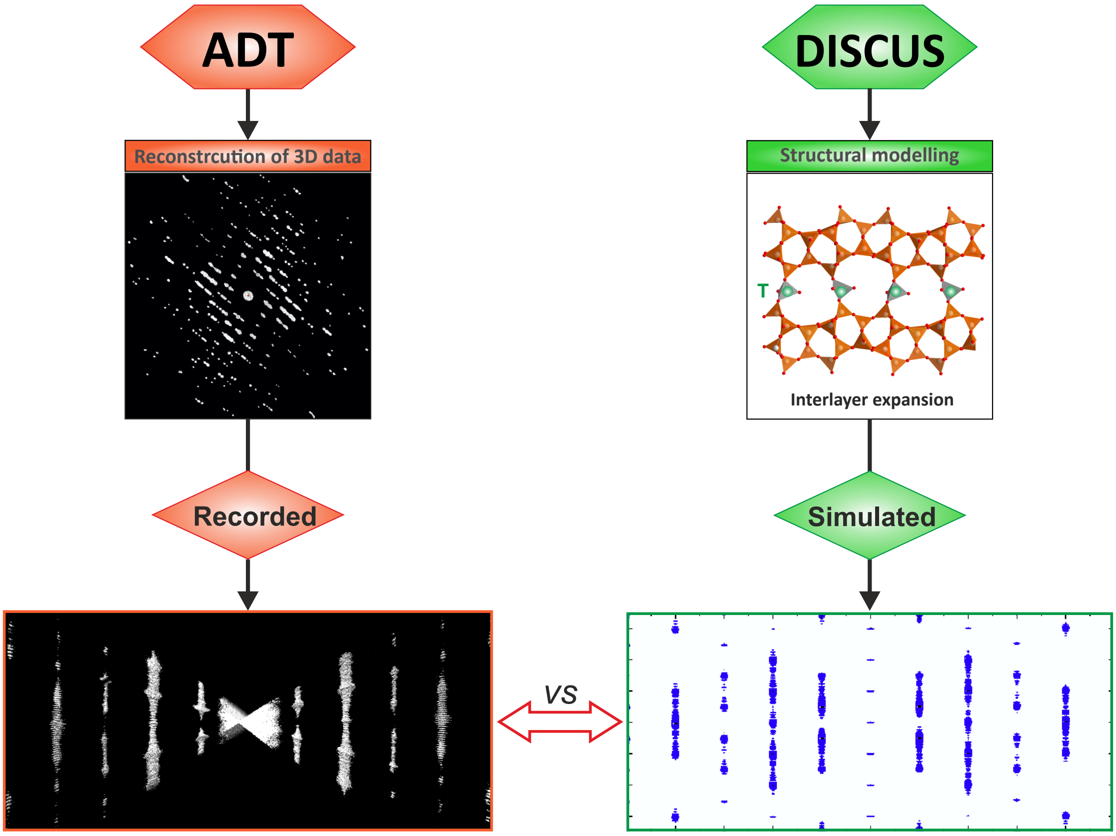

Stacking disorder in M-IEZ-RUB-36 elucidated by structure modelling and simulation of ED pattern

The structural characterization of metal interlayer expanded zeolites M-IEZ-RUB-36 was performed in collaboration with the work group of Prof. Dr. Hermann Gies from Ruhr-University Bochum, Germany. The presence of strong disorder in the structure could not be explained by one-dimensional XRPD data. My research on the materials focuses on detecting the disorder and confirming the disorder type on basis of reconstructed electron diffraction tomography data. In order to study the structural details, superstructure modelling and simulation of electron diffraction pattern in the program `DISCUS` were conducted for the porous M-IEZ-RUB-36 materials. The investigation of two types of materials, Zn-IEZ-RUB-36 and Ti-IEZ-RUB-36, were concluded in the dissertation. The results are in preparation for publishing. The experimental section is concluded in 5.4.

6.4.1 General information

Similar to RUB-36, M-IEZ-RUB-36 zeolites consist of thin plate-like crystals as shown in Fig. 6.39a-c. The presence of metal atoms in M-IEZ-RUB-36 was proved by EDX analysis, in which the signals of Zn and Ti were significantly visible in each EDX spectrum (Fig. 6.39d-e). Separate nano electron diffraction pattern and the sharp reflections in XRPD diagrams (Fig. 6.39f) reveal the good crystallinity of M-IEZ-RUB-36 zeolites. The crystals with the micrometer size are suitable for TEM experiments.

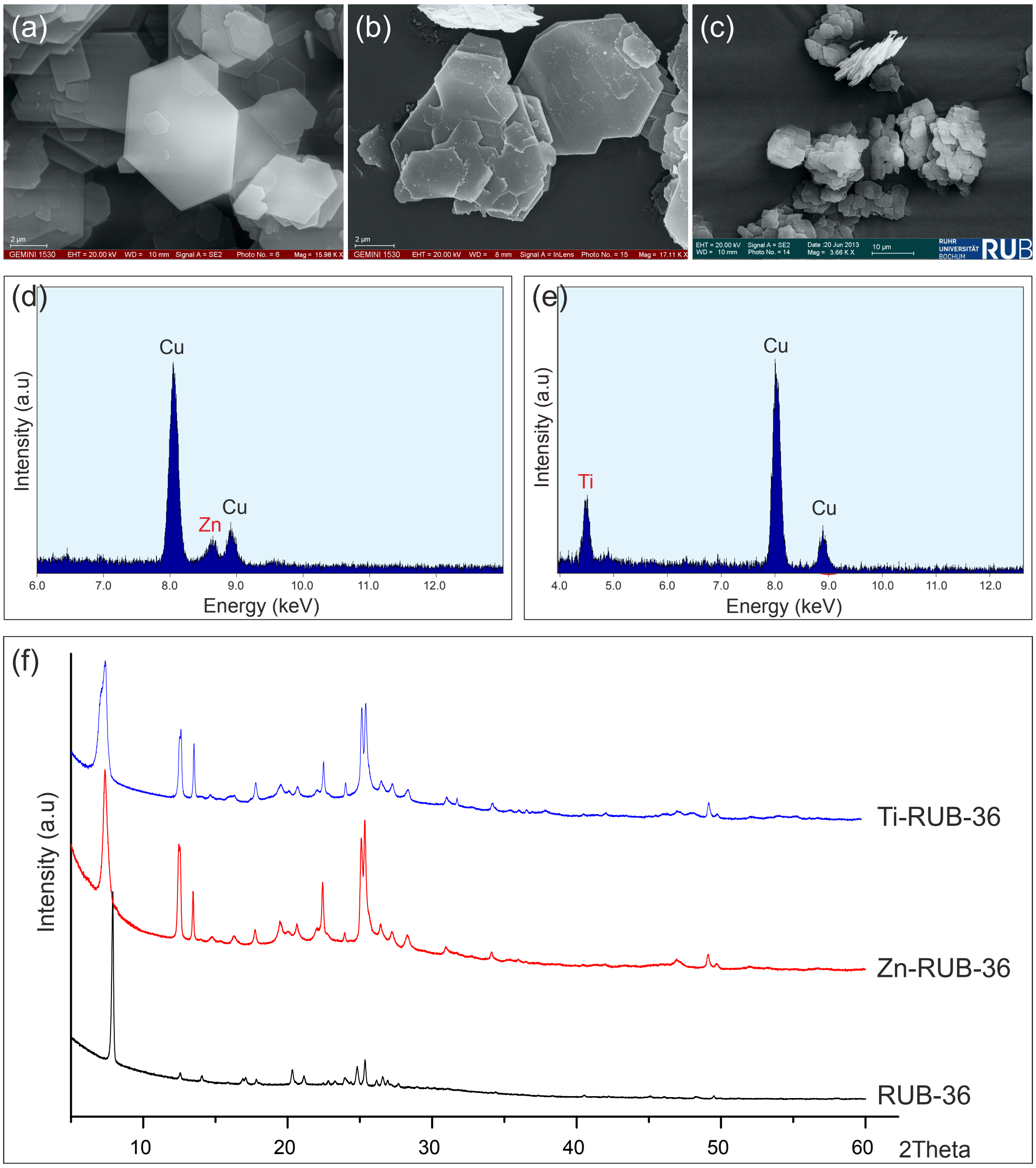

Figure 6.39: General information about Zn-IEZ-RUB-36 and Ti-IEZ-RUB-36. SEM images: (a) RUB-36, (b) Zn-IEZ-RUB-36 and (c) Ti-IEZ-RUB-36. EDX spectra: (d) Zn-IEZ-RUB-36 and (e) Ti-IEZ-RUB-36. The sigal of Cu was induced by Cu TEM grid. (f) XRPD diagrams of M-IEZ-RUB-36 (M = Zn,Ti). Cu $K\alpha1$ radiation.

6.4.2 Interlayer expansion

We can observe several XRPD peaks with a large full width at half maximum (FWHM). Due to the known micrometer crystal size, the appearance of broad XRPD peaks is not caused by a non-scaled particle size but the disordered structure[238]. The first peak in each diagram (Fig. 6.39f) has a lower θ value (larger d value) in comparison to that of the zeolite precursor as-made RUB-36[216], showing an enlarged interlayer distance. This change in XRPD diagrams confirms that an interlayer expansion reaction happened. There is no reflection of a metal oxide, indicating a pure phase of products. Fig. 6.40 demonstrates the interlayer expansion of as as-made RUB-36 with corresponding T atoms (T = Si or metal) to form M-IEZ-RUB-36 materials. If the T-sites are occupied by Si atoms, the interlayer expanded zeolites are called COE-3 or COE-4.[51,239]. M-IEZ-RUB-36 zeolites can be produced if the Si-linked positions between the layers are replaced by tetravalent heteroatoms. The heteroatoms are e. g. Ti, Al, Fe, Sn, Zr in previous works[214,215,240,241] or Zn, Ti, Eu, V, Co in our present study. The difficulties of incorporation of heteroatoms depend on the type of metal atom type, which was confirmed by Li et al.[240] using DFT calculation investigations. Several factors like the type of metal atoms, variability of layer shift and stacking sequence can lead to a disordered crystal structure in the process of layer expansion.

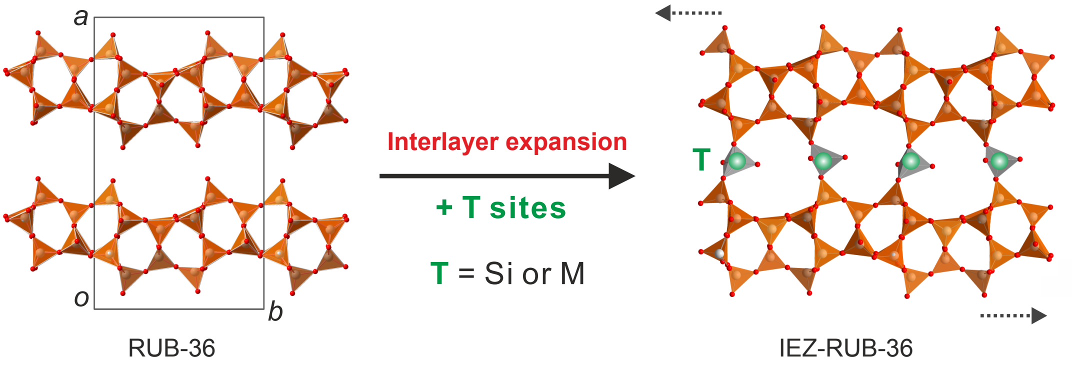

Figure 6.40: Schematic representation of the interlayer expansion of RUB-36 into a M-IEZ-RUB-36. Note that the organic molecule between the layer in RUB-36 was omitted for clarity.

6.4.3 ADT data evaluation

The ADT approach was applied to collected 3D electron diffraction data from single crystals. Strong rod-like diffuse scattering can be observed running along the ***a***** axis in the reconstructed 3D reciprocal space as exemplarily shown for Ti-IEZ-RUB-36 in Fig. 6.41. The streaks can be found in each ADT dataset, indicating that disorder occurs in all crystals. Taking into account only the strong intensities as shown in Fig. 6.42, we could index the ADT data with averaged orthorhombic lattices and identify the type of lattice system. If the diffuse streaks are ignored, the reflection conditions are concluded as following, $h + k + l = 2n$ for all hkl and no additional extinction in Zn-IEZ-RUB-36; $h + l = 2n$ for all hkl and h

+ l = 2*n* for *h*0*l* plane in Ti-IEZ-RUB-36, which led to the extinction symbols *I* - - - and *Bb* - -, respectively. M-IEZ-RUB-36 (M = Co, V) zeolites showed as well orthorhombic lattice parameters and lead also to extinctions of a *B*-centred lattice. The refined averaged cell parameters from Pawley fit against XRPD data are listed in Table 6.10.

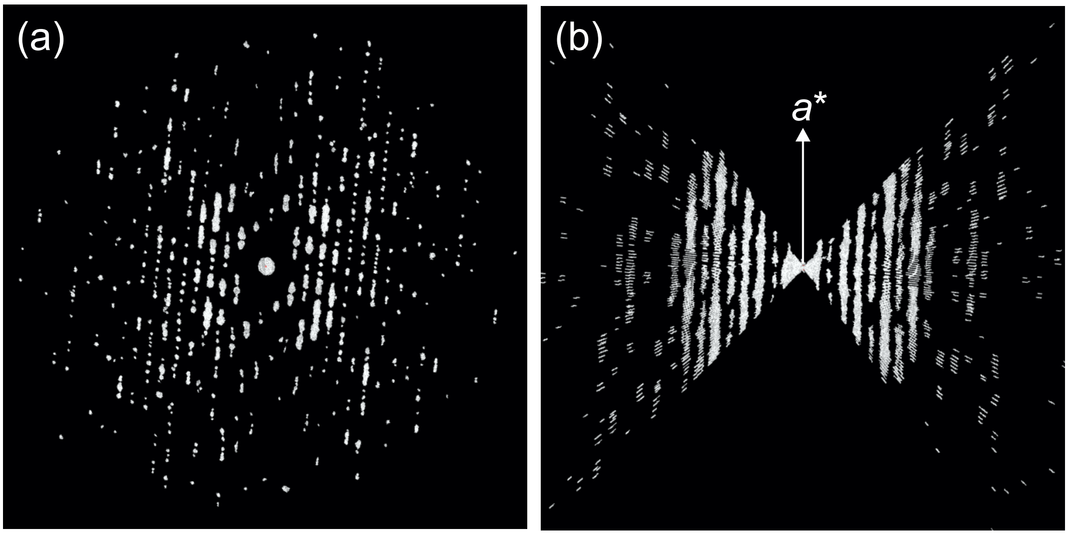

Figure 6.41: Overview of 3D projections of the reconstructed reciprocal space of Ti-IEZ-RUB-36. (a) View along an arbitrary direction. (b) View along the tilt axis, showing 100° angular range. The running direction of diffuse streaks is along the ***a**** axis as marked in (b).

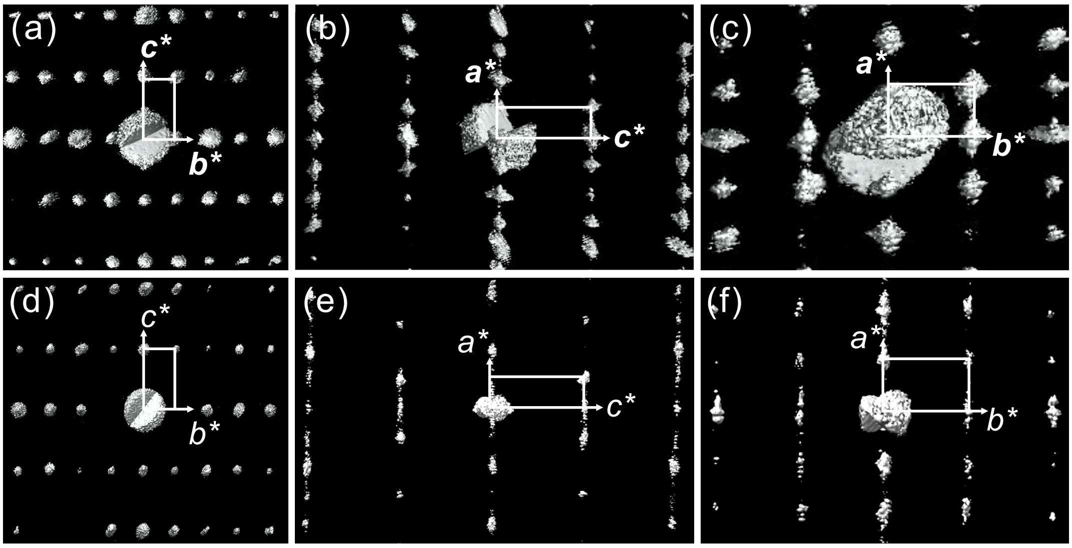

Figure 6.42: 3D projections of the reconstructed reciprocal space viewed along the three main axis. (a-c) for Zn-RUB-36 and (d-f) for Ti-RUB-36. Noted that a high threshold of intensity was set in the 3D volume calculation in order to only show the strong intensities of reflections.

Table 6.10: Average orthorhombic lattice parameters of M-IEZ-RUB-36 refined by pofil fit from XRPD data.

Material	RUB-36	M = Zn	M = Ti	M = Co	M = V
a (Å)	22.239(1)	23.894(3)	24.100(1)	23.870(3)	23.837(5)
b (Å)	14.025(1)	14.092(4)	14.012(2)	14.056(4)	14.071(2)
c (Å)	7.391(1)	7.431(1)	7.400(1)	7.422(3)	7.397(5)
System*	*P*	*I*	*B*	*B*	*B*

*Only strong intensities taken into consideration.

6.4.4 Structure solution for the average structures

As mentioned above, ADT data could be indexed to a body-centred orthorhombic lattice for Zn-IEZ-RUB-36 and a face-centred lattice for Ti-IEZ-RUB-36, only using reflections with strong intensities. We tried to solve the average crystal structures using the intensities extracted from ADT data. As shown in Fig. 6.43, the average frameworks of Zn-IEZ-RUB-36 and Ti-IEZ-RUB-36 could be described using ADT data in the space groups *Immm* and *Bbmm*, respectively. Due to the low amount of metal atoms detected in the sample, we set all the T-sites as Si atoms in the structure solution. The bridging atoms (Zn, Ti, Si) between the layer can be recognized. The structures illustrate different ring channels and the arrangement of those channels. In addition, we tried to use the average structure as initial model for the structure refinement with Rietveld method from XRPD data. But the final results were not satisfying due to the neglect of disorder in the structure. Hence, this structure can only be used as the average structure to describe the main atomic arrangement.

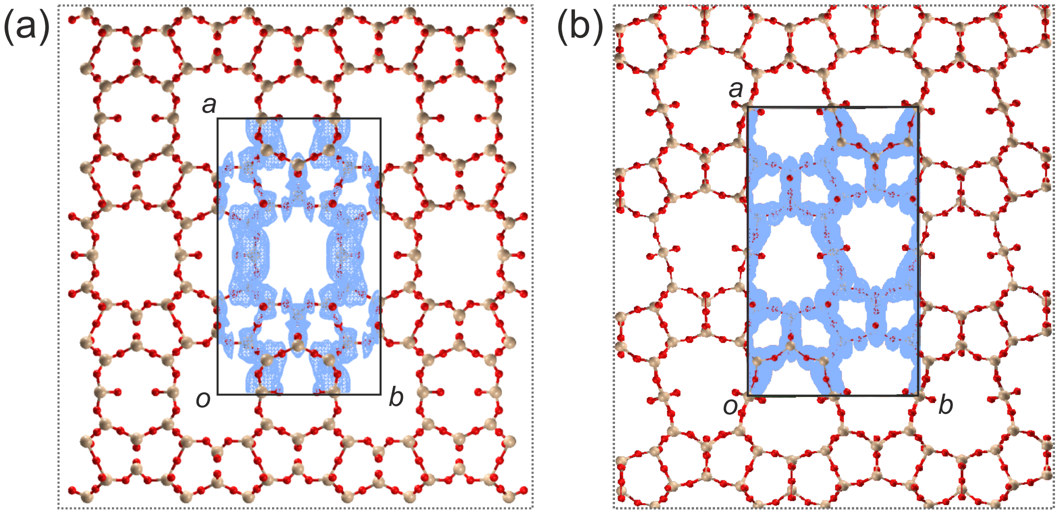

Figure 6.43: Electron potential map of structure solution overlaid with the atomic model of M-IEZ-RUB-36, viewed along the [001] zone. (a) Zn-IEZ-RUB-36 in the space group *Immm*. (b) Ti-IEZ-RUB-36 in the space group *Bbmm*. Potential map: blue, Si: light yellow, O: red.

6.4.5 Disorder analysis and simulation

In order to get much more structural details about M-IEZ-RUB-36, the general process as shown in Fig. 6.44 was taken into consideration to elucidate the disorder, similar to the disorder simulation for the ceramic material $Al_4B_2O_9$ described in section 5.1.5. Firstly, a superstructure was modelled in the software package `DISCUS` with a possible disorder type (here the stacking disorder). Then the electron diffraction pattern was simulated after a Fourier transform based on the superstructure. By comparison of recorded and simulated diffraction patterns, it can be quantitatively confirmed how near our modelled structure is to the real structure. Noted that the three important factors for the simulation of electron diffraction pattern are the type of layers, the translation vectors from one layer to another, and the probability of stacking from one layer onto the other layer.[120] The factors result in different stacking sequences and further produce the electron diffraction patterns with streaks.

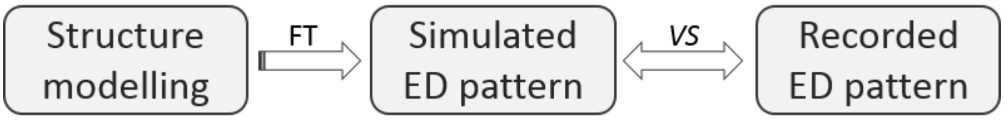

Figure 6.44: Scheme for the process of disorder analysis.

As illustrated in Fig. 6.41 and 6.42, the observed diffuse streaks run only along ***a****** direction. After examination of the reconstructed 3D reciprocal space, it could be pointed out that they are indeed one-dimensional streaks. Associated with the synthesis of interlayer expansion, it can be confirmed that the one-dimensional diffuse streaks in the reciprocal space are caused by an irregular stacking sequence of layers along the ***a*** axis in real space. One layer stacks partially on the other with a shift within *bc*-plane based on an interlayer connection along the ***a*** axis. The structure modelling was performed on the basis of the evaluation results of recorded electron diffraction. As the structure of M-IEZ-RUB-36 is stacked by layers, the framework is constructed by a convolution product of all atoms within a single layer type with the list of the layer positions. Similar to the disorder simulations of $Al_4B_2O_9$[30] and zeolite beta[73], the individual Fourier transformation was first calculated just based on the atom positions within a single layer and the simulated diffraction pattern is the regular product of the individual Fourier transformations. The method reduces the simulation time in comparison to the calculation for the all atoms of a whole crystal.

The crystal structure of RUB-36 consists of two separate layers parallel to the (*bc*)-plane. The two layers, distinguished only by a shift in (*bc*) plane, are the basic units for interlayer expansion to construct three-dimensional frameworks. The modelling of superstructure starts with one layer of RUB-36 (layer *A*). Layer *B* is created by a shift of layer *A* with the vector [0, 1/2, 1/2], as shown in the top of Fig. 6.45. The layers stack along the crystallographic ***a*** axis to built up a superstructure. A perfect stacking sequence with *AAA*••• (or *BBB*•••) leads to a face-centred lattice. However, the perfect sequence of

ABABAB••• produces a body-centred lattice (Fig. 6.45). Taken consideration of the average structure solutions in different crystal lattices, it indicates that the type of stacking sequence *ABABAB*••• is dominant in Zn-IEZ-RUB-36 and the sequence of *AAA*••• occurs much often in Ti-IEZ-RUB-36.

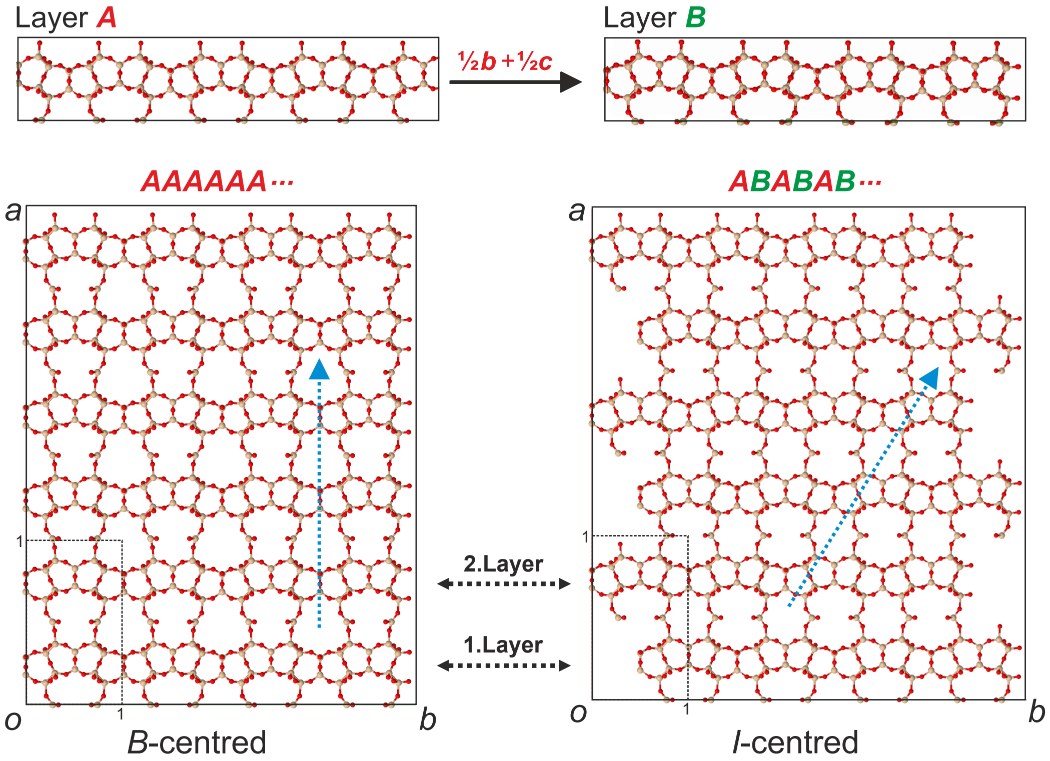

Figure 6.45: Superstructure modelling with ordered stack sequences. Top: basic structure components: layer *A* and layer *B*. Bottom: 3*x* x 4*y* x 1*z* supercells with 6 layers with stacking sequence *AAA*••• and *ABABAB*•••. The 10-ring in face-centered cell (bottom left) and 8-ring body-centered cell (bottom right) were traced by blue dotted lines. The unit cells are marked with black dotted lines.

The simulation of ED patterns were performed from the modelled superstructures. In the final total sequence, one layer type can be followed by one of the possible layers or by itself. This possibility occurs only with a transition vector which enables a reasonable layer connection. Here, the transition probability of layer *A* stacking onto layer *A* is referred to as p, which indicates that the probability for stacking of *B* on *A* = 1 - p. As the sequence of *AAA*••• is same with *BBB*•••, the probability of layer *B* onto layer *B* is p and *A* on *B* = 1 - p. If $p = 1$, a perfect *AAA*••• or *BBB*••• sequence will be produced to form a face-centred unit cell. $p = 0$ leads to a perfect *ABABAB*••• sequence with a body-centred lattice. The values between 0 and 1 result in the random sequence of both layers, a disordered structure. Fig. 6.46 shows the simulated electron diffraction patterns of [001] zone from a 10x x 15y x 4z supercell (20 layers) with different p values. The simulated diffraction patterns with $p = 0$ and 1 show only discrete peaks without any diffuse streaks. With an increasing p value, the streaks emerge at first with $p = 0.05$ and then become slowly stronger, at last disappear at $p = 0.98$. However, the crystal system changes from a pure body-centred lattice ($p = 0$) to the final face-centered lattice with $p = 1$. It is notable that symmetry conditions $h + k = 2n$ in Fig. 6.46a as well as $h = 2n$ and $k = 2n$ in Fig. 6.46j fulfil the extinctions in the [001] zones in body-centred and face-centred lattices, respectively. The intermediate p values produce a disordered structure with random stacking sequences, associated with observed diffuse streaks in the simulated diffraction patterns (Fig. 6.46c-h).

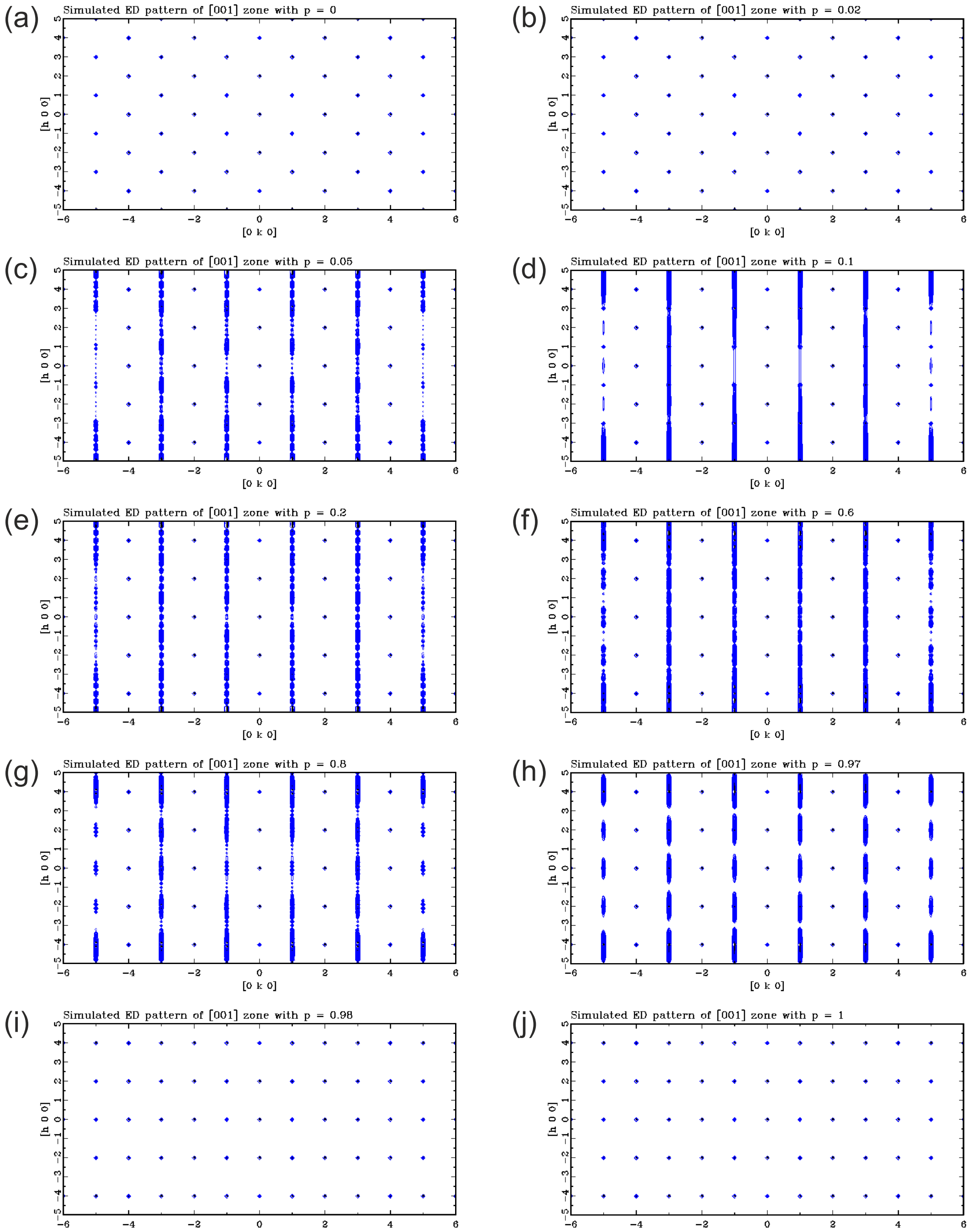

Figure 6.46: Simulated electron diffraction patterns of [010] zone from a 10x x 15y x 4z superstructure with different probability p values. (a) $p = 0$; (b) $p = 0.02$; (c) $p = 0.05$; (d) $p = 0.1$; (e) $p = 0.2$; (f) $p = 0.6$; (g) $p = 0.8$; (h) $p = 0.97$; (i) $p = 0.98$; (j) $p = 1$.

As shown in Fig. 6.46, the stacking sequence from two layer types produced diffused reflections only with k odd in the [001] zone. This phenomenon was resulted by the shift vector along $\boldsymbol{b}$ axis with 1/2b from layer A to layer B. However, the diffuse streaks can also be found for the $hk0$ Bragg reflections with k even in the recorded diffraction patterns. It indicates that a third layer type must be introduced and the vector shifts are not equal to the half of the axis. In addition, significant rod-like Bragg reflections could be discovered along $\boldsymbol{a}^*$ in the [010] zone. Taken into account the inserted metal atoms and the bond lengths $d_{M-O} > d_{Si-O}$, a new layer type C was modelled from layer A with a shift vector [0, Δy, Δz]. Since the distance of M-O is different to that of Si-O, the (bc)-plane of layer C does not shift the half axis values along b and $\boldsymbol{a}$ axis, $\Delta y \neq 1/2$ and $\Delta z \neq 1/2$, but close to 1/2. Superstructures were constructed by the three layer types. Fig. 6.47 presents the possible stacking on layer A to produce different types of crystal lattices as well as an example of a supercell with a random stacking sequence. In the structure modelling, the superstructure of M-IEZ-RUB-36 material is established layer by layer using the three layer types: A, B and C. There are totally 9 possibilities to stack one layer to another with possible translation vectors (Table 6.11). The probability depends on the type of crystal lattice of the materials which provides the most emerged sequence. The other factor is the amount of the layer C.

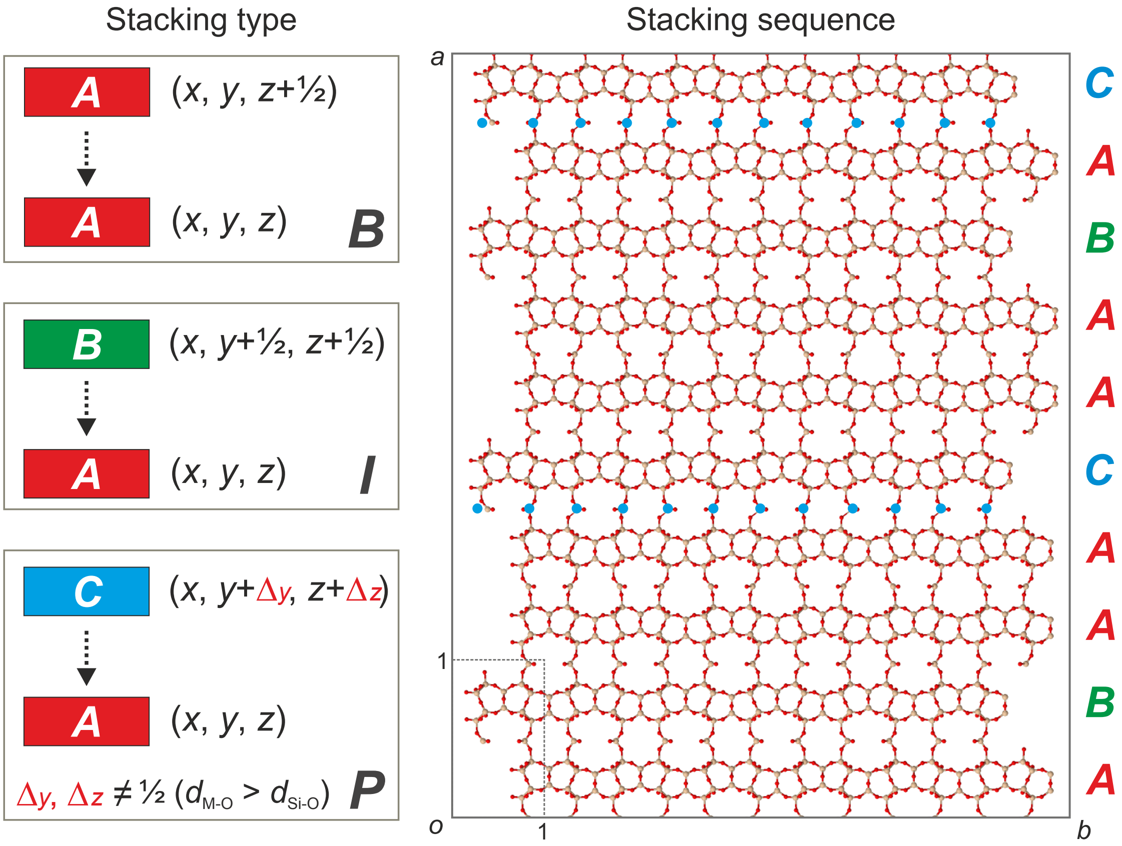

Figure 6.47: Left: Possible stacking on layer *A* with corresponding changes of translation vectors. Right: an example of 5*x* x 6*y* x 1*z* with 10 randomly stacked layers.

Table 6.11: Element operation and corresponding shift vector between the layers.

Layer stacked onto A		Layer stacked onto B		Layer stacked onto C	
Element	Vector	Element	Vector	Element	Vector
$A \rightarrow A$	[1/2, 0, 1/2]	$A \rightarrow B$	[1/2, -1/2, -1/2]	$A \rightarrow C$	[1/2, -1/2, -1/2]
$B \rightarrow A$	[1/2, 1/2, 1/2]	$B \rightarrow B$	[1/2, 0, -1/2]	$B \rightarrow C$	[1/2, -1/2, -1/2]
$C \rightarrow A$	[1/2, Δy, Δz]	$C \rightarrow B$	[1/2, Δy, Δz]	$C \rightarrow C$	[1/2, 0, Δz]

Here we simulated the electron diffraction patterns for Zn-IEZ-RUB-36 and Ti-IEZ-RUB-36 with $\Delta y = \Delta z = 0.45$. We set a special stacking sequence in the light of the stacking in the average structure. As aforementioned, stacking sequence *AAA*••• prefers to occur in Zn-IEZ-RUB-36, thus we set a higher probability of *AA* type than *AB* type in the input for stacking sequence. On the contrast, the probability of *AB* type should be higher than *AA* type in Ti-IEZ-RUB-36, in which the sequence of *ABAB*••• is favoured. In addition, the amount of layer *C* was adjusted less than 10% due to the small amount of metal atoms. The simulated electron diffraction patterns in the [001] and [010] zones show good agreement with the recorded data (Fig. 6.48 and Fig. 6.49) The observed diffuse scattering in Ti-IEZ-RUB-36 is stronger that in Zn-IEZ-RUB-36 (Fig. 6.48b and 6.48d and Fig. 6.49)b and 6.48d, indicating that the stacking with *AA* sequence type is easier to result in disordered stacking. The diffuse streaks occur dominantly through the Bragg reflections *hk0* with k even *h0l* with l even in the slices cut from 3D reconstructions for Zn-IEZ-RUB-36. In contrast, diffuse rods run along all *hk0* and *h0l* Bragg reflections. This might be attributed to a greater percentage of layer *C* in Ti-IEZ-RUB-36, indicating a higher incorporation of Ti atoms in comparison to Zn atoms.

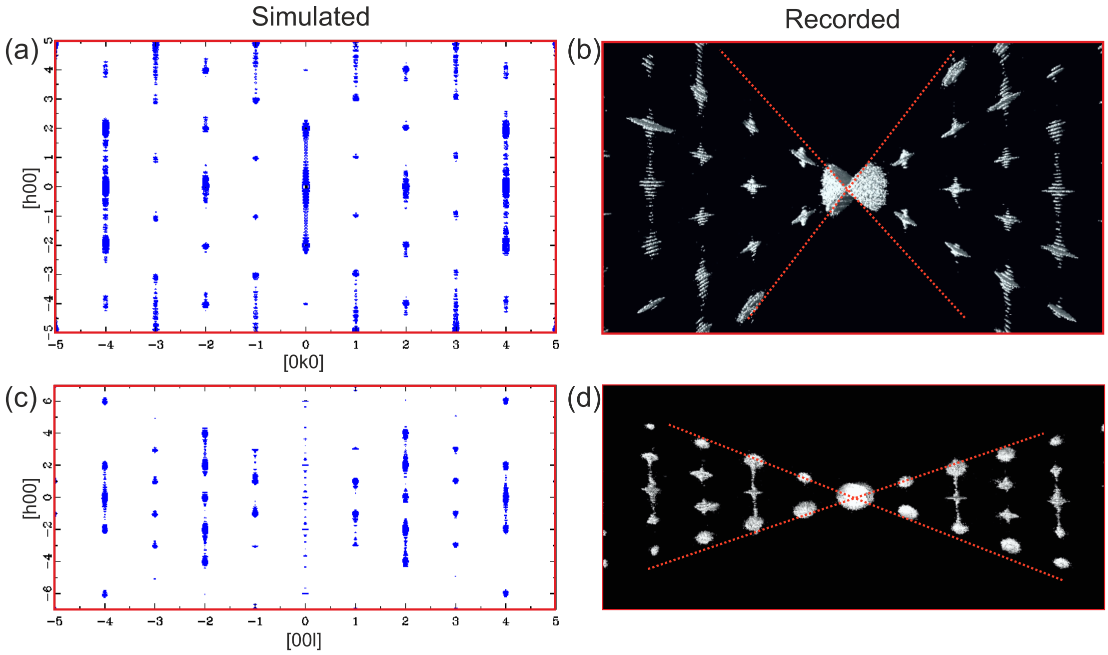

Figure 6.48: Simulated and recorded electron diffraction patterns of Zn-IEZ-RUB-36. Simulation of the (a) [001] and (c) [010] zones. Slice cut from reconstructed reciprocal space through the (b) [001] and (d) [010] zones. The section of recorded reciprocal space is marked with red dotted lines in (b) and (d).

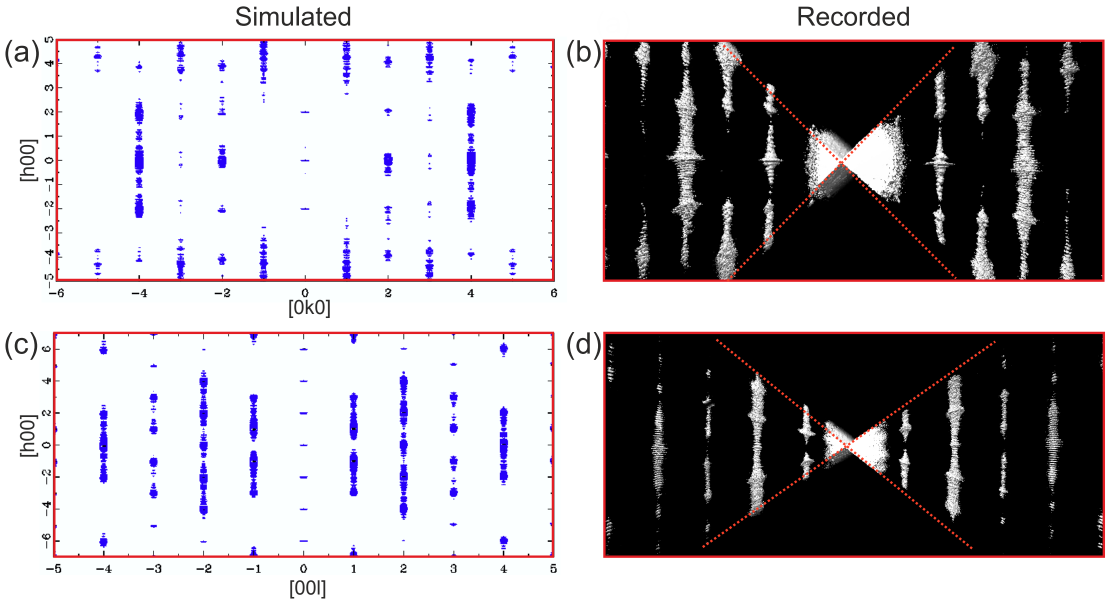

Figure 6.49: Simulated and recorded electron diffraction patterns of Ti-IEZ-RUB-36. Simulation of the (a) [001] and (c) [010] zones. Slice cut from reconstructed reciprocal space through the (b) [001] and (d) [010] zones. The section of recorded reciprocal space is marked with red dotted lines in (b) and (d).

6.4.6 Summary

The disorder in M-IEZ-RUB-36 zeolite catalysts was determined as stacking disorder. The average crystal structures of Zn-IEZ-RUB-36 and Ti-IEZ-RUB-36 were performed from ADT data. Superstructure modelling was carried out with various sequences in the program `DISCUS`. It confirmed that layer shift, stacking sequence and metal atoms showed the influence on disorder at the interlayer expansion reactions of M-IEZ-RUB-36 zeolites.

6.5 Organic template in SSZ-51 and SOD zeolite

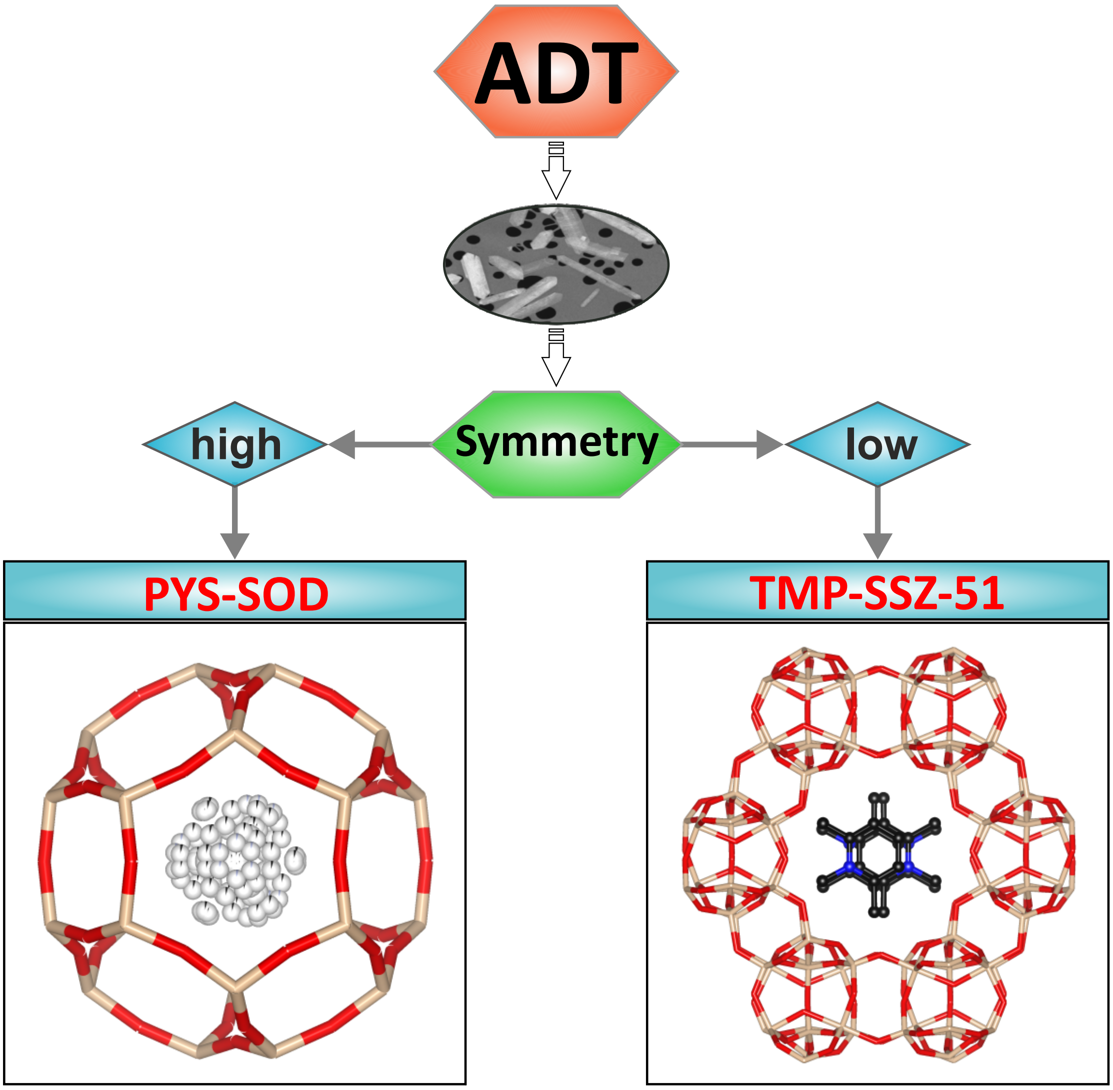

Location of organic templates in zeolites determined by electron diffraction tomography

In the project, we focused on determining the positions of organic structure directing agents in two as-synthesized zeolites, 1,2,6-trimethylpridinium aluminophosphate (TMP-SSZ-51) and pyrrolidine silica sodalite (PYS-SOD), using fast ADT technique. TMP-SSZ-51 was prepared with a novel organic template 1,2,6-trimethylpridinium. TMP-SSZ-51 was investigated by thermogravimetric analysis, temperature-dependent XRPD, and Solid-state ^{13}C-NMR spectroscopy. The positions of organic molecule were determined from combined method of electron diffraction tomography and X-ray powder diffraction. The experimental details are summarized in section 5.5. The results on the part of TMP-SSZ-51 are partly reprinted from the submitted script entitled "Detection of organic cations in the pores of aluminophosphate SSZ-51 by electron diffraction tomography – elucidating the effect of molecular stacking ".

6.5.1 Sample overview of TMP-SSZ-51

TMP-SSZ-51 consists of thin plate-like micro-sized crystals observed in STEM image (Fig. 6.50a). The crystals are suitable for ADT data acquisition under cooling conditions using low beam illumination in TEM. Strong and discrete diffracted spots were observed in electron diffraction patterns and its calcined phase, indicating high crystallinities of as-synthesized and calcined phases, which were also confirmed by the XRPD data (Fig. 5.5 in experimental section). A semi-quantitative EDX analysis (Fig. 6.50b) show averaged ratios of O/(Al+P) = 2.1 and Al/P = 1.

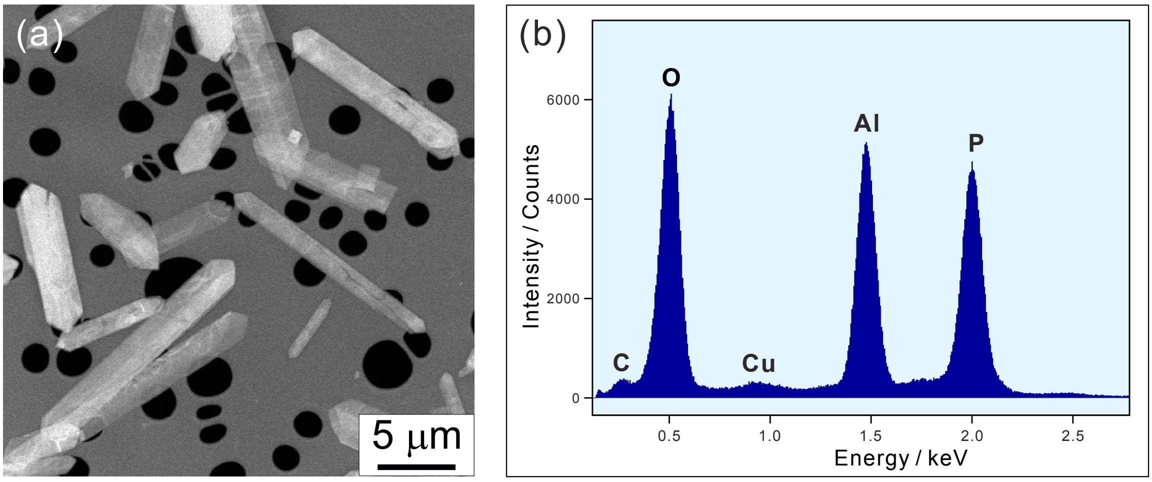

Figure 6.50: STEM image (a) and EDX spectrum (b) of TMP-SSZ-51. Cu TEM grid covered by carbon-film contributes the slight signals of C and Cu in (b).

Table 6.12: Quantitative EDX results taken from different single crystals.

Dataset	Al (%)	P (%)	O(%)	Al/P	O/(Al+P)
Nr.1 (%)	15.77	14.75	69.48	1.07	**2.28**
Nr.2 (%)	16.63	15.53	67.84	1.07	**2.11**
Nr.3 (%)	16.72	14.78	68.50	1.13	**2.17**
Nr.4 (%)	18.34	16.59	65.07	1.11	**1.86**
Mean	16.87	15.41	67.72	1.09	**2.11**

6.5.2 Solid-state ^{13}C-NMR

Solid-state ^{13}C-NMR measurements were performed to detect the presence of the organic template which was part of the reaction mixture in the as-synthesized zeolites. Fig. 6.51 shows the solid-state ^{13}C-NMR spectrum of as TMP-SSZ-51. The ^{13}C-NMR spectrum of TMP-SSZ-51 presents five signals with chemical shifts of 157.5, 144.8, 126.8, 40.5 and 23.2 ppm, which are comparable with the corresponding values of the free template cation in solution in the literature[242]. The pyrrolidine molecules are still stable inside the SOD cages though the sample was prepared eighteen years ago, which was confirmed by the comparable values of chemical shift of the previous measured value of as-synthesized PYS-SOD[229] and and those of the free pyrrolidine molecule[243].

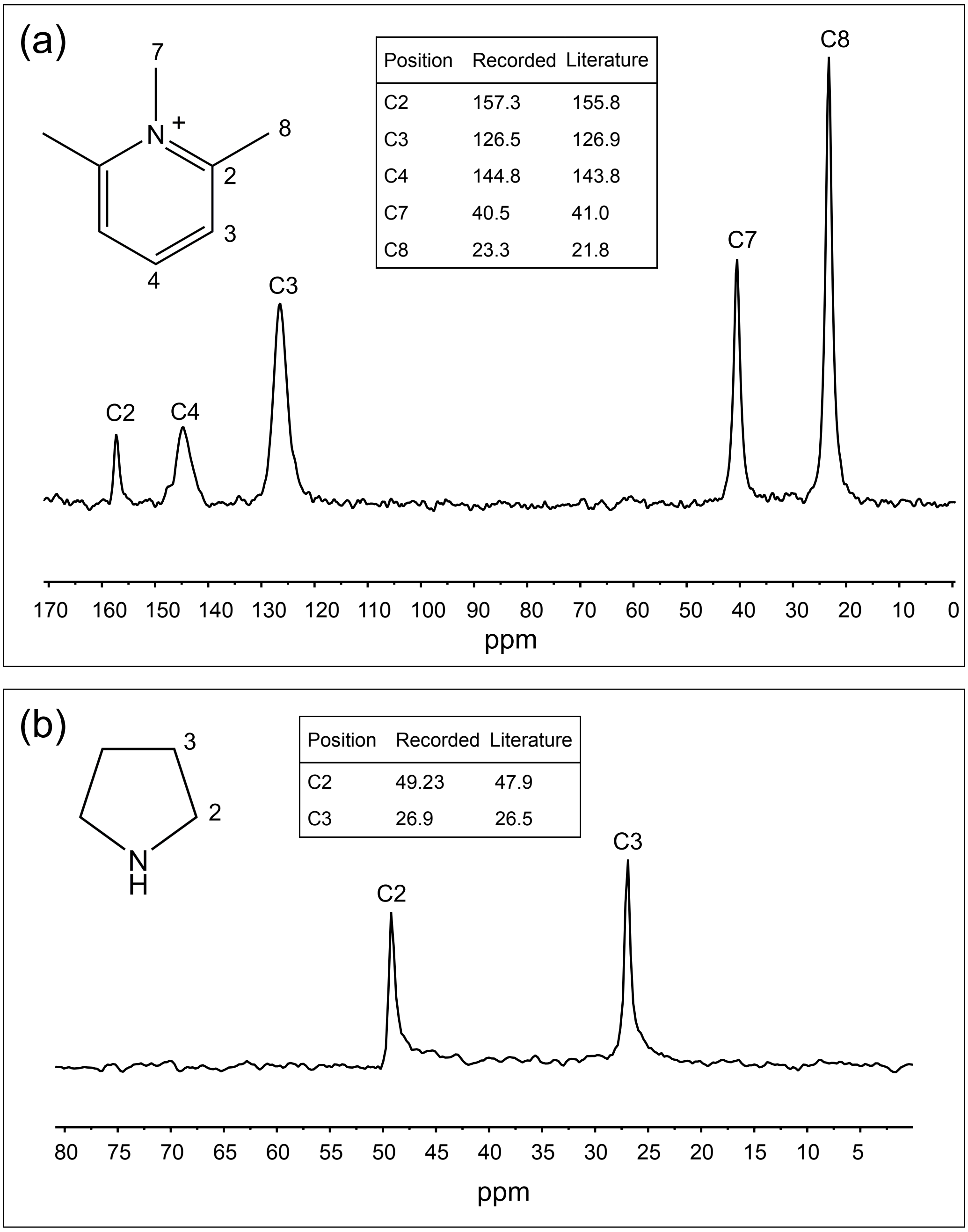

Position	Recorded	Literature
C2	157.3	155.8
C3	126.5	126.9
C4	144.8	143.8
C7	40.5	41.0
C8	23.3	21.8

Position	Recorded	Literature
C2	49.23	47.9
C3	26.9	26.5

Figure 6.51: ^{13}C-CP/MAS NMR spectra of TMP-SSZ-51 (a) and PYS-SOD (b). Inserted tables show the recorded chemical shifts of organic SDA in zeolites and the values of free molecules in the literature.

6.5.3 Thermal stability of TMP-SSZ-51

The thermal behaviour of TMP-SSZ-51 was studied by differential scanning calorimetry and thermogravimetric analysis (DSC/TGA). The TG curve (Fig. 6.52) shows two steps of weight loss. The first step up to 100 °C is associated with the evaporation of free water molecules from the zeolite pores. The second step of loss weight was caused by the decomposition of the organic template, corresponding to the exothermic signals in the DSC curve. The exothermic signal is assigned to the burn off of template molecules at ca. 440 °C. At about 720 °C the framework of SSZ-51 begins to decompose, which could also be detected by high-temperature XRPD measurements.

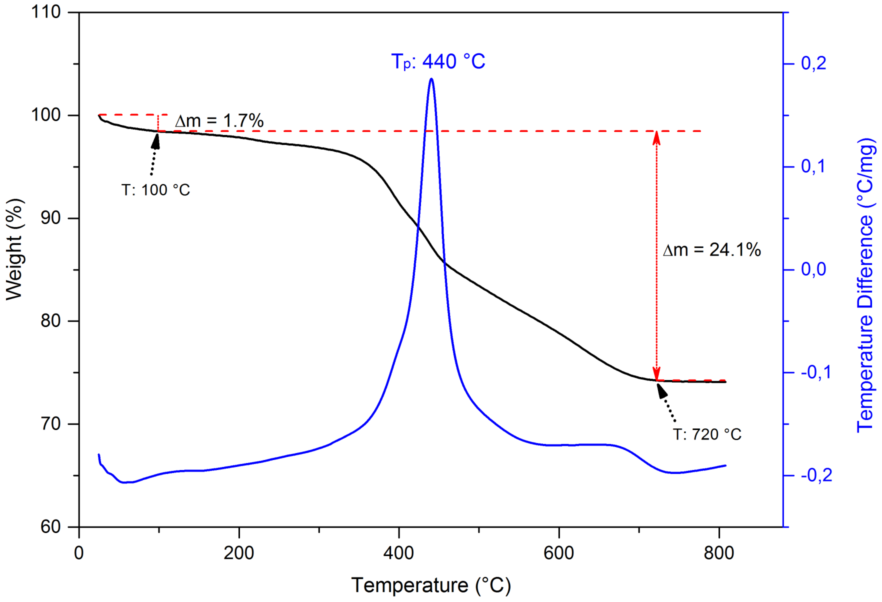

Figure 6.52: DSC/TG curves of TMP-SSZ-51. Tp: peak temperature.

6.5.4 Temperature-dependent XRPD of TMP-SSZ-51

Temperature-dependent X-ray powder diffraction measurements (Fig.6.53) were performed from 50 °C to 840 °C in order to investigate the calcination process and the decomposition of the SSZ-51 framework at increasing temperature. The organic template stays stable in the zeolite pores up to 250 °C and then begins to escape from the material. From about 300 °C the reflection at 14 ° starts to split up to form two reflections, indicating the formation of a calcined phase. A significant change (e.g., lower background) of the powder patterns after 400 °C is due to an artefact. The framework of calcined SSZ-51 remains stable up to about 720 °C. The reflections representing the SSZ-51 phase disappear and a few new peak forms from 720 °C, indicating the decomposition process of calcined SSZ-51. The observed phenomena are consistent with the results of DSC-TG measurement.

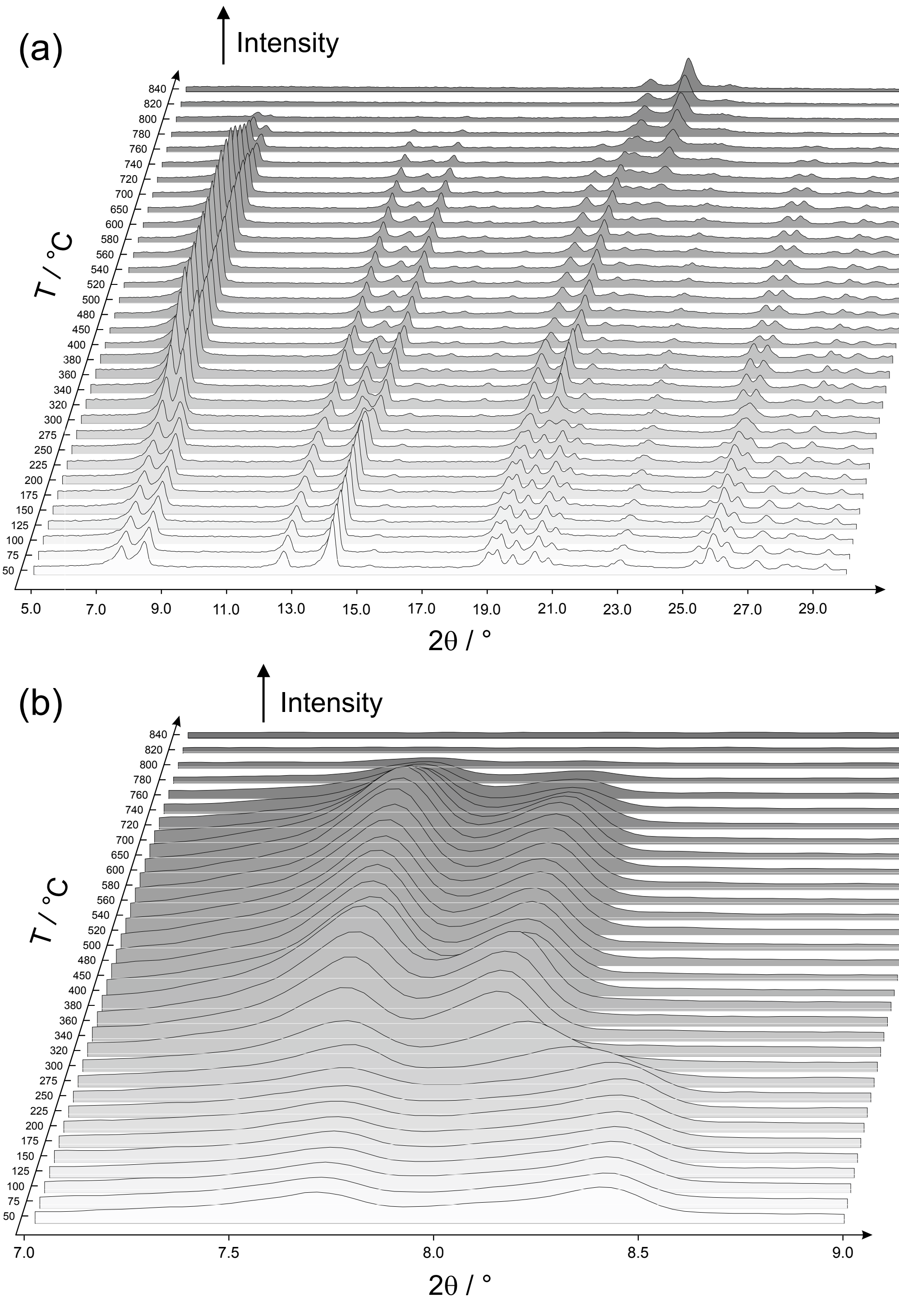

Figure 6.53: Temperature dependent X-Ray powder diffraction diagrams of the thermal decomposition of TMP-SSZ-51 (Cu Ka1 radiation), showing the release of template molecule as well as the decomposition of SSZ-51 at high temperature. 2θ range from 5^{o} to 30^{o} in (a) and from 7^{o} to 9^{o} in (b). Note that the sample was cooled down from 400 °C to RT (faulty program) and was heated up again by hand.

6.5.5 Structure determination of TMP-SSZ-51

Structure solution from ADT data

The reconstruction of ADT data (Fig. 6.54) delivered a monoclinic unit-cell with a = 21.54 Å, b = 13.81 Å, c = 14.32 Å, α = 90.4°, β = 100.7°, γ = 89.8°, which were further refined by a Pawley fit of the XRPD data for structure solution. Systematic extinctions for hkl reflections with $h + l = 2n$ indicated an C-centred Bravais lattice. In addition, the reflection conditions as observed for $h0l$ reflections with $k = 2n$ and $l = 2n$ are indicative of a c glide-plane ($l = 2n$) (Fig. 6.54), associated with two possible space groups Cc (No. 9) and $C2/c$ (No. 15).

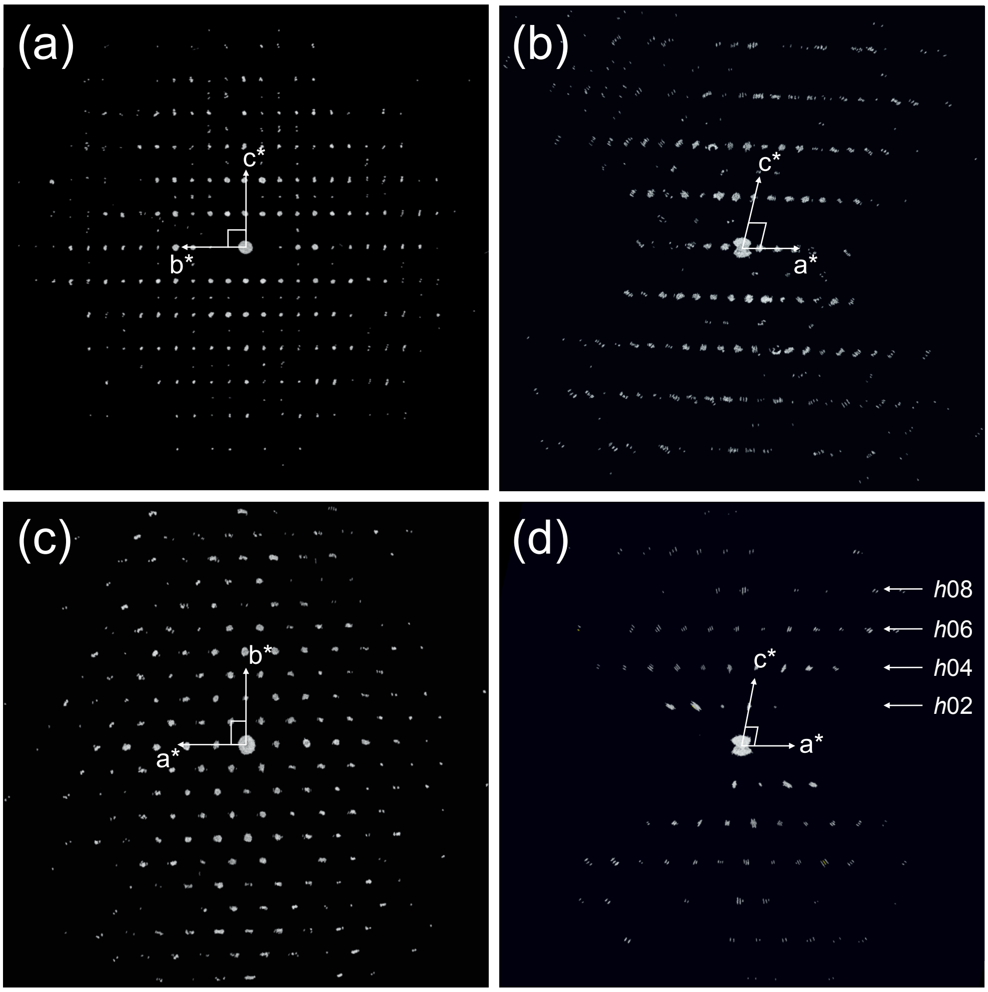

Figure 6.54: (a-c) Reconstructed three-dimensional diffraction volumes of TMP-SSZ-51 obtained from ADT data viewed down the three main axis. (d) h0l slice cut from 3D reciprocal space; symmetry rule: $k = 2n$ and $l = 2n$ in $h0l$ zone.

A PED ADT dataset with a tilt range of ±60° was used for crystal structure solution with direct methods. The *ab initio* structure solution converged with a final residual R of 18.14%. The structure solution delivered a well-resolved Fourier potential map (Fig. 6.55) showing not only all the atoms of the zeolite framework but also a clear view of all atoms of the organic template.

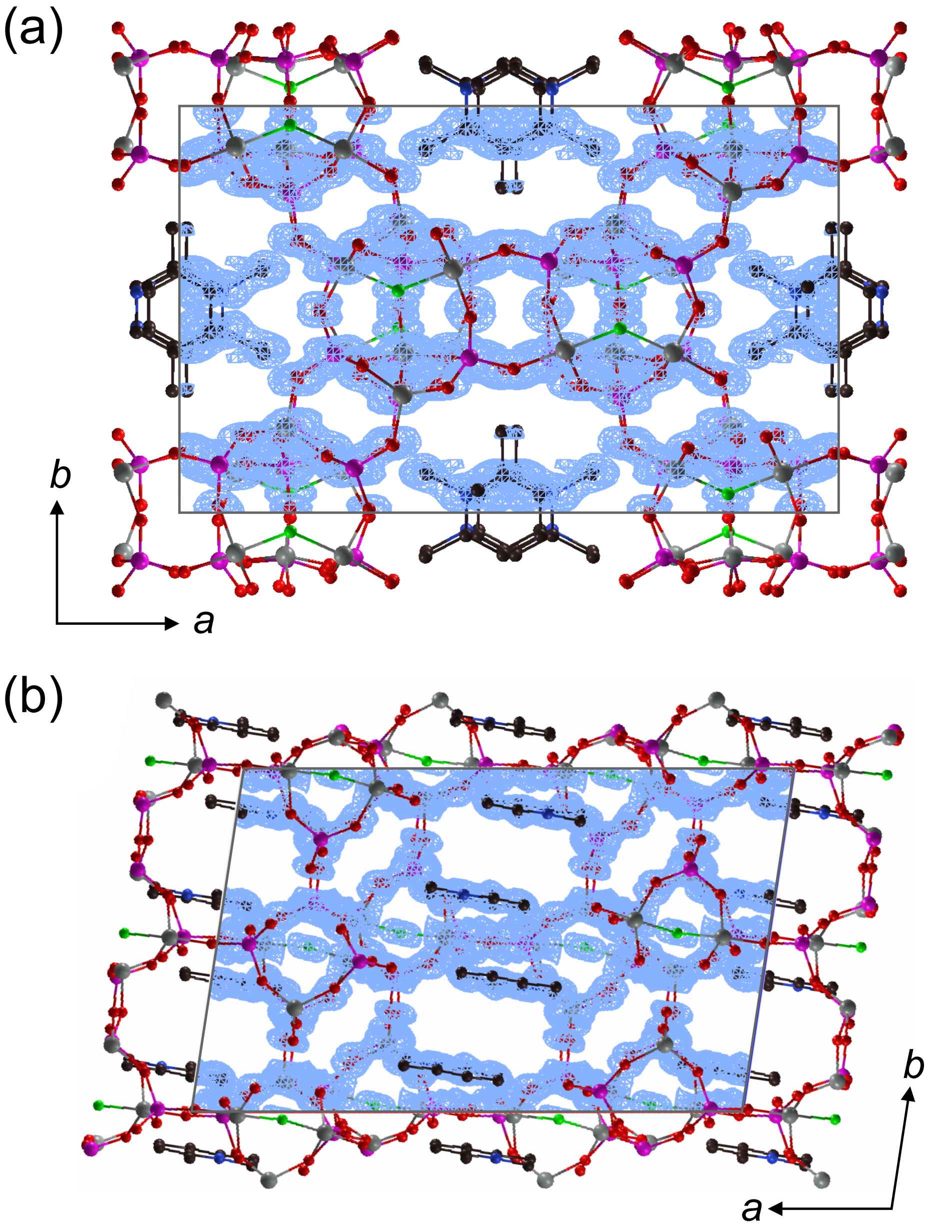

Figure 6.55: Fourier potential map of TMP-SSZ-51 derived from structure solution in `Sir2014` using ADT data with the overlaid atomic framework model viewed in [100] and [001] directions, respectively. Colour of atoms: Al (grey), P (lilac), O (red), F (green) C (black) and N (blue).

The strong maxima from 2.41 to 1.88 $e^-/\text{Å}^3$ correspond to P and Al atoms, respectively. The following peaks for O and F atoms were detected with a scattering potential range of 1.64 down to 0.98 $e^-/\text{Å}^3$. The C and N atoms in the template were detected from a 0.94 to 0.38 $e^-/\text{Å}^3$. All the C and N atoms in 1,2,6-trimethylpyridinium could be clearly detected from the structure solution. The ADT method is well suited to determine a complete structure model of a microporous material including even the atoms of weak scattering power (C, N). Only the hydrogen atoms could not be located. Such a structure model may directly be used as a starting model for a more detailed structure analysis.

Structure refinement from XRPD data

The Rietveld refinement was firstly carried out using the starting model obtained from the structure solution based on ADT data. However, the refinement was not satisfactory. On the other side, the observed defective fits occurred only at the first two second reflections with 2θ of 7.6° and 8.3° in the Pawley fit with the unit parameters of TMP-SSZ-51 (Fig.6.56). Taking under consideration that this reflection shifts to a lower diffraction angle as showing in Fig. 6.53b when the template molecules are released from the pores. This phenomena indicates that a small part of crystals or domains do not contain the organic template which probably results from the crystallization process. In this occasion, these types of domains can be described with a calcined phase. The monoclinic structural model of calcined SSZ-51 could also be directly solved from ADT data in the space group of $C2/m$ and was applied for the combined refinement. A combined Rietveld refinement including two phases, TMP-SSZ-51 and calcined SSZ-51, was performed from X-ray data and converged in a R-value with R_{wp} of 3.725%. The Plot of Rietveld refinement is shown in Fig. 6.57. Selected crystallographic data are summarized in Table 6.13.

Table 6.13: Selected crystallographic data parameter of Rietveld refinement of SSZ-51.

Compound	TMP-SSZ-51
Cell formula	$Al_{32}P_{32}O_{128}F_8 \cdot C_{64}N_8H_{96} \cdot (H_2O)_{2.93}$
Crystal system	Monoclinic
Space group (No.)	$C2/c$
a (Å)	21.5370(5)
b (Å)	13.8795(3)
c (Å)	14.2658(3)
$\alpha = \gamma$ (°)	90
β (°)	99.889 (1)
V (Å^3)	4201.1(1)
Z	8
D_{calc} (Mg/m^3)	2.008
T (K)	294
Radiation type	Cu$K\alpha$1
Wavelength (Å)	1.540598
θ_{max} (°)	50
R_p (%)	2.631
R_{wp} (%)	3.725
R_{exp} (%)	2.181
gof	1.708

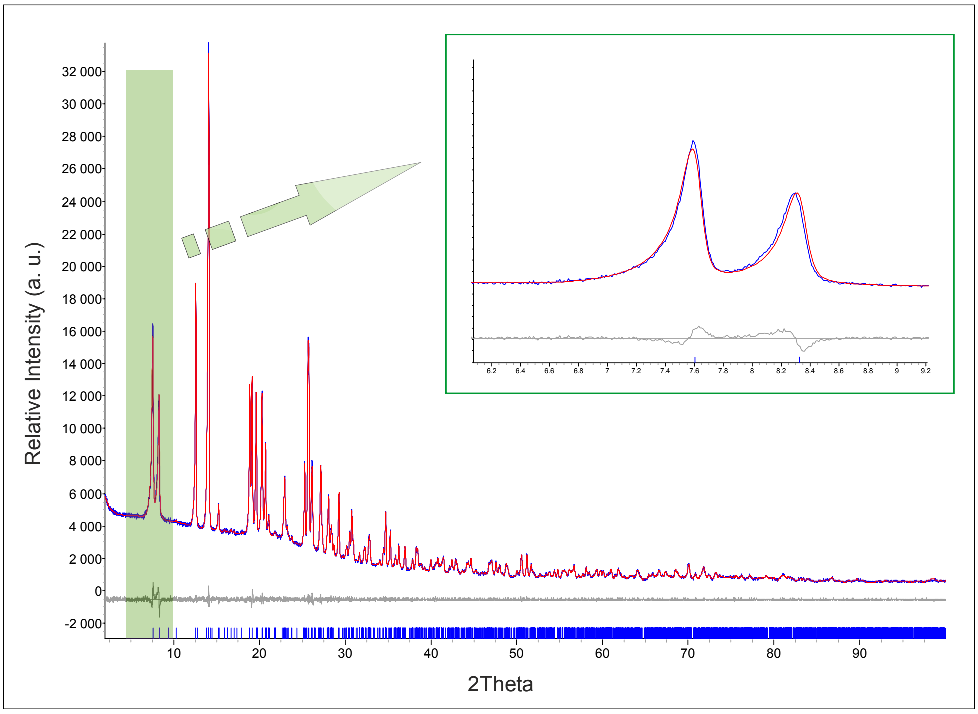

Figure 6.56: Plot of Pawley fit in the space group *C*2/*c* only with the unit cell of TMP-SSZ-51 . Observed powder diagram (blue solid line), simulated powder diagram (red solid line), difference profile (grey solid line), reflection positions (blue ticks). Insert: enlarged area of 2θ from 6° to 9.2°.

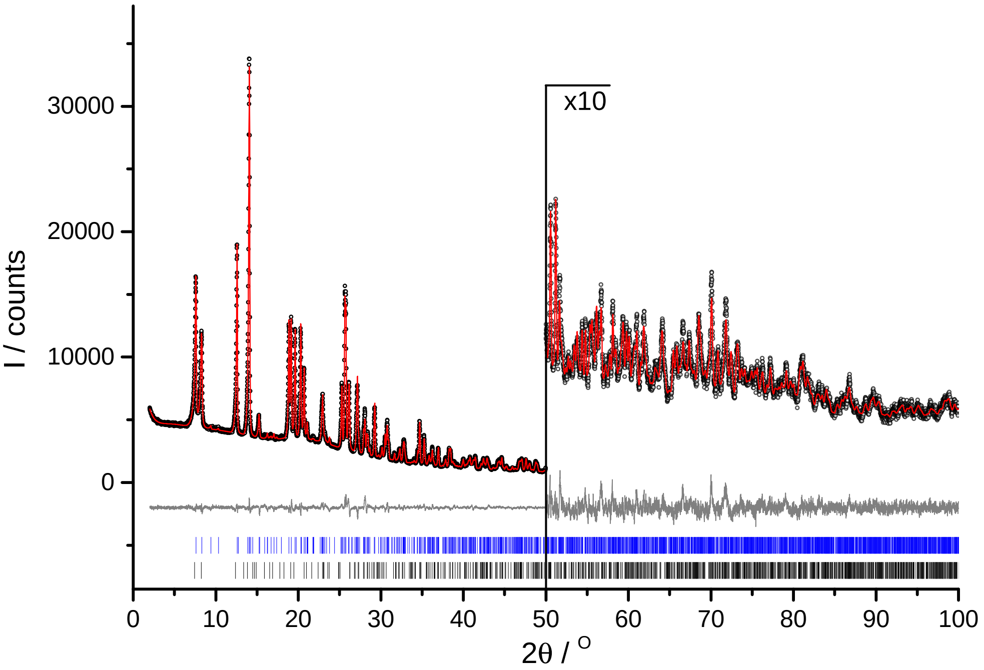

Figure 6.57: Plot of Rietveld refinement of SSZ-51. Observed powder diagram (black circles), simulated powder diagram (red solid line), difference profile (grey solid line), reflection positions (blue ticks for as-synthesized phase and black ticks for calcined phase). Change of the scales with factor 10 is indicated in the diagram.

The calcined phase content was refined by Rietveld method to 6.8(2)%. The refinement led to a meaningful framework structure and an acceptable geometry of the organic template. All the refined independent atoms own reasonable temperature factors.

6.5.6 Structure description of TMP-SSZ-51

The crystal structure of TMP-SSZ-51 is illustrated in Fig. 6.58. The fluorine ion not only acts as mineralizer in the synthesis but is included in the structure of TMP-SSZ-51 generating a negatively loaded framework. F atoms bridge two Al atoms (Al2 and Al4) in the crystal structure forming AlO_4F trigonal bipyramids. The other Al atoms (Al1 and Al3) are four-coordinated by O atoms forming AlO_4 tetrahedra. All P atoms are fourfold coordinated by O atoms with tetrahedron geometry. The Al containing polyhedra are interconnected with PO_4 groups constructing a microporous 3D framework of zeolite type SFO[219,244]. The 2D pore system consists of wide 12-Ring channels (free diameter ca. 7.0 Å) running along the ***a*** axis which intersect with narrow 8-ring channels (free diameter ca. 3.8 Å) (Fig. 6.58a). 1,2,6-trimethylpridinium molecules fill the straight channels limited by 12-Rings and stack along ***a*** axis with inter-planar distances from 3.5 Å to 3.7 Å (Fig. 6.58b), which are in the typical range of distances observed for π–π interactions (about 3.3 - 3.8 Å)[245]. The atoms of template molecules show larger temperature factors (B_{iso}) than the framework atoms, indicating that the stacked organic molecule possess some free moving space. Selected bond lengths and bond angles are listed in Table 6.14. The crystallographic data is added as a supplementary data *Appendix D* in section Appendix.

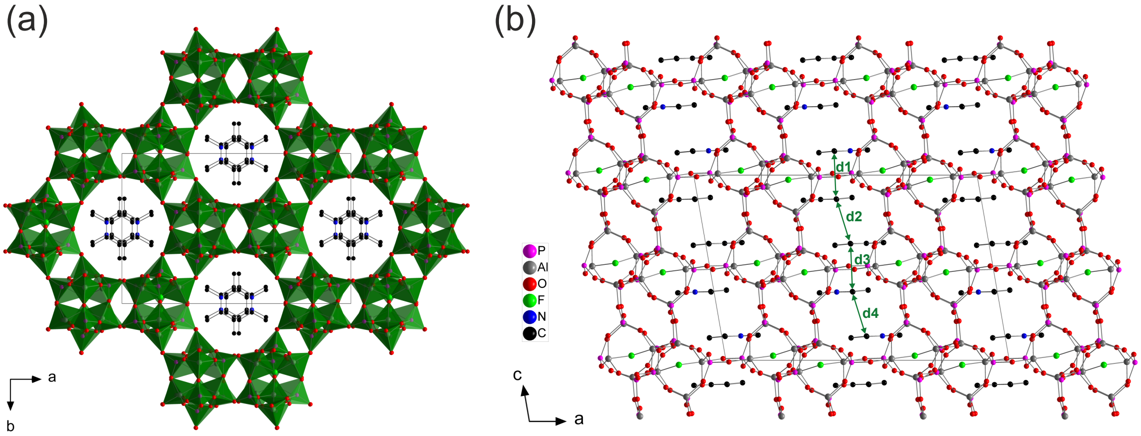

Figure 6.58: (a) Crystal structure of TMP-SSZ-51 with AlO_4, AlO_4F and PO_44 polyhedron viewed along the crystallographic ***a*** axis. (b) Crystal structure viewed along the crystallographic ***b*** axis. The distances between neighbouring molecules are highlighted: d1 = 3.63 Å, d2 = 3.61 Å, d3 = 3.63 Å and d4 = 3.59 Å, respectively. H atoms are omitted for clarity.

Table 6.14: Selected bond lengths (Å) and bond angles (°) of SSZ-51.

Framework of SSZ-51							
PO_4 octahedra							
P1-O4	1.503(4)	P2-O16	1.505(4)	P3-O5	1.519(3)	P4-O2	1.510(4)
P1-O3	1.519(4)	P2-O1	1.511(4)	P3-O11	1.521(4)	P4-O10	1.518(5)
P1-O6	1.527(4)	P2-O8	1.524(4)	P3-O14	1.525(4)	P4-O7	1.526(4)
P1-O12	1.529(4)	P2-O13	1.527(4)	P3-O9	1.539(4)	P4-O15	1.537(4)
AlO_4 octahedra				**AO_5 bi-pyramids**			
Al1-O5	1.745(4)	Al3-O4	1.740(4)	Al2-O1	1.788(4)	Al4-O11	1.781(4)
Al1-O16	1.745(4)	Al3-O10	1.751(4)	Al2-O6	1.795(4)	Al4-O3	1.786(4)
Al1-O7	1.754(4)	Al3-O13	1.7520(4)	Al2-O14	1.796(4)	Al4-O2	1.792(4)
Al1-O12	1.760(4)	Al3-O8	1.760(4)	Al2-O9	1.806(4)	Al4-O15	1.800(4)
				Al2-F1	1.913(3)	Al4-F1	1.923(3)
Organic SDA in SSZ-51 SSZ-51							
N1-C1	1.382(5)	C1-C2	1.379(6)	C5-C4	1.378(6)	C2-C1	1.379(6)
N1-C5	1.392(6)	C1-N1	1.382(5)	C5-N1	1.392(6)	C2-C3	1.384(6)
N1-C6	1.494(5)	C1-C7	1.483(6)	C5-C8	1.501(6)	C6-N1	1.494(5)
C3-C2	1.384(6)	C3-C4	1.398(6)	C7-C1	1.483(6)	C8-C5	1.501(6)
Selected angles in SDA							
C1-N1-C5	120.0(3)	C2-C1-N1	120.6(4)	C4-C5-N1	119.5(4)	C1-C2-C3	119.5(4)
C1-N1-C6	118.0(3)	C2-C1-C7	120.7(4)	C4-C5-C8	119.5(4)	C2-C3-C4	120.0(4)
C5-N1-C6	121.9(3)	N1-C1-C7	118.6(3)	N1-C5-C8	120.9(4)	C5-C4-C3	120.1(4)

Until now, almost all the SSZ-51 type porous materials were synthesized using 4-dimethylamino-pyridine (DMAP) as organic structure directing agents[219,245–247]. However, Park et al.[248] found that 1,2,3,4-tetramethyl-imidazolium and 1,2,3,4,5-pentamethyl-imidazolium cations could also direct the formation of aluminophosphate SSZ-51. In this work, another example is the OSD 1,2,6-trimethylpridinium in this study. In all cases, the OSDs molecules arrange with π-π stacking interactions leading to a rod-shaped template group in the solution. The type of template groups direct in turn the formation of the channels in the structure during the crystallization process. The use of such a "composite template" is quite unique when trying to synthesize microporous materials. Typically, individual molecules/cations act as OSDAs; e.g. long chain-like molecules of a specific thickness like e.g. 1,3-dipiperidinium-propane are used as the OSDA to direct the hydrothermal crystallization of aluminophosphates or zeolites in such a way that structures with a pore system comprising 12-ring channels are formed.

6.5.7 Organic template in PYS-SOD

The as-synthesized silica PYS-SOD was selected as a reference material and reinvestigated by electron diffraction tomography in order to compare and study the influence of symmetry of framework on the position of OSDs. The porous material SOD has a highly symmetric structure. As described in literature[229,249], PYS-SOD crystallizes in a cubic system with space group $I\bar{4}3m$ (No. 217) and the neutral pyrrolidine molecules distribute dynamically in the cages of SOD. The crystal structure was first analyzed in the setting of cubic crystal class. A cubic lattice could be reconstructed from ADT data (Fig. 6.59).

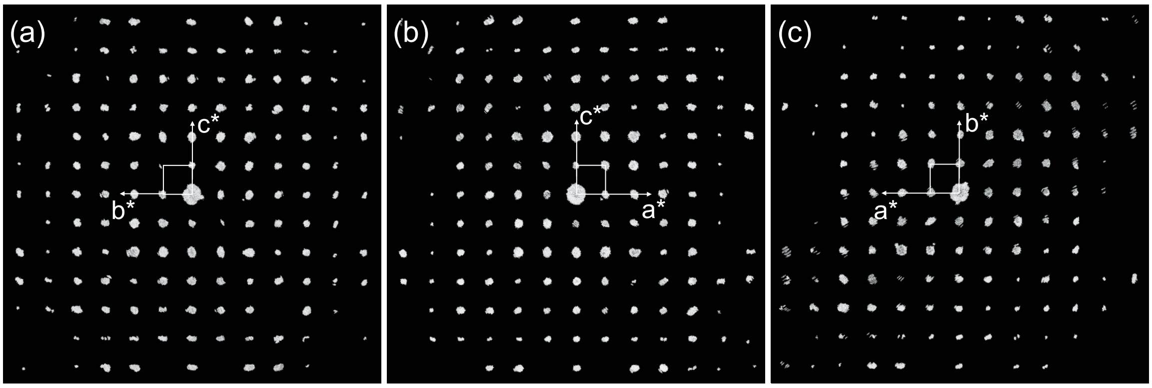

Figure 6.59: Reconstructed three-dimensional diffraction volumes of PYS-SOD obtained from ADT data viewed down the three main axse.

Structure solution was performed in space group $I\bar{4}3m$ with lattice parameters $a = b = c = 8.88$ Å and $\alpha = \beta = \gamma = 90°$. by 3D electron diffraction data. Difference Fourier electron potential map (F_{obs}-F_{cal}) results a spherical isosurface in the middle of the cage (Fig. 6.60a), associated with the position of disordered template molecules. Structure refinements were carried out with Rietveld method from XRPD data and dynamic refinement from ADT data, respectively. The Plot of Rietveld refinement from XRPD data is shown in Fig. 6.61. The high symmetry causes the template molecule located in the general positions with partial occupancies (Fig. 6.60b). Dynamic refinement from ADT data delivered resolved difference electron potential map (Fig. 6.60c) and a structure model with two special positions of template atoms (Fig. 6.60d), which are comparable with single X-ray crystal structure analysis[249] (Table 6.15). The atomic positions refined dynamically resemble the shape of the residual potential, as visible in the cage, derived by kinematical structure solution (see Fig. 6.60a). The symmetry of framework and the low symmetry of pyrrolidine molecule enforce the template to locate in the cage with a dynamical distribution. Therefore, the special positions from dynamic refinement and single crystal structure analysis only represent a dynamic statistic locations for the template atoms with a higher overlap probability.

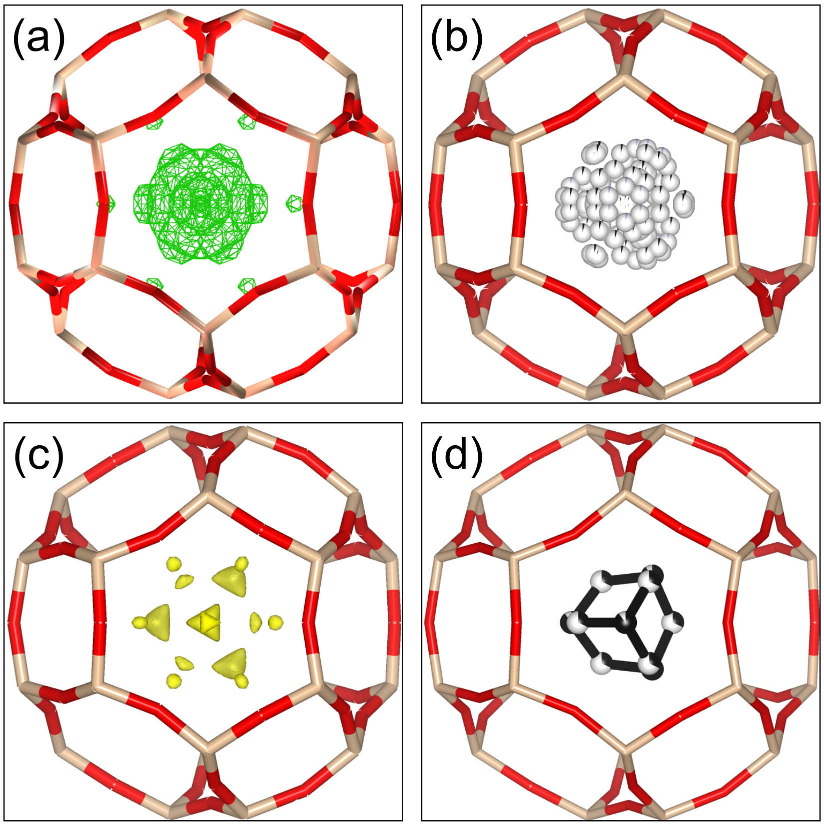

Figure 6.60: (a) Crystal structure with difference Fourier potential map (green) of PYS-SOD derived from structure solution in `SIR2014`. (b)Crystal structure refined with Rietveld method with partly occupied pyrrolidine molecule. (c) Crystal structure with difference Fourier potential map (yellow) of PYS-SOD derived from dynamic structure refinement in `Jana2006`. (d) Crystal structure from dynamic refinement with partly occupied atoms of pyrrolidine molecule. All structures are viewed down [111] zone. H atoms are omitted for clarity. O atom in red , Si atom in light yellow.

Table 6.15: Atomic coordination and occupation parameter of partial atoms for pyrrolidine molecule in PYS-SOD refined from single single crystal x-ray diffraction data and ADT data.

Single X-ray crystal structure analysis (Wertmann et al.[249])				
	x	x	x	Occupation
C1	0.081	0.081	0.081	0.63
C1	0.081	0.081	0.081	0.63
C2	0	0	0.154	0.42
C3	0.086	0.086	0.105	0.20
Structure analysis by dynamic refinement from ADT data				
	x	x	x	Occupation
C1	0.090	0.090	0.090	0.89
C2	0	0	0.159	0.32

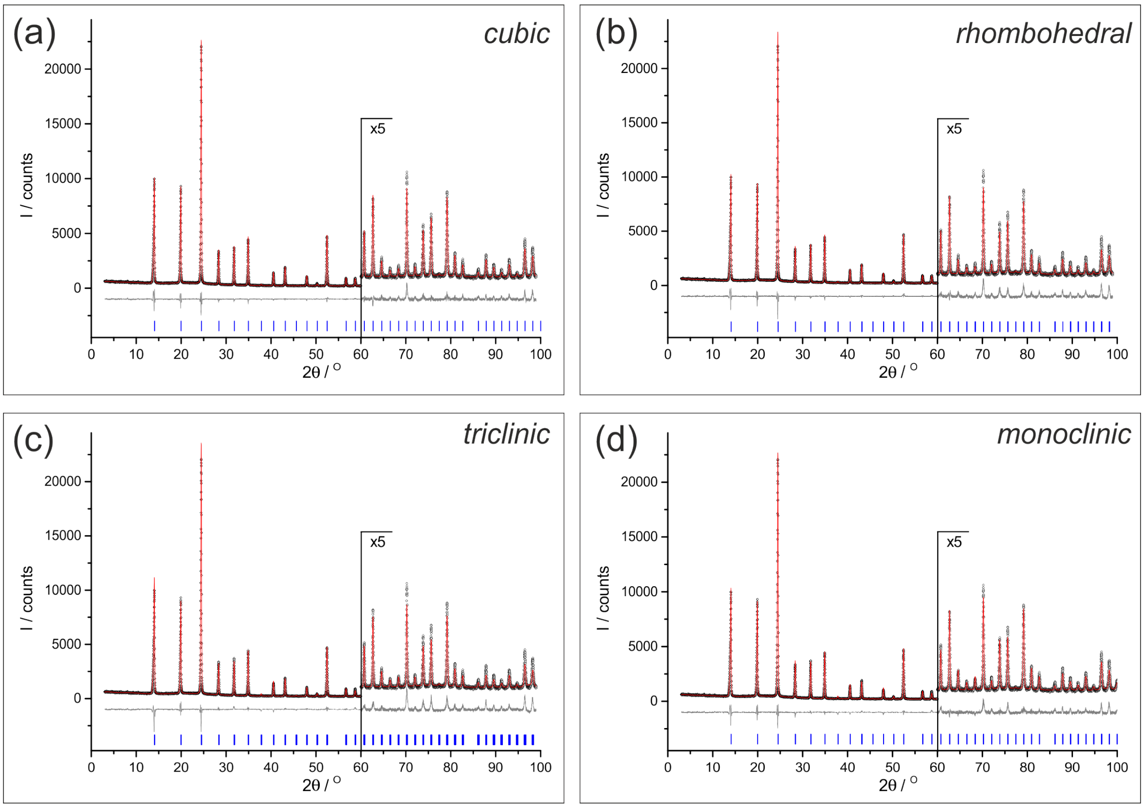

Figure 6.61: Plot of Rietveld refinements of PYS-SOD in different crystal lattices. Observed powder diagram (black circles), simulated powder diagram (red solid line), difference profile (grey solid line), and reflection positions (blue ticks). Change of the scale with factor 5 is indicated in each diagram.

Table 6.16: Selected parameters of Rietveld refinements in different crystal systems of PYS-SOD.

Crystal system	Cubic	Rhombohedral	Triclinic	Monoclinic
Space group (No.)	$I\bar{4}3m$ (217)	$R3$ (146)	$P1$ (1)	Cm (8)
a (Å)	8.8801(1)	7.6915(4)	7.6861(7)	8.8763(6)
b (Å)	8.8801(1)	7.6915(4)	7.69412(6)	12.5619(8)
c (Å)	8.8801(1)	7.6915(4)	7.6985(6)	7.6904(6)
α (°)	90	109.483(4)	109.523(5)	90
β (°)	90	109.483(4)	109.576(7)	125.248(8)
γ (°)	90	109.483(4)	109.391(5)	90
V (Å^3)	700.24(2)	350.12 (7)	350.15(6)	700.30(11)
R_p (%)	5.321	6.083	6.692	5.585
R_{wp} (%)	6.877	7.871	9.060	7.511
R_{exp} (%)	4.617	4.600	4.589	4.611

In order to increase the freedom for template molecule, symmetry reduction was taken into account for further analysis. The relationship between space group $I3\bar{4}m$ and its possible subgroups including corresponding unit cells are shown in Fig. 6.62. The structure solutions in all subgroups (even in P1 in a pseudo-rhombohedral crystal system) delivered a nice sodalite framework and some extra potentials in the middle of SOD cages. After running dynamic refinements, no resolved position for template atoms could be observed in the middle of SOD cage. On the other hand, the Rietveld refinements in the subgroups (Table 6.16) show worse fits than the refinement in the setting of cubic lattice. It must be noted that the monoclinic (Cm) and triclinic ($P1$, pseudo-rhombohedral) settings allow the template molecule to locate in all SOD cages with the same orientation. The defective fits in space groups Cm and $P1$ indicate that the position of template molecules cannot be described using one definite orientation but indeed in dynamic distribution in SOD cages, confirming the correctness of a cubic lattice.

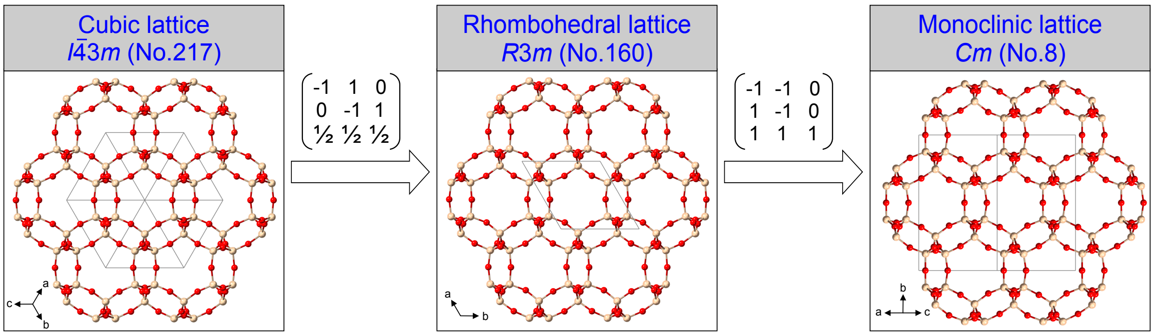

Figure 6.62: Possible translationsgleiche subgroups of SOD starting from $I3\bar{4}m$ (No. 217) by reducing crystal class with corresponding unit cell and transformation matrix. O atom in red , Si atom in light yellow.

In comparison with the ordered template position in SSZ-51 framework with a monoclinic symmetry, the organic template molecule locates with a dynamic ordered orientation in the pore of SOD framework with a higher symmetry. It indicates that the template molecules could not change the symmetry of the whole structure and the symmetry of the framework decides the orientation of the template molecules.

6.5.8 Summary

In this work, a new as-synthesized aluminophosphate SSZ-51 was prepared and investigated by thermogravimetric analysis, solid-state NMR, XRPD and TEM technique. The structural characterization was performed with electron diffraction tomography and XRPD. The symmetry of framework shows an influence on the arrangement of SDAs. The organic SDA locates in monoclinic SSZ-51 with an ordered arrangement whereas the SDA distributes with a dynamic ordered orientation (disordered distribution) in high symmetric SOD.

6.6 Metal atom in the pore of CHA zeolite

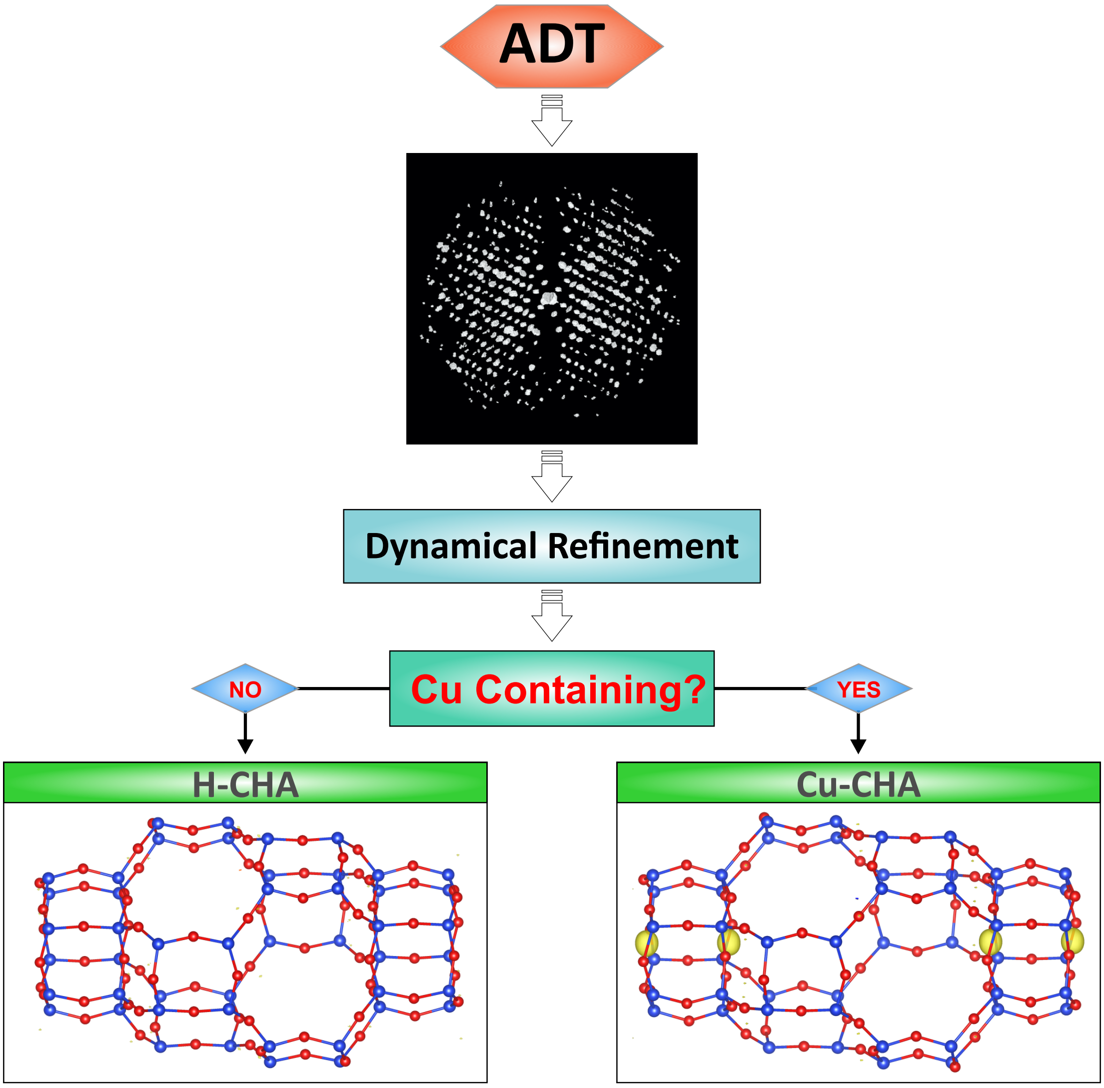

Cu position in dehydrated CHA zeolite determined by dynamical refinement using ADT data

The structural investigation of chabazite (CHA) zeolites is a sub-project of INCOE (International Network of Centers of Excellence) project coordinated by BASF SE, Ludwigshafen Germany. The Cu-chabazite (Cu-CHA) zeolite was studied in comparison to a reference material without metal-containing zeolite H form chabazite (H-CHA). The water molecules were removed by heating at 400 °C in high vacuum condition to gain dehydrated phases. The location of Cu ions in Cu-CHA, as the active sites in the catalytic reaction, was difficult/impossible to detect directly using XRPD approach. Electron diffraction tomography was applied to confirm/detect the position of Cu atoms in dehydrated Cu-CHA on the basis of the method of dynamical refinements. The results are in preparation for publishing. The experimental details are summarized in section 5.6.

6.6.1 General information

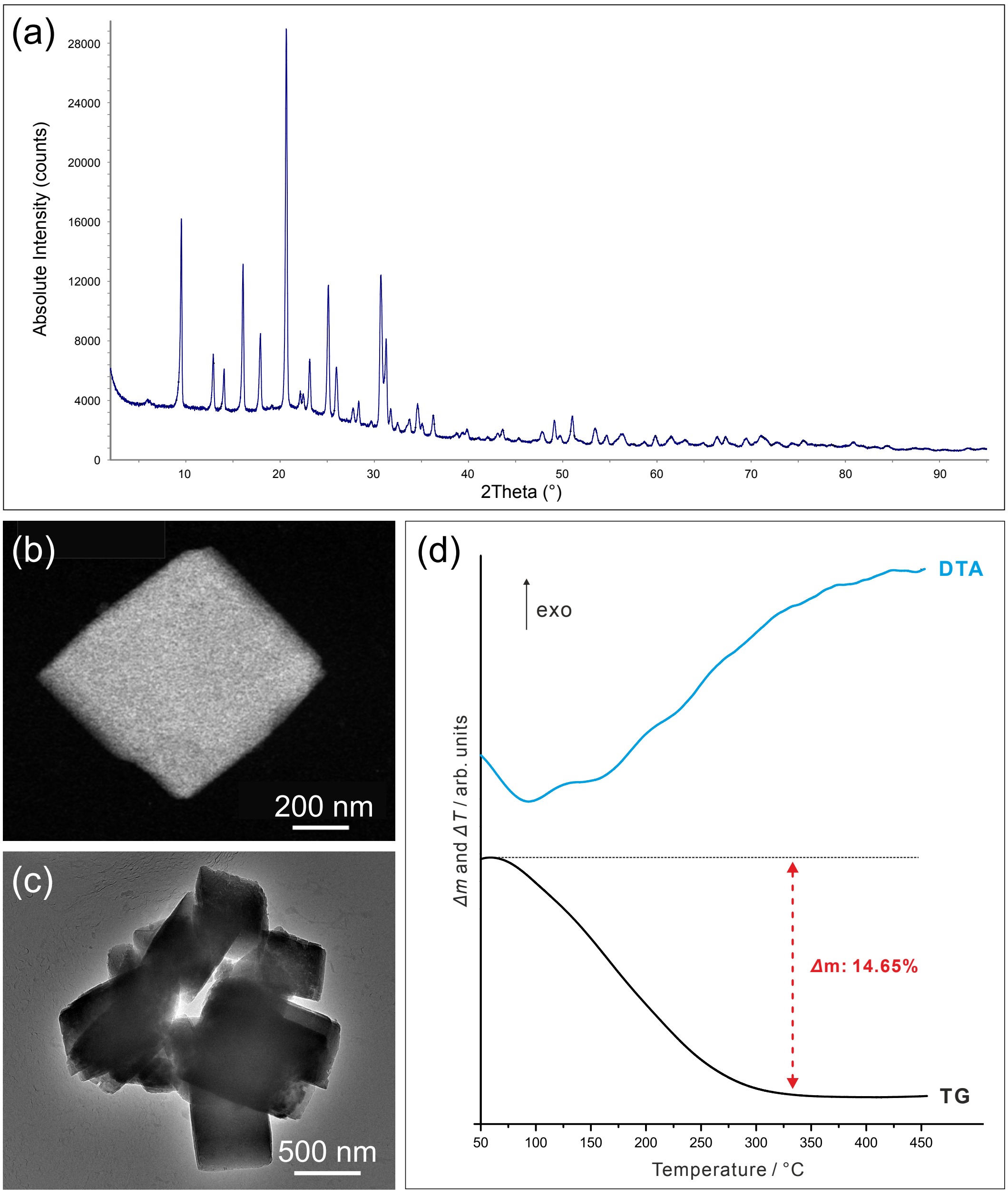

Figure 6.63: (a) XRPD of hydrated Cu-CHA with $K\alpha 1$ radiation; (b) STEM image of single Cu-CHA crystal; (c) TEM image of H-CHA paricles; (d) DTA-TG curve of Cu-CHA.

H-CHA and Cu-CHA zeolites consist of cubic crystals. They are electron beam stable under mild dose condition. The high crystallinity of Cu-CHA was confirmed by XRPD data (Fig. 6.63a) and discrete electron diffraction pattern. The water molecules release from the cages of CHA with the increasing temperature up to 350 °C. The weight loss is 14.65 wt% as observed in thermogravimetric (TG) curve (Fig.6.63d). Element analysis base on inductively coupled plasma (ICP) technique indicated 6.0 wt% Cu in Cu-CHA zeolite.

6.6.2 Structure solution

The crystal structures were solved in the space group $R\overline{3}$ from the reflection data extracted by the program PETS. The hexagonal lattice parameters, $a = b = 13.569$ Å, $c = 14.840$ Å, $\alpha = \beta = 90°$, $\gamma = 120°$ for dehydrated H-CHA and $a = b = 13.472$ Å, $c = 15.132$ Å, $\alpha = \beta = 90°$, $\gamma = 120°$ for dehydrated Cu-CHA, were used for the structure solutions and refinements. Both structure solutions delivered well-resolved electron potential maps (Fig. 6.64) and a good structural model with all Si and O atoms of the framework. In addition, an extra potential was only observed over the six-member ring (6-MR) in the pore of H-CHA (marked with a lilac circle in Fig. 6.64a) while another extra potential located in the middle of 6-MR in Cu-CHA (marked with a lilac circle in Fig. 6.64b). Since the water were removed by heating at a high vacuum, we could exclude that the extra potentials were caused by water molecules.

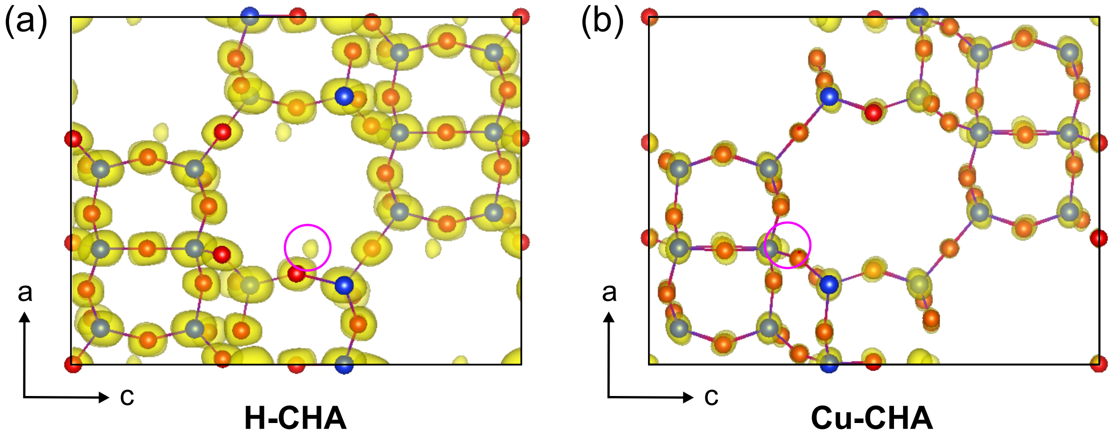

Figure 6.64: Potential maps from structure solutions of CHA zeolites viewed along the ***b*** axis. The extra observed potentials were marked with lilac circles. Potential in yellow, Si atom in blue and O atom in red.

6.6.3 Kinematical refinement

In order to distinguish the observed extra potentials, kinematical refinements were performed using isotropic atomic displacement parameters (ADPs) from the same electron diffraction datasets. The refinements converged at $R1$ of 29.34% for H-CHA and 34.77% for Cu-CHA (Table 6.17), respectively. The residuals are plotted in the difference electron potential maps (Fig. 6.65) using a $4\sigma(\Delta V)$ threshold. Note that σ is the standard deviation. Similar to the structure solution, the residual potentials were observed over the 6-MR in the pore of H-CHA and in the 6-MR of Cu-CHA. No other additional residual potential was observed. The structural models remained stable after the refinements. The observed residual potentials of both materials still remained after kinematical refinement.

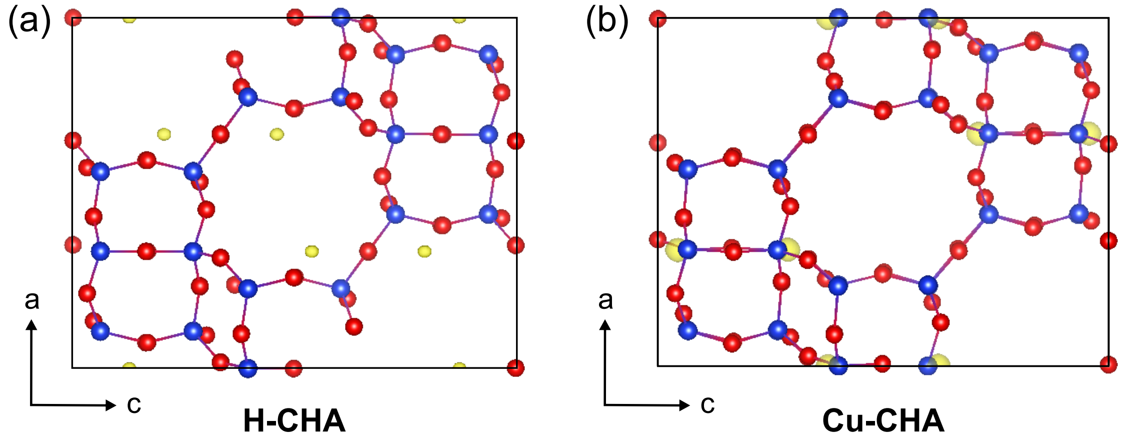

Figure 6.65: Difference potential maps from kinematical refinements of CHA zeolites viewed along the ***b*** axis. Isosurface levels are $4\sigma(\Delta V)$. Residual potential in yellow, Si atom in blue and O atom in red.

Table 6.17: Parameters of kinematical and dynamical structure refinements in `JANA2006` for CHA zeolites.

	Parameter	max(ΔV) (e/Å)	$\sigma(\Delta V)$ (e/Å)	$R1$ (%)	Res.*	Formula
H-CHA	kin. ref. (iso.)	2.41	0.498	29.34	yes	$Si_{36}O_{72}$
	dyn. ref. (iso.)	0.60	0.148	13.01	no	$Si_{36}O_{72}$
	dyn. ref. (aniso.)	0.60	0.143	11.44	no	$Si_{36}O_{72}$
Cu-CHA	kin. ref. (iso.)	6.21	0.597	34.77	yes	$Si36O_{72}$
	dyn. ref. (iso.)	4.98	0.305	19.73	yes	$Si_{36}O_{72}$
	ref. with Cu (iso.)	0.62	0.191	15.15	✗	$Si_{36}O_{72}Cu_{2.97}$
	ref. with Cu (aniso.)	0.56	0.147	11.38	✗	$Si_{36}O_{72}Cu_{2.63}$

*Referred to as residual Coulomb potential in this work.

6.6.4 Dynamical refinement

As described in the literature of Bowden et al.[62], the kinematical approximation often delivers unreliable result and the additional potential maximum can serve as a kind of artefact. Dynamical refinements with isotropic ADPs were performed in order to confirm the presence of the residual potentials. The refinements delivered stable frameworks and converged at much lower $R1$ values of 13.01% for H-CHA and 15.15% for Cu-CHA (Table 6.17). There was no residual potential observed over the 6-MR in the dynamical refinement of H-CHA whereas the extra potential was still clearly visible in 6-MR of Cu-CHA (Fig. 6.66). The further dynamical refinement with anisotropic ADPs delivered better temperature factors for H-CHA. The $R1$ reduced from 19.73% to 15.15% after inputting Cu atom to the site of residual potential maximum in the dynamical refinement of Cu-CHA using isotropic

ADPs. The refined occupancy of Cu atom is 49.45% in Cu-CHA which is corresponding to 8.0wt% in Cu-CHA and 2.97 Cu atom in a hexagonal unit cell. Further refinement with anisotropic ADPs resulted in a much lower *R*1 of 11.38% and stable structural model with a 43.81% occupied Cu atom, corresponding with 7.17 wt% of Cu-CHA and 2.63 atom in one unit cell.

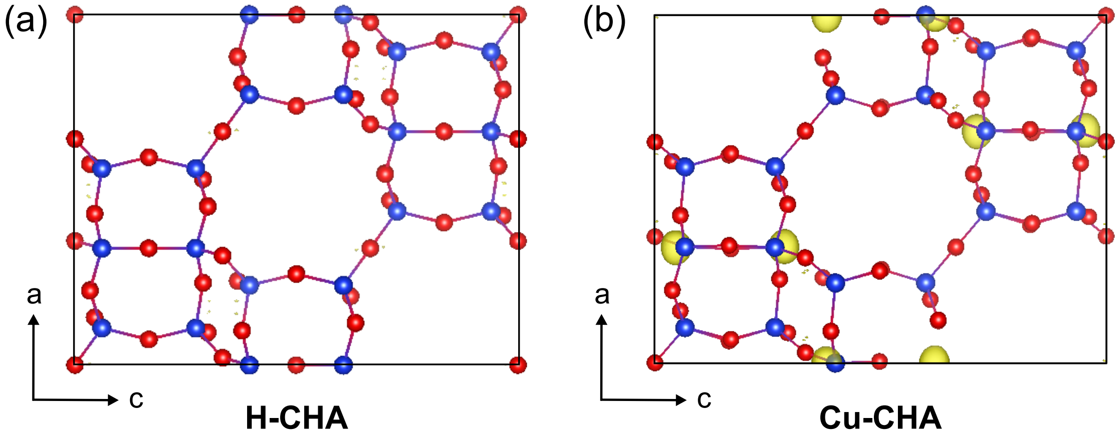

Figure 6.66: Difference potential maps from dynamical refinements of CHA zeolites viewed along the ***b*** axis. Isosurface levels are $4\sigma(\Delta V)$. Residual potential in yellow, Si atom in blue and O atom in red.

6.6.5 Discussion

After the application of the approach of dynamical refinement, no additional potential remained in dehydrated H-CHA and the residual potential indicated the site of Cu atom in dehydrated Cu-CHA. Furthermore, *R*1 values reduced dramatically after taking the dynamical effect into account. The results were agreement with the fact of the presence of Cu in Cu-CHA and confirmed partially occupied Cu atom in the 6-MR of dehydrated Cu-CHA. The refinements of both materials stayed stably even using anisotropic ADPs, leading to reasonable and positive values of temperature factor for all atoms *U*ani (Table 6.18). The refinement process converged finally to produce meaningful structure models (Fig. 6.67) with reasonable bond lengths and bond angles as summarized in Table 6.19. The Cu atom was confirmed to locate in the middle of 6-MR with threefold coordination with O atoms with a good geometry (Cu-O bond distance of 2.102 Å and O-Cu-O bond angle of 118.85°). The crystallographic cif-data are attached in the supplementary data *Appendix E* in section Appendix.

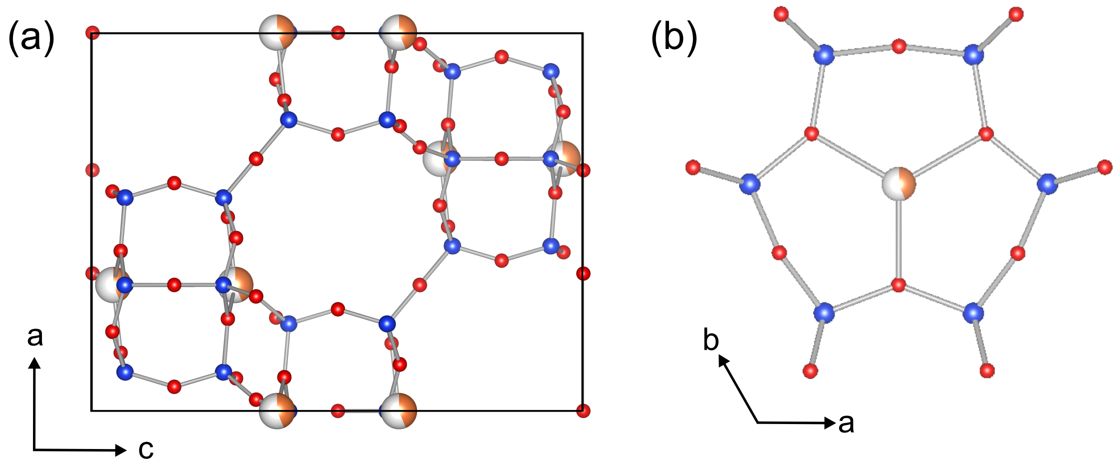

Figure 6.67: (a) Crystal structure of Cu-CHA viewed along the ***b*** axis. (b) Structural segment of single 6 member ring with Cu atom viewed along the ***a*** axis. Si atom in blue, O atom in red and Cu in yellow.

Table 6.18: Temperature factors Uani (Å^2) in the refined structures of CHA zeolites.

	Si1	Si2	O1	O2	O3	O4	Cu1
H-CHA	0.0190	0.0186	0.0460	0.0386	0.0482	0.0453	✗
Cu-CHA	0.0131	0.0144	0.0623	0.0454	0.0337	0.0403	0.0412

Table 6.19: Selected bond lengths (Å) and bond angles (°) of dehydrated dehydrated CHA zeolites.

	H-CHA		Cu-CHA	
Bond lengths (Å)	Si1-O2 1.5925	Si2-O4 1.5921	Si1-O1 1.6265	Si2-O1 1.5946
	Si1-O3 1.6116	Si2-O2 1.6006	Si1-O2 1.6637	Si2-O2 1.6751
	Si1-O4 1.6132	Si2-O3 1.6056	Si1-O3 1.5954	Si2-O3 1.6141
	Si1-O1 1.6215	Si2-O1 1.6324	Si1-O4 1.5946	Si2-O4 1.5888
			Cu1-O2 2.1016	
Bond angles (°)	O2-Si1-O3 110.088	O4-Si2-O2 108.573	O4-Si1-O3 110.988	O4-Si2-O1 109.231
	O2-Si1-O4 108.845	O4-Si2-O3 108.638	O4-Si1-O1 109.018	O4-Si2-O3 110.597
	O2-Si1-O1 109.002	O4-Si2-O1 111.060	O4-Si1-O2 112.653	O4-Si2-O2 112.806
	O3-Si1-O4 108.465	O2-Si2-O3 109.907	O3-Si1-O1 110.501	O1-Si2-O3 110.579
	O3-Si1-O1 109.417	O2-Si2-O1 109.179	O3-Si1-O2 109.607	O1-Si2-O2 104.855
	O4-Si1-O1 111.015	O3-Si2-O1 109.469	O1-Si1-O2 103.852	O3-Si2-O2 108.635
			O2-Cu1-O2 118.845	

In this work, the residual potential over 6-MR could be observed not only from the structure solution but also from the kinematical refinement of dehydrated H-CHA. It is well-known that the dynamical diffraction effect occurs in electron diffraction data. Hence, the structure investigation based on kinematical approximation could not deliver unbiased structural model and are was not suitable for detecting a partial occupied Cu atom in our case. Finally it was confirmed by dynamical refinement of H-CHA that the additional potential maximum was artefact caused by the application kinematical approximation. Similar phenomenon happened also in the kinematical refinement of a silicide phase using electron diffraction data reported by Bowden et al.[62]. In kinematical approximation, it is assumed that the reflection intensity (I) derived from electron diffraction data is proportional to the amplitude square of structure factor (F^2_{hkl}).[139] However, the orientation and thickness of the measured crystal are additionally taken into account in the dynamical diffraction theory[66,139]. The consideration of dynamical diffraction effect produced a dramatic reduction of $R1$ values for both materials.

6.6.6 Summary

Cu-CHA was heated at 400 °C in high vacuum condition in TEM in order to remove water molecules. The position of Cu atom in dehydrated Cu-CHA was successfully detected and quantitatively determined with dynamical refinements of ADT data. In comparison with H-CHA, the extra potential in the middle of 6-MR indicated the location of Cu atom.

7 Conclusion

In this dissertation detailed structure analyses of nanocrystalline solids at an atomic resolution was performed. Apart from aluminium borate ($Al_4B_2O_9$) as a ceramic material several microporous materials (metal-organic frameworks and zeolites) have been investigated, already used industrially or with a perspective for future application. The projects foci, some carried out on the basis of advanced measurement conditions (low electron dose, low or high temperature), were set on the elucidation of complicated structural features, including *ab initio* structure solution of material with extra-large unit cell, structure determination of a polyphasic sample, elucidation of strong disordered crystal structures, detection of the position of organic molecules in zeolites, confirmation of the position of partially occupied metal atoms in a zeolite catalyst. The main applied technique was automated electron diffraction tomography (ADT), developed within the last decade, allowing for the automatic acquisition and reliable evaluation of three-dimensional electron diffraction data from single crystals, even on a nanometre-scale. To realize unbiased results, the structural characterization was supported by other approaches such as high-resolution TEM imaging (HRTEM or HAADF-STEM), X-ray powder diffraction (XRPD), solid-state NMR and thermal analysis (DTA/TG or DSC/TG). The beam sensitivity of the investigated compounds reached from stable inorganic ceramics $Al_4B_2O_9$ to highly beam sensitive MOFs and zeolites.

1. *Ab initio* structure solutions of beam sensitive metal-organic frameworks

In this work, the crystal structures of two new Zr-MOFs, CAU-27-BDC and Zr-CAU-30, both exhibiting needle-like nano-sized crystals, were determined using electron diffraction tomography and refined subsequently on X-ray powder diffraction data. This class of materials is highly electron beam sensitive rendering data acquisition had to be performed under sample cooling with a cryo-holder. CAU-27-BDC crystallizes in a unit cell with a volume of 4232 Å^3. Due to the large large unit cell of Zr-CAU-30, with a volume larger than 15000 Å^3, overlapping peaks and limited number of reflections, XRPD methods were not applicable for reliable crystal structure determination.

ADT data delivered body-centred tetragonal unit-cells in space groups $I4/mcm$ and $I4_1/acd$, respectively. *Ab initio* structure solution resulted in a complete and reasonable structural model. The refinement of the CAU-27-BDC crystal structure was possible with Rietveld-method against XRPD data. Because Zr-CAU-30 (as-synthesized phase) exhibits a large amount of water molecules in the channels, it was challenging to refine the crystal structure against XRPD data thus the crystal structure of the dehydrated phase was refined based on the structure model of as made phase from XRPD data. Transmission electron microscopic images for the elucidation of further structural details, accessible only through the application of a low-dose holographic routine, confirmed both crystal structures.

2. Structure determination of a new type zeolite in polyphasic sample/Confirmation of the metal atom in the framework

The structural characterization of a zinc-containing porous material is given in this work. As a novel zeolite type, the framework of THK-2 was elucidated by a combination of electron diffraction tomography, X-ray powder diffraction and HRTEM from a phase mixture with impure MTW zeolite. Since ADT, providing 3D reciprocal data, focuses on data collection from a single nano crystal this method is suitable to collect the crystallographic information of nano crystals distinguished by morphology. After indexing the reconstructed ADT data, the phases in the sample could be identified as a new phase of THK-2 (needle-liked crystals) and the known zeolite MTW (spherical particles). The structure was solved with direct methods from ADT data and finally refined with Rietveld methods against XRPD data. The position of the Zn atom is the centre of a disordered ZnO_4 tetrahedron with a partial occupancy of 0.2806. Quantitative refinement also confirmed a chemical composition of 82.35 wt% THK-2 and 17.65% MTW. HRTEM images viewed along [110] and [001] show the atomic details, which are consistent with the determined structure, confirming the final crystallographic data. The reliable structure solution of THK-2 indicates that ADT is the optimal method for structural characterization of samples containing phase mixtures.

3. Explanation of order-disorder phenomena in the crystal structure of $Al_4B_2O_9$

Aluminium borate $Al_4B_2O_9$, synthesized in a sol-gel approach, comprises of needle-like nanocrystals. Based on the crystal structure of synthetic $Al_4B_2O_9$ verified in the monoclinic space group $C2/m$ by electron diffraction tomographic data the focus of investigation was set on the observed order and disorder phenomena even occurring in the same crystal.

The crystal structure, later considered as the average structure, was determined from ADT data of an ordered crystal domain, where no diffuse scattering was observed. The *ab initio* structure solution delivered a well-resolved electron potentials map and a chemically meaningful model. High resolution techniques, HRTEM and HAADF-HRSTEM imaging, were utilized to verified reliable structure determination of the ordered $Al_4B_2O_9$. The observed diffuse scattering in the modulated diffraction patterns acquired from disordered domains/crystals indicates a mean superstructure with a threefold **b** axis. The crystal defects are caused by the stacking disorder of the ordered structure (Layer *A*) and a shifted model (Layer *B*: ½**a** and ½**c** shifts of layer *A*). Several superstructures were modelled based on the layers *A* and *B* and corresponding electron diffraction patterns were calculated. With a main *AAB* sequence including random inserts of *A* and *B* layers, simulated diffraction patterns involving additional stacking disorder illustrate a good agreement with experimental data. After analysing the ordered and disordered structure in a reliable way, the structural characteristic of $Al_4B_2O_9$ could be described completely. As the disorder occurs in mullite-type compounds frequently, the described combined approach may deliver a helpful strategy to study and explain the order and disorder structure in other mullite-type materials. In this work the approach was applied to a series of disordered zeolites.

4. Elucidation of disordered structure in zeolite

M-IEZ-RUB-36 comprises of a series of zeolite catalysts which are plate-like micrometre-sized crystals. Due to the difficulties in the structural analysis with XRPD, the structures of Zn-IEZ-RUB-36 and Ti-IEZ-RUB-36 were characterized by ADT technique. Strong diffuse streaks indicating disorder were detected and confirmed as stacking faults along the crystallographic *a* axis by reconstructed ADT data. The average crystal structures were solved in space group *Immm* for Zn-IEZ-RUB-36 and *Bbmm* for Ti-IEZ-RUB-36 directly from ADT data. Evaluation of 3D reciprocal space reveals a preferred layer stacking sequence of •••*ABAB*••• for Zn-IEZ-RUB-36 and •••*AAA*••• for Ti-IEZ-RUB-36. Additional disorder results from intercalation of layer *C* with metal atoms. Superstructures were modelled with various sequences in the software package DISCUS. Observed diffuse streaks were explained by simulation of electron diffraction patterns. The type of layer shift, the stacking sequence and the influence of metal atoms resulted in the disorder in the interlayer expansion reactions. It also revealed that the Ti atom replaces the Si atom in T-site much easier than Zn atom. As the occupancy of T-sites could not be exactly determined and the placement of metal atom in T-sites is also not clear, we could describe the disorder of M-IEZ-RUB-36 materials only qualitatively. The understanding of the structures details of M-IEZ-RUB-36 zeolite catalysts is essential to rationalize the excellent catalytic activity of the materials and to envisage possible modifications to improve the performance.

5. Determining the position of organic molecule in zeolites

In the study, as made aluminophosphate SSZ-51 was prepared with a novel organic template 1,2,6-trimethylpyridinium (TMP) and its calcination process was investigated by thermogravimetric analysis and temperature-dependent XRPD. Solid-state C-13 NMR spectroscopy was used to confirm the existence of organic templates inside the porous materials SSZ-51 and SOD. The crystal structure determinations were elucidated by a combination of single crystal electron diffraction and X-ray powder diffraction. The application of electron diffraction tomography on detecting the position of organic templates in inorganic as made porous materials was carried out based on the study of a new aluminophosphate TPM-SSZ-51 and the reinvestigation of reference sample silicate sodalite PYS-SOD. Structure analysis shows an ordered template position in monoclinic SSZ-51 and a dynamic ordered position in cubic SOD, which indicates that the probability to determine a definite template position is much higher with the appearance of low symmetric framework and high symmetric template molecules. The study shows that electron diffraction tomography, especially for a fast data acquisition from single nanosized crystals, can serve as a reliable and applicable method to determine the position of organic template in inorganic porous materials and can be further applied for the structural elucidation of new porous materials.

6. Detecting the position of metal atom in zeolite

Cu-chabazite (Cu-CHA) zeolite was investigated with a reference material H-CHA using electron diffraction tomography in order to confirm the Cu position in dehydrated phase. Cu-CHA consists of homogeneous cubic crystals with a diameter of about 600 nm. The dehydration was realized by heating in vacuum of TEM at 400 °C for 2 h. Cu-CHA is zeolite catalyst for selective catalytic reduction (SCR) in which Cu atoms are catalytic active sites. Structure solutions from ADT data delivered well-resolved electron potential maps with all framework atoms and additional potentials for both materials. Difference electrostatic potential maps from kinematic structure refinements show the extra potential above the 6-member ring (MR) in dehydrated H-CHA but in the 6-MR in dehydrated Cu-CHA. Taking into account the dynamic effect of electron diffraction data, dynamical refinements were introduced to distinguish the observed extra potentials in the pores. Successful dynamical refinements identified the existence of the observed potentials in the 6-MR in dehydrated Cu-CHA and delivered reasonable bond lengths and angles. The refined Cu occupancy of 43.81%, in accordance with 7.17 wt%, is comparable with the value from element analyse (about 6.0 wt% from ICP).

In summary, the structural characterizations of different microporous crystalline materials, all exhibiting problems for structure analysis by X-ray powder diffraction, could be performed with the application of electron diffraction tomography method, and confirmed with other techniques such as HRTEM and XRPD. Based on the investigation of the electron beam stable but disordered material $Al_4B_2O_9$ it was possible to deliver a deeper insight into disorder effects in zeolites. Other objectives including not only crystal structure determination of new frameworks but also the atomic arrangement of a guest molecule/ion are the location of metal atoms in the framework or in the cavities as well as the determination of the position of organic molecules in the pores.

In this dissertation, the studies cover almost all structural features of microporous materials – atomic arrangement of framework atoms and guest molecule/ion in the pose and contribute the referential experience upon the structural investigation of porous materials. The detailed structural characterization gives clear insights into the chemical and physical properties, which further enables to optimize industrial applications and to design new types of functional materials. The utilization of electron diffraction tomography allows to investigate porous materials with respect to e.g. explanation for the intergrowth of zeolites, the determination of the metal atom position with larger radius in SCR zeolite catalysts (e.g. Y-CHA) in the future. The technique of electron diffraction tomography has shown its power on the structural investigation of nanosized materials with crystallographic challenges in the case of structures with large unit cells, disorder, superstructures, pseudosymmetry, low crystallinity and for impure or multiphase samples. It can be applied to a wide field of open questions in the field of structure analysis and has the potential to develop into a standard method in the research for material science and related fields.

References

[1] Robert W. Cahn. *The coming of materials science*, volume v. 5 of *Pergamon materials series*. New York, Amsterdam, 1st ed. edition, 2010. ISBN 9781281071989.

[2] Xiao Dong Li. Application of New Materials in Industrial Design. *Key Engineering Materials*, 693:1960–1965, 2016.

[3] Marc A. Meyers and Krishan Kumar Chawla. *Mechanical behavior of materials*. Cambridge University Press, Cambridge and New York, 2nd edition, 2009. ISBN 9780521866750.

[4] Eric J. Mittemeijer. *Fundamentals of Materials Science: The Microstructure-Property Relationship Using Metals as Model Systems*. (Keine Angabe). Springer-Verlag Berlin Heidelberg, Berlin, Heidelberg, 2011. ISBN 9783642104992.

[5] William D. Callister and David G. Rethwisch. *Materials science and engineering: An introduction*. Wiley, Hoboken, NJ, 9th edition, wiley binder version edition, opyright 2014. ISBN 1118477707.

[6] Hugh O. Pierson. *Handbook of carbon, graphite, diamond and fullerenes: Properties, processing and applications*. Noyes Publ, Park Ridge, NJ, 1993. ISBN 0815513399.

[7] Catherine E. Housecroft and Alan G. Sharpe. *Anorganische Chemie*. Addison-Wesley Verlag, München, auflage: 2., aktualisierte auflage edition, 2006. ISBN 978-3-8273-7192-8.

[8] Christian Baerlocher, Lynne B. McCusker, and David H. Olson. *Atlas of zeolite framework types*. Elsevier, Amsterdam, 6th rev. ed. edition, 2007. ISBN 0444530649. URL `http://www.iza-structure.org/databases/`.

[9] Herman van Bekkum. *Introduction to zeolite science and practice*, volume 137 of *Studies in surface science and catalysis*. Elsevier, Amsterdam, 2nd edition edition, 2001. ISBN 0444824219.

[10] Miki Niwa, Naonobu Katada, and Kazu Okumura. *Characterization and design of zeolite catalysts: Solid acidity, shape selectivity and loading properties*, volume 141 of *Springer Series in Materials Science*. Springer, Berlin, 2010. ISBN 9783642126208.

[11] A. R. West. *Grundlagen Der Festkörperchemie*. Wiley-VCH, Weinheim, 2000.

[12] Lesley Smart and E. Moore. *Solid State Chemistry*. CRC, Boca Raton and Fla and London, 3 edition, 2004. ISBN 978-0-7487-7516-3.

[13] M. K. Wilkinson, J. W. Cable, E. O. Wollan, and W. C. Koehler. Neutron Diffraction Investigations of the Magnetic Ordering in FeBr2 , CoBr2, FeCl2 , and CoCl2. *Physical Review*, 113(2):497–507, 1959.

[14] Russell E. Morris, Scott J. Weigel, Neil J. Henson, Lucy M. Bull, Michael T. Janicke, Bradley F. Chmelka, and Anthony K. Cheetham. A Synchrotron X-ray Diffraction, Neutron Diffraction, 29Si MAS-NMR, and Computational Study of the Siliceous Form of Zeolite Ferrierite. *Journal of the American Chemical Society*, 116(26):11849–11855, 1994.

[15] Chick C. Wilson. *Single crystal neutron diffraction from molecular materials*, volume 2 of *Series on neutron techniques and applications*. World Scientific, Singapore u.a., 2000. ISBN 981-02-3776-6.

[16] Jeffrey E. Post, Peter J. Heaney, and Jonathan Hanson. Synchrotron X-ray diffraction study of the structure and dehydration behavior of todorokite. *American Mineralogist*, 88(1):142–150, 2003.

[17] Paula M. B. Piccoli, Thomas F. Koetzle, and Arthur J. Schultz. Single crystal neutron diffraction for the inorganic chemist - a practical guide. *Comments on Inorganic Chemistry*, 28(1-2):3–38, 2007.

[18] R. E. Dinnebier and S. J. L. Billinge. *Powder Diffraction: Theory and Practice*. Royal Society of Chemistry, Cambridge, 2008. ISBN 0-85404-231-8.

[19] Ludwig Reimer. *Scanning Electron Microscopy: Physics of Image Formation and Microanalysis*, volume 45 of *Springer Series in Optical Sciences*. Springer Berlin Heidelberg, Berlin, Heidelberg and s.l., second completely revised and updated edition edition, 1998. ISBN 9783642083723.

[20] Joseph I. Goldstein, Dale E. Newbury, Patrick Echlin, David C. Joy, Charles Fiori, and Eric Lifshin. *Scanning Electron Microscopy and X-Ray Microanalysis: A Text for Biologist, Materials Scientist, and Geologists*. Springer US, Boston, MA, 1981. ISBN 9781461332756.

[21] D. B. Williams and C. B. Carter. *Transmission Electron Microscopy: A Textbook for Materials Science*. Springer, New York, 2 edition, 2009. ISBN 0-387-76500-X.

[22] C. Kisielowski, B. Freitag, M. Bischoff, H. van Lin, S. Lazar, G. Knippels, P. Tiemeijer, M. van der Stam, S. von Harrach, M. Stekelenburg, M. Haider, S. Uhlemann, H. Mueller, P. Hartel, B. Kabius, D. Miller, I. Petrov, E. A. Olson, T. Donchev, E. A. Kenik, A. R. Lupini, J. Bentley, S. J. Pennycook, I. M. Anderson, A. M. Minor, A. K. Schmid, T. Duden, V. Radmilovic, Q. M. Ramasse, M. Watanabe, R. Erni, E. A. Stach, P. Denes, and U. Dahmen. Detection of Single Atoms and Buried Defects in Three Dimensions by Aberration-Corrected Electron Microscope with 0.5-Angstrom Information Limit. *Microsc. microanal.*, 14(5):469–477, 2008.

[23] C. A. Fyfe, H. Gies, G. T. Kokotailo, B. Marler, and D. E. Cox. Crystal structure of silica-ZSM-12 by the combined use of hgh-resolution solid-state MAS NMR spectroscopy and synchrotron x-ray powder diffraction. *The Journal of Physical Chemistry*, 94(9): 3718–3721, 1990.

[24] Scott J. Weigel, Jean-Christophe Gabriel, E. Guttierez Puebla, A. Monge Bravo, Neil J. Henson, Lucy M. Bull, and Anthony K. Cheetham. Structure-Directing Effects in Zeolite Synthesis: A Single-Crystal X-ray Diffraction, 29 Si MAS NMR, and Computational Study of the Competitive Formation of Siliceous Ferrierite and Dodecasil-3C (ZSM-39). *Journal of the American Chemical Society*, 118(10):2427–2435, 1996.

[25] Benjaram M. Reddy, Ataullah Khan, Pandian Lakshmanan, Mimoun Aouine, Stéphane Loridant, and Jean-Claude Volta. Structural characterization of nanosized CeO(2)-SiO(2), CeO(2)-TiO(2), and CeO(2)-ZrO(2) catalysts by XRD, Raman, and HREM techniques. *The journal of physical chemistry. B*, 109(8):3355–3363, 2005.

[26] G. M. Ingo, S. Balbi, T. de Caro, I. Fragalà, E. Angelini, and G. Bultrini. Combined use of SEM-EDS, OM and XRD for the characterization of corrosion products grown on silver roman coins. *Applied Physics A*, 83(4):493–497, 2006.

[27] Benjaram M. Reddy, Pankaj Bharali, Pranjal Saikia, Gode Thrimurthulu, Yusuke Yamada, and Tetsuhiko Kobayashi. Thermal Stability and Dispersion Behavior of Nanostructured Ce x Zr 1− x O 2 Mixed Oxides over Anatase-TiO 2 : A Combined Study of CO Oxidation and Characterization by XRD, XPS, TPR, HREM, and UV−Vis DRS. *Industrial & Engineering Chemistry Research*, 48(1):453–462, 2009.

[28] William Morris, Caitlin J. Stevens, R. E. Taylor, C. Dybowski, Omar M. Yaghi, and Miguel A. Garcia-Garibay. NMR and X-Ray Study Revealing the Rigidity of Zeolitic Imidazolate Frameworks. *J. Phys. Chem. C*, 116(24):13307–13312, 2012.

[29] K. Hoffmann, T. J. N. Hooper, H. Zhao, U. Kolb, M. M. Murshed, M. Fischer, H. Lührs, G. Nénert, P. Kud\v ejová, A. Senyshyn, H. Schneider, J. V. Hanna, Th. M. Gesing, and R. X. Fischer. Crystal Chemical Characterization of Mullite-Type Aluminum Borate Compounds. *Journal of Solid State Chemistry*, 247:173–187, 2017.

[30] H. Zhao, Y. Krysiak, Kristin Hoffmann, Bastian Barton, Leopoldo Molina-Luna, Reinhard B. Neder, Hans Joachim Kleebe, Thorsten M. Gesing, Hartmut Schneider, Reinhard X. Fischer, and Ute Kolb. Elucidating Structural Order and Disorder Phenomena in Mullite-Type Al4B2O9 by Automated Electron Diffraction Tomography. *Journal of Solid State Chemistry*, 249:114–123, 2017.

[31] W. Massa. *Kristallstrukturbestimmung*. Studienbücher Chemie. Vieweg & Teubner, Wiesbaden, 7 edition, 2011. ISBN 3-8348-1726-0.

[32] Vitalij K. Pecharsky and Peter Y. Zavalij. *Fundamentals of Powder Diffraction and Structural Characterization of Materials*. Springer US, Boston, MA, 2. ed. edition, 2009. ISBN 9780387095783. URL `http://site.ebrary.com/lib/alltitles/docDetail.action?docID=10266944`.

[33] R. Allmann. *Röntgenpulverdiffraktometrie: Rechnergestützte Auswertung, Phasenanalyse Und Strukturbestimmung*. Springer, Heidelberg, 2 edition, 2003. ISBN 3-540-43967-6.

[34] Jian Li and Junliang Sun. Application of X-ray Diffraction and Electron Crystallography for Solving Complex Structure Problems. *Accounts of Chemical Research*, 50(11):2737–2745, 2017.

[35] Kuei-Jung Chao, Jia-Ching Lin, Y. Wang, and G. H. Lee. Single crystal structure refinement of TPA ZSM-5 zeolite. *Zeolites*, 6(1):35–38, 1986.

[36] S. Liu, Y. J. Lu, M. M. Kappes, and J. A. Ibers. The structure of the c60 molecule: x-ray crystal structure determination of a twin at 110 k. *Science (New York, N.Y.)*, 254(5030): 408–410, 1991.

[37] M. U. Schmidt, M. Ermrich, and R. E. Dinnebier. Determination of the Structure of the Violet Pigment C22H12Cl2N6O4 from a Non-Indexed X-Ray Powder Diagram. *Acta Crystallographica Section B: Structural Science*, 61(1):37–45, 2005.

[38] Martin U. Schmidt, Detlef W. M. Hofmann, Christian Buchsbaum, and Hans Joachim Metz. Kristallstrukturen von Pigment Red 170 und Derivaten, bestimmt aus Röntgenpulverdiagrammen. *Angewandte Chemie*, 118(8):1335–1340, 2006.

[39] Avelino Corma, Maria J. Diaz-Cabanas, Jose L. Jorda, Fernando Rey, German Sastre, and Karl G. Strohmaier. A zeolitic structure (ITQ-34) with connected 9- and 10-ring channels obtained with phosphonium cations as structure directing agents. *Journal of the American Chemical Society*, 130(49):16482–16483, 2008.

[40] Haishuang Zhao, Alexander Bodach, Miriam Heine, Yasar Krysiak, Jürgen Glinnemann, Edith Alig, Lothar Fink, and Martin U. Schmidt. 4-Cyanopyridine, a versatile mono- and bidentate ligand. Crystal structures of related coordination polymers determined by X-ray powder diffraction. *CrystEngComm*, 19(16):2216–2228, 2017.

[41] X. Zou, S. Hovmöller, and P. Oleynikov. *Electron Crystallography: Electron Microscopy and Electron Diffraction*, volume 16 of *IUCr texts on crystallography*. Oxford University Press, Oxford and New York, 2011. ISBN 978-0-19-958020-0.

[42] U. Kolb, K. Shankland, L. Meshi, A. Avilov, and W. David. *Uniting Electron Crystallography and Powder Diffraction*. NATO science for peace and security. Series B: physics and biophysics. Springer, Dordrecht, 2012. ISBN 978-94-007-5579-6.

[43] U. Kolb, T. Gorelik, C. Kübel, M. T. Otten, and D. Hubert. Towards Automated Diffraction Tomography. Part I Data Acquisition. *Ultramicroscopy*, 107(6):507–513, 2007.

[44] U. Kolb, T. Gorelik, and M. T. Otten. Towards Automated Diffraction Tomography. Part II Cell Parameter Determination. *Ultramicroscopy*, 108(8):763–772, 2008.

[45] U. Kolb, E. Mugnaioli, and T. E. Gorelik. Automated Electron Diffraction Tomography a New Tool for Nano Crystal Structure Analysis. *Cryst. Res. Technol.*, 46(6):542–554, 2011.

[46] T. E. Gorelik, A. A. Stewart, and U. Kolb. Structure solution with automated electron diffraction tomography data: different instrumental approaches. *Journal of microscopy*, 244(3):325–331, 2011.

[47] E. Mugnaioli and Ute Kolb. Applications of Automated Diffraction Tomography (ADT) on Nanocrystalline Porous Materials. *Microporous Mesoporous Mat*, 166:93–101, 2013.

[48] D. Zhang, P. Oleynikov, S. Hovmöller, and X. Zou. Collecting 3D Electron Diffraction Data by the Rotation Method. *Z. Kristallogr.*, 225(2-3):94–102, 2010.

[49] Wei Wan, Junliang Sun, Jie Su, Sven Hovmöller, and Xiaodong Zou. Three-dimensional rotation electron diffraction: software RED for automated data collection and data processing. *Journal of Applied Crystallography*, 46(Pt 6):1863–1873, 2013.

[50] Jie Su, Elina Kapaca, Leifeng Liu, Veselina Georgieva, Wei Wan, Junliang Sun, Valentin Valtchev, S. Hovmöller, and X. Zou. Structure Analysis of Zeolites by Rotation Electron Diffraction (RED). *Microporous and Mesoporous Materials*, 189:115–125, 2014.

[51] Peng Guo, Leifeng Liu, Yifeng Yun, Jie Su, Wei Wan, Hermann Gies, Haiyan Zhang, Feng-Shou Xiao, and X. Zou. Ab Initio Structure Determination of Interlayer Expanded Zeolites by Single Crystal Rotation Electron Diffraction. *Dalton Transactions*, 43(27): 10593, 2014.

[52] Peng Guo, Jiho Shin, Alex G. Greenaway, Jung Gi Min, Jie Su, Hyun June Choi, Leifeng Liu, Paul A. Cox, Suk Bong Hong, Paul A. Wright, and X. Zou. A Zeolite Family with Expanding Structural Complexity and Embedded Isoreticular Structures. *Nature*, 524 (7563):74–78, 2015.

[53] M. Gemmi, La Placa, M. G. I., A. S. Galanis, E. F. Rauch, and S. Nicolopoulos. Fast electron diffraction tomography. *Journal of Applied Crystallography*, 48(3):718–727, 2015.

[54] J. Simancas, R. Simancas, P. J. Bereciartua, J. L. Jorda, F. Rey, A. Corma, S. Nicolopoulos, P. Pratim Das, M. Gemmi, and E. Mugnaioli. Ultrafast Electron Diffraction Tomography for Structure Determination of the New Zeolite ITQ-58. *Journal of the American Chemical Society*, 138(32):10116–10119, 2016.

[55] Yunchen Wang, Sofia Takki, Ocean Cheung, Hongyi Xu, Wei Wan, Lars Öhrström, and A. Ken Inge. Elucidation of the elusive structure and formula of the active pharmaceutical ingredient bismuth subgallate by continuous rotation electron diffraction. *Chemical communications (Cambridge, England)*, 53(52):7018–7021, 2017.

[56] Bin Wang, Timo Rhauderwiek, A. Ken Inge, Hongyi Xu, Taimin Yang, Zhehao Huang, Norbert Stock, and Xiaodong Zou. A Porous Cobalt Tetraphosphonate Metal-Organic Framework: Accurate Structure and Guest Molecule Location Determined by Continuous-Rotation Electron Diffraction. *Chemistry (Weinheim an der Bergstrasse, Germany)*, 24(66):17429–17433, 2018.

[57] J. Jiang, J. L. Jorda, J. Yu, L. A. Baumes, E. Mugnaioli, M. J. Diaz-Cabanas, U. Kolb, and A. Corma. Synthesis and Structure Determination of the Hierarchical Meso-Microporous Zeolite ITQ-43. *Science*, 333(6046):1131–1134, 2011.

[58] E. Mugnaioli, Iryna Andrusenko, Timo Schüler, Niklas Loges, Robert E. Dinnebier, Martin Panthöfer, Wolfgang Tremel, and Ute Kolb. Ab Initio Structure Determination of Vaterite by Automated Electron Diffraction. *Angewandte Chemie International Edition*, 51(28):7041–7045, 2012.

[59] Tom Willhammar, Yifeng Yun, and X. Zou. Structural Determination of Ordered Porous Solids by Electron Crystallography. *Advanced Functional Materials*, 24(2):182–199, 2014.

[60] Wei Hua, Hong Chen, Zheng-Bao Yu, X. Zou, Jianhua Lin, and Junliang Sun. A Germanosilicate Structure with 11 x 11 x 12-Ring Channels Solved by Electron Crystallography. *Angew. Chem.-Int. Edit.*, 53(23):5868–5871, 2014.

[61] A. Ken Inge, Milan Köppen, Jie Su, Mark Feyand, Hongyi Xu, Xiaodong Zou, Michael O'Keeffe, and Norbert Stock. Unprecedented Topological Complexity in a Metal-Organic Framework Constructed from Simple Building Units. *Journal of the American Chemical Society*, 138(6):1970–1976, 2016.

[62] D. Bowden, Y. Krysiak, L. Palatinus, D. Tsivoulas, S. Plana-Ruiz, E. Sarakinou, U. Kolb, D. Stewart, and M. Preuss. A high-strength silicide phase in a stainless steel alloy designed for wear-resistant applications. *Nature communications*, 9(1):1374, 2018.

[63] W. Wan, J. Su, X. d. Zou, and T. Willhammar. Transmission electron microscopy as an important tool for characterization of zeolite structures. *Inorganic Chemistry Frontiers*, 5(11):2836–2855, 2018.

[64] A. Avilov, K. Kuligin, S. Nicolopoulos, M. Nickolskiy, K. Boulahya, J. Portillo, G. Lepeshov, B. Sobolev, J. P. Collette, N. Martin, A. C. Robins, and P. Fischione. Precession technique and electron diffractometry as new tools for crystal structure analysis and chemical bonding determination. *Ultramicroscopy*, 107(6-7):431–444, 2007.

[65] E. Mugnaioli, T. Gorelik, and U. Kolb. "Ab initio" structure solution from electron diffraction data obtained by a combination of automated diffraction tomography and precession technique. *Ultramicroscopy*, 109(6):758–765, 2009.

[66] Lukáš Palatinus, Cinthia Antunes Corrêa, Gwladys Steciuk, Damien Jacob, Pascal Roussel, Philippe Boullay, Mariana Klementová, Mauro Gemmi, Jaromír Kopeček, M. Chiara Domeneghetti, Fernando Cámara, and Václav Petříček. Structure refinement using precession electron diffraction tomography and dynamical diffraction: tests on experimental data. *Acta crystallographica Section B, Structural science, crystal engineering and materials*, 71(Pt 6):740–751, 2015.

[67] Ute Kolb, Tatiana E. Gorelik, Enrico Mugnaioli, and Andrew Stewart. Structural Characterization of Organics Using Manual and Automated Electron Diffraction. *Polymer Reviews*, 50(3):385–409, 2010.

[68] Mark Feyand, E. Mugnaioli, Frederik Vermoortele, Bart Bueken, Johannes M. Dieterich, Tim Reimer, Ute Kolb, Dirk de Vos, and Norbert Stock. Automated Diffraction Tomography for the Structure Elucidation of Twinned, Sub-Micrometer Crystals of a Highly Porous, Catalytically Active Bismuth Metal-Organic Framework. *Angewandte Chemie International Edition*, 51(41):10373–10376, 2012.

[69] Iryna Andrusenko, Y. Krysiak, E. Mugnaioli, T. E. Gorelik, Diana Nihtianova, and Ute Kolb. Structural Insights into M 2 OAl 2 O 3 WO 3 (M = Na, K) System by Electron Diffraction Tomography. *Acta Crystallographica Section B Structural Science, Crystal Engineering and Materials*, 71(3):349–357, 2015.

[70] T. E. Gorelik, C. Czech, S. M. Hammer, and M. U. Schmidt. Crystal Structure of Disordered Nanocrystalline II -Quinacridone Determined by Electron Diffraction. *CrystEngComm*, 18(4):529–535, 2016.

[71] Haishuang Zhao, Yaşar Krysiak, Kristin Hoffmann, Bastian Barton, Leopoldo Molina-Luna, Reinhard B. Neder, Hans-Joachim Kleebe, Thorsten M. Gesing, Hartmut Schneider, Reinhard X. Fischer, and Ute Kolb. Elucidating structural order and disorder

phenomena in mullite-type Al 4 B 2 O 9 by automated electron diffraction tomography. *Journal of Solid State Chemistry*, 249:114–123, 2017.

[72] Timo Rhauderwiek, Haishuang Zhao, Patrick Hirschle, Markus Döblinger, Bart Bueken, Helge Reinsch, Dirk de Vos, Stefan Wuttke, Ute Kolb, and Norbert Stock. Highly stable and porous porphyrin-based zirconium and hafnium phosphonates – electron crystallography as an important tool for structure elucidation. *Chemical Science*, 9(24):5467–5478, 2018.

[73] Yaşar Krysiak, Bastian Barton, Bernd Marler, Reinhard B. Neder, and Ute Kolb. Ab initio structure determination and quantitative disorder analysis on nanoparticles by electron diffraction tomography. *Acta crystallographica. Section A, Foundations and advances*, 74(Pt 2):93–101, 2018.

[74] Renzhi Ma, Yoshio Bando, Tadao Sato, Chengchun Tang, and Fangfang Xu. Single-Crystal Al18B4O33 Microtubes. *Journal of the American Chemical Society*, 124(36):10668–10669, 2002.

[75] J. Zhang, Y. Huang, J. Lin, X. X. Ding, Z. X. Huang, S. R. Qi, and C. C. Tang. From Al4B2O9 Nanowires to BN-Coated Al18B4O33 Nanowires. *The Journal of Physical Chemistry B*, 109(27):13060–13062, 2005.

[76] J. Zhang, J. Lin, H. S. Song, E. M. Elssfah, S. J. Liu, J. J. Luo, X. X. Ding, C. Tang, and S. R. Qi. Bulk-Quantity Fast Production of Al4B2O9/Al18B4O33 Single-Crystal Nanorods by a Novel Technique. *Materials Letters*, 60(27):3292–3295, 2006.

[77] Reinhard X. Fischer, Volker Kahlenberg, Dietmar Voll, Kenneth J. D. MacKenzie, Mark E. Smith, Bernhard Schnetger, Hans-Jürgen Brumsack, and Hartmut Schneider. Crystal Structure of Synthetic Al4B2O9: A Member of the Mullite Family Closely Related to Boralsilite. *American Mineralogist*, 93(5-6):918–927, 2008.

[78] Martin Fisch, Thomas Armbruster, Daniel Rentsch, Eugen Libowitzky, and Thomas Pettke. Crystal-Chemistry of Mullite-Type Aluminoborates Al18B4O33 and Al5BO9: A Stoichiometry Puzzle. *Journal of Solid State Chemistry*, 184(1):70–80, 2011.

[79] Anja Stachowiak and Werner Schreyer. Synthesis, stability and breakdown products of the hydroxyl end member of jeremejevite in the system Al2O3-B2O3-H2O. *European Journal of Mineralogy*, 10(5):875–888, 1998.

[80] Xinyong Tao, Xinnan Wang, and Xiaodong Li. Nanomechanical Characterization of One-Step Combustion-Synthesized Al4B2O9 and Al18B4O33 Nanowires. *Nano Letters*, 7(10):3172–3176, 2007.

[81] Reinhard X. Fischer and Hartmut Schneider. Crystal Chemistry of Borates and Borosilicates with Mullite-Type Structures: A Review. *European Journal of Mineralogy*, 20(5):917–933, 2008.

[82] G. Diego Gatta, Nicola Rotiroti, Martin Fisch, and Thomas Armbruster. Stability at High Pressure, Elastic Behavior and Pressure-Induced Structural Evolution of "Al5BO9", a Mullite-Type Ceramic Material. *Physics and Chemistry of Minerals*, 37(4): 227–236, 2010.

[83] David J. Tranchemontagne, José L. Mendoza-Cortés, Michael O'Keeffe, and Omar M. Yaghi. Secondary building units, nets and bonding in the chemistry of metal-organic frameworks. *Chemical Society Reviews*, 38(5):1257–1283, 2009.

[84] Alexander Schoedel, Mian Li, Dan Li, Michael O'Keeffe, and Omar M. Yaghi. Structures of Metal-Organic Frameworks with Rod Secondary Building Units. *Chemical Reviews*, 116(19):12466–12535, 2016.

[85] J. Haber. Manual on catalyst characterization (Recommendations 1991). *Pure and Applied Chemistry*, 63(9):1227–1246, 1991.

[86] J. Rouquerol, D. Avnir, C. W. Fairbridge, D. H. Everett, J. M. Haynes, N. Pernicone, J. D. F. Ramsay, K. S. W. Sing, and K. K. Unger. Recommendations for the Characterization of Porous Solids. *Pure and Applied Chemistry*, 66(8):1739–1758, 2009.

[87] Adrien P. Côté, Annabelle I. Benin, Nathan W. Ockwig, Michael O'Keeffe, Adam J. Matzger, and Omar M. Yaghi. Porous, crystalline, covalent organic frameworks. *Science (New York, N.Y.)*, 310(5751):1166–1170, 2005.

[88] Norbert Stock and Shyam Biswas. Synthesis of metal-organic frameworks (MOFs): Routes to various MOF topologies, morphologies, and composites. *Chemical Reviews*, 112(2):933–969, 2012.

[89] Geoffrey A. Ozin, Alex Kuperman, and Andreas Stein. Advanced Zeolite, Materials Science. *Angewandte Chemie International Edition in English*, 28(3):359–376, 1989.

[90] S. G. Hedge, P. Ratnasamy, L. M. Kustov, and V. B. Kazansky. Acidity and catalytic activity of SAPO-5 and AlPO-5 molecular sieves. *Zeolites*, 8(2):137–141, 1988.

[91] Michel Guisnet and Jean-Pierre Gilson. *Zeolites for Cleaner Technologies*, volume 3. PUBLISHED BY IMPERIAL COLLEGE PRESS AND DISTRIBUTED BY WORLD SCIENTIFIC PUBLISHING CO, 2002. ISBN 978-1-86094-329-4.

[92] Dang-guo Cheng, Xiaoxu Zhao, Fengqiu Chen, and Xiaoli Zhan. Effect of preparation method on iron-containing AlPO-5 for selective catalytic reduction of N2O with methane in the presence of steam. *Catalysis Communications*, 10(10):1450–1453, 2009.

[93] Minyoung Yoon, Renganathan Srirambalaji, and Kimoon Kim. Homochiral metal-organic frameworks for asymmetric heterogeneous catalysis. *Chemical Reviews*, 112(2): 1196–1231, 2012.

[94] JeongYong Lee, Omar K. Farha, John Roberts, Karl A. Scheidt, SonBinh T. Nguyen, and Joseph T. Hupp. Metal-organic framework materials as catalysts. *Chemical Society Reviews*, 38(5):1450–1459, 2009.

[95] J. Juan-Juan, J. P. Marco-Lozar, F. Suárez-García, D. Cazorla-Amorós, and A. Linares-Solano. A comparison of hydrogen storage in activated carbons and a metal–organic framework (MOF-5). *Carbon*, 48(10):2906–2909, 2010.

[96] Sang Soo Han, Hiroyasu Furukawa, Omar M. Yaghi, and William A. Goddard. Covalent organic frameworks as exceptional hydrogen storage materials. *Journal of the American Chemical Society*, 130(35):11580–11581, 2008.

[97] Manuel Moliner, Fernando Rey, and Avelino Corma. Towards the rational design of efficient organic structure-directing agents for zeolite synthesis. *Angewandte Chemie (International ed. in English)*, 52(52):13880–13889, 2013.

[98] Qing Min Wang, Dongmin Shen, Martin Bülow, Miu Ling Lau, Shuguang Deng, Frank R. Fitch, Norberto O. Lemcoff, and Jessica Semanscin. Metallo-organic molecular sieve for gas separation and purification. *Microporous and Mesoporous Materials*, 55(2): 217–230, 2002.

[99] Min Hui Yap, Kam Loon Fow, and George Zheng Chen. Synthesis and applications of MOF-derived porous nanostructures. *Green Energy & Environment*, 2(3):218–245, 2017.

[100] Alexander U. Czaja, Natalia Trukhan, and Ulrich Müller. Industrial applications of metal-organic frameworks. *Chemical Society Reviews*, 38(5):1284–1293, 2009.

[101] Patricia Horcajada, Christian Serre, María Vallet-Regí, Muriel Sebban, Francis Taulelle, and Gérard Férey. Metal–Organic Frameworks as Efficient Materials for Drug Delivery. *Angewandte Chemie*, 118(36):6120–6124, 2006.

[102] Patricia Horcajada, Christian Serre, Guillaume Maurin, Naseem A. Ramsahye, Francisco Balas, María Vallet-Regí, Muriel Sebban, Francis Taulelle, and Gérard Férey. Flexible porous metal-organic frameworks for a controlled drug delivery. *Journal of the American Chemical Society*, 130(21):6774–6780, 2008.

[103] Juan Liang, Hongyuan Li, Sugin Zhao, Wenggui Guo, Ronghui Wang, and Muliang Ying. Characteristics and performance of SAPO-34 catalyst for methanol-to-olefin conversion. *Applied Catalysis*, 64:31–40, 1990.

[104] Bart P.C. Hereijgers, Francesca Bleken, Merete H. Nilsen, Stian Svelle, Karl-Petter Lillerud, Morten Bjørgen, Bert M. Weckhuysen, and Unni Olsbye. Product shape selectivity dominates the Methanol-to-Olefins (MTO) reaction over H-SAPO-34 catalysts. *Journal of Catalysis*, 264(1):77–87, 2009.

[105] W. Vermeiren and J.-P. Gilson. Impact of Zeolites on the Petroleum and Petrochemical Industry. *Topics in Catalysis*, 52(9):1131–1161, 2009.

[106] Lu Zhang and Yining Huang. Crystallization and catalytic properties of molecular sieve SAPO-34 by a vapor-phase transport method. *J. Mater. Chem. A*, 3(8):4522–4529, 2015.

[107] Hao Xu, Qinming Wu, Yueying Chu, Jingang Jiang, Ling Zhang, Shuxiang Pan, Changsheng Zhang, Longfeng Zhu, Feng Deng, Xiangju Meng, Stefan Maurer, Robert McGuire, Andrei-Nicolae Parvulescu, Ulrich Müller, and Feng-Shou Xiao. Efficient synthesis of aluminosilicate RTH zeolite with good catalytic performances in NH 3 -SCR and MTO reactions. *J. Mater. Chem. A*, 6(18):8705–8711, 2018.

[108] Limin Ren, Longfeng Zhu, Chengguang Yang, Yanmei Chen, Qi Sun, Haiyan Zhang, Caijin Li, Faisal Nawaz, Xiangju Meng, and Feng-Shou Xiao. Designed copper-amine complex as an efficient template for one-pot synthesis of Cu-SSZ-13 zeolite with excellent activity for selective catalytic reduction of NOx by NH3. *Chemical communications (Cambridge, England)*, 47(35):9789–9791, 2011.

[109] Kirill A. Lomachenko, Elisa Borfecchia, Silvia Bordiga, Alexander V. Soldatov, Pablo Beato, and Carlo Lamberti. Active Sites in Cu-SSZ-13 deNOx Catalyst under Reaction Conditions: A XAS/XES Perspective. *Journal of Physics: Conference Series*, 712:012041, 2016.

[110] A. M. Beale, I. Lezcano-Gonzalez, W. A. Slawinksi, and D. S. Wragg. Correlation between Cu Ion Migration Behaviour and deNO x Activity in Cu-SSZ-13 for the Standard NH 3 -SCR Reaction. *Chem. Commun.*, 52(36):6170–6173, 2016.

[111] Douglas W. Crandell, H. Zhu, Xiaofan Yang, John Hochmuth, and Mu-Hyun Baik. The Mechanism of Selective Catalytic Reduction of NO x on Cu-SSZ-13 a Computational Study. *Dalton Trans*, 2017.

[112] Walter Borchardt-Ott. *Crystallography: An Introduction*. Springer-Verlag Berlin Heidelberg, Berlin, Heidelberg, 2012. ISBN 9783642164514. URL `http://dx.doi.org/10.1007/978-3-642-16452-1`.

[113] Horst Scholze. *Glas: Natur, Struktur und Eigenschaften*. Springer Berlin Heidelberg, Berlin, Heidelberg and s.l., dritte, neubearbeitete auflage edition, 1988. ISBN 9783662074961. URL `http://dx.doi.org/10.1007/978-3-662-07495-4`.

[114] D. Schwarzenbach. *Kristallographie*. Springer, Heidelberg, 2001.

[115] Christopher Hammond. *The basics of crystallography and diffraction*, volume 21 of *International Union of Crystallography book series*. Oxford University Press, Oxford and New York, fourth edition, reprinted (with corrections) edition, 2016. ISBN 9780198738688.

[116] Th. Hahn, H. Fuess, H. Wondratschek, U. Müller, U. Shmueli, E. Prince, A. Authier, V. Kopský, D. B. Litvin, M. G. Rossmann, E. Arnold, S. Hall, and B. McMahon, editors. *International Tables for Crystallography: Space-Group Symmetry*, volume A of *International Tables for Crystallography*. International Union of Crystallography, Chester, England, 1 edition, 2006. ISBN 978-0-7923-6590-7 978-1-4020-5406-8.

[117] W. Kleber, H. J. Bautsch, and J. Bohm. *Einführung in Die Kristallographie*. Oldenbourg, München, 19 edition, 2010.

[118] Govindhan Dhanaraj, Kullaiah Byrappa, Vishwanath Prasad, and Michael Dudley. *Springer Handbook of Crystal Growth*. Springer-Verlag Berlin Heidelberg, Berlin, Heidelberg, 2010. ISBN 9783540741824. URL `http://site.ebrary.com/lib/alltitles/docDetail.action?docID=10425347`.

[119] Anthony Kelly and Kevin M. Knowles. *Crystallography and crystal defects*. Wiley, Chichester, 2. ed. edition, 2012. ISBN 9781119961468.

[120] Reinhard B. Neder and Thomas Proffen. *Diffuse scattering and defect structure simulations: A cook book using the program DISCUS*, volume no. 11 of *International Union of Crystallography book series. Texts on crystallography*. Oxford University Press, Oxford, 2008. ISBN 9780199233694. URL `http://site.ebrary.com/lib/alltitles/docDetail.action?docID=10282048`.

[121] J. B. Higgins, R. B. LaPierre, J. L. Schlenker, A. C. Rohrman, J. D. Wood, G. T. Kerr, and W. J. Rohrbaugh. The framework topology of zeolite beta. *Zeolites*, 8(6):446–452, 1988.

[122] J. M. Newsam, M. M. J. Treacy, W. T. Koetsier, and C. B. de Gruyter. Structural Characterization of Zeolite Beta. *Proc. R. Soc. Lond. A*, 420(1859):375–405, 1988.

[123] B. Mihailova, V. Valtchev, S. Mintova, A-C Faust, N. Petkov, and T. Bein. Interlayer stacking disorder in zeolite beta family: a Raman spectroscopic study. *Physical chemistry chemical physics : PCCP*, 7(14):2756–2763, 2005.

[124] Tom Willhammar, Junliang Sun, Wei Wan, Peter Oleynikov, Daliang Zhang, Xiaodong Zou, Manuel Moliner, Jorge Gonzalez, Cristina Martínez, Fernando Rey, and Avelino Corma. Structure and catalytic properties of the most complex intergrown zeolite ITQ-39 determined by electron crystallography. *Nature chemistry*, 4(3):188–194, 2012.

[125] Thomas Proffen and R. B. Neder. DISCUS: A Program for Diffuse Scattering and Defect-Structure Simulation. *Journal of Applied Crystallography*, 30(2):171–175, 1997.

[126] Gustaaf van Tendeloo, Dirk van Dyck, and Stephen J. Pennycook. *Handbook of Nanoscopy*. Wiley-VCH, s.l., 1. aufl. edition, 2012. ISBN 9783527641895. URL `http://search.ebscohost.com/login.aspx?direct=true&scope=site&db=nlebk&db=nlabk&AN=490396`.

[127] M. Gemmi, H. Klein, F. Le Cras, A. Rageau, and P. Strobel. Structure solution of the new titanate Li4Ti8Ni3O21 using precession electron diffraction. *Acta crystallographica. Section B, Structural science*, 66(Pt 1):60–68, 2010.

[128] T. Gorelik, M. U. Schmidt, J. Brüning, S. Bekő, and U. Kolb. Using Electron Diffraction to Solve the Crystal Structure of a Laked Azo Pigment. *Crystal Growth & Design*, 9(9): 3898–3903, 2009.

[129] D. L. Dorset. *Structural electron crystallography*. The language of science. Plenum Press, New York, 1995. ISBN 1475766211.

[130] R. Vincent and P. A. Midgley. Double Conical Beam-Rocking System for Measurement of Integrated Electron Diffraction Intensities. *Ultramicroscopy*, 53(3):271–282, 1994.

[131] T. E. Gorelik, A. A. Stewart, and U. Kolb. Structure solution with automated electron diffraction tomography data: Different instrumental approaches. *Journal of microscopy*, 244(3):325–331, 2011.

[132] R. A. Crowther, R. Henderson, and J. M. Smith. MRC image processing programs. *Journal of structural biology*, 116(1):9–16, 1996.

[133] E. Mugnaioli and U. Kolb. Structure Solution of Zeolites by Automated Electron Diffraction Tomography Impact and Treatment of Preferential Orientation. *Microporous and Mesoporous Materials*, 189:107–114, 2014.

[134] Maria Cristina Burla, Rocco Caliandro, Benedetta Carrozzini, Giovanni Luca Cascarano, Corrado Cuocci, Carmelo Giacovazzo, Mariarosaria Mallamo, Annamaria Mazzone, and Giampiero Polidori. Crystal Structure Determination and Refinement via SIR2014. *Journal of Applied Crystallography*, 48(1):306–309, 2015.

[135] George M. Sheldrick. SHELX-97, Program for the Solution and Refinement of Crystal Structures. 1997.

[136] Václav Petříček, Michal Dušek, and Lukáš Palatinus. Crystallographic Computing System JANA2006: General features. *Zeitschrift für Kristallographie - Crystalline Materials*, 229(5), 2014.

[137] Giovanni Luca Cascarano, Carmelo Giacovazzo, and Benedetta Carrozzini. Crystal structure solution via precession electron diffraction data: The BEA algorithm. *Ultramicroscopy*, 111(1):56–61, 2010. URL `http://www.sciencedirect.com/science/article/pii/S0304399110002548`.

[138] Lukáš Palatinus, Damien Jacob, Priscille Cuvillier, Mariana Klementová, Wharton Sinkler, and Laurence D. Marks. Structure refinement from precession electron diffraction data. *Acta crystallographica. Section A, Foundations of crystallography*, 69(Pt 2):171–188, 2013.

[139] Lukáš Palatinus, Václav Petříček, and Cinthia Antunes Corrêa. Structure refinement using precession electron diffraction tomography and dynamical diffraction: theory and implementation. *Acta crystallographica. Section A, Foundations and advances*, 71(Pt 2):235–244, 2015.

[140] Václav Petříček, Michal Dušek, and Plášil, Jakub, et al. Jana2006 Cookbook (Version October 2017). *Institute of Physics, Prague, Czech Republic.*, 2017.

[141] Lukas Palatinus. PETS - Program for Analysis of Electron Diffraction Data. Institute of Physics of the ASCR: Prague, Czech Republic., 2011.

[142] Koichi Momma and Fujio Izumi. VESTA 3 for Three-Dimensional Visualization of Crystal, Volumetric and Morphology Data. *Journal of Applied Crystallography*, 44(6): 1272–1276, 2011.

[143] Joseph Goldstein, Dale E. Newbury, Joseph R. Michael, Nicholas W. M. Ritchie, John Henry J. Scott, and David C. Joy. *Scanning electron microscopy and X-ray microanalysis*. Springer, New York, NY, U.S.A., fourth edition edition, 2018. ISBN 9781493966769. URL `http://www.springer.com/de/book/978-1-4939-6674-5`.

[144] Joseph I. Goldstein, Dale E. Newbury, Patrick Echlin, David C. Joy, Charles E. Lyman, Eric Lifshin, Linda Sawyer, and Joseph R. Michael. *Scanning Electron Microscopy and X-ray Microanalysis: Third Edition*. Springer, Boston, MA, 2003. ISBN 9781461349693.

[145] T.R.L.C. Paixão, W.K.T. Coltro, and M. O. Salles. *Forensic Analytical Methods*. Royal Society of Chemistry, 2019. ISBN 9781788014595. URL `https://books.google.de/books?id=NyqqDwAAQBAJ`.

[146] W. I. F. David. *Structure Determination from Powder Diffraction Data*, volume 13 of *IUCr monographs on crystallography*. Oxford University Press, Oxford and New York, 2002. ISBN 0-19-920553-1.

[147] A. Le Bail. Monte Carlo Indexing with McMaille. *Powder Diffraction*, 19(03):249–254, 2004.

[148] A. A. Coelho. Indexing of Powder Diffraction Patterns by Iterative Use of Singular Value Decomposition. *J. Appl. Crystallogr.*, 36(1):86–95, 2003.

[149] A. Altomare, C. Giacovazzo, A. Guagliardi, A. G. G. Moliterni, R. Rizzi, and P. E. Werner. New Techniques for Indexing: N-TREOR in EXPO. *Journal of Applied Crystallography*, 33(4):1180–1186, 2000.

[150] STOE &. Cie GmbH. STOE WinXPOW 2.10. *STOE WinXPOW 2.10*, pages Darmstadt, Germany, 2004.

[151] William I. F. David, Kenneth Shankland, Jacco van de Streek, Elna Pidcock, W. D. Samuel Motherwell, and Jason C. Cole. DASH: A Program for Crystal Structure Determination from Powder Diffraction Data. *Journal of Applied Crystallography*, 39(6): 910–915, 2006.

[152] Angela Altomare, Mercedes Camalli, Corrado Cuocci, Carmelo Giacovazzo, Anna Moliterni, and Rosanna Rizzi. EXPO2009: Structure Solution by Powder Data in Direct and Reciprocal Space. *Journal of Applied Crystallography*, 42(6):1197–1202, 2009.

[153] H. M. Rietveld. A Profile Refinement Method for Nuclear and Magnetic Structures. *Journal of Applied Crystallography*, 2(2):65–71, 1969.

[154] F. Izumi and R. A. Young. The Rietveld Method. *by RA Young, Oxford University Press, Oxford*, pages 236–253, 1993.

[155] Gatan Inc., Pleasanton, CA, 2007. Digital Micrograph™ software. URL `http://www.gatan.com/products/tem-analysis/gatan-microscopy-suite-software`.

[156] Sebastian Schlitt, Tatiana E. Gorelik, Andrew A. Stewart, Elmar Schömer, Thorsten Raasch, and Ute Kolb. Application of clustering techniques to electron-diffraction data: Determination of unit-cell parameters. *Acta crystallographica. Section A, Foundations of crystallography*, 68(Pt 5):536–546, 2012.

[157] Hartmut Schneider, Jürgen Schreuer, and Bernd Hildmann. Structure and Properties of Mullite -A Review. *Journal of the European Ceramic Society*, 28(2):329–344, 2008.

[158] Reinhard X. Fischer, Hartmut Schneider, and Dietmar Voll. Formation of aluminum rich 9: 1 mullite and its transformation to low alumina mullite upon heating. *Journal of the European Ceramic Society*, 16(2):109–113, 1996.

[159] H. Schneider and Sridhar Komarneni, editors. *Mullite*. Wiley-VCH & Co, Weinheim, 2005. ISBN 978-3-527-30974-0.

[160] R. Cong, T. Yang, K. Li, H. Li, L. You, F. Liao, Y. Wang, and J. Lin. Mullite-type Ga4B2O9: Structure and order–disorder phenomenon. *Acta Crystallographica Section B: Structural Science*, 66(2):141–150, 2010. URL `http://journals.iucr.org/b/issues/2010/02/00/kd5038/kd5038.pdf`.

[161] J. Anggono. Mullite Ceramics: Its Properties Structure and Synthesis. *Jurnal Teknik Mesin*, 2005(7):1–10.

[162] Reinhard X. Fischer, Andrea Gaede-Köhler, Johannes Birkenstock, and Hartmut Schneider. Mullite and Mullite-Type Crystal Structures. *International Journal of Materials Research*, 103(4):402–407, 2012.

[163] R. J. Angel and C. T. Prewitt. Crystal structure of mullite; a re-examination of the average structure. *American Mineralogist*, 71(11-12):1476, 1986.

[164] Ai Dietzel and H. Scholze. Untersuchungen im System B2O3-Al2O3-SiO2. *Glastechnische Berichte*, 28(2):47–52, 1955.

[165] G. Werding and W. Schreyer. Experimental Studies on Borosilicates and Selected Borates. *Reviews in Mineralogy and Geochemistry*, 33:117–163, 1996.

[166] Horst Scholze. Über Aluminiumborate. *Z. anorg. allg. Chem.*, 284(4-6):272–277, 1956.

[167] Daniele Mazza, Mario Vallino, and Guido Busca. Mullite-Type Structures in the Systems Al2O3Me2O (Me = Na, K) and Al2O3B2O3. *Journal of the American Ceramic Society*, 75(7):1929–1934, 1992.

[168] Thorsten M. Gesing, Reinhard X. Fischer, Manfred Burianek, Manfred Mühlberg, Tapas Debnath, Claus H. Rüscher, Jan Ottinger, J.-Christian Buhl, and Hartmut Schneider. Synthesis and Properties of Mullite-Type (Bi1-xSrx)2(M11-yM2y)4O9-x(M= Al, Ga, Fe). *Journal of the European Ceramic Society*, 31(16):3055–3062, 2011.

[169] Kristin Hoffmann, M. Mangir Murshed, Reinhard X. Fischer, Hartmut Schneider, and Thorsten M. Gesing. Synthesis and characterization of mullite-type (Al1-xGax)4B2O9. *Zeitschrift für Kristallographie - Crystalline Materials*, 229(10), 2014.

[170] Hiroyasu Furukawa, Nakeun Ko, Yong Bok Go, Naoki Aratani, Sang Beom Choi, Eunwoo Choi, A. Ozgür Yazaydin, Randall Q. Snurr, Michael O'Keeffe, Jaheon Kim, and Omar M. Yaghi. Ultrahigh porosity in metal-organic frameworks. *Science (New York, N.Y.)*, 329(5990):424–428, 2010.

[171] Omar K. Farha, Ibrahim Eryazici, Nak Cheon Jeong, Brad G. Hauser, Christopher E. Wilmer, Amy A. Sarjeant, Randall Q. Snurr, SonBinh T. Nguyen, A. Özgür Yazaydın, and Joseph T. Hupp. Metal-organic framework materials with ultrahigh surface areas: Is the sky the limit? *Journal of the American Chemical Society*, 134(36):15016–15021, 2012.

[172] Jian-Rong Li, Julian Sculley, and Hong-Cai Zhou. Metal-organic frameworks for separations. *Chemical Reviews*, 112(2):869–932, 2012.

[173] Kevin J. Gagnon, Houston P. Perry, and Abraham Clearfield. Conventional and unconventional metal-organic frameworks based on phosphonate ligands: MOFs and UMOFs. *Chemical Reviews*, 112(2):1034–1054, 2012.

[174] Gérard Férey. Hybrid porous solids: Past, present, future. *Chemical Society Reviews*, 37 (1):191–214, 2008.

[175] Kyo Sung Park, Zheng Ni, Adrien P. Côté, Jae Yong Choi, Rudan Huang, Fernando J. Uribe-Romo, Hee K. Chae, Michael O'Keeffe, and Omar M. Yaghi. Exceptional Chemical and Thermal Stability of Zeolitic Imidazolate Frameworks. *Proceedings of the National Academy of Sciences*, 103(27):10186–10191, 2006.

[176] Mohamed Eddaoudi, David B. Moler, Hailian Li, Banglin Chen, Theresa M. Reineke, Michael O'Keeffe, and Omar M. Yaghi. Modular Chemistry: Secondary Building Units as a Basis for the Design of Highly Porous and Robust Metal−Organic Carboxylate Frameworks. *Accounts of Chemical Research*, 34(4):319–330, 2001.

[177] Jesse L.C. Rowsell and Omar M. Yaghi. Metal–organic frameworks: A new class of porous materials. *Microporous and Mesoporous Materials*, 73(1-2):3–14, 2004.

[178] John A. Groves, Stuart R. Miller, Stewart J. Warrender, Caroline Mellot-Draznieks, Philip Lightfoot, and Paul A. Wright. The first route to large pore metal phosphonates. *Chemical communications (Cambridge, England)*, (31):3305–3307, 2006.

[179] Yu-Ri Lee, Jun Kim, and Wha-Seung Ahn. Synthesis of metal-organic frameworks: A mini review. *Korean Journal of Chemical Engineering*, 30(9):1667–1680, 2013.

[180] Yujia Sun and Hong-Cai Zhou. Recent progress in the synthesis of metal-organic frameworks. *Science and technology of advanced materials*, 16(5):054202, 2015.

[181] Nazmul Abedin Khan and Sung Hwa Jhung. Synthesis of metal-organic frameworks (MOFs) with microwave or ultrasound: Rapid reaction, phase-selectivity, and size reduction. *Coordination Chemistry Reviews*, 285:11–23, 2015.

[182] Jun-ya Hasegawa, Masakazu Higuchi, Yuh Hijikata, and Susumu Kitagawa. Charge-Polarized Coordination Space for H2 Adsorption. *Chemistry of Materials*, 21(9):1829–1833, 2009.

[183] Rob Ameloot, Linda Stappers, Jan Fransaer, Luc Alaerts, Bert F. Sels, and Dirk E. de Vos. Patterned Growth of Metal-Organic Framework Coatings by Electrochemical Synthesis. *Chemistry of Materials*, 21(13):2580–2582, 2009.

[184] Carmen Munuera, Osama Shekhah, Hui Wang, Christof Wöll, and Carmen Ocal. The controlled growth of oriented metal-organic frameworks on functionalized surfaces as followed by scanning force microscopy. *Physical chemistry chemical physics : PCCP*, 10 (48):7257–7261, 2008.

[185] Osama Shekhah, Hui Wang, Denise Zacher, Roland A. Fischer, and Christof Wöll. Growth mechanism of metal-organic frameworks: Insights into the nucleation by employing a step-by-step route. *Angewandte Chemie (International ed. in English)*, 48 (27):5038–5041, 2009.

[186] Denise Zacher, Rochus Schmid, Christof Wöll, and Roland A. Fischer. Surface chemistry of metal-organic frameworks at the liquid-solid interface. *Angewandte Chemie (International ed. in English)*, 50(1):176–199, 2011.

[187] Herbert Hoffmann, Marta Debowski, Philipp Müller, Silvia Paasch, Irena Senkovska, Stefan Kaskel, and Eike Brunner. Solid-State NMR Spectroscopy of Metal–Organic Framework Compounds (MOFs). *Materials*, 5(12):2537–2572, 2012.

[188] Andre Sutrisno and Yining Huang. Solid-state NMR: a powerful tool for characterization of metal-organic frameworks. *Solid State Nuclear Magnetic Resonance*, 49-50:1–11, 2013.

[189] Daqiang Yuan, Dan Zhao, Daofeng Sun, and Hong-Cai Zhou. An isoreticular series of metal-organic frameworks with dendritic hexacarboxylate ligands and exceptionally high gas-uptake capacity. *Angewandte Chemie (International ed. in English)*, 49(31): 5357–5361, 2010.

[190] Omar K. Farha, A. Özgür Yazaydın, Ibrahim Eryazici, Christos D. Malliakas, Brad G. Hauser, Mercouri G. Kanatzidis, SonBinh T. Nguyen, Randall Q. Snurr, and Joseph T. Hupp. De novo synthesis of a metal-organic framework material featuring ultrahigh surface area and gas storage capacities. *Nature chemistry*, 2(11):944–948, 2010.

[191] Patricia Horcajada, Tamim Chalati, Christian Serre, Brigitte Gillet, Catherine Sebrie, Tarek Baati, Jarrod F. Eubank, Daniela Heurtaux, Pascal Clayette, Christine Kreuz, Jong-San Chang, Young Kyu Hwang, Veronique Marsaud, Phuong-Nhi Bories, Luc Cynober, Sophie Gil, Gérard Férey, Patrick Couvreur, and Ruxandra Gref. Porous metal-organic-framework nanoscale carriers as a potential platform for drug delivery and imaging. *Nature materials*, 9(2):172–178, 2010.

[192] María Vallet-Regí, Francisco Balas, and Daniel Arcos. Mesoporous materials for drug delivery. *Angewandte Chemie (International ed. in English)*, 46(40):7548–7558, 2007.

[193] Osama Shekhah, Hui Wang, Stefan Kowarik, Frank Schreiber, Michael Paulus, Metin Tolan, Christian Sternemann, Florian Evers, Denise Zacher, Roland A. Fischer, and Christof Wöll. Step-by-step route for the synthesis of metal-organic frameworks. *Journal of the American Chemical Society*, 129(49):15118–15119, 2007.

[194] Enrica Biemmi, Camilla Scherb, and Thomas Bein. Oriented growth of the metal organic framework Cu(3)(BTC)(2)(H(2)O)(3).xH(2)O tunable with functionalized self-assembled monolayers. *Journal of the American Chemical Society*, 129(26):8054–8055, 2007.

[195] Denise Zacher, Osama Shekhah, Christof Wöll, and Roland A. Fischer. Thin films of metal-organic frameworks. *Chemical Society Reviews*, 38(5):1418–1429, 2009.

[196] Victor Varela Guerrero, Yeonshick Yoo, Michael C. McCarthy, and Hae-Kwon Jeong. HKUST-1 Membranes on Porous Supports Using Secondary Growth. *Journal of Materials Chemistry*, 20(19):3938–3943, 2010.

[197] Guang Lu, Omar K. Farha, Weina Zhang, Fengwei Huo, and Joseph T. Hupp. Engineering ZIF-8 thin films for hybrid MOF-based devices. *Advanced materials (Deerfield Beach, Fla.)*, 24(29):3970–3974, 2012.

[198] Sebastian Leubner, Haishuang Zhao, Niels Van Velthoven, Mickaël Henrion, Helge Reinsch, Dirk E. De Vos, Ute Kolb, and Norbert Stock. Expanding the Variety of Zirconium–based Inorganic Building Units for Metal–Organic Frameworks. *Angewandte Chemie*, 343:1, 2019.

[199] Helge Reinsch, Mark Feyand, Tim Ahnfeldt, and Norbert Stock. CAU-3: A new family of porous MOFs with a novel Al-based brick: Al2(OCH3)4(O2C-X-CO2) (X = aryl). *Dalton transactions (Cambridge, England : 2003)*, 41(14):4164–4171, 2012.

[200] Helge Reinsch, Steve Waitschat, and Norbert Stock. Mixed-linker MOFs with CAU-10 structure: Synthesis and gas sorption characteristics. *Dalton transactions (Cambridge, England : 2003)*, 42(14):4840–4847, 2013.

[201] Partha P. Das, Enrico Mugnaioli, Stavros Nicolopoulos, Camilla Tossi, Mauro Gemmi, Athanasios Galanis, Gheorghe Borodi, and Mihaela M. Pop. Crystal Structures of Two Important Pharmaceuticals Solved by 3D Precession Electron Diffraction Tomography. *Organic Process Research & Development*, 22(10):1365–1372, 2018.

[202] R. M. Barrer. 435. Syntheses and reactions of mordenite. *Journal of the Chemical Society (Resumed)*, page 2158, 1948.

[203] D. W. Breck, W. G. Eversole, R. M. Milton, T. B. Reed, and T. L. Thomas. Crystalline Zeolites. I. The Properties of a New Synthetic Zeolite, Type A. *Journal of the American Chemical Society*, 78(23):5963–5972, 1956.

[204] Colin S. Cundy and Paul A. Cox. The hydrothermal synthesis of zeolites: Precursors, intermediates and reaction mechanism. *Microporous and Mesoporous Materials*, 82(1-2): 1–78, 2005.

[205] J. Rouquerol, D. Avnir, C. W. Fairbridge, D. H. Everett, J. M. Haynes, N. Pernicone, J. D. F. Ramsay, K. S. W. Sing, and K. K. Unger. Recommendations for the Characterization of Porous Solids. *Pure and Applied Chemistry*, 66(8), 1994.

[206] Bilge Yilmaz and Ulrich Müller. Catalytic Applications of Zeolites in Chemical Industry. *Topics in Catalysis*, 52(6-7):888–895, 2009.

[207] Manuel Moliner, Yuriy Román-Leshkov, and Mark E. Davis. Tin-containing zeolites are highly active catalysts for the isomerization of glucose in water. *Proceedings of the National Academy of Sciences of the United States of America*, 107(14):6164–6168, 2010.

[208] Li Xu, Chuan Shi, Bingbing Chen, Qi Zhao, Yongjun Zhu, Hermann Gies, Feng-Shou Xiao, Dirk de Vos, Toshiyuki Yokoi, Xinhe Bao, Ute Kolb, Mathias Feyen, Stefan Maurer, Ahmad Moini, Ulrich Müller, and Weiping Zhang. Improvement of catalytic activity over Cu–Fe modified Al-rich Beta catalyst for the selective catalytic reduction of NOx with NH3. *Microporous and Mesoporous Materials*, 236:211–217, 2016. URL `http://www.sciencedirect.com/science/article/pii/S1387181116303778`.

[209] Yongjun Zhu, Bingbing Chen, Rongrong Zhao, Qi Zhao, Hermann Gies, Feng-Shou Xiao, Dirk de Vos, Toshiyuki Yokoi, Xinhe Bao, Ute Kolb, Mathias Feyen, Stefan Maurer, Ahmad Moini, Ulrich Müller, Chuan Shi, and Weiping Zhang. Fe-doped Beta zeolite from organotemplate-free synthesis for NH 3 -SCR of NO x. *Catalysis Science & Technology*, 6(17):6581–6592, 2016.

[210] Donghui Jo, Taekyung Ryu, Gi Tae Park, Pyung Soon Kim, Chang Hwan Kim, In-Sik Nam, and Suk Bong Hong. Synthesis of High-Silica LTA and UFI Zeolites and NH 3 –SCR Performance of Their Copper-Exchanged Form. *ACS Catalysis*, 6(4):2443–2447, 2016.

[211] Zhenchao Zhao, Rui Yu, Rongrong Zhao, Chuan Shi, Hermann Gies, Feng-Shou Xiao, Dirk de Vos, Toshiyuki Yokoi, Xinhe Bao, Ute Kolb, Mathias Feyen, Robert McGuire, Stefan Maurer, Ahmad Moini, Ulrich Müller, and Weiping Zhang. Cu-exchanged Al-rich SSZ-13 zeolite from organotemplate-free synthesis as NH3-SCR catalyst: Effects of Na+ ions on the activity and hydrothermal stability. *Applied Catalysis B: Environmental*, 217:421–428, 2017. URL `http://www.sciencedirect.com/science/article/pii/S0926337317305568`.

[212] Nuria Martín, Peter N. R. Vennestrøm, Joakim R. Thøgersen, Manuel Moliner, and Avelino Corma. Iron-Containing SSZ-39 (AEI) Zeolite: An Active and Stable High-Temperature NH 3 -SCR Catalyst. *ChemCatChem*, 9(10):1754–1757, 2017.

[213] Jens Weitkamp. Zeolites and catalysis. *Solid State Ionics*, 131(1):175–188, 2000. URL `http://www.sciencedirect.com/science/article/pii/S0167273800006329`.

[214] Feng-Shou Xiao, Bin Xie, Haiyan Zhang, Liang Wang, Xiangju Meng, Weiping Zhang, Xinhe Bao, Bilge Yilmaz, Ulrich Müller, Hermann Gies, Hiroyuki Imai, Takashi Tatsumi, and Dirk de Vos. Interlayer-Expanded Microporous Titanosilicate Catalysts with Functionalized Hydroxyl Groups. *ChemCatChem*, 3(9):1442–1446, 2011.

[215] Bilge Yilmaz, Ulrich Müller, Mathias Feyen, Haiyan Zhang, Feng-Shou Xiao, Trees de Baerdemaeker, Bart Tijsebaert, Pierre Jacobs, Dirk de Vos, Weiping Zhang, Xinhe Bao, Hiroyuki Imai, Takashi Tatsumi, and Hermann Gies. New Zeolite Al-COE-4: Reaching Highly Shape-Selective Catalytic Performance through Interlayer Expansion. *Chemical communications*, 48(94):11549–11551, 2012.

[216] Trees de Baerdemaeker, Hermann Gies, Bilge Yilmaz, Ulrich Müller, Mathias Feyen, Feng-Shou Xiao, Weiping Zhang, Toshiyuki Yokoi, Xinhe Bao, and Dirk E. de Vos. A new class of solid Lewis acid catalysts based on interlayer expansion of layered silicates of the RUB-36 type with heteroatoms. *J. Mater. Chem. A*, 2(25):9709–9717, 2014.

[217] Junliang Sun, Charlotte Bonneau, Cant\′\ia J, Manuel Moliner, Daliang Zhang, Mingrun Li, and X. Zou. The ITQ-37 Mesoporous Chiral Zeolite. *Nature*, 458(7242): 1154–1157, 2009.

[218] B. M. Lok, T. R. Cannan, and C. A. Messina. The role of organic molecules in molecular sieve synthesis. *Zeolites*, 3(4):282–291, 1983.

[219] Russell E. Morris, Allen Burton, Lucy M. Bull, and Stacey I. Zones. SSZ-51A New Aluminophosphate Zeotype: Synthesis, Crystal Structure, NMR, and Dehydration Properties. *Chemistry of Materials*, 16(15):2844–2851, 2004.

[220] B. Marler, U. Werthmann, and H. Gies. Synthesis and structure of pure silica-RUB-10 (structure type: RUT) obtained with pyrrolidine as the structure directing agent. *Microporous and Mesoporous Materials*, 43(3):329–340, 2001.

[221] Nana Yan, Hongyi Xu, Wenna Zhang, Tantan Sun, Peng Guo, Peng Tian, and Zhongmin Liu. Probing Locations of Organic Structure-Directing Agents (OSDAs) and Host-Guest Interactions in CHA-Type SAPO-34/44. *Microporous Mesoporous Mat*, 2018.

[222] Allen Burton, Richard J. Darton, Mark E. Davis, Song-Jong Hwang, Russell E. Morris, Isao Ogino, and Stacey I. Zones. Structure-directing agent location and non-centrosymmetric structure of fluoride-containing zeolite SSZ-55. *The journal of physical chemistry. B*, 110(11):5273–5278, 2006.

[223] A. Coelho. Coelho Software. *TOPAS Academic User Manual*, pages Brisbane, Australia, 2007.

[224] F. R. Chen, C. Kisielowski, and D. van Dyck. Prospects for Atomic Resolution In-Line Holography for a 3D Determination of Atomic Structures from Single Projections. *Adv Struct Chem Imag*, 3(1):8, 2017.

[225] Travis E. Oliphant. Python for Scientific Computing. *Computing in Science & Engineering*, 9(3):10–20, 2007.

[226] J. Barthel. Dr. Probe - High-Resolution (S)TEM Image Simulation Software, 2016. URL `http://www.er-c.org/barthel/drprobe/`.

[227] Christoph Tobias Koch. Determination of Core Structure Periodicity and Point Defect Density along Dislocations. *Ph.D. Thesis*, 2002.

[228] M. D. Abràmoff, Paulo J. Magalhães, and Sunanda J. Ram. Image Processing with ImageJ. *Biophotonics international*, 11(7):36–42, 2004.

[229] Ulrike Werthmann, Bernd Marler, and Hermann Gies. Pyrrolidine Silica Sodalite and Ethylamine Silica Sodalite-two New Silica Sodalite Materials Synthesized from Different Solid Silica Sources. *Microporous and Mesoporous Materials*, 39(3):549–562, 2000.

[230] Frank H. Allen. The Cambridge Structural Database: A Quarter of a Million Crystal Structures and Rising. *Acta Crystallographica Section B Structural Science*, 58(3):380–388, 2002.

[231] Ian J. Bruno, Jason C. Cole, Paul R. Edgington, Magnus Kessler, Clare F. Macrae, Patrick McCabe, Jonathan Pearson, and Robin Taylor. New Software for Searching the Cambridge Structural Database and Visualizing Crystal Structures. *Acta Crystallographica Section B Structural Science*, 58(3):389–397, 2002.

[232] Lukáš Palatinus and Gervais Chapuis. SUPERFLIP – a computer program for the solution of crystal structures by charge flipping in arbitrary dimensions. *Journal of Applied Crystallography*, 40(4):786–790, 2007.

[233] W. Kraus and G. Nolze. POWDER CELL – a program for the representation and manipulation of crystal structures and calculation of the resulting X-ray powder patterns. *Journal of Applied Crystallography*, 29(3):301–303, 1996.

[234] Inc, Materials Studio Accelrys Software. Materials Studio. *San Diego*, 2009.

[235] Sylvian Cadars, Darren H. Brouwer, and Bradley F. Chmelka. Probing Local Structures of Siliceous Zeolite Frameworks by Solid-State NMR and First-Principles Calculations of 29SiO29Si Scalar Couplings. *Phys. Chem. Chem. Phys.*, 11(11):1825–1837, 2009.

[236] Yasuhiro Sakamoto, Zhao, Haishuang, Kolb, Ute, and et al. : in preparation. 2019.

[237] David C. Palmer. Visualization and analysis of crystal structures using CrystalMaker software. *Zeitschrift für Kristallographie - Crystalline Materials*, 230(9-10):82, 2015.

[238] Jung-Min Kim and Hoon-Taek Chung. Electrochemical characteristics of orthorhombic LiMnO2 with different degrees of stacking faults. *Journal of Power Sources*, 115(1): 125–130, 2003.

[239] Hermann Gies, Ulrich Müller, Bilge Yilmaz, Mathias Feyen, Takashi Tatsumi, Hiroyuki Imai, Haiyan Zhang, Bin Xie, Feng-Shou Xiao, Xinhe Bao, Weiping Zhang, Trees de Baerdemaeker, and Dirk de Vos. Interlayer Expansion of the Hydrous Layer Silicate RUB-36 to a Functionalized, Microporous Framework Silicate: Crystal Structure Analysis and Physical and Chemical Characterization. *Chemistry of Materials*, 24(8): 1536–1545, 2012.

[240] Haichao Li, Juan Wang, Danhong Zhou, Dongxu Tian, Chuan Shi, Ulrich Müller, Mathias Feyen, Hermann Gies, Feng-Shou Xiao, Dirk de Vos, Toshiyuki Yokoi, Xinhe Bao, and Weiping Zhang. Structural stability and Lewis acidity of tetravalent Ti, Sn, or Zr-linked interlayer-expanded zeolite COE-4: A DFT study. *Microporous and Mesoporous Materials*, 218:160–166, 2015.

[241] Hermann Gies, Mathias Feyen, Trees de Baerdemaeker, Dirk E. de Vos, Bilge Yilmaz, Ulrich Müller, Xiangju Meng, Feng-Shou Xiao, Weiping Zhang, Toshiyuki Yokoi, Takashi Tatsumi, and Xinhe Bao. Interlayer Expansion Using Metal-Linker Units: Crystalline Microporous Silicate Zeolites with Metal Centers on Specific Framework Sites. *Microporous and Mesoporous Materials*, 222:235–240, 2016.

[242] Markus Mateescu, Isabell Nuss, Alexander Southan, Hayley Messenger, Seraphine Wegner, Julia Kupka, Monika Bach, Günter Tovar, Heike Boehm, and Sabine Laschat. Synthesis of Pyridine Acrylates and Acrylamides and Their Corresponding Pyridinium Ions as Versatile Cross-Linkers for Tunable Hydrogels. *Synthesis*, 46(09):1243–1253, 2014.

[243] Derek J. Chadwick and Dudley H. Williams. Lanthanide-induced shifts in the carbon-13 nuclear magnetic resonance spectra of some ketones, alcohols, and amines. An analysis of contact, pseudo-contact, and complex-formation contributions to the observed shifts. *Journal of the Chemical Society, Perkin Transactions 2*, (10):1202, 1974.

[244] Guang Cao, Mobae Afeworki, Gordon J. Kennedy, Karl G. Strohmaier, and Douglas L. Dorset. Structure of an aluminophosphate EMM-8: a multi-technique approach. *Acta crystallographica. Section B, Structural science*, 63(Pt 1):56–62, 2007.

[245] S. M. Pai, B. L. Newalkar, and N. V. Choudary. Investigation on crystallization of aluminophosphate gel in the presence of 4-dimethylaminopyridine/hydrofluoric acid system. *Journal of Porous Materials*, 16(2):119–127, 2009.

[246] S. Pai, B. L. Newalkar, and N. V. Choudary. Synthesis and characterization of cobalt substituted aluminophosphate molecular sieve: Co-SSZ-51 under microwave-hydrothermal conditions. *Microporous and Mesoporous Materials*, 96(1-3):135–140, 2006.

[247] S. M. Pai, B. L. Newalkar, and N. V. Choudary. Microwave-hydrothermal synthesis and characterization of silico-aluminophosphate molecular sieve: SSZ-51. *Microporous and Mesoporous Materials*, 112(1-3):357–367, 2008.

[248] Gi Tae Park, Donghui Jo, Nak Ho Ahn, Jung Cho, and Suk Bong Hong. Synthesis and Structural Characterization of a CHA-type AlPO4 Molecular Sieve with Penta-Coordinated Framework Aluminum Atoms. *Inorganic Chemistry*, 56(14):8504–8512, 2017.

[249] Ulrike Werthmann, Bernd Marler, and Hermann Gies, editors. *Special Issue B, ECM-18 Poster Abstracts, vol. 5*, Bull. Czech Slovak Cryst. Assoc., 1999.

Appendix

Appendix A: Supplementary data for $Al_4B_2O_9$

A1 Front cover paper of reseached project $Al_4B_2O_9$

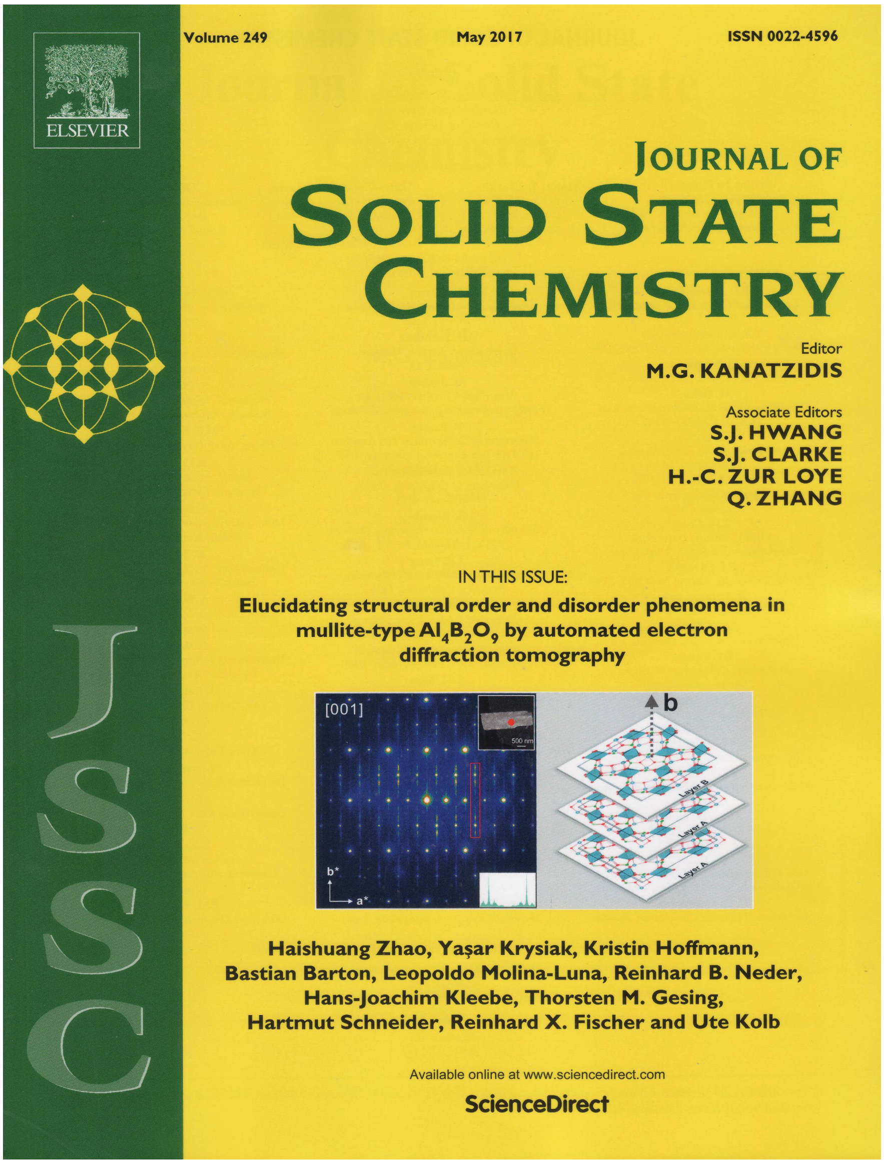

Volume 249 May 2017 ISSN 0022-4596

ELSEVIER

JOURNAL OF
SOLID STATE
CHEMISTRY

Editor
M.G. KANATZIDIS

Associate Editors
S.J. HWANG
S.J. CLARKE
H.-C. ZUR LOYE
Q. ZHANG

IN THIS ISSUE:
Elucidating structural order and disorder phenomena in mullite-type $Al_4B_2O_9$ by automated electron diffraction tomography

Haishuang Zhao, Yaşar Krysiak, Kristin Hoffmann, Bastian Barton, Leopoldo Molina-Luna, Reinhard B. Neder, Hans-Joachim Kleebe, Thorsten M. Gesing, Hartmut Schneider, Reinhard X. Fischer and Ute Kolb

Available online at www.sciencedirect.com
ScienceDirect

JSSC

Front cover for this issue. Zhao et al. "Elucidating structural order and disorder phenomena in mullite-type $Al_4B_2O_9$ by automated electron diffraction tomography" in "*Journal of Solid State Chemistry*", 249 (2017), page: 114-123. Doi: 10.1016/j.jssc.2017.02.023.

A2 Crystallographic data of ordered $Al_4B_2O_9$

```
data_shelx

_audit_creation_method            ’SHELXL-2014/7’
_shelx_SHELXL_version_number      ’2014/7’
_chemical_name_systematic         ?
_chemical_name_common             ?
_chemical_melting_point           ?
_chemical_formula_moiety          ?
_chemical_formula_sum
 ’Al4 B2 O9’
_chemical_formula_weight          273.54

loop_
 _atom_type_symbol
 _atom_type_description
 _atom_type_scat_dispersion_real
 _atom_type_scat_dispersion_imag
 _atom_type_scat_source
 ’B’  ’B’   0.0000   0.0000
 ’International Tables Vol C Tables 4.2.6.8 and 6.1.1.4’
 ’O’  ’O’   0.0000   0.0000
 ’International Tables Vol C Tables 4.2.6.8 and 6.1.1.4’
 ’Al’  ’Al’   0.0000   0.0000
 ’International Tables Vol C Tables 4.2.6.8 and 6.1.1.4’

_space_group_crystal_system       monoclinic
_space_group_IT_number            12
_space_group_name_H-M_alt         ’C 2/m’
_space_group_name_Hall            ’-C 2y’

_shelx_space_group_comment
;
The symmetry employed for this shelxl refinement is uniquely defined by the following
loop, which should always be used as a source of symmetry information in preference to
the above space-group names. They are only intended as comments.
;

loop_
 _space_group_symop_operation_xyz
 ’x, y, z’
 ’-x, y, -z’
 ’x+1/2, y+1/2, z’
 ’-x+1/2, y+1/2, -z’
 ’-x, -y, -z’
 ’x, -y, z’
 ’-x+1/2, -y+1/2, -z’
 ’x+1/2, -y+1/2, z’

_cell_length_a                    14.8130(10)
_cell_length_b                    5.5418(3)
_cell_length_c                    15.0593(9)
_cell_angle_alpha                 90
_cell_angle_beta                  90.930(2)
_cell_angle_gamma                 90
_cell_volume                      1236.07(13)
_cell_formula_units_Z             8
_cell_measurement_temperature     293(2)
```

```
_cell_measurement_reflns_used     ?
_cell_measurement_theta_min       ?
_cell_measurement_theta_max       ?

_exptl_crystal_description        ?
_exptl_crystal_colour             ?
_exptl_crystal_density_meas       ?
_exptl_crystal_density_method     ?
_exptl_crystal_density_diffrn     2.940
_exptl_crystal_F_000              375
_exptl_transmission_factor_min    ?
_exptl_transmission_factor_max    ?
_exptl_crystal_size_max           ?
_exptl_crystal_size_mid           ?
_exptl_crystal_size_min           ?
_exptl_absorpt_coefficient_mu     0.000
_shelx_estimated_absorpt_T_min    ?
_shelx_estimated_absorpt_T_max    ?
_exptl_absorpt_correction_type    ?
_exptl_absorpt_correction_T_min   ?
_exptl_absorpt_correction_T_max   ?
_exptl_absorpt_process_details    ?
_exptl_absorpt_special_details    ?
_diffrn_ambient_temperature       293(2)
_diffrn_radiation_wavelength      0.0197
_diffrn_radiation_type            ?
_diffrn_source                    'electron'
_diffrn_measurement_device_type   'FEI Tecnai F30 ST'
_diffrn_measurement_method        'electron precession and ADT'
_diffrn_reflns_number             4602
_diffrn_reflns_av_unetI/netI      0.1360
_diffrn_reflns_av_R_equivalents   0.2035
_diffrn_reflns_limit_h_min        -18
_diffrn_reflns_limit_h_max        18
_diffrn_reflns_limit_k_min        -6
_diffrn_reflns_limit_k_max        6
_diffrn_reflns_limit_l_min        -18
_diffrn_reflns_limit_l_max        18
_diffrn_reflns_theta_min          0.037
_diffrn_reflns_theta_max          0.705
_diffrn_reflns_theta_full         0.677
_diffrn_measured_fraction_theta_max   0.976
_diffrn_measured_fraction_theta_full  0.975
_diffrn_reflns_Laue_measured_fraction_max    0.976
_diffrn_reflns_Laue_measured_fraction_full   0.975
_diffrn_reflns_point_group_measured_fraction_max   0.976
_diffrn_reflns_point_group_measured_fraction_full  0.975
_reflns_number_total              1365
_reflns_number_gt                 1239
_reflns_threshold_expression      'I > 2\s(I)'
_reflns_Friedel_coverage          0.000
_reflns_Friedel_fraction_max      .
_reflns_Friedel_fraction_full     .

_reflns_special_details
;
Reflections were merged by SHELXL according to the crystal class for the
calculation of statistics and refinement.
_reflns_Friedel_fraction is defined as the number of unique Friedel pairs
```

```
 measured divided by the number that would be    possible theoretically,
ignoring centric projections and systematic absences.
;

_computing_data_collection        'ADT'
_computing_cell_refinement
_computing_data_reduction         ?
_computing_structure_solution     'SIR2014'
_computing_structure_refinement   'SHELXL-2014/7 (Sheldrick, 2014)'
_computing_molecular_graphics     ?
_computing_publication_material   ?
_refine_special_details          ?
_refine_ls_structure_factor_coef  Fsqd
_refine_ls_matrix_type            full
_refine_ls_weighting_scheme       calc
_refine_ls_weighting_details
'w=1/[\s^2^(Fo^2^)+(0.1000P)^2^] where P=(Fo^2^+2Fc^2^)/3'
_atom_sites_solution_primary      ?
_atom_sites_solution_secondary    ?
_atom_sites_solution_hydrogens    .
_refine_ls_hydrogen_treatment     undef
_refine_ls_extinction_method      none
_refine_ls_extinction_coef        .
_refine_ls_number_reflns          1365
_refine_ls_number_parameters      77
_refine_ls_number_restraints      39
_refine_ls_R_factor_all           0.3599
_refine_ls_R_factor_gt            0.3434
_refine_ls_wR_factor_ref          0.6491
_refine_ls_wR_factor_gt           0.6346
_refine_ls_goodness_of_fit_ref    4.454
_refine_ls_restrained_S_all       4.608
_refine_ls_shift/su_max           0.849
_refine_ls_shift/su_mean          0.225

loop_
 _atom_site_label
 _atom_site_type_symbol
 _atom_site_fract_x
 _atom_site_fract_y
 _atom_site_fract_z
 _atom_site_U_iso_or_equiv
 _atom_site_adp_type
 _atom_site_occupancy

Al1   Al   0.8627(8)   0.0000      0.3351(8)   0.018(3)  Uiso   1.00
Al2   Al   0.8094(10)  0.0000      0.1556(9)   0.029(3)  Uiso   1.00
Al3   Al   0.5732(11)  0.0000      0.0729(11)  0.033(4)  Uiso   1.00
Al4   Al   0.6699(11)  0.0000      0.3426(10)  0.030(4)  Uiso   1.00
Al5   Al   0.0007(4)   0.7411(13)  0.2425(5)   0.010(2)  Uiso   1.00
Al6   Al   0.2500      0.2500      0.0000      0.024(3)  Uiso   1.00
Al7   Al   0.2500      0.2500      0.5000      0.029(3)  Uiso   1.00
B1    B    0.1029(16)  0.0000      0.1078(16)  0.010(5)  Uiso   1.00
B2    B    0.3762(14)  0.0000      0.1144(14)  0.042(9)  Uiso   1.00
B3    B    0.1252(2)   0.0000      0.3708(2)   0.036(8)  Uiso   1.00
B4    B    0.3874(16)  0.0000      0.3880(17)  0.021(6)  Uiso   1.00
O1    O    0.7618(14)  0.0000      0.2670(12)  0.033(5)  Uiso   1.00
O2    O    0.7873(14)  0.0000      0.4338(12)  0.037(5)  Uiso   1.00
O3    O    0.9180(14)  0.0000      0.2233(12)  0.031(5)  Uiso   1.00
```

O4	O	0.9219(8)	0.7120(2)	0.3560(8)	0.021(3)	Uiso	1.00
O6	O	0.3190(9)	0.0000	0.4507(10)	0.010(3)	Uiso	1.00
O7	O	0.8183(8)	0.7049(2)	0.1041(8)	0.023(3)	Uiso	1.00
O8	O	0.6965(12)	0.0000	0.0578(12)	0.022(4)	Uiso	1.00
O9	O	0.0679(8)	0.7774(3)	0.1367(9)	0.022(3)	Uiso	1.00
O10	O	0.4431(13)	0.0000	0.0485(13)	0.035(5)	Uiso	1.00
O11	O	0.6611(9)	0.2822(3)	0.4047(10)	0.031(3)	Uiso	1.00
O12	O	0.5746(11)	0.0000	0.2763(12)	0.020(4)	Uiso	1.00
O13	O	0.4255(10)	0.0000	0.1950(10)	0.015(3)	Uiso	1.00
O14	O	0.0691(13)	0.0000	0.3023(12)	0.023(4)	Uiso	1.00
O15	O	0.8341(11)	0.0000	0.9615(11)	0.018(4)	Uiso	1.00

A3 List of selected bond distances (Å) and angles (°) of $Al_4B_2O_9$

```
 ---------------------------------------------------------------------------------------
  AlO5 bi-pyramids or AlO4 groups
--------------------------------
  Al1-O1   1.821(32)    Al2-O1 1.643(38)    Al3-O8   1.860(33)    Al4-O1   1.803(34)
  Al1-O2   1.792(33)    Al2-O3 1.788(39)    Al3-O9   2x1.850(21)  Al4-O2   2.216(32)
  Al1-O3   1.858(47)    Al2-O7 2x1.828(21)  Al3-O10  1.749(35)    Al4-O11  2x1.819(21)
  Al1-O4   2x1.844(18)  Al2-O8 2.328(36)    Al3-O10  2.005(30)    Al4-O12  1.667(33)
  Mean     1.832               1.883               1.863                  1.923
--------------------------------
  AlO6 octahedra
  Al5-O3   1.922(23)    Al6-O7   2x1.878(19)   Al7-O2    2x1.862(19)
  Al5-O4   2.083(22)    Al6-O8   2x1.758(18)   Al7-O6    2x1.906(15)
  Al5-O9   1.926(23)    Al6-O15  2x1.975(13)   Al7-O11   2x1.994(18)
  Al5-O12  1.806(21)    Mean     1.870         Mean      1.921
  Al5-O13  1.884(18)
  Al5-O14  1.945(19)
  Mean     1.928
--------------------------------
  BO3 triangles and BO4 tetrahedra
  B1-O9  2x1.390(21)   O9-B1-O15  2x118.8(8) B3-O11   2x1.378(38)  O11-B3-O14  2x116.2(7)
  B1-O15 1.374(36)     O9-B1-O9   122.3(10)  B3-O14   1.377(22)    O11-B3-O11  122.5(9)
  Mean   1.385                                        1.378

  B2-O7   2x1.427(37)  O7-B2-O10   109.7(7)  B4-O4    2x1.392(23)  O4-B4-O6   2x120.2(7)
  B2-O10  1.446(21)    O13-B2-O7   111.2(7)  B4-O6    1.375(19)    O4-B4-O4   117.5(9)
  B2-O13  1.439(33)    O13-B2-O10  105.1(20) Mean     1.386
  Mean    1.439        O7-B2-O7    109.8(9)
---------------------------------------------------------------------------------------
```

Appendix B: Supplementary data for Zr-MOFs

B1 Crystallographic data of dehydrated Zr-CAU-30

```
data_Zr-CAU-30
_audit_block_doi                 10.5517/ccdc.csd.cc1zh5rd
_database_code_depnum_ccdc_archive 'CCDC 1831844'
loop_
_citation_id
_citation_doi
_citation_year
1 10.1039/C8SC01533C 2018
_audit_update_record
;
_chemical_name_mineral           Zr-CAU-30
_cell_length_a                   44.7776(58)
_cell_length_b                   44.7776(58)
_cell_length_c                   7.6581(39)
_cell_angle_alpha                90
_cell_angle_beta                 90
_cell_angle_gamma                90
_cell_volume                     15354.7(87)
_cell_formula_units_Z            8
_symmetry_space_group_name_H-M   I41cd
_symmetry_cell_setting           tetragonal
_symmetry_int_tables_number      110
_symmetry_space_group_name_Hall  I4bw-2c

loop_
_symmetry_equiv_pos_as_xyz
'-x+1/2, -y+1/2, z+1/2'
'-x+1/2, y+1/2, z'
'-y, x+1/2, z+1/4'
'-y+1/2, -x, z+1/4'
'y, x+1/2, z-1/4'
'y+1/2, -x, z-1/4'
'x, -y, z+1/2'
'x, y, z'
'-x, -y, z'
'-x, y, z+1/2'
'-y+1/2, x, z-1/4'
'-y, -x+1/2, z-1/4'
'y+1/2, x, z+1/4'
'y, -x+1/2, z+1/4'
'x+1/2, -y+1/2, z'
'x+1/2, y+1/2, z+1/2'
loop_
_atom_type_symbol
_atom_type_oxidation_number
_atom_type_radius_bond
Zr ? 1.200
Ni ? 1.200
O ? 1.200
C ? 1.200
N ? 1.200
P ? 1.200

loop_
_atom_site_label
```

```
_atom_site_type_symbol
_atom_site_symmetry_multiplicity
_atom_site_fract_x
_atom_site_fract_y
_atom_site_fract_z
_atom_site_occupancy
_atom_site_B_iso_or_equiv
Zr1 Zr 0 0.24396(42) 1.0014(13) 0.88317 1 0.8(13)
O1 O 0 0.2400(16) 1.0202(10) 0.63383 1 0.8(13)
O2 O 0 0.2656981 0.9650856 0.7840204 1 0.8(13)
O3 O 0 0.2834432 0.9878845 0.4541586 1 0.8(13)
O4 O 0 0.2913353 0.9365291 0.5492413 1 0.8(13)
P1 P 0 0.2925501 0.969309 0.6315845 1 0.8(13)
C1 C 0 0.3943694 0.9763461 0.696565 1 0.8(13)
C2 C 0 0.3821127 0.963863 0.5540059 1 0.8(13)
C3 C 0 0.351278 0.9614016 0.5386706 1 0.8(13)
C4 C 0 0.3324096 0.971243 0.6658565 1 0.8(13)
C5 C 0 0.3445192 0.9825235 0.8116816 1 0.8(13)
C6 C 0 0.375482 0.9851153 0.8267405 1 0.8(13)
C7 C 0 0.42582 0.98412 0.72871 1 0.8(13)
O5 O 0 0.5379327 0.7735877 0.7543677 1 0.8(13)
O6 O 0 0.5159233 0.7953857 1.079706 1 0.8(13)
O7 O 0 0.5749358 0.7939624 0.9841597 1 0.8(13)
P2 P 0 0.5405569 0.7985579 0.9126111 1 0.8(13)
C11 C 0 0.5194173 0.8953867 0.7809164 1 0.8(13)
C12 C 0 0.539253 0.8880845 0.9157986 1 0.8(13)
C13 C 0 0.5477179 0.8586836 0.9446722 1 0.8(13)
C14 C 0 0.5368705 0.83613 0.8369207 1 0.8(13)
C15 C 0 0.5173071 0.8430438 0.7003296 1 0.8(13)
C16 C 0 0.5088709 0.8727044 0.6708395 1 0.8(13)
C17 C 0 0.51612 0.92659 0.73863 1 0.8(13)
C21 C 0 0.48655 0.93559 0.74571 1 0.8(13)
C22 C 0 0.46338 0.91546 0.76352 1 0.8(13)
C23 C 0 0.44646 0.96113 0.7396 1 0.8(13)
C24 C 0 0.43769 0.93176 0.75809 1 0.8(13)
N25 N 0 0.47671 0.96418 0.73381 1 0.8(13)
C31 C 0 0.56462 0.98669 0.7172 1 0.8(13)
C32 C 0 0.58469 0.96357 0.69736 1 0.8(13)
C33 C 0 0.53888 0.94712 0.72034 1 0.8(13)
C34 C 0 0.56824 0.93827 0.69947 1 0.8(13)
N35 N 0 0.53589 0.97713 0.72702 1 0.8(13)
Ni1 Ni 0 0.5 1 0.73067 1 0.8(13)
G1 O 0 0.6223(74) 0.5391(44) 0.982(34) 1.00(17) 0.8(13)
G2 O 0 0.2327(79) 0.7968(63) 0.19(11) 0.526(91) 0.8(13)
G3 O 0 0.3214(53) 0.5382(42) 0.574(36) 1.00(20) 0.8(13)
G4 O 0 0.3921(32) 0.7539(72) 0.648(37) 1.00(10) 0.8(13)
```

B2 Crystallographic data of CAU-27-BDC

```
data_
_chemical_name_mineral ??
_cell_length_a  20.39214(80)
_cell_length_b  20.39214(80)
_cell_length_c  10.17787(50)
_cell_angle_alpha 90
_cell_angle_beta  90
_cell_angle_gamma 90
_cell_volume 4232.36(39)
```

```
_symmetry_space_group_name_H-M I4/MCM
loop_
_symmetry_equiv_pos_as_xyz
’-x, -y, -z’
’-x, -y, z’
’-x, y, -z+1/2’
’-x, y, z+1/2’
’-y, -x, -z+1/2’
’-y, -x, z+1/2’
’-y, x, -z’
’-y, x, z’
’y, -x, -z’
’y, -x, z’
’y, x, -z+1/2’
’y, x, z+1/2’
’x, -y, -z+1/2’
’x, -y, z+1/2’
’x, y, -z’
’x, y, z’
’-x+1/2, -y+1/2, -z+1/2’
’-x+1/2, -y+1/2, z+1/2’
’-x+1/2, y+1/2, -z’
’-x+1/2, y+1/2, z’
’-y+1/2, -x+1/2, -z’
’-y+1/2, -x+1/2, z’
’-y+1/2, x+1/2, -z+1/2’
’-y+1/2, x+1/2, z+1/2’
’y+1/2, -x+1/2, -z+1/2’
’y+1/2, -x+1/2, z+1/2’
’y+1/2, x+1/2, -z’
’y+1/2, x+1/2, z’
’x+1/2, -y+1/2, -z’
’x+1/2, -y+1/2, z’
’x+1/2, y+1/2, -z+1/2’
’x+1/2, y+1/2, z+1/2’
loop_
_atom_site_label
_atom_site_type_symbol
_atom_site_symmetry_multiplicity
_atom_site_fract_x
_atom_site_fract_y
_atom_site_fract_z
_atom_site_occupancy
_atom_site_B_iso_or_equiv
Zr1 Zr   0 0.5 0.5 0.75 1 1.43(13)
Zr2 Zr   0 0.10142(15) 0.06735(17) 0.5 1 1.43(13)
O1 O   0 -0.07928(62) 0.01612(48) 0.37469(79) 1 1.86(26)
O2 O   0 0.65424(67) 0.39895(49) 0.33186(80) 1 1.86(26)
O3 O   0 0.19611(44) 0.01571(53) 0.5 1 1.86(26)
O4 O   0 0.59541(55) 0.32373(40) 0.5 1 1.86(26)
C1 C   0 0.45482(75) 0.71448(62) 0.5 1 1.39(49)
C2 C   0 0.78699(62) 0.55838(90) 0.5 1 1.39(49)
C3 C   0 0.30144(45) 0.24612(57) 0.6656(11) 1 1.39(49)
C4 C   0 0.35161(44) 0.35161(44) 0.75 1 1.39(49)
C5 C   0 0.29881(46) 0.29881(46) 0.75 1 1.39(49)
Og3 O   0 0.4956(26) 0.0794(29) 0.3438(39) 0.221(10) 1.86(26)
Og4 O   0 0.5388(31) 1.1112(30) 0 0.285(23) 1.86(26)
```

Appendix C: Supplementary data for THK-2

Crystallographic data of THK-2

```
data_THK-2_structure
_symmetry_cell_setting            orthorhombic
_symmetry_space_group_name_H-M    ’P c c n’
_symmetry_Int_Tables_number       56
_space_group_name_Hall            ’-P 2ab 2ac’
loop_
_symmetry_equiv_pos_site_id
_symmetry_equiv_pos_as_xyz
1 x,y,z
2 1/2-x,1/2-y,z
3 -x,1/2+y,1/2-z
4 1/2+x,-y,1/2-z
5 -x,-y,-z
6 1/2+x,1/2+y,-z
7 x,1/2-y,1/2+z
8 1/2-x,y,1/2+z
_cell_length_a                    24.7887(32)
_cell_length_b                    14.3775(21)
_cell_length_c                    5.0351(5)
_cell_angle_alpha                 90.0000
_cell_angle_beta                  90.0000
_cell_angle_gamma                 90.0000
_cell_volume                      1794.51(39)
loop_
_atom_site_label
_atom_site_type_symbol
_atom_site_fract_x
_atom_site_fract_y
_atom_site_fract_z
_atom_site_U_iso_or_equiv
_atom_site_adp_type
_atom_site_occupancy
SI1    Si   0.95729(38)   0.68340(77)   0.76783(27)   0.03158(52)  Uiso  1.00
SI2    Si   0.07303(43)   0.60420(81)   0.72008(29)   0.03158(52)  Uiso  1.00
SI3    Si   0.90072(36)   0.50490(79)   0.79682(29)   0.03158(52)  Uiso  1.00
SI4    Si   0.78415(48)   0.41547(74)   0.81678(28)   0.03158(52)  Uiso  1.00
O1     O    0.90937(77)   0.61133(155)  0.75348(58)   0.03252(171) Uiso  1.00
O2     O    0.79839(73)   0.30248(143)  0.82348(44)   0.03252(171) Uiso  1.00
O3     O    0.83352(76)   0.49414(114)  0.81079(37)   0.03252(171) Uiso  1.00
O4     O    0.01739(85)   0.65120(130)  0.74445(67)   0.03252(171) Uiso  1.00
Zn1    Zn   0.84272(70)   0.26891(188)  0.48393(46)   0.06420      Uiso  0.2806(64)
O5     O    0.10602(88)   0.69451(147)  0.77399(47)   0.03252(171) Uiso  1.00
O6     O    0.75876(106)  0.43457(127)  0.08808(53)   0.03252(171) Uiso  1.00
O7     O    0.91217(117)  0.46941(163)  0.07427(39)   0.03252(171) Uiso  1.00
O8     O    0.92296(95)   0.43804(151)  0.55908(44)   0.03252(171) Uiso  1.00
O9     O    0.93975(80)   0.75860(186)  0.53499(53)   0.03252(171) Uiso  1.00
O10    O    0.26017(154)  0.16544(285)  0.16989(158)  0.12665      Uiso  0.4471(111)
#END
```

Appendix D: Supplementary data for TMP-SSZ-51

Crystallographic data of TMP-SSZ-51

```
cif data_
_chemical_name_mineral ?asmade?
_cell_length_a  21.53695(52)
_cell_length_b  13.87946(27)
_cell_length_c  14.26582(30)
_cell_angle_alpha 90
_cell_angle_beta  99.8887(13)
_cell_angle_gamma 90
_cell_volume 4201.00(16)
_space_group C2/c
loop_
_symmetry_equiv_pos_as_xyz
'-x, -y, -z'
'-x, y, -z+1/2'
'-x+1/2, -y+1/2, -z'
'-x+1/2, y+1/2, -z+1/2'
'x, -y, z+1/2'
'x, y, z'
'x+1/2, -y+1/2, z+1/2'
'x+1/2, y+1/2, z'
loop_
_atom_site_label
_atom_site_type_symbol
_atom_site_symmetry_multiplicity
_atom_site_fract_x
_atom_site_fract_y
_atom_site_fract_z
_atom_site_occupancy
_atom_site_B_iso_or_equiv
_atom_site_U_iso_or_equiv

P1  P  0  0.15924(11)  0.88399(17)  0.20489(15) 1  1.28156     0.01623
P2  P  0  0.26375(10)  0.11001(17)  0.06540(16) 1  1.28156     0.01623
P3  P  0  0.17184(10)  0.21728(15)  0.39443(15) 1  1.28156     0.01623
P4  P  0  0.05771(11)  0.11968(17)  0.01165(15) 1  1.28156     0.01623
Al1 Al 0  0.16217(11)  0.10687(16)  0.19739(16) 1  1.28156     0.01623
Al2 Al 0  0.247983(95) 0.89054(15)  0.06126(15) 1  1.28156     0.01623
Al3 Al 0  0.16034(11)  0.79476(16)  0.40875(16) 1  1.28156     0.01623
Al4 Al 0  0.085938(96) 0.90104(15)  0.00827(15) 1  1.28156     0.01623
O1  O  0  0.28504(20)  0.00620(21)  0.06817(33) 1  1.48124     0.01876
O2  O  0  0.00929(14)  0.84683(28) -0.00900(34) 1  1.48124     0.01876
O3  O  0  0.09883(16)  0.87514(36)  0.13273(20) 1  1.48124     0.01876
O4  O  0  0.15359(24)  0.81984(27)  0.28789(18) 1  1.48124     0.01876
O5  O  0  0.16308(24)  0.18916(26)  0.29009(18) 1  1.48124     0.01876
O6  O  0  0.21554(14)  0.84931(34)  0.16193(21) 1  1.48124     0.01876
O7  O  0  0.09319(16)  0.12376(39)  0.11377(21) 1  1.48124     0.01876
O8  O  0  0.17653(16)  0.67089(20)  0.42337(35) 1  1.48124     0.01876
O9  O  0  0.32172(16)  0.82737(20)  0.09504(36) 1  1.48124     0.01876
O10 O  0  0.08792(14)  0.81824(32)  0.44424(24) 1  1.48124     0.01876
O11 O  0  0.11300(14)  0.81655(26) -0.06957(24) 1  1.48124     0.01876
O12 O  0  0.16623(24)  0.98787(19)  0.24072(31) 1  1.48124     0.01876
O13 O  0  0.22037(16)  0.86630(28)  0.47189(23) 1  1.48124     0.01876
O14 O  0  0.23085(18)  0.83208(28) -0.05269(22) 1  1.48124     0.01876
O15 O  0  0.05691(25)  0.01821(19) -0.03176(32) 1  1.48124     0.01876
O16 O  0  0.22880(13)  0.12894(33)  0.14623(21) 1  1.48124     0.01876
```

```
F1  F  0  0.16918(12)  0.95551(24)  0.02485(37) 1  1.48124     0.01876
OW1 O  0  0.5492(15)   0.3651(23)   0.2547(28) 0.3667(96) 7.4062     0.09380
N1  N  0  0.93270(15)  0.54018(23)  0.86853(35) 1  3.16737    0.04012
C1  C  0 -0.06712(19)  0.44058(27)  0.86852(37) 1  3.16737    0.04012
C2  C  0 -0.01163(21)  0.39020(29)  0.87145(51) 1  3.16737    0.04012
C3  C  0  1.04474(23)  0.43998(27)  0.87965(50) 1  3.16737    0.04012
C4  C  0  1.04471(22)  0.54069(31)  0.87817(49) 1  3.16737    0.04012
C5  C  0  0.98874(21)  0.59060(28)  0.87006(37) 1  3.16737    0.04012
C6  C  0  0.87096(20)  0.59049(28)  0.86416(26) 1  3.48937    0.04419
C7  C  0 -0.12786(20)  0.38911(29)  0.86457(28) 1  3.48937    0.04419
C8  C  0  0.98945(25)  0.69873(28)  0.86874(30) 1  3.48937    0.04419
H1  H  0 -0.0130(17)   0.3226(20)   0.8676(22)  1  4.187244   0.05303
H2  H  0  1.0843(16)   0.4023(20)   0.8867(20)  1  4.187244   0.05303
H3  H  0  1.0840(16)   0.5778(19)   0.8841(19)  1  4.187244   0.05303
H4  H  0  0.8706(15)   0.6278(21)   0.9200(21)  1  4.187244   0.05303
H5  H  0  0.8652(15)   0.6295(24)   0.8100(21)  1  4.187244   0.05303
H6  H  0 -0.1620(13)   0.5400(22)   0.8559(16)  1  4.187244   0.05303
H7  H  0 -0.1393(15)   0.3687(25)   0.8025(22)  1  4.187244   0.05303
H8  H  0 -0.1198(15)   0.3345(20)   0.9078(22)  1  4.187244   0.05303
H9  H  0 -0.1608(14)   0.4358(19)   0.8773(18)  1  4.187244   0.05303
H10 H  0  1.0302(17)   0.7198(19)   0.9020(21)  1  4.187244   0.05303
H11 H  0  0.9839(16)   0.7203(17)   0.8033(20)  1  4.187244   0.05303
H12 H  0  0.9548(17)   0.7230(20)   0.8990(21)  1  4.187244   0.05303
```

Appendix E: Supplementary data for dehydrated CHA zeolites

E1 Crystallographic data of dehydrated H-CHA

```
data_I
_chemical_formula_sum                    ’Si36O72’
_symmetry_cell_setting                   trigonal
_symmetry_space_group_name_H-M           ’R -3’
_symmetry_space_group_name_Hall          ’-R 3’
_symmetry_Int_Tables_number              148

loop_
 _space_group_symop_id
 _space_group_symop_operation_xyz
 1   x,y,z
 2   -y,x-y,z
 3   -x+y,-x,z
 4   -x,-y,-z
 5   y,-x+y,-z
 6   x-y,x,-z
 7   x+2/3,y+1/3,z+1/3
 8   -y+2/3,x-y+1/3,z+1/3
 9   -x+y+2/3,-x+1/3,z+1/3
 10  -x+2/3,-y+1/3,-z+1/3
 11  y+2/3,-x+y+1/3,-z+1/3
 12  x-y+2/3,x+1/3,-z+1/3
 13  x+1/3,y+2/3,z+2/3
 14  -y+1/3,x-y+2/3,z+2/3
 15  -x+y+1/3,-x+2/3,z+2/3
 16  -x+1/3,-y+2/3,-z+2/3
 17  y+1/3,-x+y+2/3,-z+2/3
 18  x-y+1/3,x+2/3,-z+2/3
```

```
_cell_length_a                         13.5692
_cell_length_b                         13.5692
_cell_length_c                         14.8401
_cell_angle_alpha                      90
_cell_angle_beta                       90
_cell_angle_gamma                      120
_cell_volume                           2366.333

loop_
 _twin_individual_id
 _twin_individual_mass_fraction_refined
 _twin_individual_twin_matrix_11
 _twin_individual_twin_matrix_12
 _twin_individual_twin_matrix_13
 _twin_individual_twin_matrix_21
 _twin_individual_twin_matrix_22
 _twin_individual_twin_matrix_23
 _twin_individual_twin_matrix_31
 _twin_individual_twin_matrix_32
 _twin_individual_twin_matrix_33

_cell_formula_units_Z                  18

loop_
 _atom_site_label
 _atom_site_type_symbol
 _atom_site_fract_x
 _atom_site_fract_y
 _atom_site_fract_z
 _atom_site_adp_type
 _atom_site_U_iso_or_equiv
 _atom_site_site_symmetry_multiplicity
 _atom_site_occupancy
 _atom_site_calc_flag
 _atom_site_refinement_flags
 _atom_site_disorder_assembly
 _atom_site_disorder_group
  Si1 Si 0.771979 -0.000163 0.105461  Uani 0.019  18 1 d . . .
  Si2 Si 0.666354  0.105477 0.227805  Uani 0.0186 18 1 d . . .
  O1  O  0.739636  0.000177 0.000316  Uani 0.046  18 1 d . . .
  O2  O  0.687649  0.020963 0.166345  Uani 0.0386 18 1 d . . .
  O3  O  0.901531  0.098845 0.122486  Uani 0.0482 18 1 d . . .
  O4  O  0.760501 -0.120438 0.13315   Uani 0.0453 18 1 d . . .

loop_
 _atom_site_aniso_label
 _atom_site_aniso_type_symbol
 _atom_site_aniso_U_11
 _atom_site_aniso_U_22
 _atom_site_aniso_U_33
 _atom_site_aniso_U_12
 _atom_site_aniso_U_13
 _atom_site_aniso_U_23
 Si1 Si 0.021547 0.01374  0.023206 0.009962  0.004965 -0.000318
 Si2 Si 0.014146 0.022331 0.022637 0.011585  0.001758 -0.00356
 O1  O  0.058156 0.058667 0.023608 0.031006 -0.000901  0.002712
 O2  O  0.04371  0.045088 0.041682 0.033181  0.008366 -0.008932
 O3  O  0.029243 0.028249 0.071616 0.002644 -0.002818  0.000716
 O4  O  0.061745 0.028536 0.0595   0.032922  0.017228  0.005557
```

E2 Crystallographic data of dehydrated Cu-CHA

```
data_I
_chemical_formula_sum                  'Si36O72Cu2.63'
_symmetry_cell_setting                 trigonal
_symmetry_space_group_name_H-M         'R -3'
_symmetry_space_group_name_Hall        '-R 3'
_symmetry_Int_Tables_number            148

loop_
 _space_group_symop_id
 _space_group_symop_operation_xyz
 1   x,y,z
 2   -y,x-y,z
 3   -x+y,-x,z
 4   -x,-y,-z
 5   y,-x+y,-z
 6   x-y,x,-z
 7   x+2/3,y+1/3,z+1/3
 8   -y+2/3,x-y+1/3,z+1/3
 9   -x+y+2/3,-x+1/3,z+1/3
 10  -x+2/3,-y+1/3,-z+1/3
 11  y+2/3,-x+y+1/3,-z+1/3
 12  x-y+2/3,x+1/3,-z+1/3
 13  x+1/3,y+2/3,z+2/3
 14  -y+1/3,x-y+2/3,z+2/3
 15  -x+y+1/3,-x+2/3,z+2/3
 16  -x+1/3,-y+2/3,-z+2/3
 17  y+1/3,-x+y+2/3,-z+2/3
 18  x-y+1/3,x+2/3,-z+2/3

_cell_length_a                         13.472
_cell_length_b                         13.472
_cell_length_c                         15.132
_cell_angle_alpha                      90
_cell_angle_beta                       90
_cell_angle_gamma                      120
_cell_volume                           2378.434

loop_
 _twin_individual_id
 _twin_individual_mass_fraction_refined
 _twin_individual_twin_matrix_11
 _twin_individual_twin_matrix_12
 _twin_individual_twin_matrix_13
 _twin_individual_twin_matrix_21
 _twin_individual_twin_matrix_22
 _twin_individual_twin_matrix_23
 _twin_individual_twin_matrix_31
 _twin_individual_twin_matrix_32
 _twin_individual_twin_matrix_33

_cell_formula_units_Z                  18

loop_
 _atom_site_label
 _atom_site_type_symbol
 _atom_site_fract_x
 _atom_site_fract_y
```

```
 _atom_site_fract_z
 _atom_site_adp_type
 _atom_site_U_iso_or_equiv
 _atom_site_site_symmetry_multiplicity
 _atom_site_occupancy
 _atom_site_calc_flag
 _atom_site_refinement_flags
 _atom_site_disorder_assembly
 _atom_site_disorder_group
  Si1 Si 0.333485 0.436045 0.066936 Uani 0.0131 18 1 d . . .
  Si2 Si 0.103394 0.436419 0.065827 Uani 0.0144 18 1 d . . .
  O1  O  0.209061 0.419661 0.040764 Uani 0.0623 18 1 d . . .
  O2  O  0.422243 0.576502 0.057546 Uani 0.0454 18 1 d . . .
  O3  O  0.332982 0.39736  0.166661 Uani 0.0337 18 1 d . . .
  O4  O  0.363831 0.363377 0.000288 Uani 0.0403 18 1 d . . .
  Cu1 Cu 0.333333 0.666667 0.042516 Uani 0.0412 6 0.4381 d . . .

loop_
 _atom_site_aniso_label
 _atom_site_aniso_type_symbol
 _atom_site_aniso_U_11
 _atom_site_aniso_U_22
 _atom_site_aniso_U_33
 _atom_site_aniso_U_12
 _atom_site_aniso_U_13
 _atom_site_aniso_U_23
 Si1 Si 0.013944 0.021674 0.003515 0.008882  0.000411 -0.00373
 Si2 Si 0.016523 0.022874 0.005962 0.011578 -0.004454 -0.004096
 O1  O  0.042003 0.14194  0.040832 0.074366 -0.011681 -0.024712
 O2  O  0.033135 0.045886 0.048187 0.013109  0.000546  0.000635
 O3  O  0.061712 0.037507 0.007958 0.029301 -0.005823 -0.00703
 O4  O  0.056016 0.060326 0.021483 0.041714  0.009239 -0.010965
 Cu1 Cu 0.034321 0.034321 0.054892 0.017164  0 0
```

Appendix F: Submitted manuscript of TMP-SSZ-51

Detection of organic cations in the pores of aluminophosphate SSZ-51 by electron diffraction tomography – elucidating the effect of molecular stacking

Haishuang Zhao[a], Hao Xu[b], Bernd Marler[c], Sergi Plana-Ruiz[d,e], Lothar Fink[f], Edith Alig[f], Xiangju Meng[b], Feng-Shou Xiao[b],and Ute Kolb*[a,d]

[a][Institute of Inorganic Chemistry and Analytical Chemistry, Johannes Gutenberg-University Mainz, Duesbergweg 10-14, 55128 Mainz, Germany]

[b][Department of Chemistry, Zhejiang University, 310028 Hangzhou, China]

[c][Institute für Geologie, Mineralogie und Geophysik, Ruhr-Universität Bochum, 44780 Bochum, Germany]

[d][Institut für Angewandte Geowissenchaften, Technische Universität Darmstadt, Schnittspahnstrasse 9, 64287 Darmstadt, Germany]

[e][LENS-MIND, Electronics and Biomedical Engineering, Faculty of Physics, University of Barcelona, Martí i Franquès 1, 08028 Barcelona, Catalonia, Spain]

[f][Institute of Inorganic and Analytical Chemistry, Goethe University, Max-von-Laue-Str. 7, 60438 Frankfurt am Main, Germany]

*Corresponding author: Ute Kolb (Email: *kolb@uni-mainz.de*)

Keywords:

- Microporous material
- Aluminophosphate SSZ-51
- Electron diffraction tomography
- Organic structure directing agent
- Crystal structure determination

Figure of Graphic Abstract:

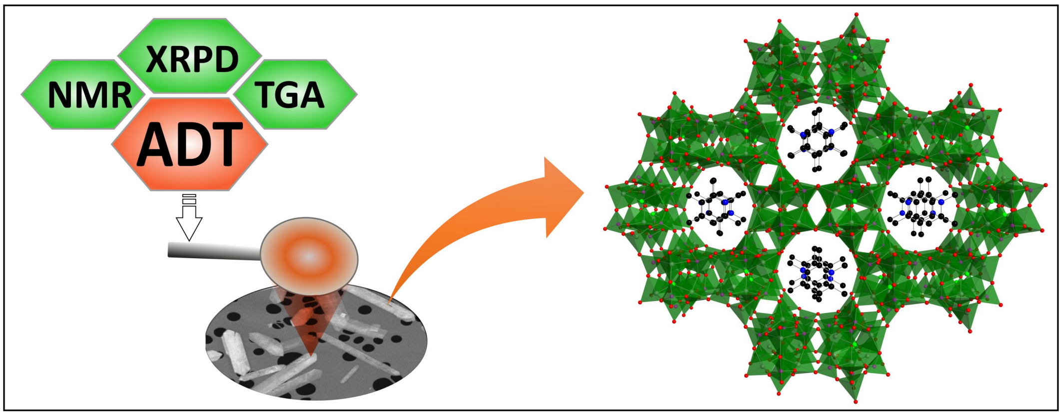

Highlights for the research:

- TMP-SSZ-51 prepared with a novel organic structure directing agent
- Successful location of the occluded organic cation by electron diffraction tomography
- Crystal structure refined from X-ray powder diffraction data
- ADT data acquisition by the fast data acquisition method

Abstract:

The structural diversity of porous materials is the reason for their broad application in industry and in many aspects of our daily lives. Structural investigations at the atomic level deliver a better understanding of the materials chemical and physical properties, necessary for optimization of present applications or even enabling the design of novel materials with desired features. In this work, we focus on detecting the position of the occluded organic structure directing agent in aluminophosphate SSZ-51 by electron diffraction tomography. Nanocrystals of SSZ-51 were synthesized using a new organic template 1,2,6-trimethylpyridinium (TMP). Thermogravimetric analysis and temperature-dependent X-ray powder diffraction were performed to observe the calcination process. Solid-state ^{13}C-NMR confirmed the presence of the organic cation in as synthesized SSZ-51. Electron diffraction datasets were collected within 13 minutes for a tilt range of ±60° using a recently developed fast data acquisition method. Structure determination using a combination of electron diffraction tomography and X-ray powder diffraction allowed locating the organic cation in the pore volume of TMP-SSZ-51.

1. Introduction

Microporous materials, a class of solid compounds with unique structural properties, have been investigated intensively since several decades. Due to interesting framework architectures comprising specific pores and modifiable solid building units, not only numerous new inorganic but also metal-organic or even pure organic novel porous materials are being designed and reported. As chemically and thermally stable inorganic materials, microporous zeolites and zeolite-type porous compounds show important applications in chemical and petrochemical industries,[1−5] e.g., as widely used catalysts in petroleum cracking, for selective catalytic reductions (SCRs), and in reforming processes. The introduction of organic structure directing agents (OSDAs) was one of the most successful factors for the synthesis and design of novel porous materials. For this reason, reliable elucidation of their crystal structures, especially locating the position of occluded OSDAs in the structure, is important for the understanding of synthesis mechanisms and crystallization processes.

The conventional way to characterize crystal structures of porous materials is to utilize X-ray diffraction methods: single crystal X-ray diffraction (XRD) and X-ray powder diffraction (XRPD). For instance, single crystal X-ray diffraction was applied to determine 4-dimethylaminopyridine in the crystal structure SSZ-51[6]. In fact, porous materials often do not grow as single crystals suitable for single crystal X-ray structure analysis. As an alternative X-ray powder diffraction was used to reveal the position of organic matter in the pores of microporous materials, e.g. (i) the pyrrolidine molecule in RUB-10 using difference electron density maps[7], (ii) guest molecules in SAPO-34/44 by means of Rietveld refinement combined with simulated annealing[8], and (iii) OSDAs in the channel-like voids of as synthesizes SSZ-55 by utilizing the approach of molecular modelling[9]. Nevertheless, it is difficult and often not possible to detect the OSDAs location directly by structure solution from one-dimensional XRPD data. Due to weak interactions between organic compounds and framework, the organic molecules/cations often show some (static or dynamic) disorder smearing out the low electron density of carbon and nitrogen atoms. Moreover, compared with the corresponding calcined phase, porous materials in the as-synthesized state possess more independent atoms, which complicate the crystal structure elucidation. A very powerful method to investigate complex structural details of porous materials, e.g. the exact location of organic SDAs , is based on using transmission electron microscopes (TEM) by combining electron diffraction and high-resolution imaging.[10] Within the last decade, several tomographic electron diffraction methods, best-known as automated diffraction tomography (ADT)[11,12] and rotation electron diffraction (RED)[13], were developed to collect three-dimensional electron diffraction data automatically. In combination with precession electron diffraction (PED)[14], the dynamical scattering effect can be reduced in order to gain a higher data quality. Electron diffraction tomography, comparable with traditional X-ray diffraction methods, focuses on data acquisition from single nanocrystals and enables complex structure elucidations involving e.g. ab initio structure determination of materials with large cell parameters [15,16] or detailed analysis of disorder phenomena[17,18]. The extremely small diffraction volume analyzed by ADT in scanning TEM (STEM) mode for low electron dose measurements increases the chance to detect defined OSDA atomic potentials.

In this work, we report the structural characterisation of as-synthesized aluminophosphate SSZ-51, focusing on the position of the OSDA by fast ADT technique. A novel organic structure directing agent - 1,2,6-trimethylpyridinium (TMP, as shown in **Figure 1**), which was recently reported for the successful preparation of RTH aluminosilicate zeolite[3], was used to synthesize templated SSZ-51. The position of the organic cation was directly determined from tomographic electron diffraction data. Details of the structure were subsequently analyzed by a Rietveld refinement against X-ray powder diffraction data. In addition, the thermal properties of TMP-SSZ-51, namely the expulsion of TMP molecules with increasing temperature, was investigated with thermogravimetric analysis and temperature dependent X-ray diffraction method.

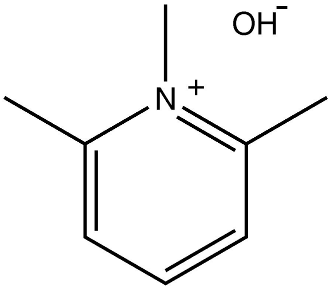

1,2,6-Trimethylpridinium hydroxide

Figure 1 The organic SDA 1,2,6-trimethylpyridinium hydroxide

2. Experimental

2.1 Synthesis

A synthetic reaction mixture with a molar ratio of $1Al_2O_3$: 2 TMPOH: $1P_2O_5$: 2HF: $40H_2O$ (TMPOH represents 1,2,6-trimethylpyridinium hydroxide) was transferred into an autoclave and sealed for further crystallization at 180 °C for 24 h. The final product was collected by filtration, washed with distilled water and dried at 100 °C for 4 h. The as-synthesized phase was calcined at 550 °C in air for 4h to obtain the guest-free SSZ-51.

2.2 Solid-state NMR spectroscopy

Solid-state NMR spectra of TMP-SSZ-51 were recorded on a Bruker Avance 400 DSX NMR spectrometer at a ^{13}C frequency of 100.55 MHz. A commercial two-channel 2.5 mm Bruker probe head at 20 kHz MAS was used for all experiments. For the solid state ^{1}H-^{13}C cross-polarisation (CP) MAS NMR experiments, an initial 90° pulse with 4.0 μs length and 3 s recycle delay were used. A ramped CP pulse (64-100%) with duration of 2 ms was used. A two pulse phase modulation (TPPM) ^{1}H decoupling scheme was used while acquiring the ^{13}C signal. Transients of 50 k were averaged for the CP experiments. The spectra were baseline-corrected and a broadening of 50 Hz was applied.

2.3 Thermal stability

Thermal stability experiments including differential scanning calorimetry and thermogravimetric analysis (DSC/TGA) were performed by a Perkin-Elmer TGA 7 unit in air with a heating rate of 10 K/min in the temperature range from room temperature to 815 °C.

2.4 X-ray powder diffraction

A Stadi-P diffractometer equipped with Ge(111) monochromator and a linear position-sensitive detector (PSD) using Cu$K_{\alpha 1}$ radiation (λ= 1.540598Å) was used for as-synthesized and calcined SSZ-51. The specimens were measured in borosilicate glass capillaries with a diameter of 0.7 mm at room temperature. The data was acquired with the program WinXPOW[19].

The temperature dependent XRPD measurements for TMP-SSZ-51 were performed on a STOE Stadi-P diffractometer equipped with a ceramic oven and an imaging plate position-sensitive detector using Cu$K_{\alpha 1}$ radiation. The measurements were carried out in a 0.7 mm glass capillary under static air. The templated phase TMP-SSZ-51was heated from 50 °C to 840 °C, while the XRPD data were collected.

2.5 TEM experiments

A small quantity of TMP-SSZ-51 was dispersed in ethanol with an ultrasonic bath. The dispersion was transferred into a caved tip with a pipette and then sprayed onto standard 300 mesh CuTEM grids with a thin amorphous carbon film, using an ultrasonic vaporizer.

Phase contrast TEM, scanning TEM (STEM), energy dispersive X-ray (EDX) spectroscopy and fast automated diffraction tomography (Fast-ADT) measurements were carried out using a Tecnai F30 S-TWIN TEM equipped with a field emission gun and operated at 300 kV. A 10 μm condenser aperture, gun lens 8 and spot size 8 were used to reduce the electron dose rate on the sample and the beam size was set to 200 nm in diameter for electron diffraction pattern acquisition. The sample was cooled down to about 97 K using a cryo-transfer holder (model 914) filled with liquid N_2 after insertion into the TEM in order to increase the stability of the sample under the electron beam. TEM images and electron diffraction patterns were acquired with a 4k x 4k Gatan US4000 CCD camera (Gatan, Pleasanton, USA) with a hardware binning of 2. STEM images were collected using a Fischione high-angle annular dark field (HAADF) detector. Fast-ADT data were collected with an automated acquisition module developed for FEI and JEOL microscopes which allows the acquisition of high angular range tomographies (up to 140°) in around 15 minutes for conventional CCD cameras and fixed tilt step of 1°.[11] The crystal position was tracked in microprobe STEM mode and electron diffraction patterns were collected using the above settings. Fast-ADT series were collected automatically between -60° and 60° with a tilt step of 1° and an exposure time for each frame of 1.5 seconds. In order to experimentally integrate reflection intensities over the tilt wedge, Fast-ADT was coupled with precession electron diffraction (PED)[14,20], which was generated by a NanoMEGAS DigiStar unit. The precession angle of the beam was kept at 1°. Each dataset acquirement for TPM-SSZ-51 took about 13 minutes.

2.6 Crystal structure solution and refinement

- **Structure solution from ADT data**

Experimental electron diffraction data were reconstructed in ADT3D (eADT) software[12,20] and further evaluated to deliver crystallographic information as lattice parameters, crystal symmetry and indexed reflections with intensities. The found unit-cell parameters were refined with a Pawley fit against XRPD data for higher accuracy. The *ab initio* structure solution was carried out with direct methods approach implemented in SIR2014[21] based on the extracted reflection intensities from electron diffraction data.

- **Structure refinement against X-ray powder data**

Rietveld refinement was performed using the program TOPAS[22]. Initially, a Pawley refinement was performed to refine background, zero point error, unit cell parameters, peak width and peak asymmetry parameters.

In the Rietveld refinement of TMP-SSZ-51, the T-O bond lengths of the tetrahedral AlO_4 and PO_4 units were restrained for Al-O: 1.76 Å and P-O: 1.53 Å, bond angles T-O-T (T = Al or P) as 109.5°. In AlO_4F unit, bond lengths of Al-O were restrained as 1.80 Å and Al-F (Al2 – F1 and Al4 – F1) bond lengths as 1.92 Å. For the cation 1,2,6-trimethylpyridinium, the initial positions of C and N atoms as obtained from the structure solution were used for the refinement with restraints applied to bond lengths and bond angles. The restrained values for bond lengths and bond angles were extracted from a statistical mean value based on 53 crystal structures from Cambridge structural database (CSD)[23]. The values of isotropic thermal parameters of H atoms were constrained to be 1.2 times of those of the carbon atom forming the pyridine ring (C-Ar). The temperature factor for water oxygen atom was set as 5 times of the framework oxygen atom.

3. Results and Discussion

3.1 Sample overview

TMP-SSZ-51 consists of thin plate-like micro-sized crystals observed in STEM image (**Fig. 2a**). The crystals are stable during low beam illumination in TEM under cooling conditions. Strong and discrete diffracted spots were observed in electron diffraction patterns of TMP-SSZ51 and its calcined phase, indicating a high crystallinity of both materials, which were also confirmed by the XRPD data (**Fig. S1**). A semi-quantitative EDX analysis (**Fig. 2b**, **Table S1**) showed averaged ratios of O/(Al+P) = 2.1 and Al/P = 1.

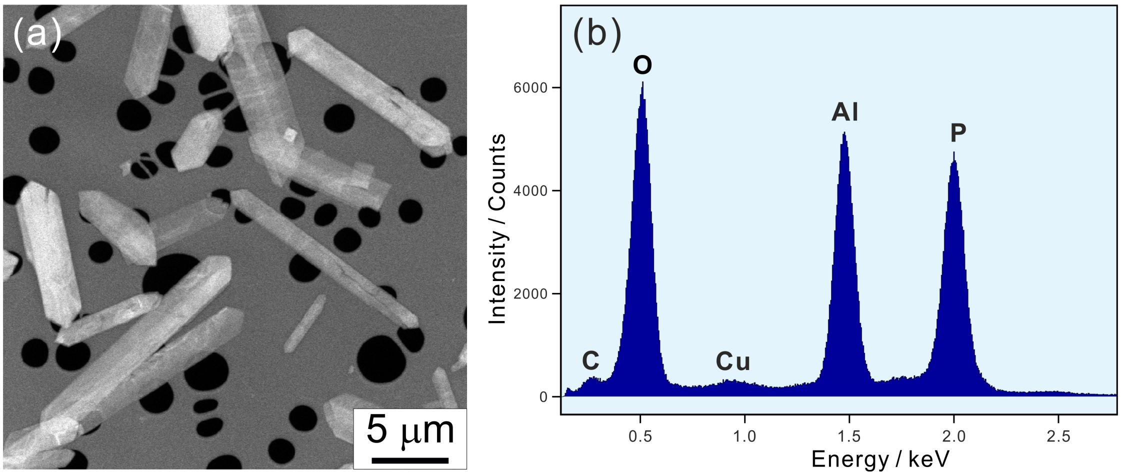

Figure 2 STEM image (a) and EDX spectrum (b) of TMP-SSZ-51. Cu TEM grid covered by carbon-film contributes the slight signals of C and Cu in (b).

3.2 Solid-state ^{13}C-NMR

Solid-state ^{13}C-NMR measurements were performed to detect the presence of the OSDA in the as-synthesized zeolites. **Figure 3** shows the solid-state ^{13}C-NMR spectrum of as TMP-SSZ-51. The ^{13}C-NMR spectrum of TMP-SSZ-51 presents five signals with chemical shifts of 157.5, 144.8, 126.8, 40.5 and 23.2 ppm, which are comparable with the corresponding values of the free cation in solution as reported in the literature (see *Supporting Information* of Mateescu et al[24]).

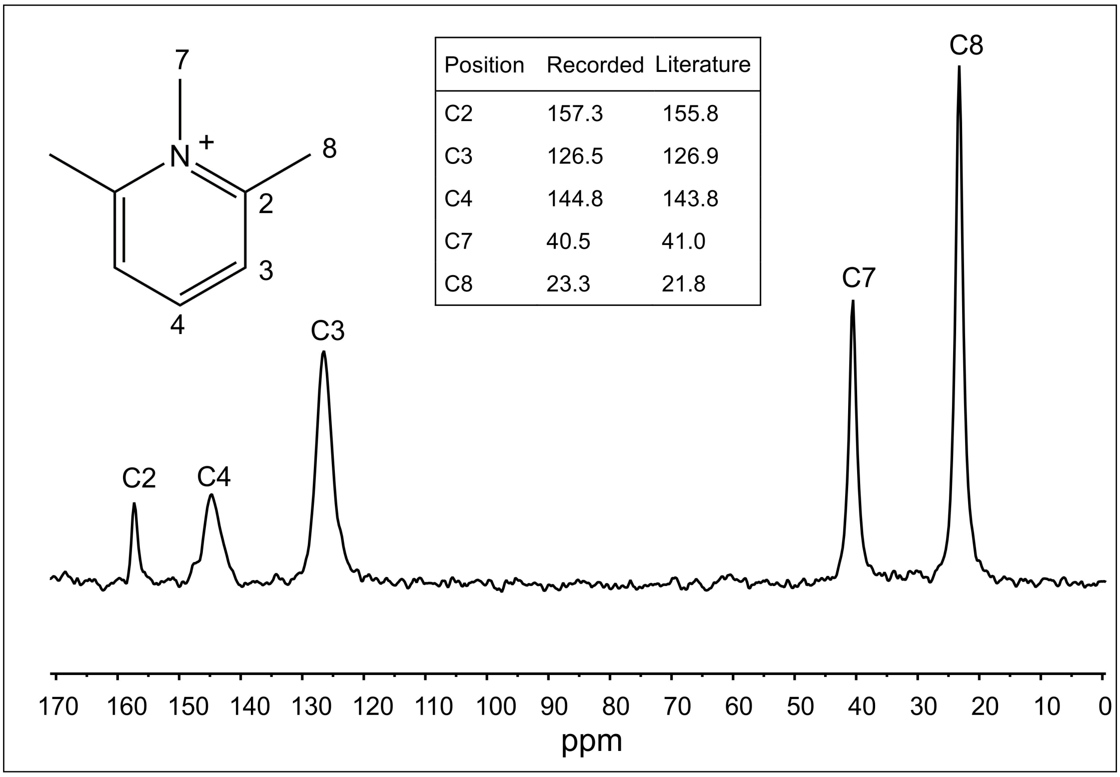

Position	Recorded	Literature
C2	157.3	155.8
C3	126.5	126.9
C4	144.8	143.8
C7	40.5	41.0
C8	23.3	21.8

Figure 3 13C-CP/MAS NMR spectrum of TMP-SSZ-51. The inserted table shows the recorded chemical shift values of the organic SDA in the pores of the aluminophosphate and the values of 1,2,6-trimethylpyridinium iodide as reported in the literature[24].

3.3 Thermal stability

The thermal behaviour of TMP-SSZ-51 was studied by differential scanning calorimetry and thermogravimetric analysis (DSC/TGA). The TG curve shows three steps of weight loss (**Figure 4**). The first step up to 100 °C is associated with a small quantity of adhesive water, while the second step between 100 °C and ca. 320 °C is due to the evaporation of free water molecules from the zeolite pores. The third step of weight loss was caused by the decomposition of the organic template, corresponding to the exothermic signals in the DTA curve. The burn-off of the organic matter starts at ca. 320 °C. This burn-off is associated with an exothermic signal having its maximum at ca. 440 °C. At about 720 °C the DSC curve indicates a phase transition (no change in weight) which was later identified by high-temperature XRPD measurements as the decomposition of the SSZ-51 framework.

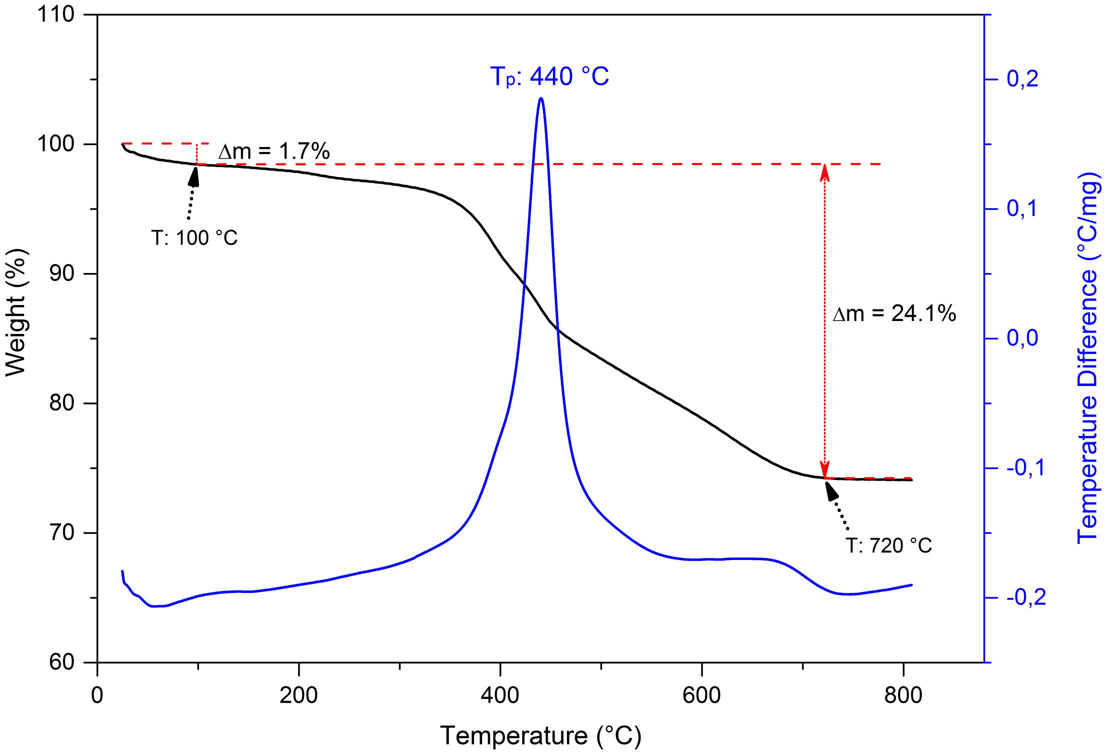

Figure 4 DSC/TG curves of TMP-SSZ-51. Tp: peak temperature .

3.4 Monitoring the calcination process of as-synthesized SSZ-51 by temperature-dependent X-ray powder diffraction

Temperature-dependent X-ray powder diffraction measurements (**Figure 5**) were performed from 50 °C to 840 °C in order to investigate the calcination process and the decomposition of the SSZ-51 framework at increasing temperature. There are three major changes visible in the powder diagram: The first event occurring with increasing temperature appears at ca. 300 °C. This is in line with the results of the DTA/TGA experiment showing that the organic template stays stable in the zeolite pores up to ca. 300 °C and after that begins to escape from the material. From about 300 °C the PXRD pattern changes. This is most prominent for the reflection at 14° which splits up to form two reflections indicating a change in symmetry as well as the first two reflections with increasing intensities during loss of organic material from the pores.

A second significant change (e.g., lower background) of the powder patterns after 400 °C is due to an artefact. At that temperature the sample was cooled down to RT (faulty program) and was heated up again by hand. Subsequently the recording of diagrams was continued using the same sample. In the temperature range between 400 °C and 720 °C the diagrams represent the guest-free SSZ-51 material (calcined phase). The guest-free SSZ-51 remains stable up to about 720 °C. At that temperature the reflections representing the SSZ-51 phase disappear and a few new peaks form (at 20.1°, 21.3, 22.8° 2theta), indicating the decomposition process of calcined SSZ-51. The new reflections prove the formation of a dense tridymite-type phase[25]. The observed phenomena are consistent with the results of DSC-TG measurement.

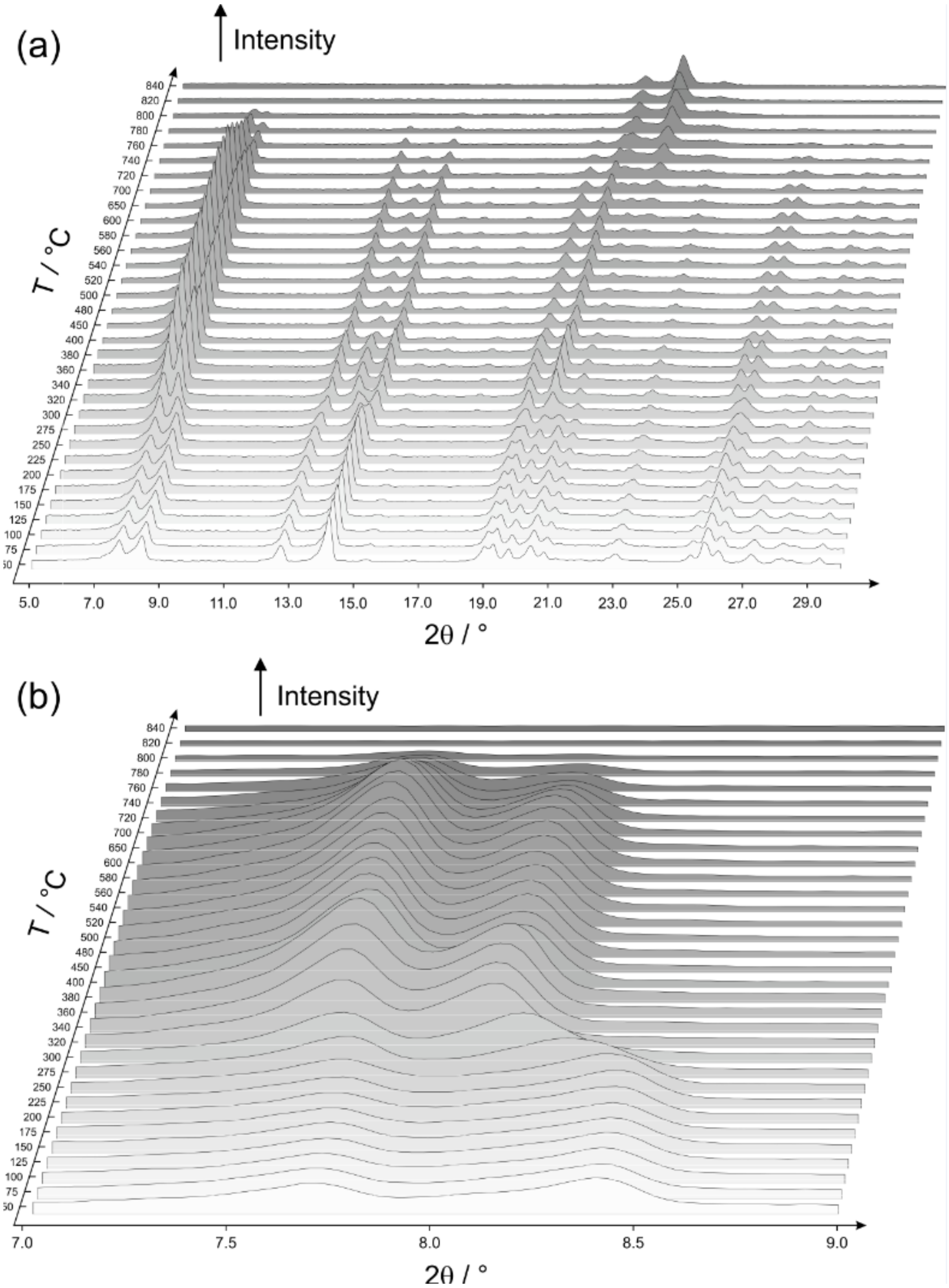

Figure 5 Temperature dependent X-Ray powder diffraction diagrams of the thermal decomposition of TMP-SSZ-51, showing the release of the organic cations as well as the decomposition of SSZ-51 at high temperature.

3.5 Structure determination of TMP-SSZ-51

- **Structure solution from ADT data**.

The reconstruction of ADT data (**Figure 6**) delivered a unit-cell with a = 21.54 Å, b = 13.81 Å, c = 14.32 Å, α = 90.4°, β = 100.7 °, γ = 89.8 °, which were further refined by a Pawley fit of the XRPD data for structure solution. Systematic extinctions for *hkl* reflections with $h + l =$

$2n$ indicated a *C*-centred monoclinic Bravais lattice. In addition, the reflection conditions as observed for *h0l* reflections with $l = 2n$ are indicative of a *c* glide-plane (**Figure 6**), associated with two possible space groups *Cc* (No. 9) and *C*2/*c* (No. 15).

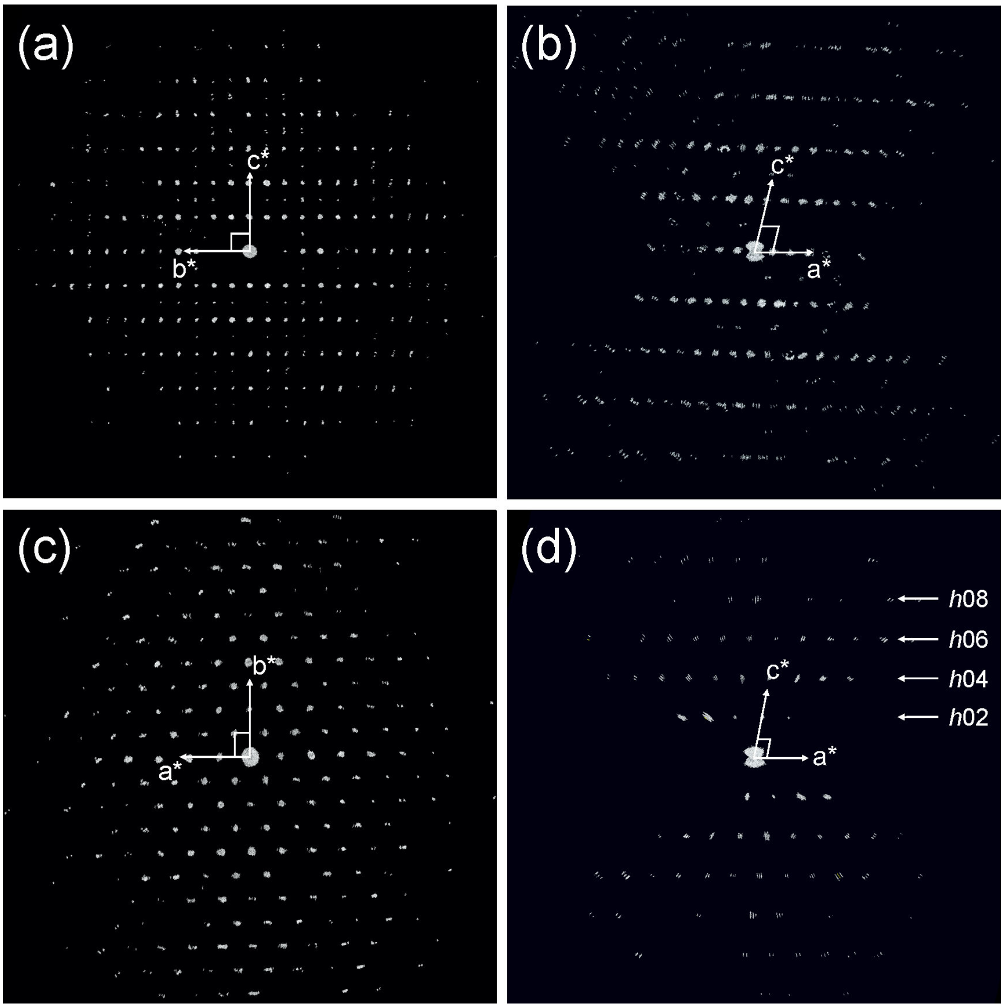

Figure 6 (a-c) Reconstructed three-dimensional diffraction volumes of TMP-SSZ-51 obtained from ADT data viewed down the three main axis. (d) *h0l* slice cut from 3D reciprocal space; symmetry rule: $k = 2n$ and $l = 2n$ in *h0l* zone.

A PED ADT dataset with a tilt range from -60 to +60 (**Table 1**) was used for crystal structure solution with direct methods. The *ab initio* structure solution converged to a final residual *R* of 18.14%. The structure solution delivered a well-resolved Fourier potential map (**Fig. 7**) showing not only all the atoms of the zeolite framework but also the atoms of the organic template in the pore.

The strong maxima from 2.41 to 1.88 $e^-/Å^3$ correspond to P and Al atoms, respectively. The maxima representing O and F atoms were detected with a scattering potential range of 1.64 down to 0.98 $e^-/Å^3$. The C and N atoms in the pores of the structure were detected as electron densities ranging from 0.94 to 0.38 $e^-/Å^3$. All the C and N atoms in 1,2,6-Trimethylpyridinium could be clearly detected from the structure solution. The ADT method is well suited to determine a complete structure model of a microporous material including even the atoms of weak scattering power (C, N). Only the hydrogen atoms could not be located. Such a structure model may directly be used as a starting model for a more detailed structure analysis e.g. by a Rietveld refinement.

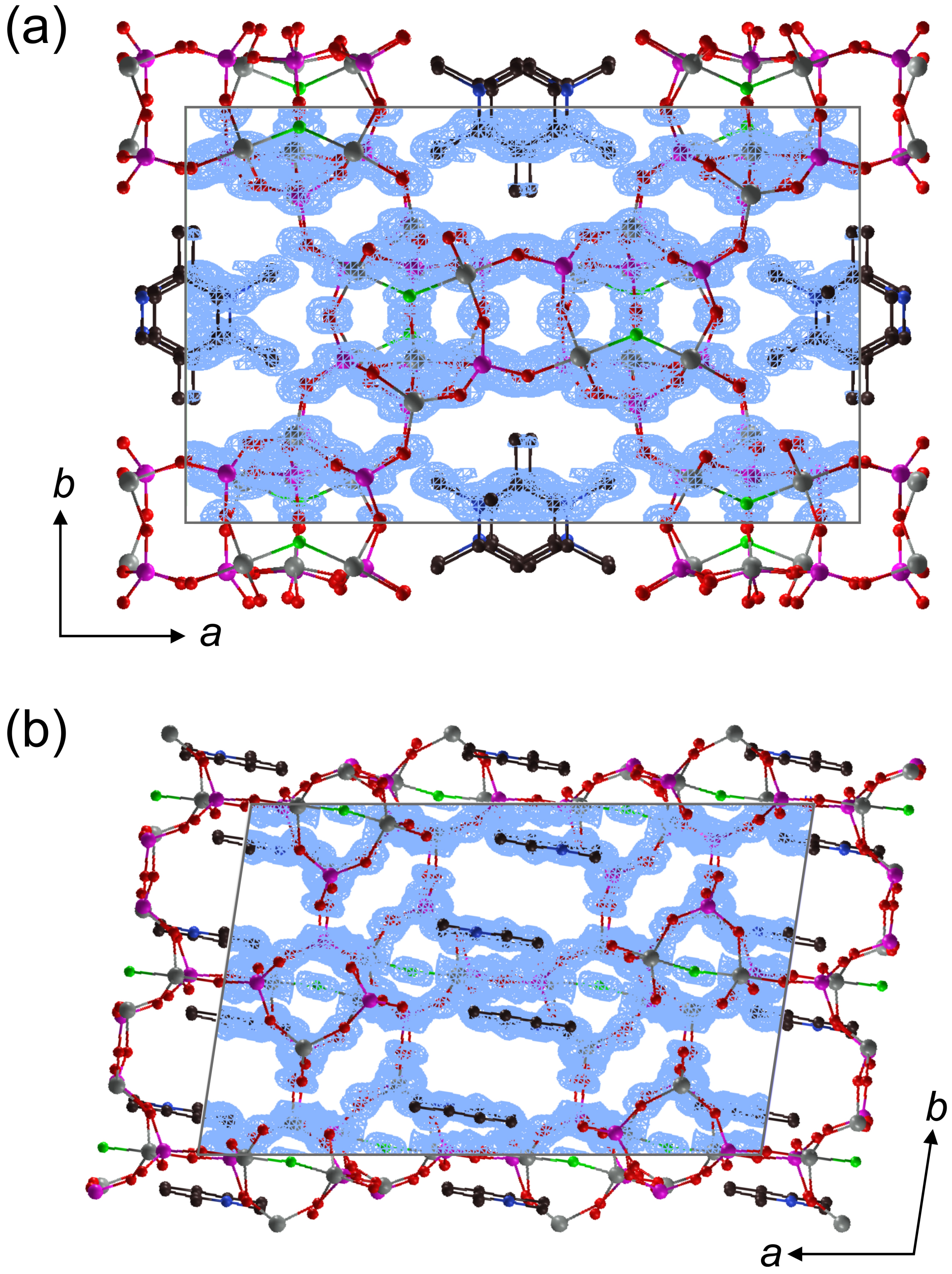

Figure7 Fourier potential map of TMP-SSZ-51 derived from structure solution in Sir2014 using ADT data with the overlaid atomic framework model viewed in [001] and [100] directions, respectively. Colour of atoms: Al (grey), P (lilac), O (red), F (green) C (black) and N (blue).

Table 1: Experimental parameters of electron diffraction dataset for structure solution of TMP-SSZ-51 in space group C2/c.

Tilt range (°)	-60/+60
No. of total reflections	9451
No. of independent reflections	3011
Reflection coverage (%)	72
Resolution (Å)	0.8
R_{int}	0.256
Overall U (Å^2)	0.027
Residual R (SIR2014)	0.195

- **Structure refinement from X-ray powder data**.

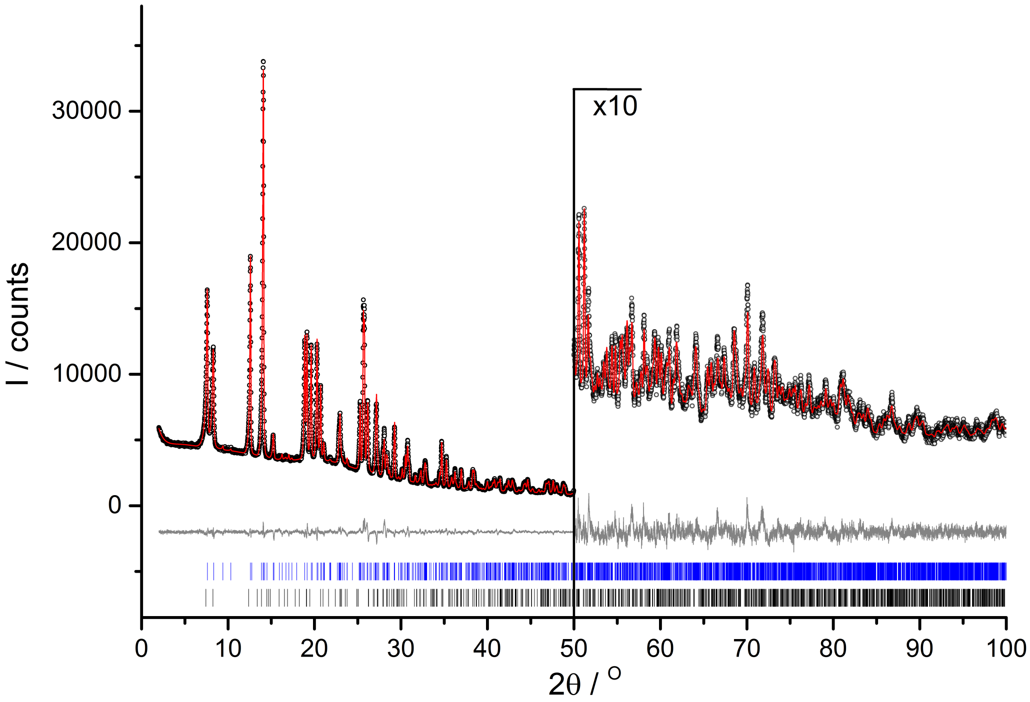

Figure 8 Plot of combined Rietveld refinement of SSZ-51. Observed powder diagram (black circles), simulated powder diagram (red solid line), difference profile (grey solid line), reflection positions (blue ticks for as-synthesized phase and black ticks for calcined phase). Change of the scales with factor 10 is indicated in the diagram.

The Rietveld refinement was carried out using the starting model obtained from the structure solution based on ADT data. However, the refinement was not satisfying. When performing the Pawley fit of TMP-SSZ-51 the presence of additional reflections at 7.6° and 8.3° 2θ became apparent (**Fig. S2**). Taking into consideration that these reflections were also visible in the temperature dependent X-ray powder diffraction experiments (**Figure 5b**) when the OSDA is released from the pores, this phenomenon indicates that a small part of the material or domains of the crystals do not contain the organic templates. These crystals or domains can be described by the calcined phase. The structure of calcined SSZ-51 could also be directly solved from ADT data based, however, on a monoclinic unit cell with c = 7.01 Å and space group symmetry $C2/m$ (**Fig. S3**). The guest free framework of calcined SSZ-51 still corresponds to the zeolite framework type SFO (**Fig. S4**). The structure of the calcined phase was used for a subsequent refinement. The combined Rietveld refinement including two phases, TMP-SSZ-51 and calcined SSZ-51, was performed from X-ray data and converged in a *R*-value with R_{wp} of 3.7%. The plot of Rietveld refinement is shown in . **Figure 8**. Selected crystallographic data are summarized in **Table 2**. The phase without template amounts to 6.8(2)% in the sample. The refinement led to a meaningful framework structure and an acceptable geometry of the organic template. Selected bond distances and angles are concluded in **Table S2**. All the independent 34 atoms except H atoms show reasonable temperature factors.

Table 2: Selected crystallographic data and refinement parameters for TMP-SSZ-51. Note that the parameters are based on a combined Rietveld refinement of TMP-SSZ-51 and calcined SSZ-51.

Compound	TMP-SSZ-51
Cell formula	$Al_{32}P_{32}O_{128}F_8 \bullet C_{64}N_8H_{96} \bullet (H_2O)_{2.93}$
Crystal system	Monoclinic
Space group (No.)	C 1 2/c 1 (15)
a (Å)	21.5370(5)
b (Å)	13.8795(3)
c (Å)	14.2658(3)
α (°)	90
$ß$ (°)	99.889 (1)
γ (°)	90
V (Å^3)	4201.1(1)
Z	8
D_{calc} (Mg•m^{-3})	2.008
T (K)	294
Radiation type	Cu $K\alpha_1$
Wavelength (Å)	1.540598
θ_{max} /°	50
R_{Bragg} /%	1.815
R_p /%	2.631
R_{wp} /%	3.725
R_{exp} /%	2.181
GOF	1.708

3.6. Structure description of TMP-SSZ-51.

The fluorine ion not only acts as mineralizer in the synthesis but is included in the structure of TMP-SSZ-51 generating a negatively loaded framework. F atoms bridge two Al atoms (Al2 and Al4) in the crystal structure forming AlO_4F trigonal bipyramids (**Fig. S5**). The other Al atoms (Al1 and Al3) are four-coordinated by O atoms forming AlO_4 tetrahedra. All P atoms are fourfold coordinated by O atoms with tetrahedron geometry. The Al containing polyhedra are interconnected with PO_4 groups constructing a microporous 3D framework of zeolite type SFO[6,26]. The 2D pore system consists of wide 12-ring channels (free diameter ca. 7.0 Å) running along the c axis which intersect with narrow 8-ring channels (free diameter ca. 3.8 Å). (**Fig. 9**). 1,2,6-trimethylpyridinium molecules fill the straight 12-ring channels and are stacked along c axis with interplanar distances from 3.5 Å to 3.7 Å (**Fig. 10**), which are in the typical range of distances observed for π–π interactions (about 3.3 - 3.8 Å)[28]. The atoms of the organic cations show larger temperature factors (B_{iso}) than the framework atoms, indicating that the stacked organic molecule possess some free moving space.

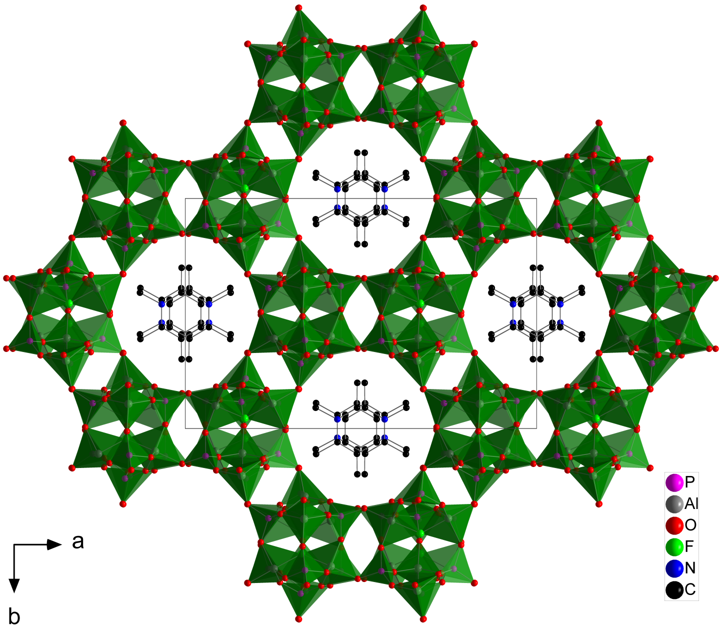

Figure 9 Crystal structure of TMP-SSZ-51 with AlO_4, AlO_4F and PO_4 polyhedron viewed along the crystallographic ***c*** axis. H atoms are omitted for clarity.

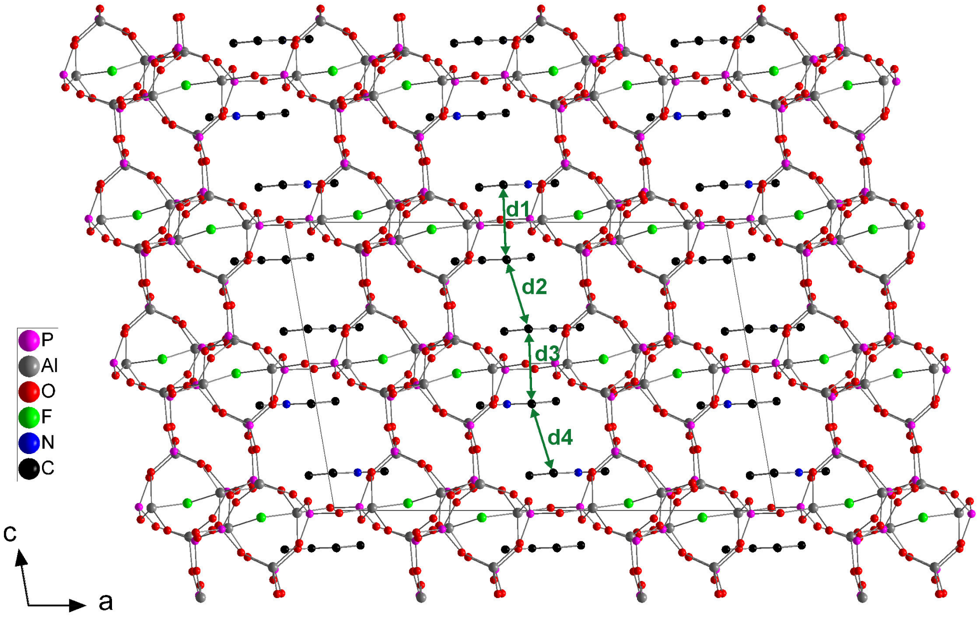

Figure 10 Crystal structure of TMP-SSZ-51 viewed along the crystallographic b axis. The distances between neighbouring molecules are highlighted: d1 = 3.63 Å, d2 = 3.61 Å d3 = 3.63 Å d4 = 3.59 Å, respectively. H atoms are omitted for clarity.

Until now, most of the SSZ-51 type porous materials were synthesized using 4-dimethylaminopyridine (DMAP) as organic structure directing agents[6,26−−29]. Only Morris et al.[6] performed a structure analysis on DMAP-SSZ-51. In addition, Park et al.[30] found that 1,2,3,4-tetramethyl-imidazolium and 1,2,3,4,5-pentamethyl-imidazolium cations could also direct the formation of aluminophosphate SSZ-51; but no structure analysis is available of these two as-synthesized materials. Now, another OSDA, 1,2,6-trimethylpyridinium, was successfully used in this study. In all cases, the OSDA molecules – both types possessing an aromatic ring – arrange with π-π stacking interactions leading to a rod-shaped "composite template". It can be assumed that the "composite template" provokes the formation of the channels in the SSZ-51 structure during the crystallization process. The use of such a "composite template" is quite unique when trying to synthesize microporous materials. Typically, individual molecules/cations act as OSDAs; e.g. long chain-like molecules of a specific thickness like e.g. 1,3-dipiperidinium-propane are used as the OSDA to direct the hydrothermal crystallization of aluminophosphates or zeolites in such a way that structures with a pore system comprising 12-ring channels are formed.

4. Conclusion

In this study, aluminophosphate SSZ-51 (TMP-SSZ-51) was prepared as a pure phase with a novel organic template 1,2,6-trimethylpyridinium. The calcination process as investigated by thermogravimetric analysis and temperature-dependent X-ray powder diffraction. Solid-state ^{13}C-NMR spectroscopy confirmed the existence of organic molecule inside the porous material SSZ-51. The structure determination, carried out by a combination of single crystal electron diffraction tomography and X-ray powder diffraction, elucidated directly the accurate ordered position of the organic cation - used as structure directing agent - in the monoclinic structure of as-synthesized SSZ-51. The study shows that electron diffraction tomography, especially for fast data acquisition from a single nanosized crystal, can serve as a reliable method to determine the position of organic molecules in inorganic porous materials and can be further applied for the structural elucidation of new nano crystalline porous materials.

Acknowledgements

Haishuang Zhao is grateful for financial support of the Carl Zeiss Stiftung. Dr. Mihail Mondeshki (University of Mainz, Germany) is acknowledged for the acquisition of solid-state NMR data.

References

[1] J. Liang, H. Li, S. Zhao, W. Guo, R. Wang, M. Ying, *Appl. Catal.* **1990**, *64*, 31–40.

[2] S. G. Hedge, P. Ratnasamy, L. M. Kustov, V. B. Kazansky, *Zeolites* **1988**, *8*, 137–141.

[3] H. Xu, Q. Wu, Y. Chu, J. Jiang, L. Zhang, S. Pan, C. Zhang, L. Zhu, F. Deng, X. Meng, et al., *J. Mater. Chem. A* **2018**, *6*, 8705–8711.

[4] B. P. C. Hereijgers, F. Bleken, M. H. Nilsen, S. Svelle, K.-P. Lillerud, M. Bjørgen, B. M. Weckhuysen, U. Olsbye, *J. Catal.* **2009**, *264*, 77–87.

[5] D. Cheng, X. Zhao, F. Chen, X. Zhan, *Catal. Commun.* **2009**, *10*, 1450–1453.

[6] R. E. Morris, A. Burton, L. M. Bull, S. I. Zones, *Chem. Mater.* **2004**, *16*, 2844–2851.

[7] B. Marler, U. Werthmann, H. Gies, *Microporous Mesoporous Mater.* **2001**, *43*, 329–340.

[8] N. Yan, H. Xu, W. Zhang, T. Sun, P. Guo, P. Tian, Z. Liu, *Microporous Mesoporous Mater.* **2018**, DOI 10.1016/j.micromeso.2018.01.002.

[9] A. Burton, R. J. Darton, M. E. Davis, S.-J. Hwang, R. E. Morris, I. Ogino, S. I. Zones, *J. Phys. Chem. B* **2006**, *110*, 5273–5278.

[10] T. Willhammar, Y. Yun, X. Zou, *Adv. Funct. Mater.* **2014**, *24*, 182–199.

[11] U. Kolb, T. Gorelik, C. Kübel, M. T. Otten, D. Hubert, *Ultramicroscopy* **2007**, *107*, 507–513.

[12] U. Kolb, T. Gorelik, M. T. Otten, *Ultramicroscopy* **2008**, *108*, 763–772.

[13] D. Zhang, P. Oleynikov, S. Hovmöller, X. Zou, *Z Krist.* **2010**, *225*, 94–102.

[14] R. Vincent, P. A. Midgley, *Ultramicroscopy* **1994**, *53*, 271–282.

[15] J. Jiang, J. L. Jorda, J. Yu, L. A. Baumes, E. Mugnaioli, M. J. Diaz-Cabanas, U. Kolb, A. Corma, *Science* **2011**, *333*, 1131–1134.

[16] T. Rhauderwiek, H. Zhao, P. Hirschle, M. Döblinger, B. Bueken, H. Reinsch, D. D. Vos, S. Wuttke, U. Kolb, N. Stock, *Chem. Sci.* **2018**, *9*, 5467–5478.

[17] H. Zhao, Y. Krysiak, K. Hoffmann, B. Barton, L. Molina-Luna, R. B. Neder, H. J. Kleebe, T. M. Gesing, H. Schneider, R. X. Fischer, et al., *J. Solid State Chem.* **2017**, *249*, 114–123.

[18] Y. Krysiak, B. Barton, B. Marler, R. B. Neder, U. Kolb, *Acta Crystallogr. Sect. Found. Adv.* **2018**, *74*, 93–101.

[19] STOE & Cie GmbH, *STOE WinXPOW 210* **2004**, Darmstadt, Germany.

[20] E. Mugnaioli, T. Gorelik, U. Kolb, *Ultramicroscopy* **2009**, *109*, 758–765.

[21] M. C. Burla, R. Caliandro, B. Carrozzini, G. L. Cascarano, C. Cuocci, C. Giacovazzo, M. Mallamo, A. Mazzone, G. Polidori, *J. Appl. Crystallogr.* **2015**, *48*, 306–309.

[22] A. Coelho, *TOPAS Acad. User Man.* **2007**, Brisbane, Australia.

[23] F. H. Allen, *Acta Crystallogr. B* **2002**, *58*, 380–388.

[24] M. Mateescu, I. Nuss, A. Southan, H. Messenger, S. V. Wegner, J. Kupka, M. Bach, G. E. M. Tovar, H. Boehm, S. Laschat, *Synthesis* **2014**, *46*, 1243–1253.

[25] H. A. Graetsch, *Acta Crystallogr. C* **2001**, *57*, 665–667.

[26] G. Cao, M. Afeworki, G. J. Kennedy, K. G. Strohmaier, D. L. Dorset, *Acta Crystallogr. B* **2007**, *63*, 56–62.

[27] S. Pai, B. L. Newalkar, N. V. Choudary, *Microporous Mesoporous Mater.* **2006**, *96*, 135–140.

[28] S. M. Pai, B. L. Newalkar, N. V. Choudary, *Microporous Mesoporous Mater.* **2008**, *112*, 357–367.

[29] S. M. Pai, B. L. Newalkar, N. V. Choudary, *J. Porous Mater.* **2009**, *16*, 119–127.

[30] G. T. Park, D. Jo, N. H. Ahn, J. Cho, S. B. Hong, *Inorg. Chem.* **2017**, *56*, 8504–8512.

List of Publications

Papers

10. **H. Zhao**, H. Xu, B. Marler, S. Plana-Ruiz, L. Fink, E. Alig, X. Meng, F-S. Xiao and U. Kolb. "Detection of organic cations in the pores of aluminophosphate SSZ-51 by electron diffraction tomography – elucidating the effect of molecular stacking." **2019**. [Submitted]
9. S. Leubner, **H. Zhao**, N. Van Velthoven, M. Henrion, H, Reinsch, D. De Vos, U. Kolb and N. Stock. "Expanding the Variety of Zirconium Secondary Building Units for Metal-organic Frameworks." *Angewandte Chemie*, **2019**. DOI: 10.1002/ange.201905456.
8. A. Bodach, **H. Zhao**, N. Liu, E. Alig, G. Manolikakes, U. Kolb and L. Fink. "Electron diffraction tomography and X-ray powder diffraction on photoredox catalyst PDI." *CrystEngComm*, **2019**. DOI: 10.1039/C8CE02026D
7. H. Petersen, **H. Zhao**, L. Robben, Ute Kolb and T. M. Gesing. "An average structure model of the Intermediate Phase between Sodalite and Cancrinite." *Zeitschrift für Kristallographie - Crystalline Materials*, **2018**, DOI: 10.1515/zkri-2018-2114
6. L. Konrad, **H. Zhao**, C. Gspan, J. Rehr, U. Kolb, M. Lattemann and G. Kothleitner. "A consisten path for phase determination based on transimission electron microscopy techniques and supporting simulations." *Micron*, **2018**, 115, 41-49. DOI; 10.1016/j.micron.2018.08.007
5. J. Zhang, L. Wang, B. Zhang, **H. Zhao**, U. Kolb, Y. Zhu, L. Liu, Y. Han, G. Wang, C. Wang, D. Su, B. Gates, and F, Xiao. "Sinter-resistant metal nanoparticle catalysts achieved by immobilization within zeolite crystals via seed-directed growth ." *Nature Catalysis*, **2018**, 7, 540–546. DOI: 10.1038/s41929-018-0098-1
4. T. Rhauderwiek, **H. Zhao**, P. Hirschle, M. Döblinger, B. Bueken, H. Reinsch, D. De Vos, S. Wuttke, U. Kolb, and N. Stock. "Highly stable and porous porphyrin-based zirconium and hafnium phosphonates - Electron crystallography as an important tool for structure elucidation." *Chemical Science*, **2018**, 9, 5467-5478. DOI: 10.1039/c8sc01533c
3. **H. Zhao**, A. Bodach, M. Heine, Y. Krysiak, J. Glinnemann, E. Alig, L. Fink, and M. U. Schmidt. "4-Cyanopyridine, a versatile mono-and bidentate ligand. Crystal structures of related coordination polymers determined by X-ray powder diffraction." *CrystEngComm*, **2017**, 19, 2216-2228. DOI: 10.1039/C7CE00425G
2. **H. Zhao**, Y. Krysiak, K. Hoffmann, B. Barton, L. Molina-Luna, R. Neder, H. J. Kleebe, T. M. Gesing, H. Schneider, R. X. Fischer, and U. Kolb. "Elucidating structural order and disorder phenomena in mullitetype $Al_4B_2O_9$ by automated electron diffraction

tomography." *Journal of Solid State Chemistry*, **2017**, 249, 114-123. (Front cover) DOI: 10.1016/j.jssc.2017.02.023

1. K. Hoffmann, T. J. N. Hooper, **H. Zhao**, U. Kolb, M. M. Murshed, M. Fischer, H. Lührs, G. Nénert, P. Kudějová, A. Senyshyn, H. Schneider, J. V. Hanna, T. M. Gesing, and R. X. Fischer. "Crystal chemical characterization of mullite-type aluminum borate compounds." *Journal of Solid State Chemistry*. **2017**, 247, 173-187. DOI: 10.1016/j.jssc.2016.12.027

Conference Presentations

6. "Structure characterization of nano crystalline materials using transmission electron microscopy." *30th Annual Meeting of Association of Chinese Chemists and Chemical Engineers in Germany*, **2018**, Karlsruhe. [*Oral presentation*]
5. "Structural characterization of porous materials by electron diffraction tomography." *International Symposium on Zeolites and Microporous Crystals*, **2018**, Yokohama, Japan. [*Oral presentation*]
4. "Crystal structures of two zirconium metal-organic frameworks." *26th Annual Meeting of the German Crystallographic Society*, **2018**, Essen. [*Oral presentation*]
3. "Structural characterization of porous functional materials using a combination of electron diffraction tomography, HRTEM and powder X-ray diffraction." *25th Annual Meeting of the German Crystallographic Society*, **2017**, Karlsruhe. [*Oral presentation*]
2. "Structural characterisation of $Al_4B_2O_9$ by automated electron diffraction tomography." *24th Annual Meeting of the German Crystallographic Society*, **2016**, Stuttgart. [*Oral presentation*]
1. "Structural investigation of mullite-type $Al_4B_2O_9$ by electron diffraction." *30th European Crystallography Meeting*, **2016**, Basel, Schweiz. [*Poster presentation*]

Erklärung

Hiermit erkläre ich, dass ich die vorliegende Arbeit im Zeitraum von August 2014 bis März 2019 unter der Leitung von PD. Dr. Ute Kolb an der Johannes Gutenberg-Universität Mainz selbstständig angefertigt habe. Ich versichere, die vorliegende Arbeit selbstständig und ohne fremde Hilfe verfasst zu haben. Alle verwendeten Quellen und Hilfsmittel sind vollständig angegeben.

Mainz, den 8. September 2019

Haishuang Zhao